EPFL

Snowfall microphysics: a dual-frequency and Doppler spectral radar perspective

Anne-Claire Marie BILLAULT--ROUX

■ École
polytechnique
fédérale
de Lausanne

2023

Acknowledgments

This PhD journey has been full of memorable experiences. It was particularly fulfilling to be able to participate in almost an entire research pipeline, going from campaign preparation and instrument deployment to data processing and exploration, to finally reach scientific outcomes. For this opportunity, I thank, first and foremost, my advisor Prof. Alexis Berne. His unwavering support, trust, and encouragements, together with his scientific insights, rigor, and curiosity, have made these PhD years enriching both on a professional and a personal level.

I would like to thank the members of my thesis jury, Profs. Stephen Nesbitt, Heike Kalesse-Los, Michael Lehning, and Dr. Satoshi Takahama, for their availability to review the manuscript and for their useful comments.

I greatly appreciated being a part of the ICE GENESIS project, which gave me the chance to collaborate with international partners in academia and in the industry. My special thanks go to Fabien Dezitter and Prof. Alfons Schwarzenboeck, who coordinated the work package which I took part in. As a doctoral student, this cooperation with scientists of various fields and expertise—experimentalists, modelers, experts in fluid mechanics or in-situ imaging—was instructive and mind-opening.

Before I started this thesis, my experience on the field and with research instruments, let alone meteorological radars, was virtually nonexistent. I am genuinely grateful to Antoine Wiedmer and Michael Monnet for their immense help in instrument maintenance, without which a successful field campaign would not have been possible. I would particularly like to acknowledge their resourcefulness and competence in solving delicate technical issues in often tight schedules.

The last four years would certainly have been less colorful without my fantastic colleagues at LTE. I would like to thank the lab members for eager scientific discussions and for collaborations during field work, even at times when Covid made human interactions trickier. Beyond this, I am grateful for the many good moments spent together, over lunch and coffee breaks, climbing sessions, movie nights, winter outings or at conferences. I would especially like to thank Alfonso, from whom I learned most of what I know about radars, and who has been incredibly patient when passing on to me his knowledge of the lab's instruments. My

i

Abstract

Snowfall is an essential component of the hydrological cycle, as it is involved in most precipitation on Earth, either directly as snow falling to the ground or indirectly as rain melted from snow. At the same time, the ice phase of clouds and precipitation is a key contributor to the Earth's radiative budget, making it a crucial aspect of climate-oriented research. Properly modeling snowfall for weather and climate applications requires knowledge of the "microphysics of snowfall", that is, a microscale description of snow particles and of the mechanisms by which they form, grow, and decay. Among different approaches to studying snowfall microphysics, remote sensing techniques and, in particular, meteorological radars, offer decisive insights. The interpretation of radar variables reveals information on the microphysical properties of hydrometeors over large spatial areas and in the vertical dimension. In addition to standard scalar variables, the Doppler spectrum measured by vertically-pointing radars allows separating the radar echo of hydrometeors as a function of their downward velocity. This discloses how radar signals are distributed between large, fast-falling, and small, slow-falling particles, and enables more refined analyses of snowfall.

The goal of this thesis is to investigate the microphysical properties and processes of snowfall by relying primarily on measurements from radars transmitting at different frequencies and on radar Doppler spectra. First, a multi-sensor dataset of in situ and remote sensing measurements of snowfall is presented, which was collected during the ICE GENESIS campaign in the Swiss Jura Mountains in January 2021. Methodological developments are then introduced, making use of cutting-edge machine-learning techniques to retrieve cloud and snowfall properties from remote sensing measurements. Specifically, one algorithm is developed to estimate the liquid water path, i.e., the integrated liquid water content in the atmospheric column, from radiometer brightness temperature. This quantification of atmospheric liquid water is of high relevance to snowfall studies, as microphysical processes are largely affected by mixed-phase conditions, wherein ice particles coexist with supercooled liquid water droplets. We then propose a novel framework to retrieve a number of snowfall microphysical properties from dual-frequency radar Doppler spectra, relying on a two-step, physics-driven deep learning approach. In comparison with existing methods, this framework relaxes the need for certain prior assumptions on microphysical properties, or on perfect beam alignment and non-turbulent atmosphere. The retrieval is evaluated against in situ measurements from

Abstract

ICE GENESIS, and the encouraging—albeit not perfect—results pave the way for advanced characterizations of snowfall properties on larger datasets. Finally, we focus on a specific snowfall event of ICE GENESIS. Through a detailed analysis of multi-frequency and Doppler spectral measurements, we propose interpretations of the complex signatures observed, which reveal the occurrence of distinct ice production and growth processes.

Altogether, this thesis contributes to an improved characterization of snowfall microphysics through different perspectives, with (i) an open-access multi-sensor dataset of measurements in snowfall, (ii) new methodological tools to retrieve cloud and snowfall properties, (iii) a case study that underlines the relevance of radar measurements to improve our understanding of microphysical processes.

Résumé

Les chutes de neige ont un rôle essentiel dans le cycle hydrologique. Elles contribuent de façon significative aux précipitations sur Terre – dont plus de la moitié sont sous forme de neige, ou de pluie issue de neige – et permettent de constituer en hiver un réservoir d'eau douce dans les régions montagneuses, sous la forme du manteau neigeux. En outre, dans l'atmosphère, les nuages en phase glace ou mixte ont un rôle radiatif majeur, et pourtant encore mal compris. Dans ce contexte, en vue d'améliorer les modèles météorologiques et climatiques, il est nécessaire de s'intéresser à la « microphysique des chutes de neige », c'est-à-dire de décrire avec précision les particules de neige et les processus qui gouvernent leur formation et leur croissance. Les radars météorologiques offrent un éclairage précieux sur cette question, en renseignant sur les propriétés microphysiques des hydrométéores à travers de grandes étendues spatiales. En complément des variables radar usuelles, le spectre Doppler mesuré à incidence verticale permet de distinguer la contribution des particules au signal radar en fonction de leur vitesse de chute. En révélant les différences d'écho radar entre les petites particules, à faible vitesse terminale, et les gros flocons tombant rapidement, ce spectre permet d'affiner les analyses microphysiques.

Cette thèse est consacrée à l'étude de la microphysique des chutes de neige au moyen de mesures radars à deux fréquences et de spectres Doppler. Une première partie du manuscrit présente le jeu de données issu de la campagne ICE GENESIS, qui s'est tenue dans le Jura suisse en janvier 2021, avec des mesures in situ et par télédétection. Nous présentons ensuite des développements méthodologiques utilisant des techniques d'apprentissage automatique pour quantifier les propriétés de la neige à partir de mesures de télédétection. Plus précisément, un premier algorithme est mis en place pour estimer la quantité d'eau liquide dans une colonne atmosphérique à partir de mesures d'un radiomètre. Dans le cadre de l'étude des chutes de neige, il est en effet primordial de quantifier l'eau nuageuse surfondue, qui influence fortement les processus microphysiques. Ensuite, nous présentons une nouvelle méthode d'apprentissage profond permettant d'estimer certaines propriétés microphysiques de la neige à partir de spectres Doppler double-fréquence. Cette restitution est évaluée grâce aux mesures in situ de ICE GENESIS ; sans être parfaits, les résultats sont encourageants et ouvrent la porte à une caractérisation détaillée des propriétés microphysiques de la neige sur des jeux de données plus volumineux. La dernière partie de cette thèse porte sur l'étude d'un

Résumé

épisode neigeux précis de ICE GENESIS. Une analyse poussée des mesures double-fréquence et des spectres Doppler permet de dégager des interprétations microphysiques, et de révéler que différents processus sont impliqués dans la formation des cristaux de glace au cours de cet événement.

Dans l'ensemble, cette thèse participe à une meilleure caractérisation de la microphysique des chutes de neige à partir de mesures radar, et ce à travers différents prismes : par la collecte d'un jeu de données partagé à la communauté scientifique, par des développements méthodologiques permettant de quantifier les propriétés de la neige nuageuse et précipitante, et par un éclairage qualitatif sur les processus microphysiques apporté à travers une étude de cas.

Contents

Contents

Contents

List of acronyms and symbols

The following table lists the most important acronyms and notations of physical or mathematical quantities used throughout the thesis. For acronyms and symbols of physical and mathematical quantities (e.g., LWP, ρ_{hv}), the most frequently used unit is given ([-] if the quantity is dimensionless). For other abbreviations (e.g., ERA5), the unit field is left empty.

Symbol/ Acronym	Units	Description
2D-S		2-dimensional stereo probe
α_a	$[\text{m}^{2-\beta_a}]$	Prefactor of snow area-size power law
β_a	[-]	Exponent of snow area-size power law
$\theta_{3\text{dB}}$	[°] or [rad]	3-dB (half-power) beam width
λ	[m] or [mm]	Radar wavelength
μ	[-]	Shape parameter of the gamma distribution
ν	[GHz]	Radar frequency
ρ_b	$[\text{g m}^{-3}]$	Hydrometeor bulk density
ρ_{hv}	[-]	Co-polar correlation coefficient
a_m	$[\text{kg m}^{-b_m}]$	Prefactor of snow mass-size power law
A	$[\text{m}^2]$	Cross-section area of a particle
A_r	[-]	Hydrometeor aspect ratio
ASL		Above mean sea level
b_m	[-]	Exponent of snow mass-size power law
c_0	$[\text{m s}^{-1}]$	Speed of light in vacuum
CDP-2		Cloud droplet probe
COSMO		Consortium for Small-scale MOdeling
COSMO-1		COSMO model at 1-km horizontal grid resolution
D	[m]	Maximum dimension of hydrometeor
D_0	[m]	Mean diameter of a negative exponential PSD
DFR	[dB]	Dual-frequency reflectivity ratio (unless specified, X- and W-band)
DDA		Discrete dipole approximation
DSD		Drop size distribution
ECMWF		European Center for Medium-range Weather Forecasts
e.m.		electromagnetic

ERA5		Fifth generation of the ECMWF atmospheric re-analyses dataset
FMCW		Frequency-modulated continuous wave
GPS		Global positioning system
HATPRO		Humidity And Temperature PROfiler
HM		Hallett-Mossop
HVPS		High-volume precipitation spectrometer
ICE-POP		International Collaborative Experiment for PyeongChang Olympic and Paralympics
ICNC	$[m^{-3}]$	Ice crystal number concentration
INP		Ice nucleating particle
IQR		Interquartile range
IWC	$[kg\,m^{-3}]$	Ice water content
IWV	$[kg\,m^{-2}]$	Integrated water vapor
JFJ		Jungfraujoch
LCDF		La Chaux-de-Fonds
LW		Liquid water
LWC	$[kg\,m^{-3}]$	Liquid water content
LWP	$[g\,m^{-2}]$	Liquid water path
MASC		Multi-Angle Snowflake Camera
MDV	$[m\,s^{-1}]$	Mean Doppler velocity
MMD	$[mm]$	Median mass diameter
MPC		Mixed-phase cloud
MRR		Micro Rain Radar
MSE		Mean squared error
MXPol		Mobile X-band Polarimetric radar
NCEP		National Centers for Environmental Prediction
NN		Neural network
N_T	$[m^{-3}]$	Total number concentration (= ICNC if ice)
PRF	$[s^{-1}]$	Pulse repetition frequency
P	$[Pa]$	Pressure
PAMTRA		Passive and Active Microwave Radiative TRAnsfer
PIP		Precipitation imaging probe
PPI		Plan position indicator
PSD		Particle size distribution
QPE		Quantitative precipitation estimation
r	$[m]$ or $[km]$	Range distance
R	$[-]$	Pearson correlation
RH	$[-]$ or $[\%]$	Relative humidity
RHI		Range height indicator
RMSE		Root mean squared error
ROXI		Rain Observation with an X-band Instrument

RPG		Radiometer Physics GmbH
SIP		Secondary ice production
SLDR	[dB]	Slanted LDR
SLW		Supercooled liquid water
SNR	[dB]	Signal-to-noise ratio
SSRGA		Self-similar Rayleigh-Gans approximation
sZ_e	[dBsZ]*	Spectral equivalent radar reflectivity factor
T	[°C]	Temperature
T_B	[K]	Brightness temperature
t	[s]	Time
TWC	[kg m^{-3}]	Total condensed water content (liquid and ice)
v_{DOP}	[m s^{-1}]	Doppler velocity
v_{NYQ}	[m s^{-1}]	Nyquist velocity
v_t	[m s^{-1}]	Terminal velocity
WBF		Wegener-Bergeron-Findeisen
WP		Work package
WProf		W-band profiler
WRF		Weather Research and Forecasting model
w.r.t.		with respect to
w	[m s^{-1}]	Vertical velocity
Z_e	[dBZ] or [mm^{6}m^{-3}]	Equivalent radar reflectivity factor
$Z_{e,W}$	[dBZ]	W-band Z_e
$Z_{e,X}$	[dBZ]	X-band Z_e
Z_H	[dBZ]	Z_e measured at horizontal polarization
Z_V	[dBZ]	Z_e measured at vertical polarization

---

*defined as 1 dBsZ = $10\log_{10}(1 \text{ mm}^6\text{m}^{-3}(\text{m s}^{-1})^{-1})$

1 Introduction and background

1.1 Motivations

Snowfall is a phenomenon of extraordinary complexity, which is fascinating to observe both from a neophyte's perspective and in the view of illustrious scientists (*Kepler*, 1611; *Descartes*, 1637). In addition to offering a fine spectacle with a compelling variety of snow crystals and snowflakes, snowfall is an essential ingredient of atmospheric processes and of the hydrological cycle. Its understanding is hence crucial for fields ranging from weather forecasting to water resources management through modeling of and adaptation to climate change.

Snowfall at ground level is mostly confined to high latitude or high altitude environments, and is only occasionally observed in the wintertime at lower altitudes and latitudes. However, snowfall is involved in around 60% of the total precipitation amount and half of precipitation events[*] worldwide, whether as snow falling down to the ground or as rain melted from snow (*Field and Heymsfield*, 2015; *Heymsfield et al.*, 2020). In middle and high latitudes, this proportion exceeds 80% of events. During wintertime, snow accumulates in mountainous regions, allowing for the natural build-up of freshwater reservoirs. The snowpack, which melts away in warmer seasons, contributes to a sustained water supply year-round, and is thus a critical element of the surface water balance and of our hydrological resources, with further implications on e.g., hydroelectric power generation. From the point of view of weather forecasting services, monitoring precipitation through quantitative estimates, together with accurately predicting its occurrence and intensity, are substantial challenges that also have a strong societal impact (*Lazo et al.*, 2009).

Besides these effects at ground level, ice hydrometeors also hold an important role throughout the journey of water at higher levels in the atmosphere. Ice clouds have, for instance, a significant role in the global radiative balance through their contribution to infrared radiation (*Lynch*, 1996; *Sullivan and Voigt*, 2021). More generally, clouds are consistently identified as the most important source of uncertainty and spread in climate models (as pointed out in the latest reports of the Intergovernmental Panel on Climate Change, *Boucher et al.*, 2013; *Arias et al.*,

---

[*] $> 1 \text{ mm day}^{-1}$

1

2021), in spite of great progress in modeling skill that was recently achieved. Among the unknowns that remain to characterize the radiative contributions and feedbacks of clouds, is how liquid and ice hydrometeors coexist at negative temperatures within so-called mixed-phase clouds (MPCs, *Sun and Shine*, 1994; *Curry et al.*, 1996). In MPCs, ice crystals and supercooled liquid droplets are generated or depleted—depending on atmospheric conditions—and interact with one another. This ultimately affects cloud phase partitioning and, in turn, the impact of MPCs on the Earth's radiation budget (*McCoy et al.*, 2016; *Matus and L'Ecuyer*, 2017), with a competition at the global scale between a net warming effect of the ice clouds, and a net cooling effect of liquid water clouds (*Li and Le Treut*, 1992; *Murray et al.*, 2021).

On a different note, snowfall events can have sizable socio-economical repercussions. Significant traffic perturbations, or damage due to snow buildup on power lines, are frequently reported when snow storms hit populated areas (e.g., *Poots*, 2000). Signal attenuation in wet or melting snow can cause severe deteriorations in telecommunications (*Bellon et al.*, 1997). From the perspective of the aviation industry, cold atmospheric conditions bring numerous safety-related challenges, with the risk of aircraft icing in supercooled or mixed-phase clouds being a well-known example (*Cao et al.*, 2018). Likewise, ice crystal icing, associated with flying in high-altitude regions near deep convective systems (*Hallett and Isaac*, 2008), leads to the ingestion of ice crystals by jet engines and subsequent engine damage (*Haggerty et al.*, 2019). Snowfall has also been reported to induce in-flight power interruptions, while at ground level, snow accretion on aircraft is an additional threat during takeoff (*Rasmussen et al.*, 1999; *Taszarek et al.*, 2020).

For all these purposes—ranging from weather forecasting to aircraft design and engineering—an accurate quantification and modeling of snowfall is needed, which requires knowledge of snowfall processes across scales. In particular, it is necessary to understand the mechanisms that take place at the microscale, i.e., at the scale of each snow particle. Depending on the atmospheric conditions where the particle forms and grows, it may undergo different processes, and ultimately have strikingly different physical properties in terms of e.g., shape, size, or mass. The study of this *microphysics of snowfall* addresses the following questions: How are ice and snow particles formed? By which processes do they grow, or decay? How can one quantitatively describe and model a single snow particle, or an ensemble of snow particles?

This thesis investigates how remote sensing measurements, and in particular, those from meteorological radars, can be used to better characterize snowfall properties and gain insight into the microphysical processes that take place in the ice and mixed phase of clouds and precipitation.

1.2   Snowfall microphysical processes and properties

A casual observer of snowfall would inevitably notice the stunning variety of geometrical shapes and aspects that snow particles can take on. This is well illustrated in literature classifications of ice crystal types, which can have up to 80 or 121 categories (*Magono and Lee*, 1966; *Kikuchi et al.*, 2013). This diversity results from slight differences in the history of each particle, and from the specific atmospheric conditions they encountered during their formation and growth, along their fall trajectory.

1.2.1   Large-scale drivers of snowfall

Before delving into the microphysical processes that determine how snow particles form and grow, let us briefly recall the main ingredients of snowfall and the typical situations where they are found. At the risk of stating the obvious, snowfall takes place when atmospheric conditions are both cold and moist: the occurrence of such conditions largely depends on the geographical location, through the latitude, altitude, distance to water bodies, and regional atmospheric and moisture circulation. From a synoptic perspective, snowfall may result from the uplifting of air masses through frontal activity or convergence (*DeWalle and Rango*, 2008), and can be fostered by smaller-scale vertical motion associated with e.g., radiative cooling—which sustains mixed-phase clouds—or thermodynamic instabilities leading to convective-type clouds (*Kulie et al.*, 2016). Terrain features have a determining influence; they may lead, for instance, to lake effect snowfall, as in the North American Great Lakes region (*Wilson*, 1977). In mountainous regions, orographic effects play a decisive role in enhancing snowfall through various processes (*Passarelli and Boehme*, 1983; *Roe*, 2005; *Houze*, 2012; *Chow et al.*, 2013), ranging from simple orographic lifting, which triggers condensation and precipitation formation, to more complex mechanisms such as flow blocking effects (*Reeves and Lin*, 2007), or the seeder-feeder mechanism (*Choularton and Perry*, 1986). The latter describes a configuration where ice particles precipitating from a high-level *seeding* cloud grow efficiently by accretion of cloud water as they fall through a lower-level, often orographic, *feeding* cloud (e.g., *Proske et al.*, 2021), leading to an enhanced precipitation flux.

Having in mind the large-scale drivers of snowfall, we now provide an overview of the main small-scale processes that affect the microphysical properties of snowfall, from the formation of ice crystals to their growth and decay. This introduction to snowfall microphysics is based on *Lohmann et al.* (2016), *Libbrecht* (2005), and *Pruppacher and Klett* (2010), along with additional sources mentioned throughout the text.

1.2.2   Ice nucleation

At temperatures below $\sim -38°$C, ice particles may form through the *homogeneous freezing* of supercooled liquid water (SLW) droplets or solution droplets. This mechanism typically takes place at high altitudes, where such low temperatures are reached, as in cirrus clouds or in

convective clouds with a sufficient vertical extent. At warmer temperatures, the energy barrier of homogeneous nucleation cannot be overcome in the atmosphere, and ice crystals are formed through *heterogeneous nucleation*, which involves activated ice nucleating particles (INPs). INPs are aerosol particles with specific surface properties, upon which water molecules can assemble into ice structures. They correspond to only a small fraction of aerosols (one in 10^5 or 10^6); for comparison, concentrations of cloud condensation nuclei are typically more than a thousand times greater (*Rogers et al.*, 1998). Different paths may lead to the formation of ice crystals via heterogeneous nucleation, depending on whether it occurs via the freezing of a supercooled droplet that already contains an active INP (*immersion freezing*), or upon the collision of an INP with a supercooled water droplet that subsequently freezes (*contact freezing*). Other nucleation mechanisms exist, although less frequently observed, through *condensation freezing* or direct *vapor deposition* onto an INP.

It results that, at temperatures ranging from ~-38°C to 0°C, the primary production of ice crystals is limited by the availability of both water vapor and INPs. It is noteworthy that most primary ice production processes require previously-formed cloud droplets and hence, saturated conditions with respect to (w.r.t.) liquid water, which correspond to high supersaturation over ice[*].

1.2.3 Growth and decay processes

Once an ice germ is formed, it may undergo different growth processes, depending on the surrounding temperature and supersaturation, and on the presence of other ice or liquid particles.

Vapor deposition

The first process through which the ice embryo will grow in size is through the deposition of water vapor onto it. Ice particles that have only grown through vapor deposition are referred to as *pristine crystals*. Because of the highly supersaturated environment in which an ice crystal is formed, these initial stages of depositional growth are highly efficient. Two main growth regimes exist for the crystallographic arrangement of water molecules in ice: either in the form of columns with a hexagonal base, or as hexagonal planar crystals (cf. Fig. 1.1 and Fig. 1.2a and b). Experimental studies have shown that temperature and humidity control the direction of crystallographic growth and hence the shape of the growing crystal, as illustrated in the diagram of Fig. 1.1.

At very cold temperatures, the preferred direction of growth of the ice crystals is not well differentiated, meaning crystals may grow in either columnar or planar directions depending on the saturation level. In warmer conditions, the regime is mainly constrained by temperature:

---

[*]This comes from the fact that at a same subfreezing temperature, the equilibrium vapor pressure of water vapor w.r.t. ice is less than that w.r.t. liquid water.

between roughly -20°C and -10°C, crystals grow in planar shapes, which can range from solid plates at low supersaturation to stellar dendrites when supersaturation is high. Between -10°C and around -5°C, dominant growth is in the columnar direction, with needle-like crystals growing when the availability of water vapor is high, and solid prisms when it is merely above the level of saturation w.r.t. ice. As temperatures reach warmer values ($T \gtrsim -3$°C), planar growth is dominant again. When a pristine ice crystal, which has grown in given temperature and humidity conditions, is moved to (or, in the atmosphere, precipitates into) a different environment, the properties of crystal growth in this new environment are combined with the original shape. This accounts for the formation of crystals with singular shapes, such as "capped columns", which originally grew as columnar crystals, whose ends developed into plate-like crystals when they settled into warmer temperatures, in still saturated conditions.

When ice crystals grow in an environment where the humidity exceeds the liquid water saturation level (black line in Fig. 1.1), this usually entails that they coexist with SLW droplets. Such conditions are favorable for the Wegener-Bergeron-Findeisen (WBF) process (*Wegener*, 1911; *Bergeron*, 1935; *Findeisen*, 1938), which describes a positive feedback in depositional growth: ice crystals grow very efficiently because of the high humidity content, which brings the latter down to a level that is still above the saturation w.r.t. ice, but lower than that w.r.t. liquid water. This causes liquid droplets to evaporate, which in turn increases the vapor content and feeds the depositional growth of ice crystals. This growth of ice crystals at the expense of SLW droplets is essential to the thermodynamics of mixed-phase clouds: because of the WBF effect, MPCs are intrinsically unstable and eventually become fully glaciated, unless an independent mechanism enhances the saturation (e.g., by sustaining sufficient vertical motion, *Korolev and Mazin*, 2003; *Korolev*, 2007a or by radiative cooling, *Morrison et al.*, 2012).
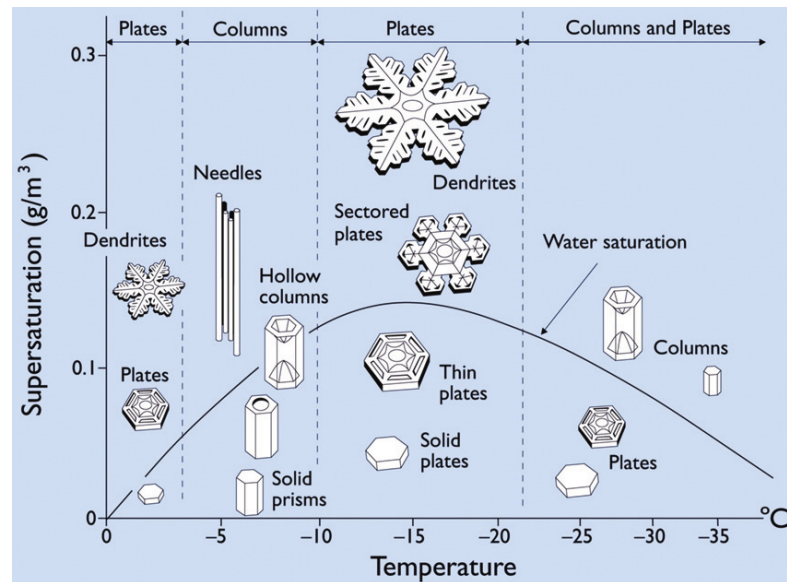
Figure 1.1: Snow crystal morphology diagram established by *Nakaya* (1954), republished from *Libbrecht* (2005); permission conveyed through Copyright Clearance Center, Inc.

Riming

Another important snowfall growth process in supersaturated conditions (over liquid water) is *riming*, whereby a supercooled liquid droplet collides with, and subsequently freezes onto, a snow particle. For riming to commence, both the ice crystals and the supercooled droplets should be large enough to enable efficient collection (resp. $\gtrsim 100~\mu m$, $\gtrsim 10~\mu m$, *Pruppacher and Klett*, 2010, Chapters 14 and 16): riming thus occurs at later stages in the growth of a crystal compared to vapor deposition. Various degrees of riming may be observed, leading to crystals with barely deformed shapes (slightly rimed particles), or to heavily rimed, quasi-spherical, *graupel* particles (Fig. 1.2d).

As SLW droplets are accreted onto a snow particle, the latter becomes rounder (more spherical) and both its mass and its bulk density increase, which results in an enhancement of its terminal velocity. These microphysical changes lead to an increased total precipitation flux (*Grazioli et al.*, 2015; *Garrett and Yuter*, 2014) and can influence the spatial distribution of precipitation (*Saleeby et al.*, 2011), by altering the fall trajectories compared to unrimed, slower-falling particles. As ice particles rime and scavenge cloud SLW droplets, they also contribute to the wet deposition of aerosols (*Poulida et al.*, 1998); at the same time, they accelerate the glaciation of MPCs through the depletion of SLW droplets. Riming additionally plays a role in the production of secondary ice particles, as will be detailed further on (Sect. 1.2.4), which reinforces its prominent role in cold precipitation processes. For these reasons, riming has been the subject of active research in recent years, both in terms of its modeling (e.g., *Leinonen and Szyrmer*, 2015; *Kalesse et al.*, 2016) and the characterization of its occurrence (e.g., *Moisseev et al.*, 2017; *Kneifel and Moisseev*, 2020).
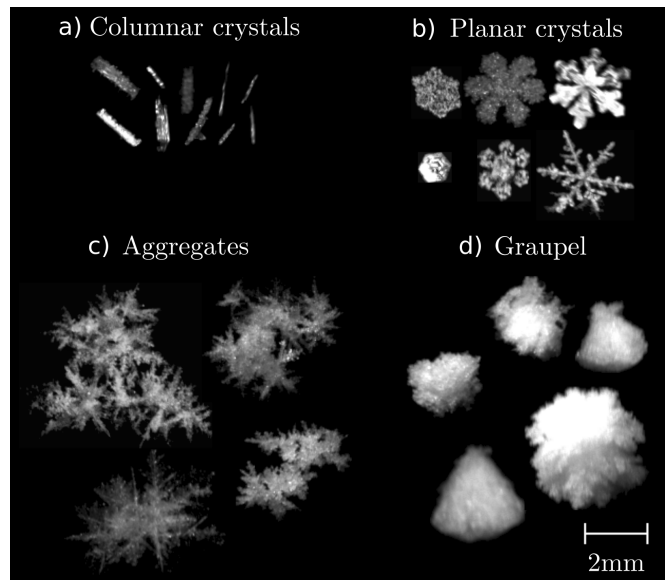
Figure 1.2: Images of the main snow particle habits: pristine crystals ((a) columnar and (b) hexagonal planar), (c) aggregates, and (d) graupel particles. Pictures are from the Multi-Angle Snowflake Camera (MASC). Source: *Praz et al.* (2017), Fig. 3, cropped and adapted, used under CC BY 3.0.

Aggregation

The last of the main snowfall growth mechanisms, aggregation, occurs when ice crystals collide with each other and become entangled, leading to a single, larger, snowflake (Fig. 1.2c). Such *aggregates* include a large variety of snow particles and cover a broad range of sizes, from roughly 1 mm up to several centimeters, depending on the number and size of the elementary crystals they are composed of, and on their arrangement. Aggregation usually results in a mild acceleration of terminal velocity, as an effect of the increase in particle size, although not to the extent that riming does (*Mitchell and Heymsfield*, 2005).

While vapor deposition and riming are growth processes by which the ice water content (IWC, i.e., the mass of ice per unit volume of air) increases, through a mass transfer from the vapor or liquid phase to ice, aggregation per se does not result in changes of IWC. Rather, it leads to a rapid increase in the size of snow particles and reduces the total number concentration of ice particles, while keeping IWC unchanged. Note that aggregates can also rime when they precipitate through SLW-containing cloud layers, leading to large and dense rimed aggregates. In fact, some studies have suggested that, because of their larger size, aggregates are more likely than individual crystals to collect SLW droplets. This implies that when saturation over water is met and SLW cloud droplets are present, aggregation can indirectly lead to an increase in IWC by facilitating riming (*Houze and Medina*, 2005).

For aggregates to form, two main ingredients are required: on the one hand, a sufficient *sticking efficiency* which makes the crystals adhere together once they collide; on the other hand, the actual occurrence of collisions between ice crystals. The first ingredient is primarily constrained by temperature: two distinct temperature ranges are associated with an enhanced sticking efficiency, each of which involving different mechanisms. Aggregation efficiency is highest at near-zero temperatures ($T \gtrsim -5°C$), as identified by *Hobbs et al.* (1974); *Heymsfield et al.* (2015). This is attributed to the formation of a quasi-liquid layer on the surface of ice crystals in this temperature range, which in turn increases their stickiness (*Hobbs et al.*, 1974; *Furukawa et al.*, 1987; *Rosenberg*, 2005). This warm aggregation regime leads to the largest snow aggregates. Another, secondary maximum in aggregation efficiency is reported around -15°C, while aggregates are virtually never observed below this temperature (*Hobbs et al.*, 1974). This second aggregation mode is related to the depositional growth of dendritic crystals at this temperature (when the saturation level is high), which enables mechanical aggregation: with their branched structure, dendrites are likely to interlock and form aggregates even at cold temperatures (*Heymsfield*, 1986; *Connolly et al.*, 2012).

Other elements foster the formation of aggregates by affecting the second ingredient, i.e., the likeliness of collisions between ice particles. Turbulence is thought to be favorable for aggregation, as it increases the collision probability between particles (*Houze and Medina*, 2005; *Sheikh et al.*, 2022). It has also been suggested that bigger particles, with a larger collection efficiency, are more likely to collide and clump together with another particle, leading to a positive feedback during aggregation (*Phillips et al.*, 2015).

Decay processes: melting and sublimation

As detailed above, snow particles can grow into different shapes through various processes depending on the temperature, saturation, and availability of liquid water. The decay of snow particles usually happens through a phase transition, either via their sublimation—in subsaturated conditions—or through their melting into raindrops—when they reach positive temperatures.

Snowfall sublimation is a significant process, mainly because of the reduction of surface precipitation it may lead to. In certain regions of Antarctica, for example, low-level sublimation caused by strong katabatic winds has an important impact on snow accumulation at the ground, which is both essential and difficult to model (*Grazioli et al.*, 2017). More generally, virga, which include sublimating snowfall but also evaporating rainfall, are a challenge for the quantification of worldwide precipitation (*Wang et al.*, 2018).

The melting of snowfall into rain is naturally a prominent mechanism, as it is involved in most midlatitude rainfall (*Heymsfield et al.*, 2020). Additionally, melting snowfall can modify precipitation patterns and mesoscale atmospheric dynamics as a consequence of diabatic cooling within the melting layer (*Wexler et al.*, 1954), which causes pressure and wind perturbations (*Heffernan and Marwitz*, 1996). Although modeling studies have helped gain insight into particle-scale melting mechanisms (*Szyrmer and Zawadzki*, 1999; *Leinonen and von Lerber*, 2018), unresolved questions remain about the microphysical processes occurring slightly above and within the melting layer, such as the actual importance and quantification of aggregation and breakup (*Fabry*, 1995; *Li and Moisseev*, 2019; *Fujiyoshi*, 2023).

1.2.4 Secondary ice production

High ice crystals number concentrations (ICNC) are sometimes measured in circumstances where temperatures are too warm for homogeneous nucleation to occur, and where INP concentrations are too low to account for the formation of all the ice crystals through heterogeneous nucleation (*Mossop et al.*, 1970; *Hobbs and Rangno*, 1985; *Lloyd et al.*, 2015; *Pasquier et al.*, 2022). This observation has led scientists to investigate the occurrence of secondary ice production (SIP) processes, through which one preexisting ice particle may induce the formation of more ice crystals via secondary mechanisms, also referred to as ice multiplication processes. Ice crystals that form through these processes can then grow by vapor deposition, riming, and aggregation, just like crystals formed through primary nucleation. In MPCs, the ICNC enhancement—sometimes of several orders of magnitude—caused by SIP is an essential feature: when the number of ice crystals is increased, the depletion of SLW droplets through the WBF process or riming is facilitated, which accelerates the glaciation of the cloud (*Field et al.*, 2016) with ultimately an impact on the radiative properties (*Young et al.*, 2019). The resulting precipitation is also affected, in terms of both its spatial distribution and its intensity, in a way which is still debated (*Field et al.*, 2016; *Sullivan et al.*, 2018; *Luke et al.*, 2021; *Dedekind et al.*, 2021, 2023).

Experimental and observational studies have identified distinct processes by which SIP can occur (*Field et al.*, 2016; *Korolev and Leisner*, 2020). Most of them are active in mixed-phase environments as they require the presence of SLW droplets and/or rimed particles. Figure 1.3 (*Korolev and Leisner*, 2020) illustrates through a conceptual diagram the three processes that are usually considered the most frequent and significant, as listed below.

- The **Hallett-Mossop** (HM) rime splintering mechanism (*Hallett and Mossop*, 1974) occurs as supercooled cloud droplets or drizzle/rain drops rime onto ice particles and generate ice splinters in the process. HM is active between -8°C and -3°C, with a maximum efficiency around -5°C, and in the presence of small (< 13 μm) and large (> 25 μm) droplets. The physics of the process is still debated (*Korolev and Leisner*, 2020, and references therein). Some hypotheses relate it to the growth of column-like crystals at these temperatures, which would favor the formation of splinters as SLW drops collide and freeze onto the rimer. Others have suggested that stress build-up within the accreted droplets, caused by different temperatures between the rimer and the freezing drop, may lead to their fragmentation. The collision velocity between the rimer and SLW droplets could also play a role in the efficiency of the process (*Saunders and Hosseini*, 2001).

- When supercooled drops freeze through heterogeneous freezing onto an INP or upon contact with an ice particle, they can shatter into several ice fragments due to the differential pressure resulting from the formation of an outer ice shell on the drop (e.g., *Takahashi and Yamashita*, 1977; *Phillips et al.*, 2018). This **droplet shattering** process requires the presence of drizzle-size drops of at least 50 μm (*Wildeman et al.*, 2017); certain studies have suggested that the process is more efficient for larger drops ($\gtrsim$ 300 μm, *Lauber et al.*, 2018; *Keinert et al.*, 2020; *Kleinheins et al.*, 2021), that could break up into a larger number of fragments. Contrary to HM, it does not seem restricted to a clearly-established temperature range as it was reported to occur at both cold (<-15°C, *Korolev and Leisner*, 2020) and warmer temperatures, with the recirculation of raindrops above the melting layer (*Korolev et al.*, 2020; *Lauber et al.*, 2021).

- Ice-ice collisions, facilitated in turbulent regions or when ice particles have different settling velocities, can also produce secondary ice fragments (*Takahashi et al.*, 1995; *Vardiman*, 1978; *Schwarzenboeck et al.*, 2009). This **collisional breakup** mechanism is thought to be a substantial source of secondary ice particles in certain environments, such as wintertime alpine clouds (*Dedekind et al.*, 2021), particularly under the frequent seeder-feeder cloud configurations observed in the Alps (*Proske et al.*, 2021; *Georgakaki et al.*, 2022), although its underlying physical mechanisms are not fully understood or constrained yet (*Korolev and Leisner*, 2020). The presence of rimed particles is considered an important ingredient (*Phillips et al.*, 2017a,b), based on the intuition that these particles, with their higher mass and fall speed, are more likely to cause efficient breakup during high-kinetic-energy collisions with other ice particles.
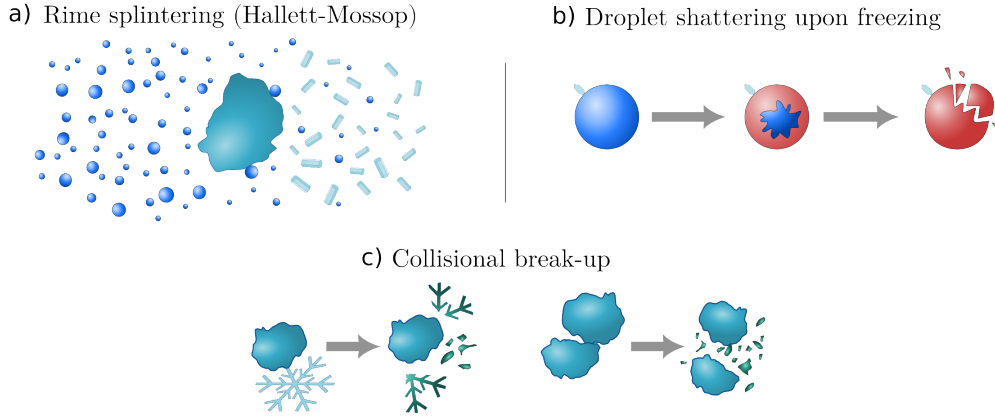
Figure 1.3: Conceptual illustration of the main SIP processes. The scale is not respected. Adapted from *Korolev and Leisner* (2020), licensed under CC BY 4.0; the color scheme was changed for consistency with further sketches in the manuscript.

There exist other SIP processes, which have been the subject of fewer experimental and model-based studies to this date. They include the fragmentation of snow particles during sublimation (*Bacon et al.*, 1998), the generation of ice splinters caused by a thermal shock associated with latent heat release during riming (*King and Fletcher*, 1976a,b), or the activation of INPs in transient high supersaturation around freezing drops, where heterogeneous nucleation would be locally enhanced (*Korolev and Leisner*, 2020).

1.2.5 Describing and modeling snowfall

After this overview of the main snowfall processes, where we also touched upon certain qualitative properties of snow particles—such as their arrangement in aggregates or their degree of riming—we introduce quantitative ways to describe the microphysical properties of snowfall. This is essential for actually parameterizing snowfall in weather and climate models. In this section, we also lay the ground for some formal concepts and notations used in further chapters of this thesis.

Particle size distribution

The *particle size distribution* (PSD), which refers to the distribution of the number concentration of hydrometeors according to their diameter, is widely used to characterize precipitation microphysics. Working with the PSD first raises the question, quite complex in the case of snow particles, of how particle size is defined. Possible metrics include the maximum diameter, melted diameter, or mean volume diameter. The choice of this definition should be specified whenever a quantitative description of snowfall is undertaken, and the most adequate choice might depend on the applications. In this thesis, unless specified otherwise, we define the diameter or size of a snow particle, D [m] (sometimes noted D_{max} in ambiguous cases), as its maximum dimension. This is consistent with many datasets and models used across snowfall

studies (e.g., *Mech et al.*, 2020; *Grazioli et al.*, 2022, to cite just two).

A frequently used mathematical formulation of the PSD $N(D)$ [m^{-4}] is the negative exponential distribution (Eq. 1.1, *Marshall and Palmer*, 1948), which is a reasonable approximation to describe snow particle populations (*Morrison et al.*, 2005; *Heymsfield et al.*, 2008). It is particularly convenient as it is described with only two parameters (mean diameter D_0 and prefactor N_0, related to the total number concentration $N_T = N_0 D_0$ [m^{-3}]), and its moments are easily computed analytically (*Straka*, 2009). In reality, snowfall PSDs can deviate from this exponential distribution, with either super- or sub-exponential behaviors; this can be partly taken into account by considering a modified gamma (Eq. 1.2, *Petty and Huang*, 2011) or a gamma distribution (Eq. 1.2 with $\gamma = 1$). We refer the reader to textbooks such as *Straka* (2009) for more detail on the parameterization of PSDs.

$$N(D) = N_0 \exp\left(-\frac{D}{D_0}\right) \tag{1.1}$$

$$N(D) = N_{0,g} D^\mu \exp\left(-\left(\frac{D}{D_{0,g}}\right)^\gamma\right) \tag{1.2}$$

The total hydrometeor number concentration is easily obtained as the integral[*] of the PSD, $N_T = \int_0^{+\infty} N(D) dD$. Additionally, it is sometimes useful to define a characteristic size to describe a hydrometeor population. A few commonly used quantities (*Straka*, 2009), which will be occasionally mentioned in this thesis, include: the number-concentration-weighted mean diameter D_0, which is the first moment of the PSD; the mass-weighted mean diameter; the median mass (resp. volume) diameter MMD (resp. MVD) such that half of the mass (resp. volume) of hydrometeors is contained in particles smaller than MMD (resp. MVD); the effective diameter D_{eff}, defined as the ratio of the third to the second moment of the PSD.

Geometrical properties

Modeling snow particles, whether for radiative transfer purposes or from a mechanical perspective (e.g., *Jiang et al.*, 2019; *Aguilar et al.*, 2021), sometimes requires making simplifying assumptions on their shape and geometry. Snowflakes are frequently approximated as spheroids, with either a prolate or an oblate shape; the former is suitable for columnar or needle-like crystals, while the latter is used for planar crystals and aggregates. From this spheroid assumption, the aspect ratio A_r [-] of the particles is computed as the ratio of particle dimension along the rotational axis, divided by the dimension in the orthogonal direction ($A_r > 1$ for prolate, $A_r < 1$ for oblate particles). Depending on the context, other definitions of the aspect ratio may be used, like the ratio of minor to major axis length (*Garrett et al.*, 2015), in which case $A_r < 1$ for all particles. Riming, and to a lesser extent aggregation, bring the snow particles' aspect ratio closer to 1 (with both definitions) as they become more spherical.

---

[*]The bounds of the integral are here for a generic PSD; in reality, true D values range from the minimum particle size $D_{MIN} > 0$ to the size of the largest particle, $D_{MAX} < +\infty$

Other parameters used to describe snow particles in a geometrical sense include the area ratio (cross-section area of the particle in a given direction, divided by the area of the disk of diameter D, *Heymsfield and Westbrook*, 2010). When considering an ensemble of snow particles, one can be interested in how the geometrical parameters are distributed vs. particle size; in that sense, area–size relations may, for instance, be fitted and are usually of the type $A = \alpha_a D^{\beta_a}$, where A [m^2] is a cross-section area, and α_a and β_a are size-independent power law coefficients.

Mass-related properties

Quantitative precipitation estimation (QPE) is a crucial aspect of precipitation studies. From a microphysical perspective, QPE requires knowledge of the PSD but also of the mass of individual particles. Many studies have focused on quantifying the bulk density[*] ρ_b [g m^{-3}] or the mass m [g] of snow particles, through size-dependent relationships that follow a power law $m = a_m D^{b_m}$ (*Locatelli and Hobbs*, 1974; *Mitchell et al.*, 1990; *Brown and Francis*, 1995; *Rees et al.*, 2021, to list a few). The exponent b_m [-] and prefactor a_m [g m$^{-b_m}$] can vary significantly depending on the particle type and its riming degree (e.g., *Mason et al.*, 2019; *Grazioli et al.*, 2022). b_m is sometimes referred to as the *fractal dimension*; it is close to 3 for heavily rimed, spherical particles such as graupel, and is usually of the order of 2 for unrimed particles.

Building upon these considerations on particle mass and density, a parameterization of particle fall speed is also needed to model precipitation and, in particular, snowfall rate. Here again, multiple empirical studies were conducted in order to fit size-dependent models of terminal velocity. *Khvorostyanov and Curry* (2002) used a pseudo-power-law approach with size-dependent coefficients; more specific to snow, *Heymsfield and Westbrook* (2010) introduced a widely used expression that takes into account the mass and the area ratio of the particles. It is worth noting that turbulence is also thought to influence particle fall speed through sweeping or loitering processes, which are still debated, and not accounted for in most models (*Garrett and Yuter*, 2014; *Li et al.*, 2021a).

---

[*]usually defined as the mass of the particle divided by the volume of its enclosing spheroid

1.3   Meteorological radars and their application to snowfall studies

1.3.1   Different approaches to studying snowfall microphysics

Advancing knowledge in cloud and precipitation microphysics is a multi-faceted challenge. While the focus of this dissertation is on remote sensing, and in particular on radar measurements, this is one, among numerous, approaches to studying snowfall microphysics. Ultimately, leveraging the information gained through different viewing angles is essential. This subsection briefly outlines the main tools to investigate snowfall microphysics—in situ observations, laboratory experiments, physical models, and remote sensing observations—to highlight how they can complement each other.

In situ observations are instrumental to characterize hydrometeor microphysical properties, including but not limited to their size, geometry, mass, or number concentration (*Baumgardner et al.*, 2017; *McFarquhar et al.*, 2017). In situ sensors onboard scientific aircraft can provide information on microphysical properties at various altitudes and temperature levels. Imaging probes are used to collect grayscale or binary images of individual hydrometeors; the combination of probes with different and overlapping size ranges gives a robust and complete picture of snowfall properties in a given volume. Other sensors are designed to measure bulk quantities such as total condensed water content (TWC), LWC or IWC [$g\,m^{-3}$], which integrates with the information on individual particles gathered by the imagers (e.g., *Schwarzenboeck et al.*, 2000). At ground level, instruments like the Multi-Angle Snowflake Camera (MASC, *Garrett et al.*, 2012, 2015; *Grazioli et al.*, 2022) have been designed to gain a more refined understanding of the geometry of snow particles. The MASC consists of three coplanar cameras that take simultaneous grayscale pictures of a falling snowflake, 36° apart. Thanks to these different views, it is possible to identify a particle's type (e.g., aggregate, columnar crystal, *Praz et al.*, 2017) and reconstruct its 3-D geometry and estimates of its mass (*Leinonen et al.*, 2021). Recent developments have paved the way for even more advanced in situ measurements of hydrometeor properties such as mass and bulk density (*Rees et al.*, 2021), which are still the subject of high uncertainties.

Laboratory experiments can investigate thoroughly snowfall microphysical processes and their underlying physical mechanisms. They allow for a quantification of the efficiency of the processes and of their dependence on external parameters, such as temperature or saturation (e.g., *Nakaya*, 1954; *Magono and Lee*, 1966; *Hallett and Mossop*, 1974; *Mitra et al.*, 1990, among many). Experimental studies are thus invaluable to gain a quantitative understanding of the processes, which in turn is required for the parameterization of numerical models (e.g., *Aguilar et al.*, 2021; *Köbschall et al.*, 2023). One major caveat comes from the high challenge of replicating in the laboratory realistic atmospheric conditions; experimental results are thus sparse, and deviations from one study to another can be significant (e.g., in the case of SIP studies, *Korolev and Leisner*, 2020).

Numerical modeling provides an alternative perspective and is especially useful to understand how processes across scales—from the microphysical to the synoptic scale—interplay. High-resolution modeling, made possible by increased computational resources, has been used to improve process understanding in various contexts (e.g., *Vignon et al.*, 2019; *Sotiropoulou et al.*, 2020; *Georgakaki et al.*, 2022; *Gehring et al.*, 2022). Nonetheless, possible discrepancies between model outputs and observations are difficult to interpret, as the microphysical parameterizations rely on a number of hypotheses, to which models may be sensitive (*Sotiropoulou et al.*, 2021).

Remote sensing observations are a complementary source of information. Although indirect, these measurements provide insights into cloud and precipitation processes over spatially extended areas, in contrast with point measurements of in-situ instruments. Passive sensors such as microwave radiometers allow monitoring integrated quantities like precipitable water vapor and liquid water path (LWP, e.g., *Löhnert and Crewell*, 2003), the latter being relevant for studies of mixed-phase systems, for instance, to detect the presence of SLW clouds. More detail on the retrieval of atmospheric liquid water and water vapor from microwave radiometers is in Chapter 3 of this manuscript. Active remote sensing, mostly with meteorological radars, opens up other possibilities in snowfall studies, both for identifying hydrometeor *properties* and for investigating production/growth/decay *processes*. In the following, we detail the principles of meteorological radars, and how radar measurements can be used to study snowfall microphysics.

1.3.2   Principles of weather radar

This section and the following are based on *Fabry* (2015), *Kumjian* (2018), and *Ryzhkov and Zrnic* (2019), to which the reader is referred for more detail.

The technique of *radar*, standing for RAdio-Detection And Ranging, was first developed for military purposes as a tool to detect, and possibly identify and monitor, a distant target. Its use became prominent during the Second World War, first to detect raiding airplanes from ground-based stations, then directly on board military aircraft, after decisive technological improvements made the instrument portable. Soon, it was observed that, besides aircraft, other types of echoes were detected, that corresponded to precipitation cells. In the following decades, meteorological radars became widely used by operational weather services, for the quantification and *nowcasting* of precipitation, and by atmospheric scientists, as they opened up possibilities to study clouds and precipitation over large spatial areas: columns of the atmosphere in the case of vertical profilers, or 3-D volumes for scanning instruments.

Radio-detection and ranging

The basic principle of a (pulsed) meteorological radar is the following (see Fig. 1.4). First, a pulse of electromagnetic (e.m.) wave with frequency ν [Hz] (and corresponding wavelength

λ [m]) is generated and emitted by the *transmitter*, then focused into a beam, in a specific direction, by the *antenna*. The electromagnetic wave interacts with the targets it encounters along its path—here, hydrometeors. As a result of this interaction, part of the pulse is backscattered towards the radar, and collected through the *receiver*. By measuring the time interval t [s] between the emission and reception of the pulse, and knowing that the e.m. wave propagates at the speed of light in vacuum c_0 [m s^{-1}], reduced by the refractive index of air $n > 1$, the *range r* [m] can be inferred, defined as the distance between the radar and the target: $r = \frac{c_0 t}{2n}$. By comparing the power and phase of the returned and the emitted signal, variables can be computed that inform on the properties of the hydrometeors encountered within the radar volume.

The maximum distance within which meteorological targets can be unambiguously detected (*maximum unambiguous range*) is controlled by the time interval between each emitted pulse, through the *pulse repetition frequency* (PRF [s^{-1}]). The radar *resolution volume V* [m^3] is determined by the beam shape, the range, and the radial resolution dr, which in turn depends on the pulse duration τ [s] ($dr = \frac{c_0 \tau}{2n}$). Specifically, in the case of a Gaussian antenna pattern, with a *half-power beam width* θ_{3dB} [rad]:

$$V = \pi \left(\frac{\theta_{3dB} r}{2} \right)^2 \frac{dr}{2\ln(2)} \tag{1.3}$$

In contrast with pulsed radars, Frequency-Modulated Continuous Wave (FMCW) radars transmit power continuously, with the frequency of the e.m. wave varying according to a modulation pattern (e.g., sawtooth). In this configuration, the range cannot be directly inferred from the time elapsed between emission and reception of the e.m. wave, the latter being continuously emitted. Instead, the difference in frequency between the returned and emitted signals is used to derive both the range and Doppler velocity[*] of the targets; this computation relies, in particular, on two Fourier transforms of the sampled received signal (e.g., *Jankiraman*, 2018). The FMCW technology requires more advanced signal processing algorithms, but offers several advantages in terms of hardware, as it requires, for instance, much less powerful transmitters.

Different types of meteorological radars and operation modes

Depending on the purpose, meteorological radars with different frequencies are used. Operational radars used in meteorological services are usually at S- or C-band, corresponding respectively to $\nu \sim 3$ GHz ($\lambda \sim 10$ cm) and $\nu \sim 6$ GHz ($\lambda \sim 5$ cm), and occasionally X-band ($\nu \sim 10$ GHz, $\lambda \sim 3$ cm). For research purposes, X-band radars can be used, as well as higher frequencies typically up to W-band ($\nu \sim 100$ GHz, $\lambda \sim 3$ mm).

Following the context, radars are operated in different modes. In a PPI (Plan Position Indicator), the elevation angle is fixed and the azimuth varies from 0° to 360°. At low elevations, this

---

[*]See Sect. 1.3.4

type of scan provides information on the horizontal extent of a precipitating system. It is used in operational radars, which aim to monitor precipitation in a 3D volume: in practice, the radars execute a series of PPI scans at different elevations. An RHI (Range-Height Indicator) scan is performed at a constant azimuth, by varying the elevation angle; it measures a vertical cross-section and informs on the vertical structure of precipitation, which is of high interest in process-oriented studies. When the radar does not scan but remains at a fixed azimuth and elevation, this corresponds to a profiling mode. It is commonly used for vertical profiling, either in a zenith (e.g., for ground-based) or a nadir (e.g., for spaceborne radars) configuration. Measurements from ground-based zenith profilers can be visualized as Height–Time Indicators (HTI) that give insight into the vertical structure of a precipitating system as it overpasses the sensor.
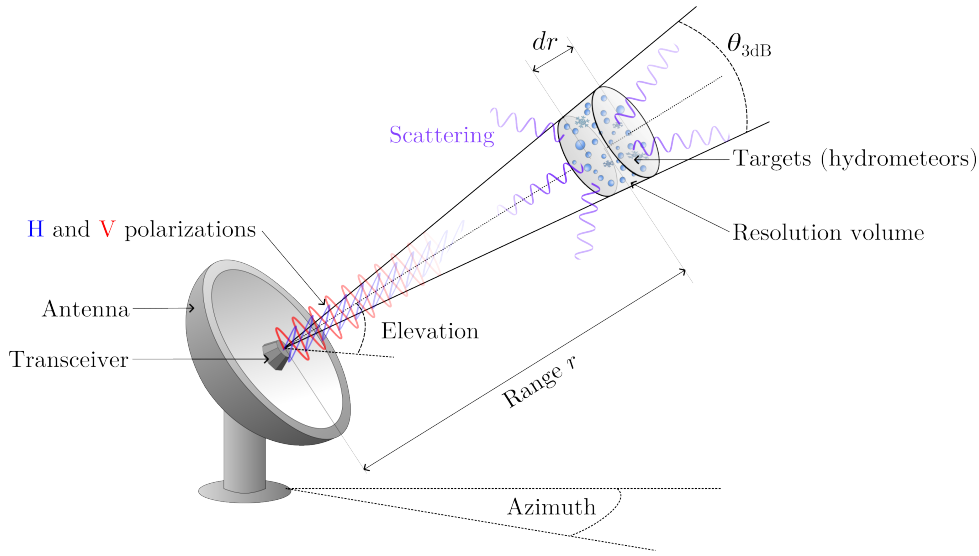
Figure 1.4: Schematic illustration of the radar principle, with notations introduced in the text. Certain radars are additionally equipped with a *radome* (not shown here) that protects the antenna.

The radar equation

As the e.m. wave propagates away from the source, the power density diminishes with the geometric spreading of the beam. The same happens with the backscattered signal as it propagates back to the radar. Combined with information on the radar properties such as antenna gain and aperture, a first generic form of the *radar equation* is obtained (Eq. 1.4), which describes the two-way propagation to and from the target. Here, P_t (resp. P_r) [W] denotes the transmitted (resp. received) power, G [-] is the gain of the antenna (defined as the ratio of the radiation intensity in the beam direction, to the radiation intensity that would be produced if the power were isotropically radiated), and Σ [m^2] is the total backscattering cross-section of the targets in the radar volume.

$$\frac{P_r}{P_t} = \frac{G^2 \lambda^2}{(4\pi)^3 r^4} \Sigma \tag{1.4}$$

In the case of hydrometeors, Σ is the sum of the contributions of all the individual targets within the resolution volume V, and can be rewritten as $\Sigma = V\eta$, where the *reflectivity* η [m^{-1}] defines the volumetric scattering properties of the targets. If $N(D)$ [m^{-4}] denotes the PSD (cf. Sect. 1.2.5), and $\sigma_b(D)$ [m^2] is the backscattering cross-section of a single particle of maximum dimension D, then η can be written as:

$$\eta = \int_0^{+\infty} \sigma_b(D) N(D) dD \tag{1.5}$$

The backscattering cross-section $\sigma_b(D)$ depends on the size D of the hydrometeors, but also on their dielectric properties through the dielectric factor $|K|^2$ [-], and on the radar wavelength. $|K|^2$ is primarily affected by the phase of the scatterers. In solid ice, $|K|^2 = 0.18$, and $|K|^2$ decreases for snow particles with decreasing density. The dielectric factor of liquid water $|K_w|^2$ is also sensitive to wavelength, and to a second order to temperature. For usual operational radar frequencies (e.g., at C-band and 20°C), $|K_w|^2 = 0.93$ (for comparison, at Ka-band and at 20°C, $|K_w|^2 = 0.90$). When the hydrometeors are much smaller than the wavelength ($D << \lambda$), this is known as the Rayleigh scattering regime. In these conditions, σ_b is approximated with a simple expression:

$$\sigma_b(D) \approx \frac{\pi^5}{\lambda^4} |K|^2 D^6 \tag{1.6}$$

Bringing together Equations 1.3, 1.4, 1.5 and 1.6, assuming the targets within the resolution volume are Rayleigh scatterers—i.e., well characterized by the Rayleigh scattering approximation—a new formulation of the radar equation is obtained (Eq. 1.7). All the constants and radar parameters (such as τ, λ, θ_{3dB}) are summarized as a constant C_0, and we introduce the *radar reflectivity factor* Z [mm^{6}m^{-3}] defined as $Z = \int_0^{+\infty} N(D) D^6 dD$. It follows that:

$$\frac{P_r}{P_t} = \frac{C_0}{r^2} |K|^2 Z \tag{1.7}$$

Building up on this, for any type of hydrometeor we define the *equivalent radar reflectivity factor* Z_e [mm^{6}m^{-3}] through the following equation, where $|K_w|^2$ is the dielectric constant of liquid water:

$$\frac{P_r}{P_t} = \frac{C_0}{r^2} |K_w|^2 Z_e \tag{1.8}$$

When the hydrometeors are liquid water drops within the Rayleigh scattering regime, $Z_e = Z$. In the general case and in the absence of attenuation, the equivalent radar reflectivity factor is expressed as:

$$Z_e = \frac{\lambda^4}{\pi^5 |K_w|^2} \int_0^{+\infty} N(D) \sigma_b(D) dD \tag{1.9}$$

From here on, the equivalent radar reflectivity factor is shortened as "reflectivity". In practice, Z_e is often expressed in logarithmic units, with $1\,dBZ = 10\log_{10}(1\,mm^6m^{-3})$. We saw that under the Rayleigh scattering assumption, Z_e is proportional to the sixth-order moment of the PSD (Eqs. 1.6 and 1.9): this means that it is sensitive to the total number concentration (N_T), and even more to the presence of large hydrometeors in the resolution volume (i.e., the

tail of the PSD). As a result, in snowfall microphysical studies, large or increasing Z_e values are interpreted as a sign of enhanced particle concentrations and/or of efficient particle growth, by vapor deposition, riming, or aggregation.

1.3.3 Dual-polarization

The *polarization* of an e.m. wave refers to the oscillation plane of its electric component (see Fig. 1.4). Dual-polarization radars operate on both horizontal and vertical linear polarizations, either through simultaneous transmission and reception or through alternate transmission/reception on each channel. Alternatively, the radar can also transmit at a single polarization and receive in both channels (e.g., *Rose and RPG*, 2018). When the radar transmits a pulse in a certain polarization, the return signal measured at this same polarization is referred to as the *co-polar* signal, while the *cross-polar* signal is the return signal received in the orthogonal polarization, when available. Dual-polarization variables are derived by combining power or phase information measured in each channel (as a co-polar and/or a cross-polar signal); they inform on the geometrical and density properties of hydrometeors and can be used to study snowfall microphysics, as briefly outlined below. Dual-polarization radars are also used operationally by weather services for e.g., more accurate precipitation nowcasting and QPE. We refer the reader to *Ryzhkov and Zrnic* (2019) or *Kumjian* (2013a) for further detail.

- **Differential reflectivity** Z_{DR} **[dB]**. This is the difference, in the logarithmic space, of the reflectivity measured at the horizontal and vertical polarization. It is independent of the hydrometeor number concentration (to the extent that N_T is high enough that Z_e values can be measured). At low elevations ($\lesssim 45°$), Z_{DR} is sensitive to the bulk density and to the aspect ratio of the hydrometeors; it increases as particles become more oblate or prolate, and decreases for sphere-like particles. In snowfall, high ($\gtrsim 2$ dB) or increasing Z_{DR} values typically reveal depositional growth of pristine crystals, while low ($\lesssim 1$ dB) or decreasing Z_{DR} is interpreted as a sign of aggregation or riming (*Grazioli et al.*, 2015; *Giangrande et al.*, 2016; *Planat et al.*, 2021).

- **Differential phase shift,** ψ_{dp} **[°]**, and **specific differential phase shift** K_{dp} **[° km^{-1}]**. ψ_{dp} is the difference in the phase of the return co-polar signals in horizontal and vertical polarization, and is the sum of different contributions:

$$\psi_{dp} = \phi_{dp} + \delta_{bs} + \psi_{dp,0} \tag{1.10}$$

where ϕ_{dp} is the phase shift due to the difference in the forward propagation velocities of the two waves, δ_{bs} is the differential backscattering phase delay (equal to 0 for spherical or Rayleigh scatterers), and $\psi_{dp,0}$ is the initial phase shift. K_{dp} is half the range derivative of ϕ_{dp}, and illustrates how the electromagnetic wave is slowed down by hydrometeors, in the vertical and horizontal planes; it is sensitive to the aspect ratio and number concentration of the particles. In snowfall microphysical studies, K_{dp} enhancement

can be used to track the formation of new ice particles through primary or secondary processes (*Andrić et al.*, 2013; *von Terzi et al.*, 2022; *Dedekind et al.*, 2023).

- **Co-polar correlation coefficient** ρ_{hv} **[-]**. This is the correlation of the co-polar signals measured at the horizontal and vertical polarization. It reflects the uniformity of the targets in their shape and size. High ρ_{hv} is observed, for example, in light rain or dry snow, while lower ρ_{hv} is measured in the melting layer where hydrometeor properties are highly non-homogeneous. ρ_{hv} is also used to identify and remove unwanted signals such as background noise and ground clutter, which typically have low correlation.

- **Linear depolarization ratio LDR [dB]**. It is available when the radar is operated with alternate transmission/reception on each channel. The LDR measures the ratio of the cross-polar to the co-polar return signal: i.e., if the radar transmits at horizontal polarization, LDR = $Z_V - Z_H$ (in logarithmic units) where Z_V (resp. Z_H) is the reflectivity measured at vertical (resp. horizontal) polarization. The depolarization phenomenon, whereby a target backscatters part of the signal at the orthogonal polarization, arises when the shape of the target is asymmetric with respect to the direction of propagation of the e.m. wave. Unlike most previously-listed variables (except ρ_{hv}), LDR can also be used with vertically-pointing radars. LDR is relevant to snowfall studies as it allows identifying different types of ice and snow particles. High LDR values ($\gtrsim -15$ dB) reflect the presence of prolate crystals (needles or columns, e.g., *Oue et al.*, 2015; *Luke et al.*, 2021), or of melting particles (*Ryzhkov and Zrnic*, 2019). Conversely, very low ($\lesssim -30$ dB), or even below-noise-floor LDR values reflect the presence of particles that are "disk-like" in the radar view, such as liquid water droplets or planar crystals (*Ryzhkov and Zrnic*, 2019). The latter, however, usually result in slightly higher LDR values. Aggregate or rimed snowflakes may lead to medium-low values of LDR depending on their composition, geometry, and orientation. When the radar is operated in simultaneous transmit and receive mode, an alternate variable can be derived, sometimes referred to as the slanted LDR (SLDR, e.g., *Myagkov et al.*, 2016; *Rose and RPG*, 2018), which yields similar interpretations (*Matrosov et al.*, 2012; *Galletti et al.*, 2014). It is computed by representing the transmitted and received signal in a rotated polarization basis: the e.m. signal simultaneously transmitted at horizontal and vertical polarizations can be seen as a 45°-rotated linearly polarized wave[*]; the equivalent co- and cross-polar components of the return signal can then be computed using an adequate rotation matrix (see e.g., *Myagkov et al.*, 2016).

Taking advantage of the distinct polarimetric signatures of different hydrometeor types, dual-polarization variables are commonly used for radar-based classifications of hydrometeors (*Straka et al.*, 2000). In particular, a semi-supervised classification algorithm was developed by *Besic et al.* (2016) and extended to additionally quantify the proportions of hydrometeor types in the radar resolution volume (*Besic et al.*, 2018). Although it is not the primary focus of this thesis, this method brings valuable information for process-oriented snowfall studies.

---

[*]if the transmission phase difference between the H and V channels is 0°

1.3.4 Radar Doppler spectrum

Doppler velocity

The notorious Doppler effect refers to the frequency shift of a wave caused by relative motion between its source and the observer. In the case of meteorological radars, the Doppler effect induces a change in the frequency of the returned signal compared to the emitted wave when the hydrometeors have a radial motion away from or toward the radar. In practice, the Doppler velocity v_{DOP} [m s^{-1}] of the target is computed via the rate of change of the phase difference ϕ [rad] between the return signal and a reference signal in phase with the emitted pulse. $\Delta\phi$ [rad] denotes the change of ϕ between two successive pulses. As detailed in *Fabry* (2015), Chapter 5:

$$\Delta\phi = -\frac{4\pi n}{\lambda}\frac{v_{DOP}}{\text{PRF}} \tag{1.11}$$

When the target consists of multiple particles, with each different radial velocities, the radar measures the reflectivity-weighted *mean Doppler velocity* (MDV), together with the *spectrum width* (SW [m s^{-1}]), which informs on the spread of the targets' Doppler velocities within the radar volume; the next subsection will come back to this. By convention, unless otherwise specified, positive Doppler velocity corresponds to motion away from the radar.

$\Delta\phi$ can only be measured unambiguously within [-π, π]; this has implications on Doppler velocity measurements, for which aliasing occurs if the target velocity exceeds a critical Nyquist velocity ($v_{NYQ} = \frac{\lambda}{4n}\text{PRF}$). This means that, for instance, targets moving away from the radar with a velocity $v > v_{NYQ}$ cannot be distinguished from targets moving toward the radar with a velocity $v - 2 v_{NYQ}$. Increasing the PRF mitigates this problem, but is detrimental to the maximum unambiguous range (see Sect. 1.3.2); depending on the context and purpose of the measurements, finding a trade-off between these two effects may be challenging. This is, however, not a major issue in the case of zenith profilers, which are used to study clouds and precipitation within a relatively narrow range (rarely above the tropopause, i.e., ~ 10 km above sea level).

When the radar is vertically pointing, the Doppler velocity of a target corresponds to its fall speed, which is the sum of its terminal velocity[*] and vertical air motion. This is remarkably interesting for microphysical studies of precipitation, as the terminal velocity of particles is related to their size and bulk density: large raindrops fall faster than drizzle drops, heavily rimed aggregates fall faster than small and pristine ice crystals. Following this rationale, MDV is frequently used to detect the presence of rimed particles in zenith-pointing radar measurements of snowfall (e.g., *Kneifel and Moisseev*, 2020). Note that for an ensemble of particles, the MDV—which, we recall, is the *reflectivity-weighted* mean Doppler velocity—is also affected by the particle size distribution and scattering properties at the chosen radar wavelength, with typically a dominant contribution of the larger particles to the MDV.

---

[*]this is valid in the case of small targets like hydrometeors, which are small enough that they reach their terminal velocity very fast in still air

Doppler spectrum and microphysical interpretations

When a succession of pulses is emitted by the radar and backscattered by the targets in a resolution volume at range r, a time series of return power values $P_r(t)$ is sampled. With a discrete Fourier transform on this time series, the distribution of power as a function of frequency shift is computed. From this, relating power to reflectivity through Eq. 1.8, and frequency shift to Doppler velocity with Eq. 1.11, the *radar Doppler spectrum* is obtained, which represents the reflectivity-weighted distribution of Doppler velocities in the resolution volume. From here on, we express the Doppler spectrum as a spectral reflectivity (sZ_e), whose units in the logarithmic scale we note dBsZ (defined as $1\,\mathrm{dBsZ} = 10\log_{10}(1\,\mathrm{mm^6 m^{-3} (m\,s^{-1})^{-1}})$). With this frequency-domain perspective, MDV and SW are readily computed as the mean and standard deviation of the Doppler spectrum. Throughout this thesis, *Doppler spectrum (pl: spectra)* refers to the measurement at a given (time, range) gate, and the stack of spectra at all range gates at a given time is denoted as the *Doppler spectrogram*. Note that this name convention is used here for clarity, but it may not be universal.

We will now focus on spectra measured by vertically-pointing profilers (e.g., *Lhermitte*, 1987; *Kollias et al.*, 2002; *Luke and Kollias*, 2013; *Kneifel et al.*, 2016). In that case, the shape of the Doppler spectrum is primarily defined by the PSD and the microphysical properties of the hydrometeors, which determine their backscattering cross-section and terminal velocity. The next paragraph will detail how this microphysics-driven spectrum is then affected by atmospheric dynamic conditions and the parameters of the radar. Focusing on the microphysical interpretation, the Doppler spectrum allows separating the contribution of slow-falling—typically small—vs. fast-falling—typically large or dense—particles to the total reflectivity. As a first-order approximation, the spectrum results from the snowfall PSD, weighted by the backscattering cross-section of the particles, and shaped by the velocity–size relation; it is thus extremely rich in terms of microphysical information. The Doppler spectrum was already used by *Atlas et al.* (1973), *Gossard* (1994), *Gossard et al.* (1997), *Babb et al.* (1999), *Williams and Gage* (2009), to retrieve rainfall or cloud drop size distributions from radar measurements. In a qualitative perspective, wider, or more/less skewed spectra, can be the sign of changes in the underlying PSD that may correspond to aggregation or new ice production processes (*Giangrande et al.*, 2016).

A specific signature occasionally observed in Doppler spectra deserves special attention. In certain cases, the Doppler spectrum deviates significantly from a Gaussian shape (Fig. 1.5a) to a point where several modes are visible (see for example, Fig. 1.5b and c). These modes, or spectral peaks, may be well separated or almost merged. Either way, they suggest that hydrometeor populations with different microphysical properties coexist within the same resolution volume, and that they have sufficiently different PSDs and/or density properties that their fall velocities are differentiated (*Zawadzki et al.*, 2001; *Verlinde et al.*, 2013). The moments of each mode (e.g., their Doppler velocity, spectral width, and reflectivity) may then be derived and analyzed to determine the hydrometeor types that are present. For example, SLW cloud droplets, because of their very small size ($< 50\,\mu$m), have both near-zero

terminal velocity and very low reflectivity (e.g., $Z_e \lesssim -20$ dBZ) and are typically identified as a Doppler peak with these characteristics (*Shupe et al.*, 2004; *Kalesse et al.*, 2016; *Li and Moisseev*, 2019), as in Fig. 1.5b. This highlights the potential of Doppler spectra to study MPCs (*Rambukkange et al.*, 2011). Figure 1.5c illustrates a quite different situation where both modes have similar reflectivity, which is more challenging to interpret without further information. When available, spectral polarimetric measurements can help refine the analysis, especially through the spectral LDR, e.g., to identify fingerprints of columnar crystals in a spectral peak (*Oue et al.*, 2018; *Luke et al.*, 2021).
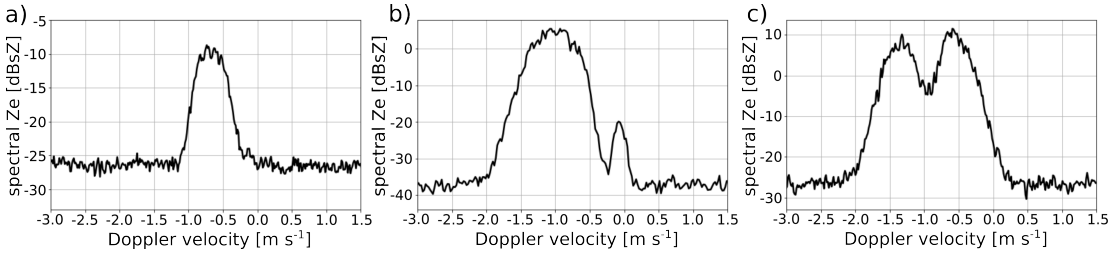
Figure 1.5: Examples of W-band Doppler spectra (27 January 2021, la Chaux-de-Fonds, Switzerland).

Contamination by non-microphysical effects

In reality, the purely microphysical spectrum is affected by atmospheric dynamic conditions—turbulence, horizontal and vertical wind—in a way that depends on the settings and parameters of the radar itself—sensitivity, beam width, or sampling frequency (e.g., *Protat and Williams*, 2011; *Williams et al.*, 2016). In this section, we briefly go through the main causes of data contamination by non-microphysical effects. We review how they affect radar measurements and in particular the Doppler spectrum, in terms of its velocity span, its shape, and its amplitude. Figure 1.6 illustrates these effects, following their numbering in the list below, with (a) a sketch of the mechanism and (b) the impact it has on the spectrum.

1. **Turbulence** leads to small-scale eddies, with small up- and downdrafts that modify the downward velocity of particles. This increases the spread of the Doppler velocities within the radar volume and results in broader spectra, with larger SW. Such broadening can be detrimental to microphysical interpretations, and even smear out possible multi-modalities.

2. **Broadening due to horizontal wind**. Since the beam width is not 0°, the horizontal motion of the hydrometeors (due to horizontal wind) results in a radial component, away from or toward the radar on either side of the beam. This again results in a broadening of the Doppler spectrum, with an enhanced SW; this effect is all the more significant that the beam width is large. See *Shupe et al.* (2008) for a general discussion on the causes of spectral broadening, including the effects of turbulence and horizontal wind.

3. **Vertical air motion**, i.e., up- and downdrafts. Uniform vertical air motion v_{air} results in a translation of the spectrum's velocity span by v_{air}, and a similar shift of MDV. As a result,

the Doppler velocity differs—possibly significantly—from the terminal velocity, and this hampers microphysical interpretations.

4. **Shift due to horizontal wind**, in case of **imperfect vertical alignment**. When the beam is not perfectly aligned with the vertical, the horizontal wind does not just cause a symmetrical broadening of the spectrum (increase of SW, item 2), but also a general shift (change of MDV, similar to item 3), which is equal to its radial component at the center of the beam.

5. **Non-uniform beam filling**. It is another consequence of beam broadening when the resolution volume is large enough that it may contain different types of hydrometeors (e.g., *Kumjian*, 2013b), or when gradients in hydrometeor number concentrations or sizes are present (*Tanelli et al.*, 2002). Furthermore, the resolution volume is in reality a complex entity; contributions of hydrometeors may differ depending on their location at the center of the beam or at the edges, and on the beam shape itself. These effects may lead to spectrum broadening or other types of spectral deformations. In the context of vertically pointing radars, however, these artifacts are of secondary importance; the range resolution is typically rather high, and the beam broadening is limited (because of the short range, and because radars with narrow beams are often used).

6. **Attenuation** of the e.m. wave is a common issue in radar meteorology, which impacts reflectivity-based products. Its effect on the Doppler spectrum is to decrease sZ_e of a constant value (in logarithmic units), for all velocity bins where a signal is present. One aspect of this concern is radome attenuation (**6a**), due to the deposition of a liquid water or wet snow layer on the radome; this causes an attenuation of the measurements at all ranges. Another aspect is attenuation along the path, due to e.m. absorption by atmospheric gases or hydrometeors (**6b**). Depending on the radar frequency and scan mode, and on the precipitation structure, this may be a more or less crucial issue. For vertically-pointing radars measuring at only short ranges, attenuation is mostly a problem for high frequencies such as W-band. There, liquid water (rain or cloud water) is the dominant source of attenuation, although the effect of atmospheric gases and ice hydrometeors should also be considered (*Kneifel et al.*, 2015). In snowfall or MPCs, attenuation of lower frequencies (e.g., X-band) is usually small (*Kneifel et al.*, 2015).

7. **Miscalibration** or drifting calibration may be due to changes in the internal noise of the system, related to temperature or pressure variations, or to aging components. Miscalibration results in an offset of the spectral reflectivity values (constant for all range gates and velocity bins, similar to 6a). It can be mitigated through automatic calibration routines (e.g., *Küchler et al.*, 2017) or by regularly conducting an absolute calibration of the instrument with appropriate reflectors or target simulators (e.g., *Toledo et al.*, 2020; *Schneebeli et al.*, 2020).

8. **Radar sensitivity (a) and noise (b)** Along this line of measurement uncertainties related to signal processing and hardware challenges, the issue of radar sensitivity should also be mentioned. Internal (and atmospheric) noise sets a lower limit on the return power (**8a**),

below which meteorological echoes cannot be detected: this is the (range-dependent) sensitivity. Radars with higher frequencies are typically more sensitive than lower frequencies, although this is controlled by multiple factors (*Fabry*, 2015, Chapter 13). Internal noise and discretization during signal processing further induce a noisiness of the spectrum (**8b**), which can be mitigated by increasing the sampling frequency and the integration time (*Acquistapace et al.*, 2017).

9. **Aliasing** or **velocity folding**, mentioned earlier, results from the ambiguity in the measurement of phase; it occurs when the Nyquist velocity cutoff is too low for an unambiguous measurement of the Doppler velocity. In the case of vertically-pointing radars in snowfall, this is only an issue in highly turbulent cases or in the presence of strong up- or downdrafts. In most cases, with usual radar settings, the fall speed of snow particles is within the Nyquist range.
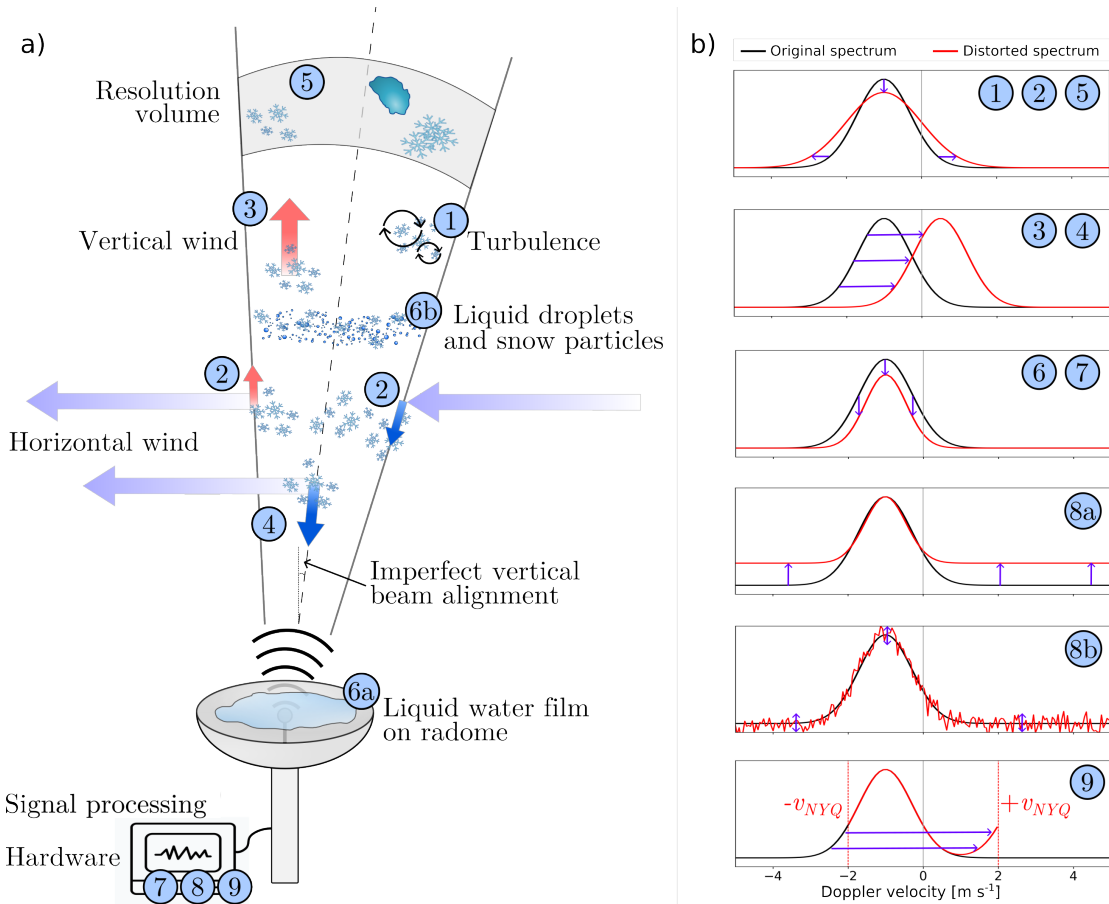
Figure 1.6: (a) Illustration of the main causes of uncertainty and data contamination by atmospheric and hardware-related effects; (b) Idealized examples of how these affect the Doppler spectrum (the spectra are drawn for illustrative purposes and do not correspond to real data). The numbering corresponds to the list given in the text.

1.3.5 Using radars with different frequencies

Principle of multi-frequency approaches

Combining measurements from radars with different frequencies to study snowfall micro-physics was first proposed by *Matrosov et al.* (1992), and may be considered as a breakthrough contribution to this field. It relies on the fact that hydrometeors, as they grow to larger sizes, transition to non-Rayleigh scattering regimes at millimeter wavelengths, while they remain Rayleigh scatterers at larger wavelengths. In what follows, we use W- and X-band as examples for the high and low frequencies, as these will be used in further chapters. Figure 1.7a illustrates this concept for the simple case of spherical water drops. In this example, a drop with diameter < 1 mm would be in the Rayleigh scattering regime both at X-band ($\lambda = 3.2$ cm) and at W-band ($\lambda = 3.2$ mm). By contrast, a larger 1.6 mm liquid water drop behaves as a Rayleigh scatterer at X-band but is within the Mie oscillation regime at W-band (*Kollias et al.*, 2002).

In terms of the radar equivalent reflectivity factor (Fig. 1.7b), this leads to $Z_{e,X} = Z_{e,W}$ for ensembles of small particles, and $Z_{e,X} > Z_{e,W}$ for large targets which are no longer W-band Rayleigh scatterers, and for which $Z_{e,W}$ no longer increases as they grow but rather plateaus. Let the dual-frequency ratio of reflectivity be defined as DFR [dB] $= Z_{e,X} - Z_{e,W}$ with $Z_{e,X}$ and $Z_{e,W}$ in dBZ; then DFR ≈ 0 dB for small particles and DFR increases with particle size (dashed gray curve). Importantly, unlike $Z_{e,X}$ and $Z_{e,W}$, DFR does not depend on particle number concentration, but solely on size- or density-related microphysical properties.
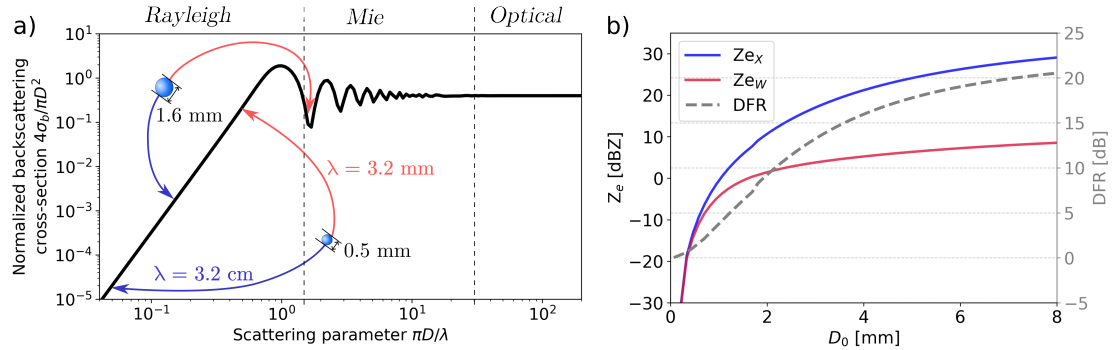
Figure 1.7: (a) Normalized backscattering cross-section as a function of the scattering parameter (circumference divided by wavelength), simulated with Mie equations for liquid water spheres; the complex refractive index[*] is taken from *Sadiku* (1985) for $\nu = 100$ GHz; two examples are shown of drops with different diameters, illustrating their normalized cross-section at X- and W-band. (b) PAMTRA simulations of $Z_{e,X}$, $Z_{e,W}$, and corresponding DFR, for an exponential PSD of snow particles with varying D_0, using the default implementation of SSRGA and a constant $N_T = 500$ m^{-3}.

---

[*]very little sensitivity of this curve to ν is noted

Multi-frequency retrievals of snowfall microphysics

The scattering properties of real snow particles are by far more complex than those of liquid spheres, described by the Mie scattering theory. The interaction of the e.m. wave with snow particles is affected by their size, but also their dielectric properties and their internal structure (e.g., *Kumjian*, 2018). Efforts have been devoted to the construction of more accurate radiative transfer models that aim to simulate, for a given frequency, the reflectivity of snowfall particles depending on their microphysical properties. Calculations based on the discrete dipole approximation (DDA; *Draine and Flatau*, 1994; *Liu*, 2004; *Kuo et al.*, 2016; *Lu et al.*, 2016) can simulate σ_b for particles with a highly complex geometry, but these methods come with high computational costs. The self-similar Rayleigh-Gans approximation (SSRGA) is a popular tool to calculate the backscattering cross-section of an ensemble of snow particles; it describes the self-similar structure of snow aggregates with a power law whose coefficients depend on the elementary crystal types (*Hogan and Westbrook*, 2014; *Hogan et al.*, 2017; *Ori et al.*, 2021), and was found to yield accurate and computationally-efficient scattering simulations.

Fig. 1.7b shows an example of snowfall reflectivity modeled with an advanced radiative transfer model (Passive and Active Microwave TRAnsfer model, PAMTRA, *Mech et al.*, 2015, 2020) using the SSRGA. Here, to simulate each reflectivity value, the mass–size relation of *Brown and Francis* (1995) is used ($a_m = 0.0185 \ \mathrm{g \ m^{-1.9}}$, $b_m = 1.9$, with the notations of Sect. 1.2.5) and an exponential PSD is assumed, whose mean D_0 is varied while keeping N_T constant. One can see the expected behavior where the DFR grows from 0 dB to large values (~ 20 dB) as D_0 increases. This illustrates that, assuming a prior knowledge of snowfall microphysical and scattering properties, the DFR can serve to retrieve a characteristic particle size (e.g., *Matrosov*, 1998; *Hogan et al.*, 2000; *Liao et al.*, 2016). While the DFR is primarily affected by particle size, it is also sensitive to the riming degree, or fractal dimension, of the snow particles (*Stein et al.*, 2015; *Battaglia et al.*, 2020). From a qualitative perspective, increasing DFR values are therefore interpreted as a sign of enhanced snowfall growth, possibly caused by aggregation or riming. The use of three well-chosen radar frequencies (e.g., W, Ka, X), instead of two, has shown promise to disentangle the contributions of particle size and mass to the reflectivity and DFR. Signatures of riming and aggregation were thus distinguished in a triple-frequency space (*Kneifel et al.*, 2011; *Kulie et al.*, 2014; *Leinonen et al.*, 2018; *Chase et al.*, 2018). Most of the cited studies, however, still rely on certain strong microphysical hypotheses, for example regarding the mass–size relation, with assumptions ranging from the use of a fixed parameterization to more flexible yet still constraining models like the "filling-in" hypothesis (*Mróz et al.*, 2021a).

Multi-frequency Doppler spectra

In view of the previous sections, combining multi-frequency and Doppler spectral techniques appears like a promising avenue: this could make use of the refined information contained in the spectrum (on particle fall speeds and PSD, among others), and of the Rayleigh/non-Rayleigh behavior of large or densely rimed particles observed through multi-frequency measurements. For the purpose of snowfall microphysical retrievals, such an approach could

allow reducing the number of required a priori assumptions. Research in this direction first consisted in using not only dual-frequency reflectivity information but also dual-frequency Doppler velocity and higher-order spectral moments, as in the studies of *Liao et al.* (2008), *Matrosov* (2011), *Szyrmer and Zawadzki* (2014) or *Maahn and Löhnert* (2017). Taking advantage of the full Doppler spectrum measured at two or more frequencies was investigated in rain by *Tridon and Battaglia* (2015); *Tridon et al.* (2017); *Mróz et al.* (2020), and in snowfall by *Kneifel et al.* (2016) and *Barrett et al.* (2019).

The transition of scattering regime at higher frequencies is visible in dual-frequency Doppler spectra (e.g., X- and W-band) with the following signature. Slow-falling particles are Rayleigh scatterers, and contribute to similar spectral reflectivity at both wavelengths: $sZ_{e,W}(v) \approx sZ_{e,X}(v)$ for $v \to 0$ m s^{-1}. On the other hand, larger, fast-falling particles are no longer Rayleigh scatterers for the higher frequency and thus have a smaller spectral reflectivity than for the lower frequency: $sZ_{e,W}(v) < sZ_{e,X}(v)$ for increasing $|v|$. This means that for well-aligned vertically-pointing radars with similar resolution volumes, the Doppler spectra at both frequencies should "match" on the low-velocity side, and diverge for large velocities, as illustrated in the simulated example of Fig. 1.8a. This was leveraged by *Barrett et al.* (2019), who retrieved full empirical PSDs from spectral dual-frequency reflectivity ratios computed on triple-frequency Doppler spectra, assuming known mass–size and velocity–size relations.
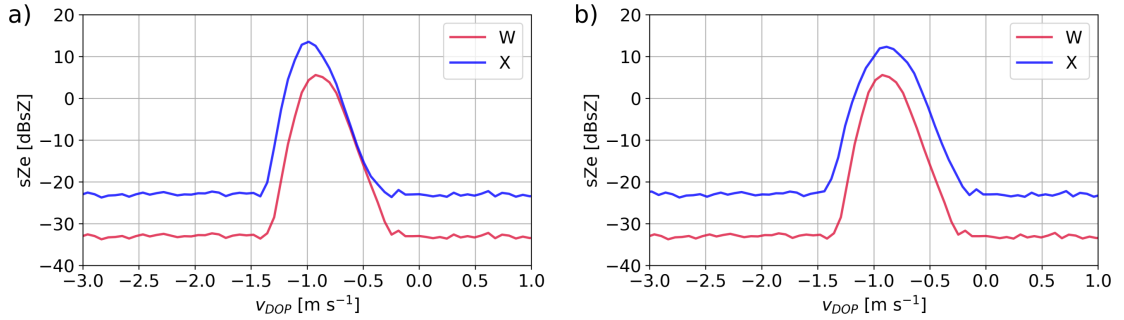
Figure 1.8: PAMTRA simulations of Doppler spectra at X- (9.4 GHz) and W-band (94 GHz). Microphysical configuration: exponential PSD with $D_0 = 1.7$ mm, $N_T = 500$ m^{-3}, mass–size coefficients $a_m = 0.0185$ g m$^{-1.9}$ and $b_m = 1.9$, area size coefficients $\alpha_a = \frac{\pi}{4}$ and $\beta_a = 2$, default SSRGA coefficients and velocity–size relation of *Heymsfield and Westbrook* (2010). Turbulent broadening is computed using an eddy dissipation rate of 5×10^{-4} m$^{2/3}$s^{-1}. Sensitivity at 1 km: -20 dBZ for W-band, -10 dBZ for X-band. (a) Half-power beamwidth $\theta_{3\text{dB},X} = \theta_{3\text{dB},W} = 0.53°$, radial wind $w_X = w_W = 0$ m s^{-1}. (b) Half-power beamwidth $\theta_{3\text{dB},X} = 1.8°$, $\theta_{3\text{dB},W} = 0.53°$, radial wind $w_X = 0.1$ m s^{-1}, $w_W = 0$ m s^{-1}.

In reality, when two radars of different frequencies are used to measure Doppler spectra, the uncertainty described in Sect. 1.3.4 (Fig. 1.6) increases significantly. Figure 1.8b is a simulated example of how different beam widths and a small misalignment causing a radial wind difference of 0.1 m s^{-1} can deform the dual-frequency spectra. Following *Orr and Kropfli* (1999), this apparent radial wind could result, for instance, from a horizontal wind of 15 m s^{-1} and a tilt angle of 0.4° off the vertical* (in the azimuth direction of the horizontal wind). Here,

---

*The apparent radial wind resulting from a horizontal wind u and a downwind tilt angle α is $w = u \sin(\alpha)$

the spectral signature of the transition to non-Rayleigh scattering for larger hydrometeors at W-band, which was well visible in Fig. 1.8, can no longer be seen, although the microphysics is unchanged. Similar artifacts may arise from both absolute and relative miscalibration, from differential attenuation, beam mismatching, differential beam broadening, or differential velocity offsets resulting from imperfect beam alignment. Workarounds were proposed (e.g., *Li and Moisseev*, 2019, for differential attenuation), but are not always possible to implement. Because of these measurement-related challenges, performing a direct inversion like *Barrett et al.* (2019) is only rarely possible. In such cases of data contamination, a direct computation of the dual-frequency spectral reflectivity ratio is difficult to interpret and may be dominated by artifacts. These measurement-related uncertainties are an important challenge that should be addressed when designing generic algorithms to retrieve microphysical information from dual-frequency Doppler spectrograms, as will be discussed in more detail in Chapters 4 and 5.

1.4 Deep learning techniques

In this section, we briefly diverge from snowfall microphysics and remote sensing retrievals to introduce certain methodological concepts and techniques that will be put to use in further chapters. Artificial intelligence, relying on machine learning techniques, has led to major advances in the past decades, across virtually all scientific fields. Its potential in atmospheric sciences as a whole is largely recognized (e.g., *Reichstein et al.*, 2019; *Bauer et al.*, 2021; *Chantry et al.*, 2021) as it opens up possibilities for precipitation and weather forecasting (*Shi et al.*, 2017; *Schultz et al.*, 2021), quantitative precipitation estimation (*Wolfensberger et al.*, 2021) or climate modeling (*Rasp et al.*, 2018). Snowfall studies are not excluded from the dissemination of machine learning techniques, and remote sensing of snowfall, in particular, has benefited from these advancements. Machine-learning-based estimations of snow accumulation (in 5 or 20 minutes intervals) from vertically-pointing K- or X-band radar measurements were recently proposed by *King et al.* (2022a,b). Deep learning was also applied to the study of microphysical properties and processes, specifically, to the detection of riming from zenith radar profiler data by *Vogl et al.* (2022), or to the retrieval of snowfall descriptors by *Chase et al.* (2021).

In what follows, we provide a succinct introduction to the main concepts behind deep learning techniques and their implementation. We will concentrate on the specific example of artificial neural networks, which are at the root of today's most popular machine learning tools, and which are used in this thesis. For more detail, the reader is referred to the textbook by *Chollet* (2017), and to articles such as *Chase et al.* (2022a,b) where a review of machine learning principles and techniques is proposed.

Basic principles

Machine learning can be very generally described as a statistical approach to fit a function f, which maps an input $\boldsymbol{x}$ to an output $\boldsymbol{y}$, and for which there is no known analytical expression. In the case of supervised machine learning, which is our focus from here on, the fit is performed on a dataset of known $(\boldsymbol{x}^*, \boldsymbol{y}^*)$. The purpose of this fit is commonly classification, where y is discrete, as in the case of image classification, or regression, where y takes values in a continuous domain. In that sense, one can say that linear, polynomial, or logarithmic regressions are already an early form of machine learning.

Neural networks are powerful tools that allow approximating a great variety of functions, with f that can be e.g., non-linear, discontinuous, or with a high-dimensional input and/or output. They rely on so-called *neurons*, which are simple building block functions, defined as follows and illustrated in Fig. 1.9a. A neuron takes as input a set of *features* $\hat{\boldsymbol{x}}$, computes an affine combination of these (each feature is multiplied with a *weight w*, and a global *bias b* is added), and passes it through a given *activation function* f_a to generate an output $\hat{\boldsymbol{y}}$. A widely used activation function is the rectified linear unit ReLU, defined as $\text{ReLU} : x \mapsto \max(x, 0)$. A "network of neurons" (neural network, NN, Fig. 1.9b) contains multiple neurons, arranged into a stack of *layers*; the outputs of the neurons in a given layer are used as input features by the neurons of the next layer. Ultimately, the NN provides a mapping $\tilde{f}$ from the initial *input layer* (containing the input $\boldsymbol{x}$) to an *output layer* which has the mathematical dimension of the output $\boldsymbol{y}$. The layers in-between are the *internal* or *hidden* layers. When all the weights and biases in each neuron are varied, $\tilde{f}$ can span a large range of functions, meaning the NN can approximate very diverse functions. Note that when ReLU is used, the mapping generated by the NN is a continuous piecewise linear function (e.g., *Goujon et al.*, 2022).
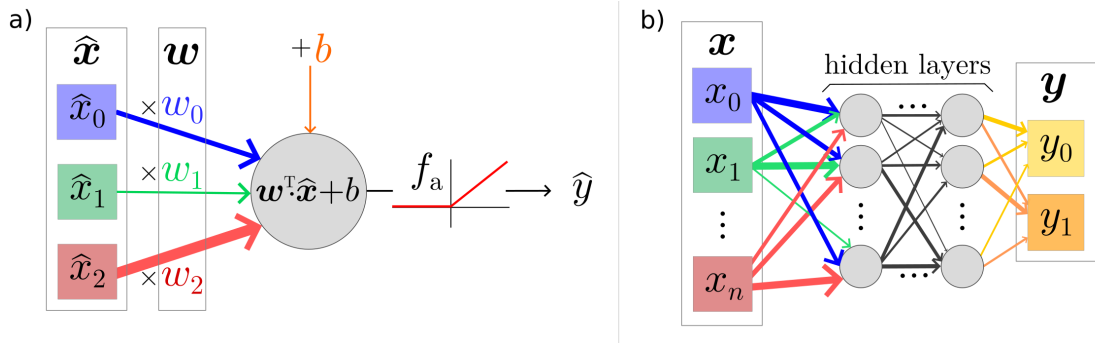
Figure 1.9: Schematic illustration of (a) an individual neuron, and (b) a neural network, following the notations defined in the text. In the example shown in (b), the input $\boldsymbol{x}$ has dimension $n+1$ while $\boldsymbol{y}$ is 2-dimensional; this is purely illustrative as $\boldsymbol{x}$ and $\boldsymbol{y}$ may be of any dimension. The width of the arrows illustrates the weight of each feature.

Given a NN architecture that produces a mapping $\tilde{f}$, the task of the *learning* algorithm is to ensure that $\tilde{f}$ is a good approximation of the true f. This is done by relying on *training data*, taken among the available known $(\boldsymbol{x}^*, \boldsymbol{y}^*)$, and adjusting the NN to minimize a *loss* function computed on these data. This loss metric (which can be, for instance, the mean squared

error) essentially measures the distance between the prediction $\tilde{\boldsymbol{y}}^* = \tilde{f}(\boldsymbol{x}^*)$ and the target $\boldsymbol{y}^*$; thus, it characterizes the quality of the approximation on the training dataset. The key step consists in modifying the NN parameters (weights and biases of every neuron) to reduce the loss; this relies on (i) the backpropagation algorithm, through which the gradient of the loss is computed with respect to each parameter. Then, the parameters are updated following a gradient descent scheme (ii). Steps (i) and (ii) are iterated until the loss no longer decreases. In practice, this basic framework is adjusted and optimized through different algorithms, which include, for example, splitting the data randomly into *batches* at each step to make the task more computationally tractable. These methods are implemented in various software codes such as *keras* (*Chollet*, 2015) or *pytorch* (*Paszke et al.*, 2019).

When building and training a machine learning model, it is good practice to split the known $(\boldsymbol{x}^*, \boldsymbol{y}^*)$ into three datasets: the *training, validation*, and *testing* sets. The machine learning model is trained on the training set. The validation set is used to tune the hyper-parameters; in the case of a NN, these define the architecture of the NN (e.g., number of layers, number of neurons per layer). After the convergence of this training/tuning procedure, the model is implemented on the independent testing set for a final evaluation. This strategy ensures that the model does not excessively *overfit* the training data, i.e., learn certain behaviors which are specific to the points of the training set and do not correspond to the mapping f itself.

Deep learning

The phrase *deep learning* refers to neural networks with multiple hidden layers. These networks have a greater number of tunable parameters, and can in principle be adjusted to represent a wider scope of functions. Deep learning has made it possible to tackle more advanced problems and work with high-dimensional inputs. In particular, a specific type of deep neural network has been instrumental to certain applications, where the input consists of images, such as image classification or image processing tasks: *convolutional neural networks* (CNN, *Lecun et al.*, 1998) use *convolution kernels* to combine a pixel with its neighbors, instead of considering each pixel independently in the input layer. This allows for the detection of spatial features such as edges, corners, or smooth areas, and has brought about major advances in image-based machine-learning problems.

Using deeper networks comes with certain challenges. In particular, deeper stacks of layers make the back-propagation step more delicate, as the gradient of the loss with respect to parameters in the early layers of the model becomes very small: this issue of vanishing gradients makes the training inefficient. Techniques were proposed to mitigate it, such as the use of batch normalization steps (*Ioffe and Szegedy*, 2015), residual blocks with skipped connections (*He et al.*, 2016), or modified routines to initialize the NN parameters (*Glorot and Bengio*, 2010). We shall not review these methods in detail; what should be noted is, that they do not actually improve the expressiveness or the complexity of the neural network, but strongly facilitate the training process.

1.5   Objectives and outline of the thesis

The previous sections have outlined the relevance of meteorological radars to study snowfall microphysics in clouds and precipitation. The microphysics of snowfall is compound, both in terms of the processes involved (i.e., the physical mechanisms at play in the formation and growth of snow particles) and in terms of the microphysical properties themselves (i.e., the geometry, size, internal structure of individual particles, and how these are distributed in an ensemble of particles). Multi-frequency radar measurements and Doppler spectra provide valuable insights into these questions. However, using radar to estimate snowfall properties is an ill-posed problem, as different sets of microphysical properties may translate into similar radar observations. To constrain this, most currently available radar-based retrievals of snowfall microphysics (Sect. 1.3.5) rely on a number of prior assumptions regarding the fractal dimension of the particles, their bulk density, or their shape. Further obstacles to quantitative radar retrievals of snowfall microphysical properties come from measurement uncertainties and contamination by non-microphysical effects. For instance, previous studies based on Doppler spectra commonly require non-turbulent atmospheric conditions; such assumptions come at the risk of overlooking the intrinsic variability of snowfall and misrepresenting some of its properties.

A specific challenge comes from mixed-phase environments, in which snow particles are present along with SLW droplets. Liquid water droplets contribute to significant path attenuation which deteriorates high-frequency radar signals; it is thus fundamental to quantify atmospheric liquid water in order to assess the reliability, and possibly correct, the radar measurements. At the same time, SLW plays an essential role in snowfall microphysics, for instance through WBF, riming, or SIP mechanisms; these microphysical processes are of high relevance to clouds and precipitation research and still subject to many unknowns.

This thesis aims to take a step forward in the joint use of Doppler spectra and multi-frequency radar measurements to study snowfall microphysics. To address this multifaceted problem, a quantitative retrieval of snowfall properties is proposed, along with qualitative perspectives on the fingerprints of microphysical processes in radar data. For these studies, we will rely on multi-sensor observations with a focus on, but not limited to, dual-frequency and Doppler spectral radar measurements. The data mostly stem from a dedicated field campaign, ICE GENESIS, that was conducted in the Swiss Jura Mountains in early 2021. The central question around which this work revolves is, how can we characterize, using remote sensing, the microphysical properties and processes of snowfall? To address this question, our investigations can be summarized through a few main objectives:

- Develop a framework for the retrieval of snowfall properties in the atmospheric column from dual-frequency Doppler spectra;

- Characterize the presence of SLW in clouds and mixed-phase precipitating systems;

- Gain insight into snowfall processes through their signatures in radar data.

The thesis is structured as follows. In Chapter 2, the setup of the ICE GENESIS deployment and the dataset collected during the campaign are presented. Chapter 3 focuses on the estimation of liquid water path, as well as integrated water vapor, from microwave radiometer brightness temperature measurements. This characterization of the liquid phase in clouds will then serve in further chapters, to correct for W-band attenuation, and to study snowfall processes in mixed-phase conditions. In Chapter 4, we introduce a deep-learning framework to retrieve snowfall properties from X- and W-band Doppler spectrograms, with a minimal number of prior assumptions. In Chapter 5, we implement the proposed approach on the ICE GENESIS dataset and evaluate its results against collocated in situ measurements. A statistical analysis of the snowfall properties retrieved during ICE GENESIS is then outlined. Chapter 6 sheds a more qualitative light on a chosen case study of the campaign, where we investigate persistent multimodal spectral signatures, in which secondary ice production is likely to play a role. A concluding discussion and perspectives on open questions are presented in Chapter 7.

2 ICE GENESIS: Synergetic aircraft, ground-based, remote sensing and in situ measurements of snowfall microphysical properties

This chapter describes a measurement campaign that was conducted in the Swiss Jura mountains from December 2020 to March 2021. The experiment was designed and conducted as a part of ICE GENESIS, a multi-partner project within Horizon 2020. The text is adapted from the published article:

- **Anne-Claire Billault-Roux**[*]**, Jacopo Grazioli**[*], Julien Delanoë, Susana Jorquera, Nicolas Pauwels, Nicolas Viltard, Audrey Martini, Vincent Mariage, Christophe Le Gac, Christophe Caudoux, Clémantyne Aubry, Fabrice Bertrand, Alfons Schwarzenboeck, Louis Jaffeux, Pierre Coutris, Guy Febvre, Jean-Marc Pichon, Fabien Dezitter, Josué Gehring, Aude Untersee, Christophe Calas, Jordi Figueras i Ventura, Benoit Vie, Adrien Peyrat, Valentin Curat, Simon Rebouissoux, Alexis Berne (2023). ICE GENESIS: Synergetic aircraft, ground-based, remote sensing and in situ measurements of snowfall microphysical properties. *Bulletin of the American Meteorological Society*, 104(2), E367–E388, doi: 10.1175/BAMS-D-21-0184.1.

Anne-Claire Billault-Roux and Alexis Berne prepared and deployed most of the instruments on the ground-based site, and ensured their operation during the campaign. A.-C. B.-R. processed the data of MXPol and WProf. Jacopo Grazioli processed MASC measurements and coordinated exchanges between the co-authors. A.-C. B.-R. and J.G. analyzed the data and wrote the manuscript with input from co-authors and supervision from A. B.
[*]: Equal contribution of the first two authors to this work.

2.1 Summary

An international field experiment took place in the Swiss Jura in January 2021 as a milestone of the European ICE GENESIS project, which aims to better measure, understand, and model the ice/snow particle properties and mechanisms responsible for icing of rotorcraft and aircraft.

The field campaign was designed to collect observations of clouds and snowfall at a prescribed range of temperatures (-10°C to +2°C). The suite of in situ and remote sensing instruments included airborne probes and imagers on-board a Safire ATR 42 aircraft, able to sample liquid and ice particles from the micron to the millimeter size range, as well as icing sensors and cameras. Two 95 GHz Doppler cloud radars were installed on the Safire ATR 42, while six Doppler weather radars operating at frequencies ranging from 10 to 95 GHz, and one lidar, were ground-based. An operational polarimetric weather radar in nearby France (Montancy) complements the coverage. Finally, observations of standard meteorological variables as well as high-resolution pictures of falling snowflakes from a multi-angle snowflake camera were collected at the ground level. The campaign showed its full potential during five multi-hourly flights where precipitation was monitored from cloud to ground. The originality of this campaign resides in the targeted specific temperature range for snowfall and in the synchronization between the ground-based remote sensing and the aircraft trajectories designed to maximize the collection of in situ observations within the column above the radar systems.

2.2 Introduction - the ICE GENESIS project

The aviation industry faces numerous safety-related challenges in cold atmospheric conditions, related to aircraft icing or the ingestion of ice crystals by jet engines. To comply with certification requirements addressing these risks, aircraft and helicopter manufacturers need to substantiate that each engine and its air inlet system can safely operate in snow, both falling and blowing, without adverse effects on engine operation. The available regulatory documents define approximations of conditions to be tested: concerning snowfall and blowing snow, the Federal Aviation Administration (FAA) in the Advisory Circular AC29-2C and Acceptable Means of Compliance AMC25.1093 prescribes temperature conditions between -9°C and +2°C. However, there are no validated engineering tools (test facilities and numerical tools) available to support the design of air inlet systems by assessing the risk of snow accretion or accumulation within this temperature range. Demonstration is thus performed at the end of the program development during certification flights, and any issue found at this stage of the development can lead to significant delays and costs. In order to secure future program development and certification, there is a need to better characterize the microphysical properties of snowfall particles or particle populations (number, mass, fractal dimension, density, sphericity, ice water content, to list a few), to support the development of engineering tools and de-risk design before in-flight demonstration.

The measurement efforts presented here are tailored to provide observations of snowfall properties at this temperature range, slightly extended to [-10, +2]°C, with the primary motivation to cover this important industrial need, as a contribution to the work package 5 (WP5) of the international project ICE GENESIS (https://www.ice-genesis.eu/). Within WP5, the main objective is to quantify the microphysical properties of snow crystal populations during snowfall; these data will then serve to specify snow properties to be generated in icing wind tunnels (WP7) and simulated in numerical tools (WP10).

Different precipitation and heat transfer processes take place between -10°C and +2°C, depending on the population of ice particles, relative humidity and availability of supercooled liquid water (*Stewart et al.*, 2015). Their proper understanding and characterization (*Grabowski et al.*, 2019; *Morrison et al.*, 2020) is a challenge beyond aircraft industrial concerns, in particular for the development of more accurate numerical weather and climate models.

The ICE GENESIS WP5 campaign is a multi-sensor experiment featuring ground-based and airborne, remote sensing and in situ measurements, which took place from December 2020 to March 2021, with an enhanced observation period during a two-week timeframe in January 2021. The added value of airborne radars onboard aircraft equipped with in situ sampling instruments has been documented (*Protat et al.*, 2007; *Wang et al.*, 2012; *Houze et al.*, 2017), as well as the synergy between ground-based weather radars and airborne instruments (*Bousquet et al.*, 2015; *Murphy et al.*, 2020). In the ICE GENESIS campaign, we consistently aimed to collect in situ data of snowfall in the predefined temperature range and at the same time sample the entire column of precipitation *from cloud to ground* with different remote sensing instruments. The setup was specifically designed to optimize the synergy of the various sensors by ensuring sequential aircraft overpasses over the ground site, between higher altitudes corresponding to the -10°C temperature level down to lower altitudes at maximum +2°C.

Other campaigns with similar setups featuring ground-based and airborne sensors have fostered the improvement of precipitation quantification and the development and validation of new retrieval algorithms (e.g., *Currier et al.*, 2017; *Leinonen et al.*, 2018; *Chase et al.*, 2018; *Mason et al.*, 2018). OLYMPEX (*Houze et al.*, 2017) was for instance designed to study precipitation at the interface between ocean, coastal and mountainous areas and had a clear target to support and improve satellite-based observations; GCPEX (*Skofronick-Jackson et al.*, 2015) was dedicated to retrieving snowfall processes and properties with the similar aim of improving satellite estimates of precipitation; IMPACTS (*McMurdie et al.*, 2022) investigated North American East Coast snowstorms and the variability of their characteristics across scales (from microphysics to large-scale precipitation patterns); BAECC (*Petäjä et al.*, 2016) was devoted to the study of clouds and aerosols in Finland.

The novelty of the ICE GENESIS experiment comes from its specific target on snowfall microphysics at mild and well-defined temperatures, and from the synergy—in terms of collocation, altitudinal range, and high resolution—between remote sensing and in situ instruments. Thanks to those features, the dataset presented here will bring new opportunities to improve the representation of snowfall properties and processes, with scientific applications extending well beyond aircraft design and related industrial challenges.

2.3 Data

2.3.1 Campaign location and sampling strategy

The location of the field campaign was chosen based on practical and climatological constraints. One objective was to maximize chances of observing snowfall at ground level, to allow for the use of ground-based in situ instruments and to reduce attenuation issues caused by rainfall for the ground-based weather radars. At the same time, the terrain should allow flights down to relatively low heights above ground to ensure that the airborne measurements sample the appropriate mild temperature range (-10°C to +2°C) as close as possible to the ground site. Based on these criteria, it was decided to set up the field campaign in the city of La Chaux-de-Fonds (LCDF) in the Swiss Jura, at an altitude of 1020 m above mean sea level (ASL), with on average 28 days of snowfall and 330 mm total precipitation per meteorological winter[*]. The ground-based sites, which included remote sensing and in situ sensors as detailed in Sect. 2.3.2, were located within and in the near vicinity of the city airport Les Éplatures, i.e., at the valley floor (Fig. 2.2). Although this is not the primary focus of the experiment, the location of LCDF in complex terrain also opens up the possibility to observe and study orographic-induced precipitation processes: in spite of a relatively modest elevation (max 1700 m ASL), the Jura Mountains benefit from orographic enhancement of precipitation (*Foresti et al.*, 2018).

The French ATR 42 environmental research aircraft of *SAFIRE* (2017), whose instrumental payload is described in Sect. 2.3.3, was stationed in the closely located Dijon airport (France), 30 minutes flight time from LCDF. Potential flights were identified a few days ahead following a daily weather briefing, jointly conducted by MeteoSwiss and Météo-France. Flight strategies and schedules were then finalized a few hours before the flights on the basis of the latest weather forecast and assessment of flight conditions. The flight plans included relatively short (15–25 km) legs in the vicinity of the ground instruments (with occasional longer ~40 km legs), following the main direction of the terrain (northeast-southwest) as can be seen on Fig. 2.1b. The sampling legs were performed at different constant-altitude flight levels as sketched on Fig. 2.1a, which were chosen depending on the temperature profile and within the authorized flight paths, constrained by the topography. Below the minimum sector altitude (MSA), the aircraft followed approach trajectories as published in IFR (Instrument Flight Rules) charts. The altitude range of each flight is referenced in Table 2.4. This strategy was preferred to other possible vertical sampling manoeuvres (e.g., Lagrangian spiral descent) due to operational and terrain constraints.

This measurement setup in the vicinity of an airport ensured that the aircraft could sample down to low heights (~100 m above ground) while ensuring almost perfect collocation with the ground-based instruments deployed at the airport. This also allowed the aircraft to adjust the altitude of its flight levels in order to sample precisely the target conditions. Given the objective of the campaign, this flexibility is a strong added-value in comparison with other experiments relying on instruments deployed at fixed altitudes (e.g., *Barthazy et al.*, 1998).

---

[*]December-January-February, compiled from MeteoSwiss automatic measurements 1980–2020

2.3.2 Ground-based data sources

The main ground measurement site (site 1 of Figs. 2.1 and 2.2), within the airport Les Éplatures, comprised a suite of remote sensing instruments: a high-sensitivity X-band Doppler spectral profiler (ROXI, *Viltard et al.*, 2019), a K-band Doppler spectral profiler (MRR-PRO; see, e.g., *Löffler-Mang et al.*, 1999; *Ferrone et al.*, 2022), a dual-polarization W-band Doppler spectral zenith profiler complemented with an 89 GHz radiometer (WProf, *Küchler et al.*, 2017), an additional W-band profiler (BASTA-mobile, *Delanoë et al.*, 2016), and a scanning system (BALI) composed of a W-band radar (mini-BASTA, *Delanoë et al.*, 2016) and a 808 nm micro-pulse lidar (SLIM, adapted from *Mariage et al.*, 2017). BALI performed hemispherical scans during aircraft flights, along the direction of the flight track.
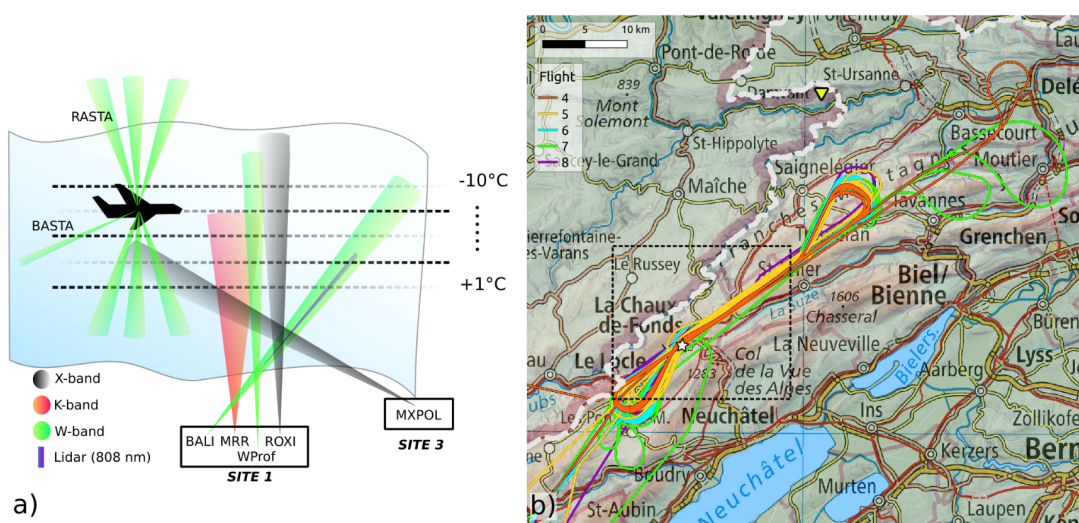
Figure 2.1: (a) Schematic illustration of the combination of remote sensing measurements collected during typical flights. (b) GPS trajectories of the aircraft during all flights of the campaign; flights are numbered as in Table 2.4. The black dashed-line rectangle delineates the area shown in Fig. 2.2; the white star corresponds to site 1; the yellow triangle shows the location of the Montancy radar. The light-gray dashed line indicates the Swiss-French border. Map: Swiss Map Raster 500 and SwissALTI3D, Federal Office of Topography swisstopo; BDALTI, Institut national de l'information géographique et forestière (IGN-F).

Table 2.1: Details of ground sensors deployed during the measurement period and the available data. All radar profilers were cross-calibrated (detail in Sect. 2.4), but no attenuation correction is performed at this stage. L2 data refer to files containing at least one variable obtained as output of a retrieval method rather than directly provided by the instrument.

Name/Description	Acronym	Deployment	Measured and retrieved quantities
W-band Doppler profiling cloud radar	WProf	Jan 14 – Feb 1	L0: Radar Doppler spectra (dual-polarization) / L2: radar moments (Z_e, MDV, SW), slanted LDR, estimates of LWP and IWV (Chapter 3, *Billault-Roux and Berne*, 2021).
Weather station coupled to WProf	WProf-AWS	Jan 14 – Feb 1	Temperature, pressure, relative humidity, wind speed
K-band Doppler profiling radar	MRR-PRO	Dec 14 – Mar 27	L0: Radar Doppler spectra / L2: radar moments (Z_e, MDV, SW), processed following *Ferrone et al.* (2022)
X-band Doppler profiling radar	ROXI	Dec 18 – Jan 28, Feb 18 – Mar 27	L0: Radar Doppler spectra / L1: radar moments (Z_e, MDV, SW)
W-band profiling radar	BASTA-mobile	Dec 18 – Mar 27	L1: Radar moments (Z_e, MDV)
W-band scanning radar + 808 nm lidar	BALI (mini-BASTA + SLIM)	Dec 18 – Mar 27	L1: Radar moments (Z_e, MDV), lidar backscatter (hemispherical RHIs)
X-band scanning polarimetric radar	MXPol	Jan 13 – Mar 27	L0: vertical PPI radar Doppler spectra (dual-polarization), L2: RHIs with radar moments (Z_e, MDV, SW, Z_{DR} [calibration with *Ferrone and Berne*, 2020], ϕ_{dp}, K_{dp}, ρ_{hv}, *Schneebeli et al.*, 2014) and hydrometeor classification with demixing (*Besic et al.*, 2018)
Multi-angle snowflake camera	MASC	Dec 14 – Mar 15	Gray-scale images of snow particles and classification of hydrometeor type (*Praz et al.*, 2017; *Grazioli et al.*, 2022)
3-D sonic anemometer	CSAT3	Dec 14 – Mar 27	High resolution measurements of 3-dimensional wind field
MeteoSwiss automatic weather station	MCH-AWS	-	Standard atmospheric parameters, weighing rain gauge and snow height measurements
Météo-France operational radar in Montancy	MTCY	-	PPIs with radar moments (Z_e, Z_{DR}, K_{dp}, ρ_{hv}, MDV, SW)

Two secondary sites, site 2 and site 3, completed the setup. 500 m away along the landing track, within the enclosure of an operational weather station of MeteoSwiss (site 2), a Multi-Angle Snowflake Camera (MASC, *Garrett et al.*, 2012; *Grazioli et al.*, 2022) and a sonic anemometer (CSAT-3) were installed. The weather station complements the measurements with standard atmospheric variables as well as 10-minute precipitation accumulation and snow height.

Finally, an X-band polarimetric radar (MXPol, e.g., *Schneebeli et al.*, 2013) was deployed 4.8 km away from the airport at site 3, and performed 5-minute scanning cycles with 4 RHI scans—alternating in Fast Fourier Transform and Dual Pulse Pair mode—in the direction of the main site (site 1) as well as one vertical *bird bath* PPI scan, for a posteriori differential reflectivity (Z_{DR}) calibration. The setup is summarized in Table 2.1 and illustrated in the map and pictures in Fig. 2.2. An operational C-band polarimetric radar of Météo-France, located in Montancy, 36 km to the NE of LCDF, performs routine volume scans at low elevations, thus providing additional large scale coverage of precipitation systems in the area of interest.
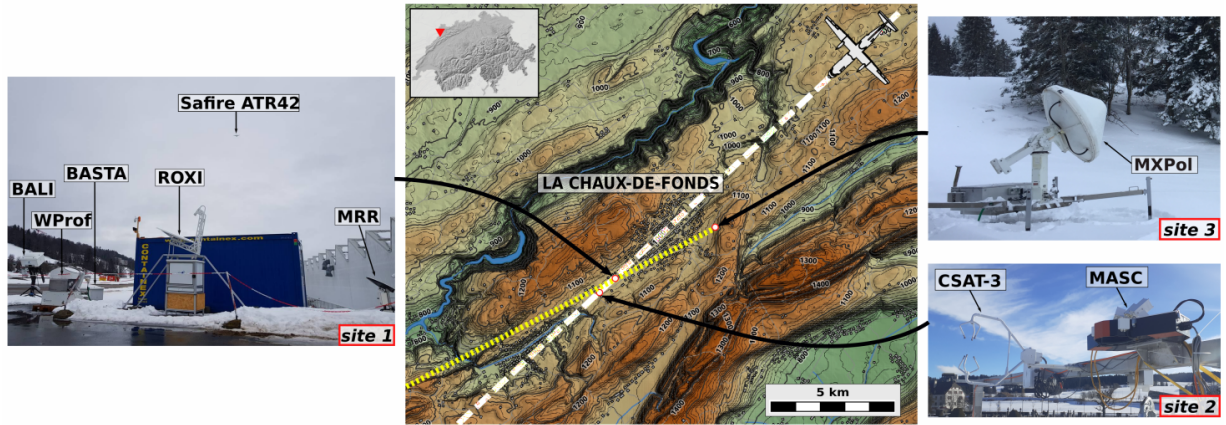
Figure 2.2: Map of the locations of the ground-based measurement sites of the field campaign, and pictures of the instruments deployed on each site. Acronyms of the instruments are defined in Table 2.1. The yellow short-dashed line indicates the direction of RHIs performed by MXPol. A white dashed line shows the approach line of ATR 42 during the overpasses, and coincides with direction of hemispherical RHI performed by BALI. The location of the sites is as follows: site 1: 47.085N, 6.797E, 1019 m ASL; site 2: 47.083N, 6.792E, 1017 m ASL; site 3: 47.102N, 6.856E, 1122 m ASL; Montancy: 47.369N, 7.019E, 913 m ASL. Map: SwissALTI3D and SwissTLM3D, Federal Office of Topography swisstopo; BDALTI, Institut national de l'information géographique et forestière (IGN-F).

2.3.3 Aircraft data

An instrumental payload was integrated on the aircraft allowing for both in situ measurements and remote sensing of snowfall conditions, as summarized in Table 2.2 and depicted in Fig. 2.3. A set of in situ imagers (optical array probes) allowed to observe hydrometeors across the full size spectrum: the 2D-S and CIP probes cover the smaller snow particle sizes, while PIP and HVPS can capture nominal particle sizes up to 6.4 mm and 19.2 mm, respectively. Measurements of snow bulk properties were performed using hot-wire probes: a ROBUST probe (e.g., *Grandin et al.*, 2014; *Strapp et al.*, 2008) which measures the total condensed water content (TWC), a Nevzorov probe which discriminates between ice and liquid water content, and the LWC-300 which measures LWC only (see e.g., *Baumgardner et al.*, 2017; *McFarquhar et al.*, 2017, for a comprehensive reference of the instruments). The payload also included a counterflow virtual impactor (CVI, *Anderson et al.*, 1994; *Schwarzenboeck et al.*, 2000) specifically adapted to measure TWC in snowfall conditions with large hydrometeors. A CDP-2 scattering probe was installed for droplet size and concentration measurements. Lastly, a snow accretion monitoring device was specifically conceived for the campaign and integrated on the aircraft. It consists of a de-iced cylinder and a dedicated camera to record potential snow accretion during the flights and collect data for subsequent validation of numerical tools within ICE GENESIS.
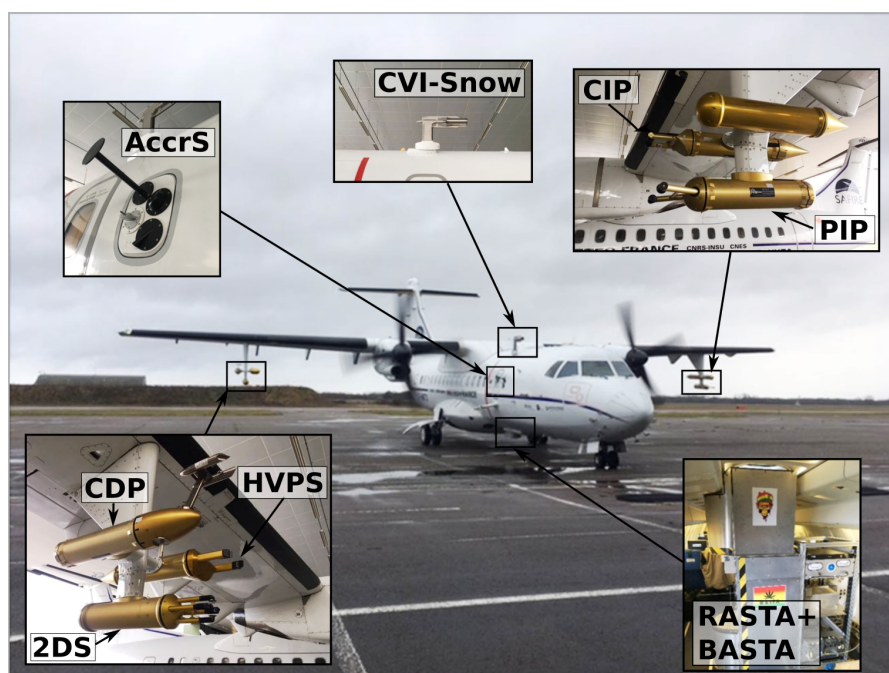
Figure 2.3: Details of the instruments deployed on the Safire ATR 42 aircraft. Acronyms are defined in Table 2.2.

Table 2.2: Instrumental configuration of the Safire ATR 42: microphysical probes and remote sensing instruments. Mass related quantities of ice crystals (ice water content and median mass diameter) are retrieved from imagers (2D-S, CIP, PIP, HVPS) following *Leroy et al.* (2016): these are estimates rather than measurements.

Name	Acronym	Measured and retrieved quantities
Aircraft probes	-	GPS, altitude, pressure, true air speed, static air temperature, heading
Dew-point and condensation hygrometers	ACH	Absolute and relative humidity
Cloud droplet probe	CDP-2	Cloud droplet size distribution (range 3–50 μm), LWC, total droplet number concentration, median volume diameter
2D-Stereo	2D-S	PSD (range 10 μm–1.28 mm), mass size distribution, total number concentration (N_T), median mass diameter (MMD), black-and-white images
Cloud imaging probe	CIP	PSD (range 25 μm–1.6 mm), mass size distribution, N_T, MMD, black-and-white images
Precipitation imaging probe	PIP	PSD (range 100 μm–6.4 mm), mass size distribution, N_T, MMD, black-and-white images
High volume precipitation spectrometer	HVPS	PSD (range 150 μm–1.92 cm), mass size distribution, N_T, MMD, black-and-white images
Counterflow virtual impactor	CVI-Snow	TWC
ROBUST WC-3000 hot-wire probe	ROBUST	TWC
Nevzorov hot-wire probe	Nevzorov	TWC, LWC
LWC-300 hot-wire probe	LWC-300	LWC
Accretion monitoring device	AccrS	Images of snow accretion on rod
Sideward-looking W-band radar	BASTA	L1: radar moments (Z_e, MDV)
Upward- and downward-looking multi-antenna W-band radar	RASTA	L0: Radar Doppler spectra, L2: radar moments (Z_e, MDV) and retrieved 3-dimensional wind field (*Bousquet et al.*, 2016).

The aircraft payload also comprised a combination of two multi-antenna W-band radars. RASTA (RAdar SysTem Airborne) is a multi-beam 95 GHz Doppler spectral cloud radar (*Plana-Fattori et al.*, 2010; *Delanoë et al.*, 2013) with one nadir-looking and three non-colinear upward-looking antennas allowing for the retrieval of the 3-dimensional wind field after correction of aircraft motion. BASTA (Bistatic rAdar SysTem for Atmospheric studies, adapted from *Delanoë et al.*, 2016) is a FMCW sideward-looking 95 GHz Doppler radar, whose purpose is to derive cloud and precipitation properties at the altitude of the aircraft up to 10 km horizontal range, thus complementing the vertical profiles measured by RASTA. The technical characteristics of all ground-based and airborne radars are summarized in Table 2.3.

Table 2.3: Properties and parameters of the ground-based and airborne radars. Note that WProf uses three chirps, whose ranges are as follows: chirp 0, 104–998 m; chirp 1, 1008–3496 m; chirp 2, 3512–8683 m. When applicable, the properties for each chirp are separated by "/". BASTA-mobile, mini-BASTA and airborne BASTA operate three modes sequentially (two for the latter) with varying range resolutions; when applicable, the properties for each mode are separated by "/".

Name	Frequency [GHz]	Transmission	3-dB beam width [°]	Sensitivity at 2 km [dBZ]	Time resolution [s]	Range resolution [m]	Nyquist velocity [m s^{-1}]
WProf	94	FMCW	0.53	-41	5	7.5/ 16/ 32	10.8/ 6.92/ 3.3
MRR	24	FMCW	1.5	-9	30	20	6
ROXI	9.48	pulsed	1.8	-19	5	50	11
BASTA-mobile	94.68	FMCW	0.4	-38/ -42/ -44	1	12.5/ 25/ 100	10/ 5/ 5
mini-BASTA	95.82	FMCW	0.8	-34/ -37/ -40	1	12.5/ 25/ 100	10/ 5/ 5
MXPol	9.41	pulsed	1.3	-18	5-min scan cycle	75	39 / 7.96
Airborne BASTA	94.56	FMCW	0.9	-15.5/-22.	0.5/1	12.5/25	10
Airborne RASTA	94.95	pulsed	0.8	-28	0.5	30	15.8

2.3.4   Dataset

The data collected during the experiment cover two nested time frames. The ground-based instruments (Sect. 2.3.2) were deployed for a longer period (mid-December 2020 to end of March 2021, see Table 2.1). Within this time interval, an enhanced observation period took place during the second half of January when the Safire ATR 42 scientific aircraft joined the continuous ground-based observations, providing the multi-instrument setup illustrated in Fig. 2.1. The flights took place between 22 January and 30 January. Overall, measurements from 14 hours of flight above the ground site were recorded, comprising a total of 100 flight legs. Table 2.4 summarizes this enhanced observation period, during which the full synergy between in situ and ground-based instruments was achieved. We hereafter focus on this period, as it is the main added value of the measurement setup presented.

The synoptic situation during this time of the year was dominated by a succession of lows over northwestern Europe, which maintained mostly dynamic and wet conditions over Switzerland after a few dry days (18–21 January). Between 23 January and 27 January, the weather was cold enough to bring snowfall at ground level, while the last days of January were characterized by warmer temperatures with rainfall at ground level and a melting layer around 1500 to 2000 m ASL. 140 mm of total precipitation were recorded during this period (22–30 January) during about 120 hours of precipitation of which 70 hours with snowfall at the ground level at the airport site.

Table 2.4: Summary of flight data during the enhanced observation period of January 2021. The time indicates take-off and landing. The temperature range sampled by the aircraft during the legs is included.

Flight reference, date and time [UTC]	Synoptic situation	No. of legs	Altitude of legs: min—max [m ASL]	Temperature range: min—max [°C]
F04 Jan 22 13:40–17:20	Cold front approaching from the northwest associated with a trough extending from Norway to southern France	18	1310 — 3214	-8.1 — +2.8
F05 Jan 23 12:30–16:30	Post-frontal showers activated by a short-wave trough	22	1238 — 2706	-12.5 — +1.7
F06 Jan 27 13:30–17:00	Behind a trough extending from Norway to Greece; passage of a jet streak in a northwesterly flow	18	1244 — 3329	-9.1 — +0.47
F07 Jan 28 08:50–12:05	Passage of a warm front associated with a low over the North Atlantic	14	1811 — 3300	-9.0 — +2.3
F08 Jan 30 10:30–15:30	Passage of a cold front and a short-wave trough associated with a low over the Celtic Sea	28	1511 — 3660	-9.3 — +1.6

Figure 2.4 summarizes the intense observation period through a selection of ground-based in situ and remote sensing data. The W-band radar data reflect the succession of multiple precipitation systems over LCDF, with both shallow and deep cloud layers. These precipitation events were associated with ground temperatures ranging from -6°C at the coldest, to +6°C at the warmest. In terms of snowfall microphysical properties, Fig. 2.4c displays the hydrometeor classification output from MASC images (from *Praz et al.*, 2017): the snow particle populations captured by the MASC were dominated by graupel-like and aggregate particles apart from small particles[*]. The apparent melting proportion, estimated from MASC images together with the hydrometeor types, correlates rather well with the measured ground temperatures, i.e., higher proportions of melting particles are identified at time steps with temperatures slightly above 0°C.

---

[*]A hydrometeor class used for all the hydrometeors too small to be reliably assigned to a given class.
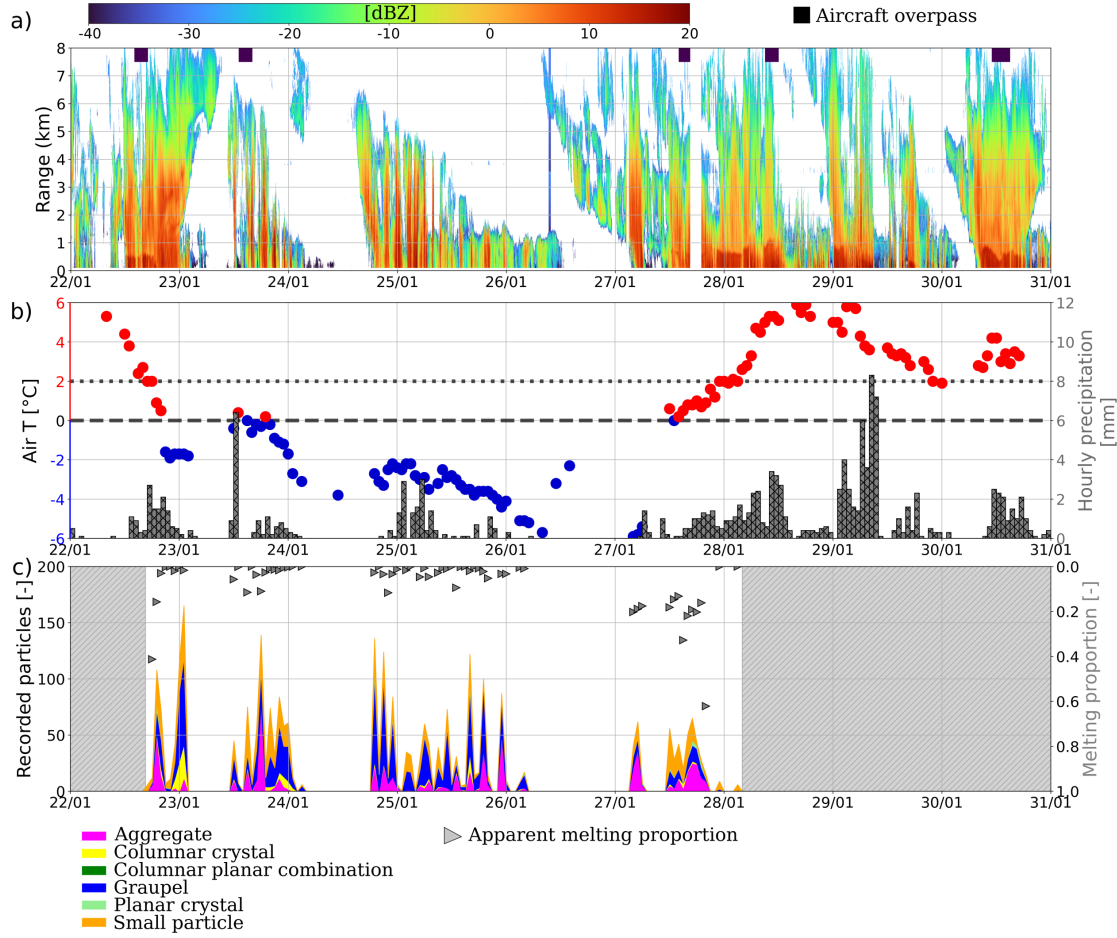
Figure 2.4: Overview of the enhanced observation period (measurements including aircraft overpasses). (a) Height–time plot of Z_e from the vertically pointing W-band profiler (WProf). (b) Average hourly temperature at ground level (only during precipitation) color coded for positive and negative temperatures; the bar plot (right y-axis) shows the hourly precipitation (source: MeteoSwiss). (c) Time evolution of hydrometeor types recorded by the MASC near ground level and average proportion of particles showing melting morphology (MASC data averaged over 1 h consecutive intervals). Only MASC data collected at temperatures lower than 2°C are shown and hourly time intervals with at least 5 particles recorded. Hatched areas correspond to time intervals with 2-meter temperatures higher than 2°C.

From an aircraft perspective, diverse snowfall conditions and microphysical properties were sampled during the five flights, as illustrated in Table 2.4 and Fig. 2.5. In terms of snow habit, rimed and fragile aggregates were the dominant particle types identified in PIP images (*Jaffeux et al.*, 2022), followed by columnar crystals and graupel. The morphological classification from the airborne 2D-S (*Jaffeux et al.*, 2022, , shown in Fig. 2.5c) reveals microphysical properties and processes at small scale ($D_{max} \leq 1280$ μm, i.e., which excludes most aggregates), and can thus help identify regions where ice production (primary or secondary) is occurring.
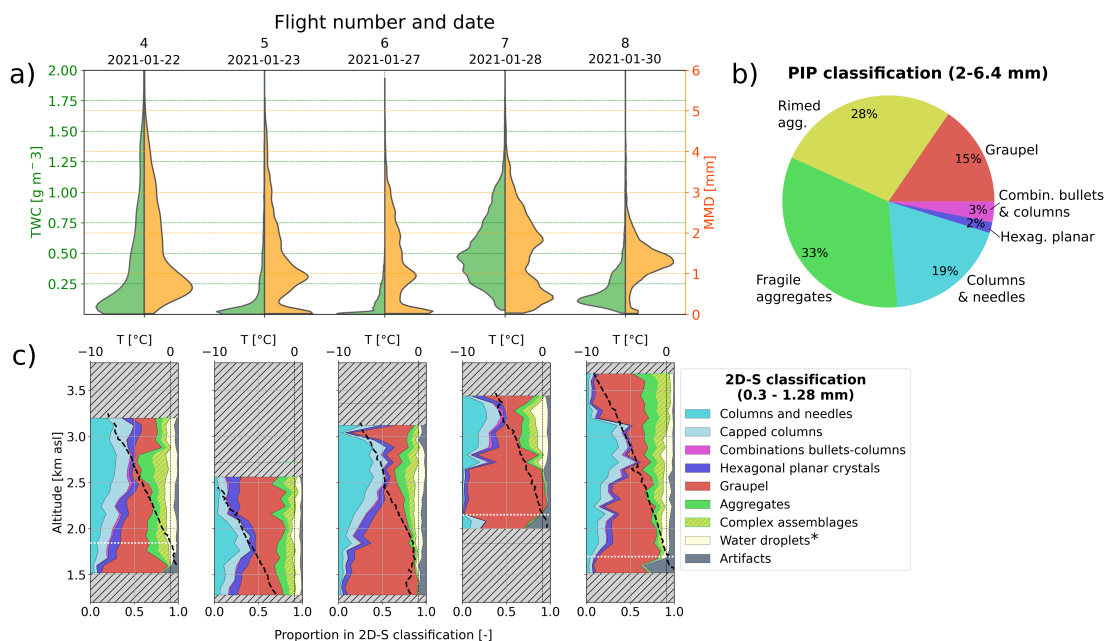
Figure 2.5: (a) Violin plots (i.e., featuring a kernel density estimation of the underlying distribution) of the TWC (CVI measurement) and MMD (calculated from 2D-S and PIP, *Leroy et al.* (2016)) for the different flights. (b) Hydrometeor classification from PIP images (size range: 2–6.4 mm), all flights merged. (c) Proportion of hydrometeor types in 2D-S images as a function of altitude, during each flight (size range: 300–1280 μm), with the mean temperature profile measured by the aircraft. Note that the morphological classes are slightly different between the two probes. The white line shows where the mean temperature profiles crosses 0°C, a rough indicator of the start of the melting layer below which the classification is less reliable. *: Out-of-focus water droplets are still classified as such, but their size is overestimated (e.g., *Korolev*, 2007b; *Vaillant De Guélis et al.*, 2019); this class therefore also includes droplets *smaller* than 300 μm.

2.4 Data showcase: 27 January flight

In this section we will focus, as a showcase, on the flight taking place on 27 January, which, as we shall see, was well representative of the ICE GENESIS target conditions. Chapter 6 of this thesis is dedicated to an in-depth analysis of the microphysical processes occurring during a subset of this event.

Synoptic and observational overview

At 12 UTC on 27 January 2021, LCDF was located behind a trough directing a strong north-westerly flow over Switzerland (Fig. 2.6b). A warm front associated with a deep low pressure system over the North Atlantic (Fig. 2.6a) led to stratiform precipitation with an increase of the snowfall line from ground level to about 2000 m ASL. This synoptic event brought a total of 35 mm of precipitation at the measurement site (from 03 UTC on 27 January to 15 UTC on 28 January), with a transition from the solid to the liquid phase around 21:30 UTC.
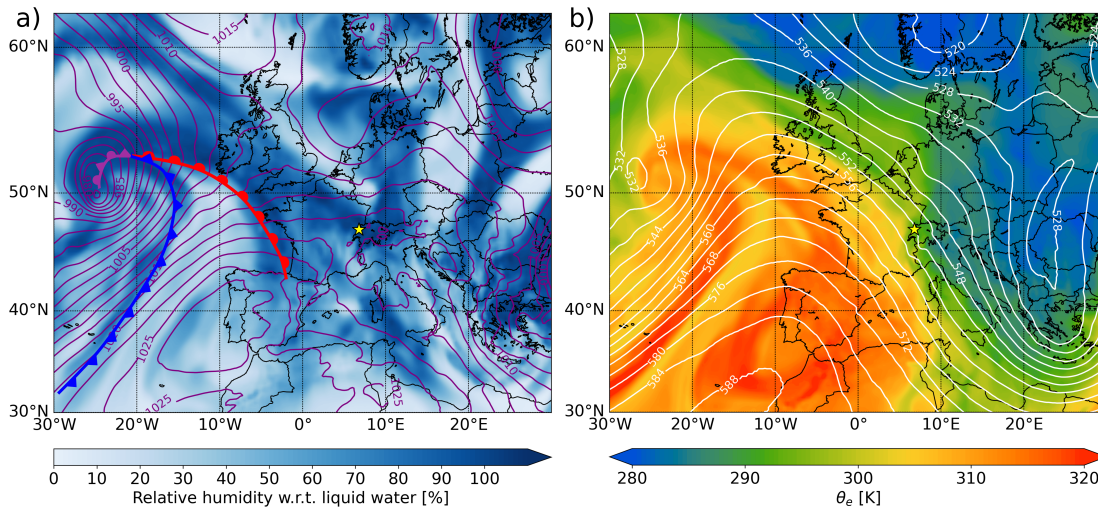
Figure 2.6: Synoptic map on 27 January at 12 UTC from ERA5 data (Fifth generation of atmospheric reanalyses of the European Center for Medium-Range Weather Forecasts). (a) Relative humidity at 700 hPa (shading) and mean sea level pressure (contours; units: hPa). The blue, red, and purple lines represent the cold, warm, and occluded fronts, respectively (analysis based on 850 hPa temperature, mean sea level pressure, and satellite images). (b) Equivalent potential temperature at 850 hPa (shading) and geopotential height at 500 hPa (contours; units: dam). Yellow stars indicate LCDF.

Flight overpasses of the ATR 42 occurred between 14 UTC and 16 UTC, with 18 flight legs performed between 1300 and 3300 m ASL, i.e., between 280 and 2300 m above ground. The TWC was up to 0.54 g m^{-3} (Table 2.4), and the temperature measured by the aircraft ranged from -9°C to +1°C (cf. mean temperature profile in Fig. 2.5 and its temporal evolution in Fig. 2.7f). At the same time, near-ground air temperatures ranged between -0.2°C and 0.5°C, with wet bulb temperatures always below 0°C due to the relative humidity around 90%. This event is therefore a perfect showcase for the objectives of the campaign: precipitation was

sampled in near-melting conditions with the top of the melting layer roughly at the ground level, where the MASC occasionally captured images of melting snowflakes (Fig. 2.10).

Figure 2.7 provides entire time series of several ground radar products during the time of the ATR 42 flight, whereas Fig. 2.8 highlights airborne and ground based observations during about 5–10 minutes corresponding to one single flight leg performed just before 14:30 UTC. Cloud signatures in the radar data (Fig. 2.7a and 2.7b) indicate the presence of several cloud layers, with high-level clouds (6–8 km above ground) above lower layers extending to 3–5 km above ground, visible for instance between 14:30 and 15:30 UTC. Active generating cells can be observed in the W-band data between 3 and 5 km, especially after 15:00.

The PIP-based classification of hydrometeor types, for particles with $D_{max} > 2$ mm (*Jaffeux et al.*, 2022), indicates the dominant particle type to be aggregates (rimed: 29% and fragile: 24%), followed by columnar crystals (20%) and graupel (20%), over the 97'836 non-truncated particles in that size range sampled during the legs of this flight. The 2D-S classification of small particles ($D_{max} < 1.28$ mm, cf. Fig. 2.5) reveals a dominant presence of columnar crystals in the region 2–3 km ASL, i.e., 1–2 km above ground; the temperature range in this region is within that of columnar crystal growth and presumably secondary ice production (-10 to -3° C, e.g., *Hallett et al.*, 1958) which suggests that ice production and growth by vapor deposition are occurring at those altitudes. The MMD (derived from 2D-S and PIP measurements, cf. Fig. 2.5), a statistical indicator of the particles mass-weighted size which is particularly relevant for aircraft industry applications (e.g., *Leroy et al.*, 2016), was between 1 and 3 mm during this flight, with maximum values up to 5 mm.

Insights from complementary measurements

Figures 2.7, 2.8 and 2.10 highlight the complementarity of the joint airborne and ground-based, remote sensing and in situ instruments. In Fig. 2.7, precipitation processes are illustrated using different ground instruments: the high-sensitivity W-band profiler (WProf) allows for measurements up to cloud tops (~9.6 km ASL) and it is complemented by X-band data. The added-value of multi-frequency radar measurements is well established for the study of snowfall properties and processes (cf. Chapter 1 and e.g., *Matrosov*, 1998; *Kneifel et al.*, 2015; *Mróz et al.*, 2021a, to list a few). Increasing values of the X- and W-band dual-frequency reflectivity ratio (DFR), resulting from a complex interplay of microphysical processes (*Mason et al.*, 2019), typically reveal the growth, within the particle size distribution, in particle size, mass, and/or density (*Liao et al.*, 2016). This is visible in the time series of Fig. 2.7e at 13:45 UTC (2–3 km ASL), 14:15 UTC (2–3 km ASL), and 14:50 UTC (1–2 km ASL) with DFR > 15 dB. It should be noted that the radar measurements, especially at W-band, are affected by attenuation, resulting from the presence of wet (and to a lesser extent, dry) snow, supercooled liquid water, and/or water vapor (e.g., *Kneifel et al.*, 2015; *Protat et al.*, 2019), as well as from the presence of liquid water on the antenna or radome of certain radars[*].

---

[*]This is not the case for WProf, which is equipped with blowers (*Küchler et al.*, 2017).
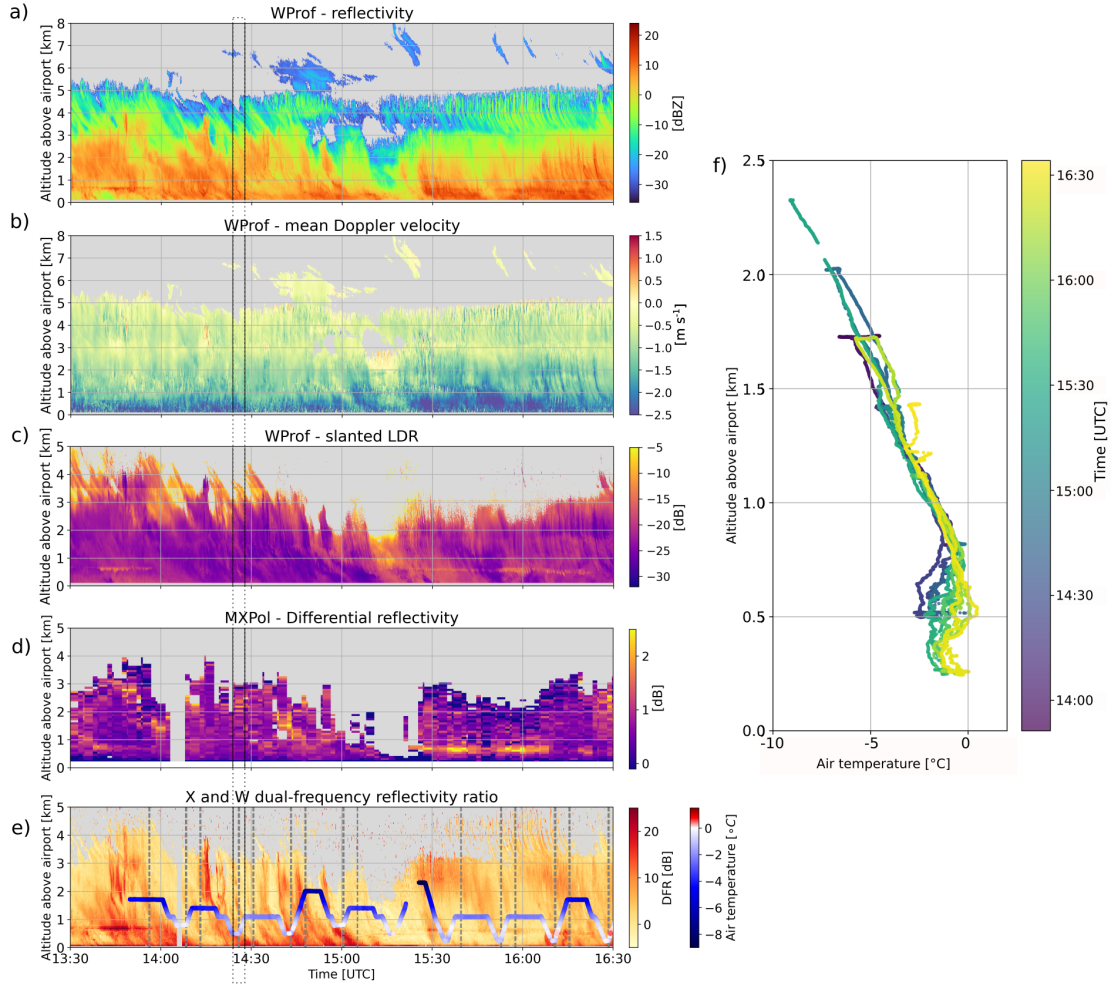
Figure 2.7: Radar time series during the ATR 42 flight on 27 January, 13:30–16:30 UTC. The three top panels display WProf zenith measurements: (a) reflectivity Z_e, (b) mean Doppler velocity MDV, and (c) slanted linear depolarization ratio SLDR. (d) Z_{DR} measured by MXPol (the RHIs are remapped to a Cartesian grid and vertical profiles are extracted at a horizontal distance corresponding to the location of the airport (±250 m), using only elevations below 45°). (d) Dual-frequency reflectivity ratio DFR, derived from ROXI and WProf data; the aircraft trajectory is overlaid, color-coded with the air temperature measured by the aircraft; dashed lines indicate time steps of aircraft overpasses. In panels a–e: vertical lines indicate the time frame (14:19–14:27 UTC) of Fig. 2.8. (f) Air temperature profile sampled by the aircraft during the flight, time is color-coded.

Without correction, quantitative analyses of the DFR should be conducted with care. A qualitative interpretation of spatio-temporal features, such as the fall streaks mentioned earlier, remains, however, relevant. Here, these regions also feature relatively low (~ -25 dB) slanted LDR (Fig. 2.7c), which are compatible with riming or aggregation processes. Combining observations of reflectivity-based variables to mean Doppler velocity allows to further refine the identification of snowfall growth mechanisms (e.g., *Mason et al.*, 2018; *Oue et al.*, 2021). For instance, the fall streak extending from 1 to 3 km around 14:35 UTC displays relatively high DFR (~8 dB) and low SLDR (~-25 dB), together with a large MDV (~-1.5 m s^{-1}), which could indicate a riming occurrence. In situ observations and Doppler spectra collected in this time frame (not shown here) support this hypothesis.

Another noticeable feature is the bright band around 600–800 m above ground, visible in Z_e, SLDR, DFR and Z_{DR} between 13:30 and 14:00 UTC, and from 15:30 to 16:30 UTC. Airborne temperature data—color-coded on the aircraft trajectory in Fig. 2.7e, and shown in Fig. 2.7f— confirm the presence of a temperature inversion, leading to near-zero temperatures both near ground and in the layer of enhanced reflectivity. The bright band is thus the signature of a partial melting layer whereby an air parcel with positive temperatures—resulting from the warm front arrival—is overlying a colder region where partially melted hydrometeors freeze again. This refreezing process may be partly responsible for the enhanced Doppler velocities observed below these layers, which are characteristic of dense, fast-falling particles.
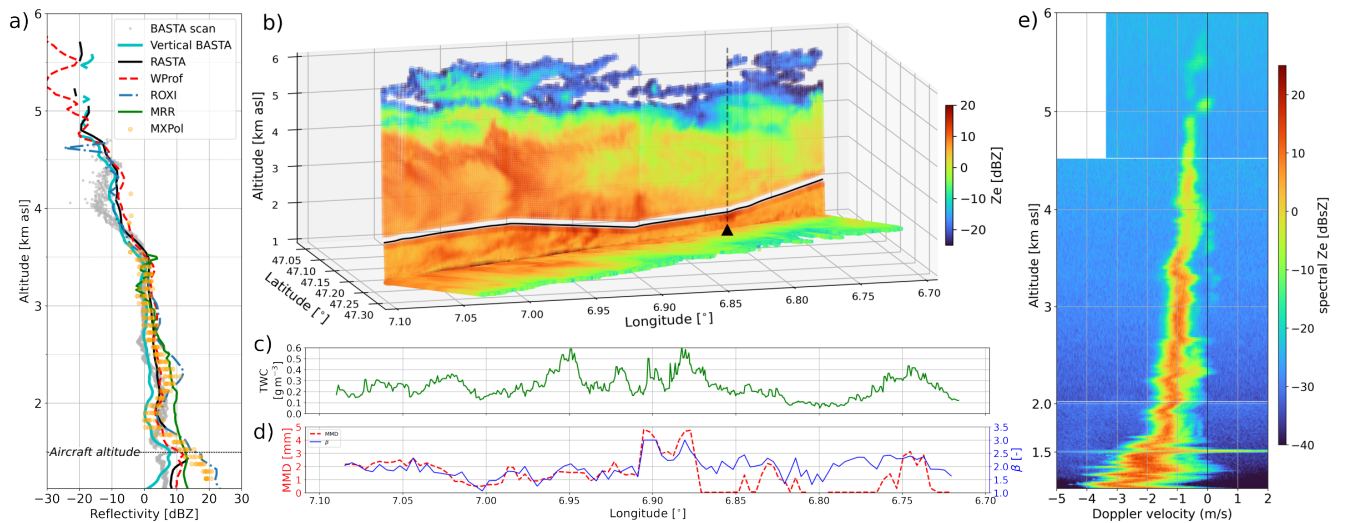
Figure 2.8: Overview of an aircraft overpass of the measurement site from ground based and airborne data sources. (a) Vertical profiles of Z_e collected by multiple data sources (ground-based and airborne radars) between 14:25 and 14:26 UTC. (b) Flight path (14:19–14:27 UTC) of the ATR 42 with airborne RASTA Z_e; airborne BASTA Z_e in the horizontal plane is also shown (projection to ground level for visualization purposes). The location of the ground based instruments is indicated by a black triangular marker. (c) Time series of TWC sampled by the CVI. (d) MMD and mass–size exponent b_m retrieved from 2D-S and PIP (*Leroy et al.*, 2016). (e) Example of a Doppler reflectivity spectrogram collected by WProf at the same time step; the broad spectrum around 1.5 km ASL is caused by the wake of the aircraft; the missing data above 4.5 km ASL is due to the smaller Nyquist velocity in this chirp.

The detailed spatio-temporal structure of precipitation can be visualized as in Fig. 2.8, by focusing on a shorter time frame during an overpass of the aircraft on the instrumented site. Reflectivity measurements from the airborne RASTA (vertical profiles), and BASTA (horizontal profiles) radars are shown on the same image (Fig. 2.8b). In situ measurements of TWC along the aircraft trajectory, displayed in Fig. 2.8c, qualitatively match expected behaviors: larger TWC values are observed when the aircraft crosses regions with enhanced radar reflectivity. Comparing TWC to retrievals of MMD and exponent b_m of the mass-dimensional relation (retrieved from 2D-S and PIP probes with an integrated mass constraint from the TWC, following *Leroy et al.*, 2016), in Fig. 2.8d, brings additional information about how the mass is distributed over the population of particles as well as some indications on active microphysical processes. For instance, aggregation can increase MMD, and riming can increase b_m from typical values around 2 to values almost reaching 3. The inspection, visual or automatic, of actual hydrometeor images, eventually allows backing up these interpretations case by case. Note that the calculated b_m exponent is just a time-dependent value, retrieved for any heterogeneous mixture of size-dependent particle morphologies observed during each second of the flight. When approaching longitude close to 7° (Fig. 2.8d), exceptionally low b_m values were retrieved with increasing 2D-S concentrations of numerous elongated columns and a simultaneous decrease in PIP large particle concentrations, giving significant weight to the 2D-S columns in the computation of b_m. Some understanding of the larger-scale spatio-temporal precipitation structures can be gained when complementing these observations with a PPI of the operational radar in Montancy, as shown in Fig. 2.9.
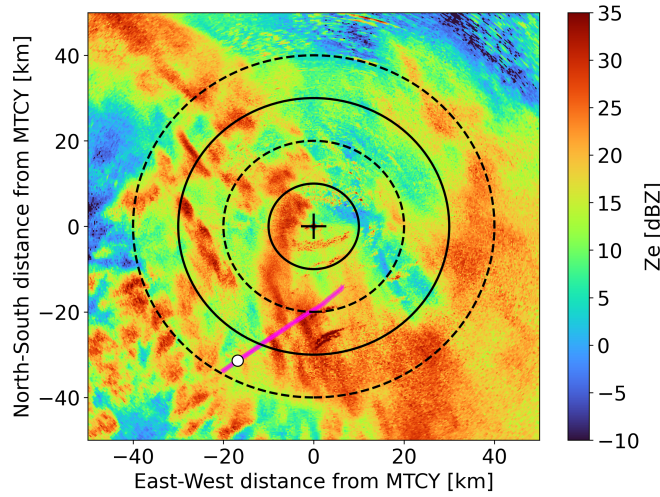
Figure 2.9: Z_e PPI (at 2.2° elevation) from the operational radar of Montancy (FR) at 14:30, coinciding with the time step shown in Fig. 2.8. The white marker indicates the location of site 1; the magenta path is the aircraft trajectory in this time frame; circles are drawn at 10 km range distances from the radar.

The reflectivity profiles of all radars at the time step of the overpass are displayed in Fig. 2.8a. For this analysis, the ground-based profilers (X- and W-band) and airborne (RASTA) radars were cross-calibrated, relying on the mini-BASTA as a reference, which had absolute calibration following *Toledo et al.* (2020). This calibration transfer was performed using a set of cloud

profiles carefully selected to avoid disparities caused by differences in sensitivity or scattering regime (*Toledo Bittner*, 2021, *Jorquera et al.*, 2023). For the cross-calibration of RASTA, the profiles were selected from time steps when the aircraft overpassed the ground site. Doppler spectra, as shown in Fig. 2.8e (same time step), reveal additional features such as secondary modes in the particle size distributions (here between 2 and 2.7 km ASL, and between 3 and 4 km ASL), indicative of the coexistence of different hydrometeor populations within the same radar resolution volumes.
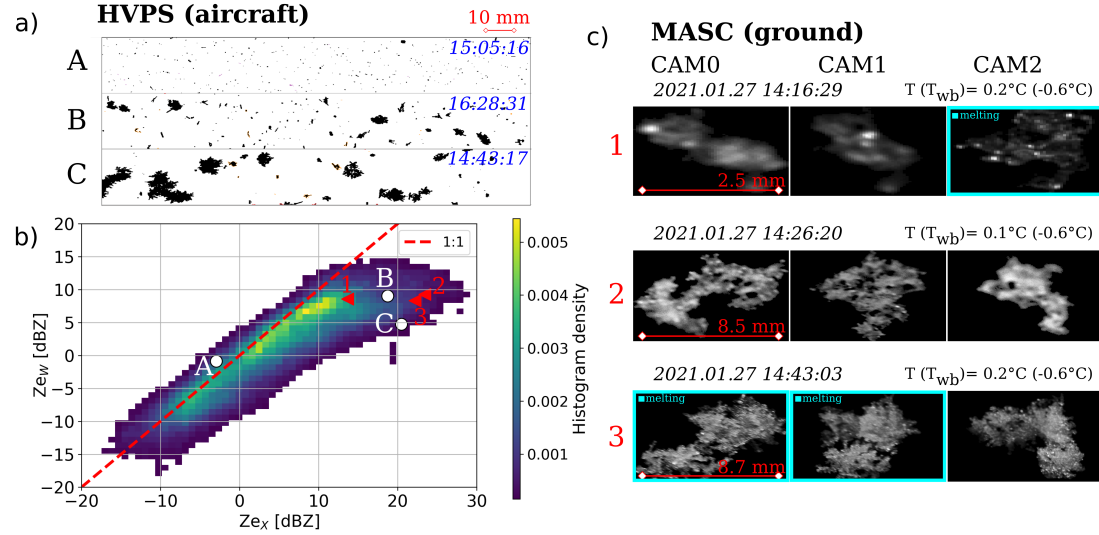
Figure 2.10: (a) A few HVPS images are shown, for time steps at which the aircraft was within 250 m horizontal distance of the radars. (b) 2-D density plot, of X- and W-band collocated Z_e observed by ROXI and WProf, respectively, during the entire time frame of the aircraft flight presented in Fig. 2.7. (c) MASC image triplets collected at ground level at three different time steps, with information about near-ground temperature and wet-bulb temperature. Particles identified as melting by the method of *Praz et al.* (2017) are highlighted with a cyan frame. MASC and HVPS images are contextualized to points of (b) by extracting the $Z_{e,X}$ and $Z_{e,W}$ at the nearest valid (time, range) gate: for the MASC (red triangles), this corresponds to the 3$^{\text{rd}}$ radar gate (150 m above ground); for the HVPS (circles), to the altitude of the aircraft above ground.

In Fig. 2.10, we take a closer look at pictures from airborne (HVPS) and ground-based (MASC) imagers, relating them to remote sensing measurements. The ($Z_{e,X}$, $Z_{e,W}$) scatterplot illustrates the deviation from the Rayleigh scattering regime at W-band for high reflectivities, corresponding to large particles—here again, a quantitative interpretation is delicate in the absence of attenuation correction. HVPS and MASC images from a few time steps are matched to points of the ($Z_{e,X}$, $Z_{e,W}$) scatterplot: it is noteworthy that aggregates with a maximum dimension of about one centimeter (red markers labeled as 2 and 3) are observed by the MASC at time steps with high Z_e and high DFR close to the ground; similarly, small particles visible in the HVPS correspond to low DFR (point A), and increasingly bigger aggregates to larger DFR (B and C). This should of course be handled with care since the radar moments reveal information on statistical distributions corresponding to much larger volumes than sampled by the HVPS or the MASC.

2.5   Conclusions

The measurements conducted during the ICE GENESIS field campaign aim to give momentum to snowfall microphysics research focused on processes and properties at temperatures ranging from -10°C to +2°C. The combination of remote sensing, in situ, ground-based, and aircraft measurement techniques, was designed to sample clouds and precipitation through the entire column and at different scales: from the large sampling volumes of radar to the depiction of individual hydrometeors by in situ imaging probes. The experimental set-up and aircraft sampling strategy were designed to maximize the overpasses above the ground site and hence the joint in situ and remote sensing measurements. This chapter provides a detailed overview of the field experiment and a few examples of preliminary analyses.

The examples shown above were selected to demonstrate the potential of the dataset. Data will be used to answer specific technical questions coming from the aviation sector: statistics of detailed microphysical snow properties (e.g., mass–size relation, morphological class, dry or wet snow, crystal density, sphericity) at the given temperatures are needed as a fundamental input for accretion simulations and laboratory experiments. At the same time, underlying scientific questions will be investigated. The setup is ideal to improve existing or develop new retrievals of snowfall rate and snowfall microphysics from remote sensing measurements (at single- or multi-frequency and polarization) and to validate those with in situ observations, with reuse potential for satellite-based products. The collocated polarimetric measurements and multi-frequency Doppler spectral profiles can be jointly used for process-oriented analyses.

The abundance of in situ data provides ground truth for hydrometeor classification algorithms based on remotely sensed observations (e.g., *Besic et al.*, 2016, 2018). This is of particular interest to operational weather services with the presence of the Montancy radar of MeteoFrance at close range. Investigations in this direction have already started. The data will be important in the field of numerical weather prediction, for example for the improvement and validation of microphysical schemes in meteorological models, through the comparison of model outputs with in situ measurements or radar retrievals in a region of complex orography.

The measurement campaign is a milestone in the broader context of ICE GENESIS. It will support the parameterization of snowfall thermo- and aerodynamic models, and the simulations of snow accretion performed by other working groups within the project, with the long-term goal being, as a bridge between research and industrial needs, to use the retrieved microphysical properties to develop engineering tools and de-risk system design early in the development process.

3 Integrated water vapor and liquid water path retrieval using a single-channel radiometer

This chapter presents an algorithm to retrieve an estimate of the liquid water path and integrated water vapor from 89 GHz radiometer measurements. It is based on the postprint version of the article:

- **Anne-Claire Billault-Roux** and Alexis Berne (2021): Integrated water vapor and liquid water path retrieval using a single-channel radiometer. *Atmospheric Measurement Techniques*, 14(4), 2749-–2769, doi: 10.5194/amt-14-2749-2021.

The algorithm was designed and evaluated on various datasets by Anne-Claire Billault-Roux with input and supervision from Alexis Berne.

3.1 Summary

Microwave radiometers are widely used for the retrieval of liquid water path (LWP) and integrated water vapor (IWV) in the context of cloud and precipitation studies. This chapter introduces a site-independent retrieval algorithm for LWP and IWV, relying on a single-frequency 89 GHz ground-based radiometer. We use a statistical approach based on a neural network, which is trained and tested on a synthetic dataset constructed from radiosonde profiles worldwide. In addition to 89 GHz brightness temperature, the input features include surface measurements of temperature, pressure, and humidity, as well as geographical information and, when available, estimates of IWV and LWP from reanalysis data. An evaluation of the algorithm is conducted to assess its accuracy, sensitivity to radiometer calibration, stability across geographical locations, and the importance of the various input features. The algorithm is shown to be quite robust, although its accuracy is inevitably lower than that obtained with state-of-the-art multi-channel radiometers, with a relative error of 18% for LWP (in cloudy cases with LWP > 30 $\mathrm{g\,m^{-2}}$) and 6.5% for IWV. The highest accuracy is obtained in midlatitude environments with a moderately moist climate, which are more represented in the training

dataset. The new method is then implemented and validated using real data that were collected during a field deployment in Switzerland and during the ICE-POP 2018 campaign in South Korea.

3.2 Introduction

One of the core challenges in cloud and climate research is the monitoring, quantification, and modeling of cloud liquid water, which contributes significantly to radiative processes on a global scale. Additionally, from the perspective of snowfall microphysical studies, identifying the presence of supercooled liquid water during a snowfall event is of paramount importance as it drives the riming of snow particles and is involved in the most important secondary ice production processes. In this perspective, highly accurate methods were developed to retrieve liquid water path (LWP) as well as integrated water vapor (IWV) from microwave radiometer measurements, relying on the fact that water in its liquid and vapor phases is the main atmospheric contributor to brightness temperatures in millimeter wavelengths, outside of the oxygen window.

The quantitative retrieval of LWP from ground-based or satellite measurements of brightness temperature (T_B) at a single-millimeter wavelength is an underdetermined, or ill-posed, problem. T_B results from the radiative contribution of gases and hydrometeors across the atmospheric column and depends on the vertical profile of temperature. To lift this underdetermination, state-of-the-art retrievals of LWP and IWV rely on multi-frequency radiometers, which measure T_B in several microwave channels. This allows for the separation of the contributions of water vapor and liquid water (e.g., *Westwater et al.*, 2001) and, to some extent, for a retrieval of the full profile of liquid water content and humidity in the atmospheric column (*Löhnert et al.*, 2004). It should be noted that IWV retrievals with similar accuracy are commonly obtained using GPS sensors, as first proposed by *Bevis et al.* (1994), but this technique does not allow for the joint retrieval of LWP.

Multi-frequency instruments, however, are not always available. *Küchler et al.* (2017) demonstrated that a radiometer channel at 89 GHz could be added to a 94 GHz cloud radar, thus allowing for collocated measurements of radar variables and brightness temperature, paving the way for an improved understanding of cloud and precipitation physics. *Küchler et al.* (2017) proposed a method to derive LWP estimates from single-frequency brightness temperature, and the present study builds on those findings.

Two approaches are commonly considered to retrieve LWP and IWV from microwave radiometer measurements, as described in *Turner et al.* (2007) and *Cadeddu et al.* (2013). The first method relies on the reconstruction of atmospheric profiles with a physical model that is iterated until modeled T_B values match the measured ones. Although this method is formally the most accurate (*Turner et al.*, 2007), it requires more than one radiometer frequency to lift the fundamental underdetermination of the retrieval. The other way to tackle the problem is to derive statistical relationships between T_B and LWP and/or IWV based on synthetic datasets

constructed using atmospheric profiles from a given location. This approach has been widely used for both ground-based and satellite applications, with varying degrees of complexity in the statistical fitting algorithms (linear, quadratic, logarithmic fits, or using neural network architectures, *Karstens et al.*, 1994; *Löhnert and Crewell*, 2003; *Mallet et al.*, 2002; *Cadeddu et al.*, 2009). The retrieval coefficients that are computed with this method are usually site-specific since they incorporate during the learning or regression stage the climatological features at the location of the dataset. The geographical range within which a site-specific algorithm would be reliable is difficult to estimate, especially if the orography of the region is complex, as highlighted by *Massaro et al.* (2015). In general, implementing a site-specific algorithm in a location with a different climatology is likely to yield erroneous retrievals (*Gaussiat et al.*, 2007). In order to implement such an algorithm at another site, a new parameterization should be developed using a suitable dataset; but there might not always be enough reliable data available for this purpose. In order to avoid this lengthy process, and in the case of instruments that are intended to be deployed in various locations, a site-independent algorithm is more adequate (*Liljegren et al.*, 2001).

We present a new site-independent statistical method for the retrieval of both LWP and IWV that relies on a single radiometer frequency. The regression is performed through a neural network, whose input consists of brightness temperature at 89 GHz, surface meteorological variables, and geographical information. Those additional input features are shown to be especially key to the retrieval of IWV. Although this new method comes with a loss of precision in comparison with state-of-the-art multi-frequency retrievals, its advantage is to be applicable in any location with constrained uncertainty.

The next section describes the data used in the different steps of this study, from the design stages to the validation of the method. Section 3.4 outlines the forward model used to build the synthetic dataset on which the LWP and IWV retrieval algorithms are trained. In Sect. 3.4, the design of the algorithms is detailed, and the results on the synthetic dataset are reviewed and analyzed in Sect. 3.6. An independent validation of the method is presented in Sect. 3.7 using two contrasted datasets that were collected during field deployments in Payerne (Switzerland) and in the Taebaek mountains (South Korea). A summary and conclusions are provided in Sect. 3.8.

3.3   Data

This work is based on two types of data: a multiyear collection of radiosonde observations across the world (for training and testing of the retrieval algorithms), and sets of measurements from an 89 GHz radiometer deployed in various regions during field campaigns limited in time.

3.3.1   Radiosonde dataset

The design of a statistical algorithm requires a large dataset on which to fit the desired model. Here, this dataset was built using radiosonde profiles collected in over 180 stations throughout the world, available through the University of Wyoming portal (*Oolman*, 2020). In total, $\sim 10^6$ radiosonde profiles are used from 20 years of data (2000–2019). It was ensured that the data included radiosonde stations from all climatic regions covering a wide range of altitudes (0 to 4000 m ASL). However, lack of available data in some areas inevitably results in an unbalanced dataset, in which polar and tropical areas are underrepresented compared to midlatitudes, especially Europe. The possible impact on the performance of the algorithm is further discussed in Sect. 3.6.

A quality check of the radiosonde profiles was performed on the relevant variables (pressure P, temperature T, relative humidity RH) through the following steps. The atmospheric column was split into nine ranges of altitudes; in each of these altitudes ranges, the minimum and maximum P, T, RH were extracted from all radiosoundings. Outliers were removed with a 10^{-4} quantile (upper and lower quantile, determined after a visual inspection of the distributions). In total, 6395 profiles were flagged and removed. It was ensured that this routine did not result in the systematic removal of some geographical locations. Following this step, the vertical profiles of P, T, RH were used as input to the forward model, as described in Sect. 3.4. The vertical extent of the profiles ranges from 1 to 50 km, with a 25% quantile at 11 km, meaning the profiles largely cover the lower troposphere. The vertical resolution is relatively low (0.37 km on average).

3.3.2   Field deployments

In the validation stage of this work, the proposed algorithm is implemented on real 89 GHz radiometer data that were collected during campaigns described below.

Instrument

The main instrument that was used for the implementation of the algorithm is the radar–radiometer system of Radiometer Physics GmbH (RPG) described in *Küchler et al.* (2017), and referred to as WProf. It consists of a 94 GHz FMCW cloud radar with an 89 GHz radiometer channel, which allows for joint active and passive retrievals of cloud and precipitation. In the data presented here, WProf was deployed together with a weather station that provided surface measurements of temperature, pressure, and relative humidity.

Payerne 2017

The first dataset on which the new algorithm was evaluated stems from a field deployment in Payerne (Switzerland) at 450 m ASL in late spring 2017 (15 May–15 June). As a means of

comparison, data from the Swiss federal office of meteorology and climatology (MeteoSwiss) were used. The MeteoSwiss facilities in Payerne comprise a multi-frequency radiometer[*] with tipping-curve calibration, HATPRO (Humidity And Temperature PROfiler, *Rose et al.*, 2005; *Löhnert and Maier*, 2012; *RPG Radiometer Physics GmbH*, 2014), which provides state-of-the-art retrievals of LWP (resp. IWV) with a nominal accuracy of 20 g m^{-2} (resp. 0.2 kg m^{-2}). During this deployment, both WProf and HATPRO measured brightness temperatures with a high temporal resolution of the order of a few seconds. The instruments were located approximately 65 m apart; this distance is small enough that it should generally not affect the comparison of the retrieved values from the two instruments. However, it cannot be ruled out that in some rare cases, a cloud might overpass one of the radiometers but not the other, leading to a discrepancy in the measured brightness temperatures.

In addition, radiosondes are launched twice daily in Payerne by MeteoSwiss, allowing for the direct computation of IWV values, which are used as a further source of validation for the IWV retrieval algorithm.

ICE-POP 2018

The second dataset on which the new algorithm was tested comes from the ICE-POP 2018 campaign, which took place in South Korea during the 2017–2018 winter in the context of the 2018 Olympic and Paralympic winter games in Pyeongchang. A description of the data is presented in *Gehring et al.* (2021). During this campaign, the weather was generally cold and dry; nine precipitation events were recorded, and occasional fog was present (about 25 occurrences during the campaign timeframe). WProf was deployed from November 2017 to April 2018 in Mayhills, 50 km southeast of Pyeongchang, at 789 m ASL. This allows for an implementation of the algorithm in a different context than Payerne, i.e., in winter and in a fully different geographical setting, at a lower latitude and closer to the sea.

In this case, contrary to Payerne, no independent measurements of LWP are available; radiosondes launched every three hours provide a means of comparison for IWV retrievals, although only with a lower spatial and temporal resolution.

3.4   Forward model

A large amount of data is required to develop a robust statistical algorithm. For this purpose, the radiosonde data described in Sect. 3.3.1 were used to build a synthetic dataset. A two-step forward model was implemented, first to identify clouds in each radiosounding and derive the corresponding liquid water content (LWC) profile, then to compute the resulting 89 GHz T_B. The different steps of this forward model are illustrated as a flowchart in Fig. 3.1.

---

[*]measuring in 7 channels at K-band, from 22.3 to 31.4 GHz, and in 7 channels at V-band, from 51 to 58 GHz
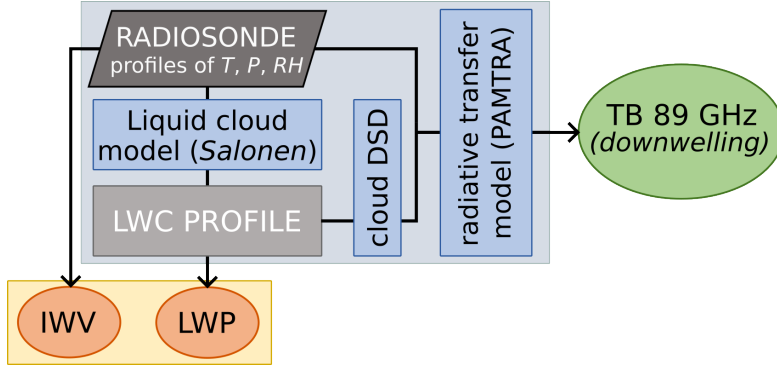
Figure 3.1: Illustration of the different steps of the forward model. It takes as input radiosonde data and outputs, on the one hand, IWV and LWP values, and on the other hand, simulated 89 GHz T_B.

3.4.1 Cloud liquid model

To derive LWC from radiosonde profiles of atmospheric variables, we used the cloud model of *Salonen and Uppala* (1991). Cloud boundaries are identified when the relative humidity exceeds a threshold RH_c [-], which depends on pressure and temperature according to Eq. 3.1.

$$RH_c = 1 - \alpha_s \, \sigma \, (1 - \sigma) \, [1 + \beta_s \, (\sigma - 0.5)] \tag{3.1}$$

Here, $\sigma = \frac{P}{P_g}$, with P and P_g respectively denoting atmospheric pressure at the current level and at the ground. Corrections from *Mattioli et al.* (2009) are used for the coefficients α_s and β_s of the Salonen model. Within the detected cloud layers, the LWC profile is then calculated with Eq. 3.2:

$$LWC(h, T) = w_0 \left(\frac{h - h_b}{h_r} \right)^{a_s} f_s(T), \tag{3.2}$$

where $f_s(T) = 1 + c_s T$ for $T \geq 0$ and $f_s(T) = \exp(c_s T)$ for $T < 0$, with T in °C; $a_s = 1.4$, $c_s = 0.04 \, °C^{-1}$, $w_0 = 0.17 \, g \, m^{-3}$, $h_r = 1.5$ km, and h and h_b respectively denoting the height above the surface and the height of the cloud base. There are some limitations to assuming a single universal cloud model, which may fail to capture specific cloud properties in certain environments; more sophisticated and accurate models could be defined on a local geographical scale to counter this (e.g., *Pierdicca et al.*, 2006). However, given the stated objective of this study to design a non-site-specific algorithm, it was considered preferable to assume a single universal liquid cloud model in spite of its potential drawbacks.

A further caveat of the cloud model is related to the relatively low resolution of the radiosonde profiles used as input (see Sect. 3.3.1); this might result in a misrepresentation of the cloud layers in their detection and their vertical extent. In order to ensure that this forward model generated the least possible bias, its results were compared against LWP values from ERA5 reanalysis data (*Hersbach et al.*, 2020). Even though the model might fail, on a given occurrence, to reproduce the actual liquid water profile in the atmospheric column, it should not produce a significant bias on average. This condition ensures that the synthetic dataset used for training

our algorithm contains realistic—if not real—profiles; this should therefore not degrade the quality of the retrieval. This cloud model was chosen over other commonly used ones (Decker model, Salonen model without correction; see *Mattioli et al.*, 2009) because it was found to produce the least bias when compared to ERA5 LWP values (mean bias of 14 g m^{-2} vs. 26 g m^{-2} (resp. -24 g m^{-2}) for the unadjusted Salonen model (resp. the Decker model with a 95% threshold). Inevitably, when using this criterion for the choice of the cloud liquid model, it is assumed that reanalysis values of LWP are themselves bias-free, which may, in turn, be questioned, especially in extreme environments (e.g., *Lenaerts et al.*, 2017).

3.4.2 Radiative transfer model

For each profile of atmospheric variables and LWC, ground-level brightness temperatures at 89 GHz are simulated using the Passive and Active Microwave TRAnsfer Model (PAMTRA; *Mech et al.*, 2020). As input to the radiative transfer calculations, vertical profiles of temperature, pressure, hydrometeor mixing ratio (computed from LWC), and water vapor mixing ratio are used. Gaseous absorption is calculated using the default parameters in PAMTRA, i.e., with the model proposed by *Rosenkranz* (1998) and modifications from *Liljegren et al.* (2005) and *Turner et al.* (2009). Liquid water absorption is modeled according to *Ellison* (2007). It should be kept in mind that some irreducible uncertainty remains tied to the choice of these parameters in the radiative transfer model.

The cloud droplet size distribution (DSD) is chosen as a monodisperse distribution with radius $r_c = 20$ μm following *Cadeddu et al.* (2017), and scattering calculations are performed with Mie equations, assuming spherical particles. Let us note here that the exact choice of the DSD has little impact on T_B modeling as long as the droplets can be approximated as Rayleigh scatterers for the given frequency, since the emission cross section in this regime is quasi-linearly related to the particle volume. When the droplet size deviates from this regime, for instance as droplets grow larger near the onset of precipitation, then the Rayleigh approximation falls short and higher-order terms in the Mie equations become non-negligible, which alters the modeling of T_B (e.g., *Zhang et al.*, 1999). This implies that the algorithm will output biased results when applied to rainfall cases, and should not be trusted in those circumstances. This shall be considered an intrinsic limitation to the algorithm.

There is no clear-cut relation between LWP values and the occurrence of precipitation, although the general trend is that higher LWP is related to more likely rain: as such, deviation from the Rayleigh regime is likely in high-LWP cases. In order to have a more rigorous grasp on when and how this drawback might affect the retrieval, criteria from *Karstens et al.* (1994) were used. In their study, the authors distinguished three types of liquid water clouds based on the value of LWC at a given altitude; for each category of cloud, a different characteristic radius is chosen for the DSD. Mie effects can start to become an issue in the second category of clouds (*cumulus congestus*), which they identify when LWC > 0.2 g m^{-3}; in our dataset, the atmospheric profiles in which this LWC threshold is exceeded in at least one gate have, on

average, a total LWP$\geq$ 830 g m^{-2}, and around 2% of the entire dataset fall into this category. Taking the third category (*cumulonimbus*) with LWC > 0.4 g m^{-3}, this applies to 1% of the entire dataset and the average LWP threshold increases to 1400 g m^{-2}. Those values can serve as a benchmark to identify LWP values at which Mie effects can start contaminating the retrieval. However, edge cases can also exist in which the total LWP is quite low, but a small layer of nearly precipitating or drizzling cloud still contaminates the retrieval without featuring an extremely high total LWP.

Finally, the forward model presented here does not include the contribution of ice clouds and snowfall. While the radiative emission of ice and snow particles has a minor influence on brightness temperature at microwave frequencies when compared to that of liquid droplets and water vapor and is in general negligible, solid hydrometeors do contribute to microwave brightness temperature, for instance through the backscattering of surface radiation. *Kneifel et al.* (2010) suggest that this effect could be notable during snowfall, depending on the microphysical properties of snow particles (increasing with their size). The present study does not take this process into account and could therefore yield biased results during intense snowfall events.

3.5 Design of the IWV and LWP retrieval algorithms

3.5.1 Input features

When a single frequency is available for the measurement of T_{B}, the ill-posedness of the problem can be partially relieved by including other available information in the measurement vector (input of the retrieval). In this study, several categories of variables were included in the input features. The first category consists of T_{B} and higher-order polynomials (up to the fourth degree) and is expected to have the greatest importance in the retrieval of LWP. The effect of higher-order polynomial terms is discussed in Sect. 3.6. In order to simulate realistic measurements, random Gaussian noise was added to the modeled brightness temperatures, with a mean and standard deviation of 0 and 0.5 K, respectively; those values were identified by *Küchler et al.* (2017) as the characteristics of the measurement noise of their 89 GHz radiometer. Secondly, surface measurements are included (temperature, sea-level pressure, and relative humidity); in the case of the radar–radiometer setup that is used here, those measurements are available through the collocated weather station. The third class of input features comprises geographical descriptors: latitude, longitude, and altitude. The day of the year is also included in this group of features as a means to account for seasonal variability in atmospheric and meteorological conditions. When available, a fourth category is added that contains ERA5 reanalysis data (precipitable water and liquid water, *Hersbach et al.*, 2020; *Copernicus Climate Change Service*, 2020). The spatial and temporal resolution of these reanalysis data is too low for them to be held as ground truth, but they can serve as a reasonable rough estimate and thus bring some improvements to the statistical learning process. Those four groups of features are used for the retrieval of both IWV and LWP. In the case of LWP, an additional input

feature is also considered, which is the output of the IWV retrieval algorithm. The impact of each of those feature groups on the retrieval will be discussed in Sect. 3.6.

3.5.2 Dataset preprocessing

Rain events should be excluded from the training set since they are out of the algorithm range of validity, as explained in Sect. 3.4. Profiles with LWP > 1000 g m^{-2} are removed (i.e., in the range of heavy rain according to *Cadeddu et al.*, 2017, and in view of the discussion conducted in Sect. 3.4.2). The resulting dataset contains $\sim 10^6$ profiles (see Fig. 3.2a) and is used without further modifications for the design of the IWV retrieval algorithm.
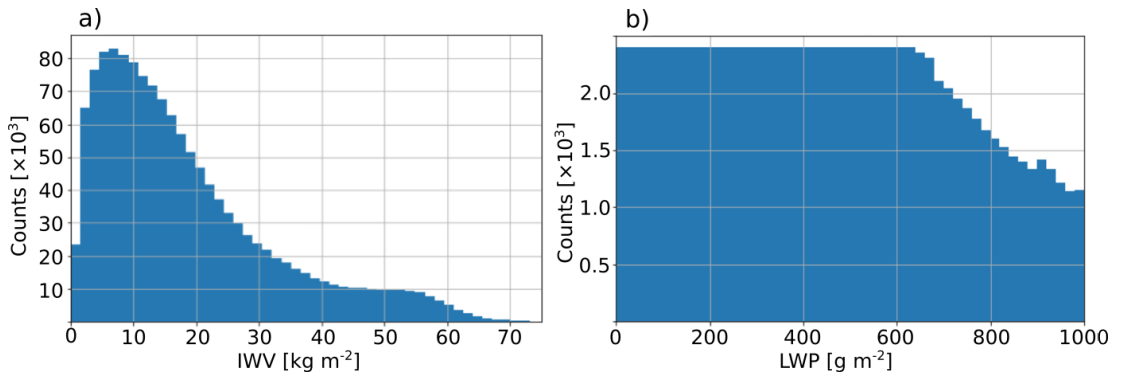
Figure 3.2: Distribution of the target variables, (a) IWV and (b) LWP, in the synthetic dataset, after preprocessing.

Further preprocessing for LWP dataset

For the LWP retrieval, additional preprocessing is needed, since the forward model produced a large majority of clear-sky cases. If left as such, the training phase would result in a strong bias of the retrieval toward low LWP values (a bias of ~ 100 g m^{-2} for LWP > 400 g m^{-2} was noted in the development stages of the algorithm): this is a common artifact in statistical learning algorithms as an effect of an unbalanced training set. In order to avoid this, the dataset was subsampled so that clear-sky and cloudy cases (up to 600 g m^{-2}) would be equally represented; this threshold results from a trade-off between bias reduction and preservation of overall accuracy. The resulting histogram is shown in Fig. 3.2, and the resulting LWP dataset contains $\sim 10^5$ profiles. In the case of IWV, the distribution is also not uniform, but it is affected by a much smaller asymmetry than the initial LWP dataset. After some trials, it was considered preferable to use the full IWV dataset rather than go through subsampling steps, which did not seem to bring significant improvements. We note that the additional preprocessing that was necessary for the LWP retrieval algorithm led us to design two separate algorithms rather than a single one that would retrieve IWV and LWP at once. Indeed, while the LWP retrieval is mostly relevant in cloudy cases, IWV can show some significant variability in clear-sky cases, which should therefore not be excluded from the training stage.

3.5.3   Statistical retrieval using a neural network

After preprocessing, the LWP and IWV datasets were randomly split into training, validation, and testing sets (70%–15%–15%) and normalized using the mean and standard deviation of each input feature in the training set. The validation set is used for tuning the hyperparameters of the neural network (NN), while the final evaluation metrics are computed on the testing set. A densely connected NN architecture was chosen over linear regression and decision-tree-based retrieval techniques as it was found to produce more reliable results with higher accuracy than the former, and it is less prone to overfitting than the latter. The algorithm was designed using the Keras library in Python (*Chollet*, 2015). The NN was trained through mini-batch gradient descent using the RMSprop optimizer, which allows for learning rate adaptation and is often used for statistical regression problems (*Chollet*, 2017).
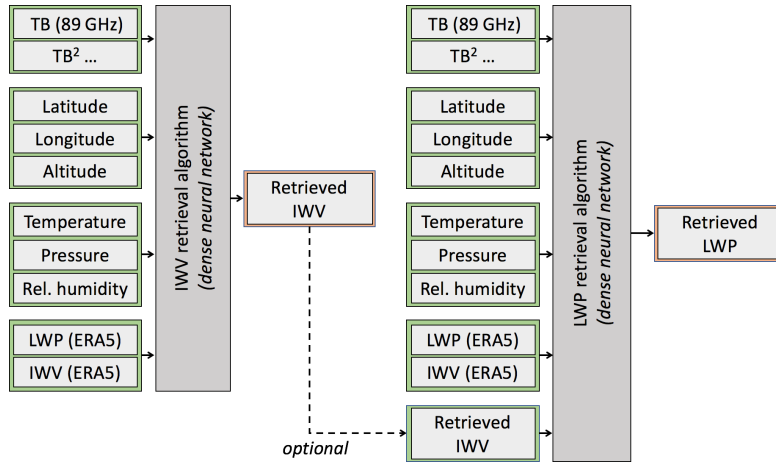
Figure 3.3: Structure of the retrieval algorithms. Some versions of the LWP retrieval include, among the input features, the output of the IWV retrieval. Note that the IWV and LWP algorithms are trained on different datasets.

Table 3.1: Main parameters of the neural networks and training process.

Target	Neurons	Layers	Cost function	Optimizer	Activation	Epochs	Batch size
IWV	120	7	Mean squared error	RMS prop	ReLU	70	512
LWP	150	6	Mean squared error	RMS prop	ReLU	90	512

Figure 3.3 and Table 3.1 summarize the final architecture and relevant parameters of the algorithm. These include the description of the NN (number of neurons and hidden layers) and training parameters such as the batch size and number of epochs, i.e., the number of iterations through the entire dataset during the learning phase. Different versions of the algorithm were trained using various sets of input features to assess the importance of each category (discussed in Sect. 3.6). We ensured that the training set is large enough that overfitting would not be an issue with the chosen NN architecture (cf. training curve in Fig. 3.4): the error on the validation set quickly drops with the size of the training set, then plateaus with a slight decrease.
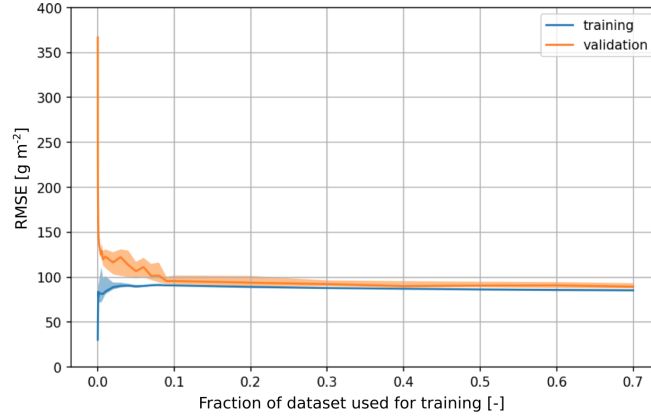
Figure 3.4: Learning curves for the LWP retrieval, showing the root mean squared error (RMSE) on training and validation set with varying training set size. Shaded areas correspond to the interquartile range calculated over 50 realizations of random splitting of the dataset into training and validation sets, bold lines are the median.

3.6 Results on the synthetic dataset

In this section, the algorithm is evaluated on the synthetic dataset (testing set) through different criteria. Overall, results are encouraging and the retrieval appears to be robust in spite of some shortcomings, which will be discussed here. Additionally, the importance of the various input features on the retrieval of IWV and LWP is assessed.

3.6.1 Error curves

Figure 3.5 illustrates the distribution of the error on the testing set for the best version of the algorithm, which is the one that uses the full set of input features. In Fig. 3.5c (resp. Fig. 3.5d), the target variables IWV (resp. LWP), are binned into intervals on which the RMSE is calculated. This illustrates the behavior of the algorithm across the entire range of values rather than summarizing the performance with a single metric such as total RMSE, which can conceal specific behaviors related to the distribution of the target variable in the dataset. Along the same line, we emphasize that comparing total RMSE values to those from other studies should be done carefully because they strongly depend on the dataset from which they are calculated. In a similar way, Fig. 3.5e (resp. Fig. 3.5f) illustrates the distribution of the mean bias across the range of IWV (resp. LWP) values. For reference, the definitions of the error metrics that we use here and further on are recalled in Table 3.2.

Table 3.2: Error metrics. X is either LWP or IWV; N is the size of the considered dataset. $\vec{X}_{\text{pred}}$ and $\vec{X}_{\text{target}}$ are length-N real positive vectors with the values of predicted (i.e., retrieved) and target values, respectively. To compute the relative error, $X_{\text{target},k} = 0 \text{ g m}^{-2}$ is excluded from the dataset.

Root mean squared error (RMSE)	Relative error	Bias	Correlation coeff. (R)
$\left[\frac{1}{N} \sum_{k=1}^{N} \left(X_{\text{pred},k} - X_{\text{target},k} \right)^2 \right]^{\frac{1}{2}}$	$\frac{1}{N} \sum_{k=1}^{N} \frac{|X_{\text{pred},k} - X_{\text{target},k}|}{X_{\text{target},k}}$	$\frac{1}{N} \sum_{k=1}^{N} \left(X_{\text{pred},k} - X_{\text{target},k} \right)$	Pearson
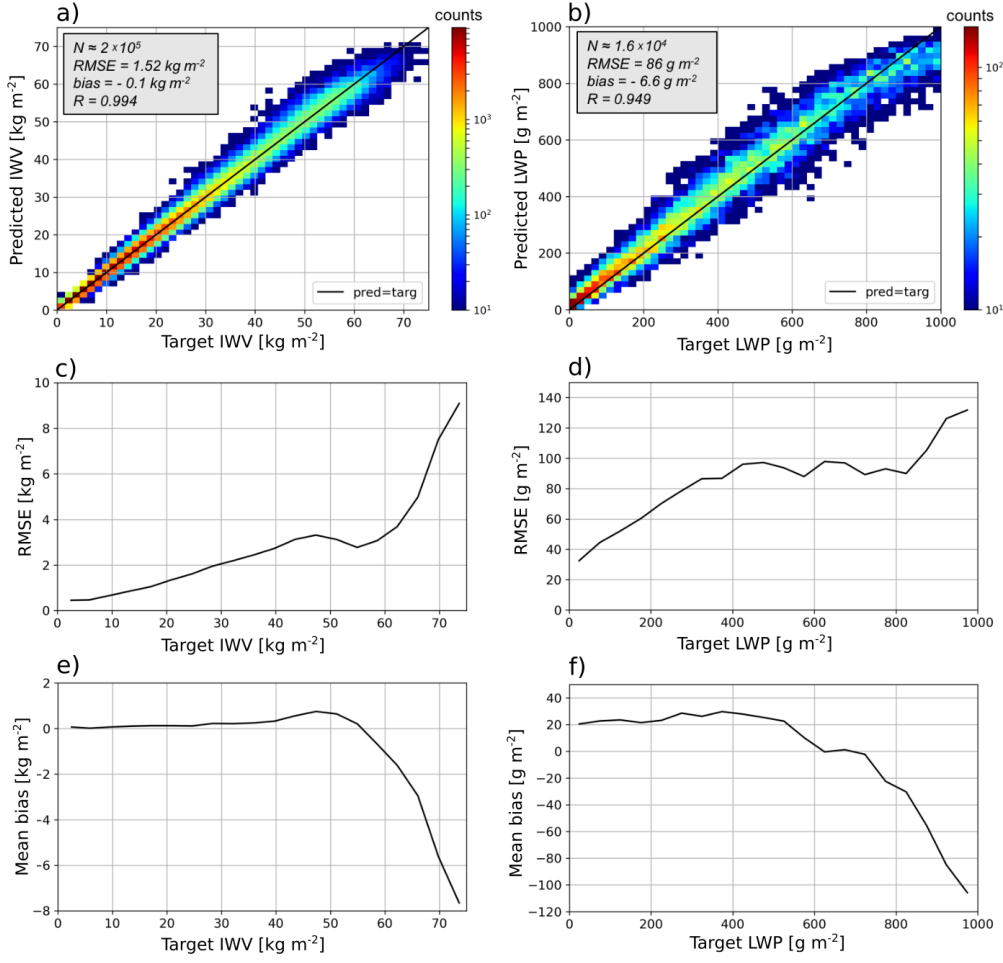
Figure 3.5: Results of the retrieval algorithms on the synthetic testing dataset. The best versions of the algorithms are presented, i.e., the ones which use the full set of input features. (a) Distribution of predicted vs. target IWV. (b) Distribution of predicted vs. target LWP. The size N of the testing set is indicated as well as relevant error metrics (RMSE, mean bias, R). (c) Distribution of RMSE on IWV vs. target IWV, binned into intervals of 4 kg m^{-2}. (d) Distribution of RMSE on LWP vs target LWP, binned into intervals of 50 g m^{-2}. (e) Same as (c) but with mean bias. (f) Same as (d) but with mean bias.

Figure 3.6 shows how this total error, quantified with the RMSE (left panels) and the correlation coefficient (R, right panels), is affected by the addition or removal of input features. For each set of input features, a full tuning of the algorithm was performed (on the validation set), and the results that are presented correspond to those from the tuned version (i.e., best on the validation set) when implemented on the testing set.

IWV algorithm

Overall, the IWV retrieval algorithm yields an RMSE of 1.53 kg m^{-2} for the testing set, which corresponds to a relative error of 6.5%. For comparison, the ERA5 data alone have a higher RMSE (3.4 kg m^{-2}) for the same dataset. Looking at Fig. 3.5a, c, and e, it comes across that the retrieval performs quite well over the full range of IWV values, and the error distribution is
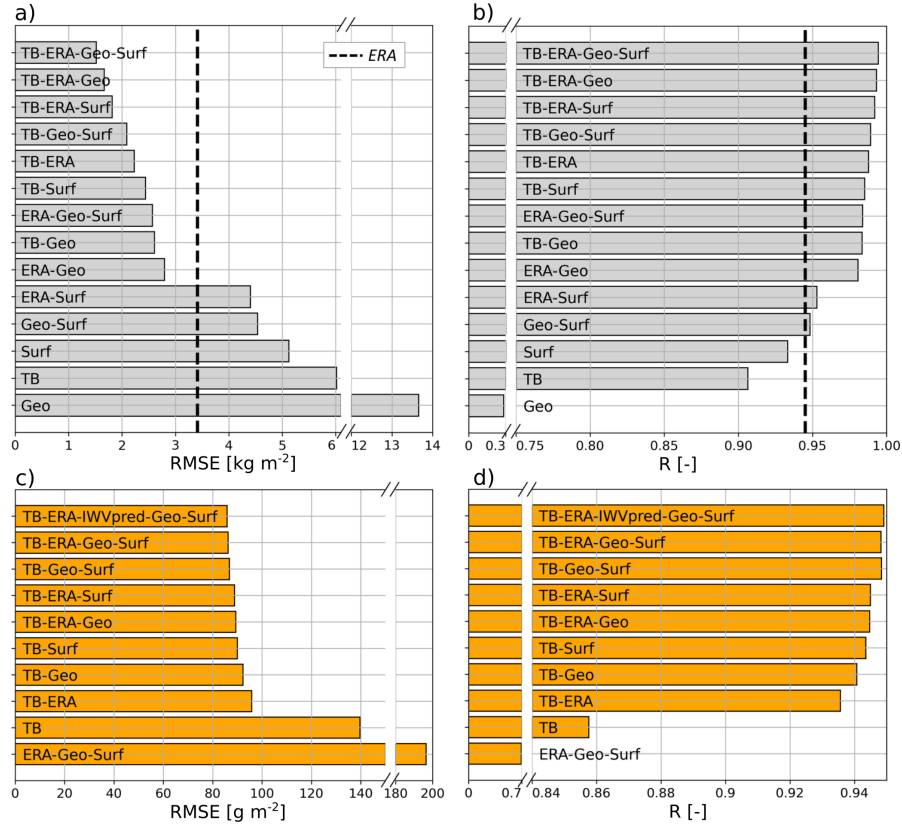
Figure 3.6: Global error metrics (RMSE in a, c; *R* in b, d) computed on the testing set for different versions of the (a,b) IWV and (c,d) LWP retrievals. Each bar shows the result of a version whose input features are specified in the label. For example, "ERA-IWVpred-Geo-Surf" corresponds to the version of the LWP retrieval algorithm that uses the following categories of input features: ERA5 variables, IWV obtained from the IWV retrieval, geographical information, and surface measurements. The bars are sorted with increasing RMSE. For the IWV retrieval, the accuracy of the algorithm is compared to that of reanalysis data alone (dashed lines).

relatively homogeneous. For high IWV values, however, a significant negative bias is present (as large as -6 kg m^{-2}). Because such high values are underrepresented in the dataset, they are not well captured during the statistical learning stage, which leads to a systematic underestimation. However, these are by definition border cases for which a decrease in accuracy is to be expected.

Figs. 3.6a–b suggest that the IWV retrieval is significantly improved by the addition of multiple input features. The highest accuracy is obtained with the full set of input features. Including solely T_{B} measurements in the input deteriorates the RMSE to nearly 6 kg m^{-2}. If only one input feature were available, all the versions would predict worse results than those given by reanalysis data. Including T_{B} in the retrieval does not lead to the same leap in accuracy as for LWP (discussed in the following subsection); however, excluding T_{B} from the input features degrades the RMSE to 2.56 kg m^{-2}, i.e., +67% error, which clearly shows that brightness temperature incorporates additional relevant information into the retrieval.

An analysis was conducted to identify the importance of higher-order polynomials in the algorithm, a summary of which is in Fig. 3.7. It was found that the most accurate retrieval is obtained by including T_B and T_B^2. If higher-order terms are added, this slightly reduces the accuracy of the retrieval and also degrades its robustness to T_B miscalibration (Fig. 3.7c). On the other hand, including only T_B, while it makes the algorithm slightly more stable, has lower accuracy. Hence, the IWV results presented here and in the following sections are those obtained using T_B and T_B^2.

Figure 3.7: Effect of higher-order T_B polynomials on the IWV retrieval, through (a) RMSE and (b) R on the testing set. (c) Change in RMSE when a constant T_B offset is added to the testing input, simulating radiometer miscalibration.

LWP algorithm

The LWP retrieval has an RMSE of 86 g m^{-2} at best for the testing set (training set: 84 g m^{-2}, validation set: 86 g m^{-2}). This corresponds to a relative error of 29% (testing set). Let us underline the fact that the subsampling performed on the dataset for the retrieval of LWP is applied to training, validation, and testing sets: the results that are presented here are therefore computed on the testing set with a truncated distribution—i.e., after subsampling. If clear-sky cases are removed using 30 g m^{-2} as a threshold value, following *Löhnert and Crewell* (2003), the relative error is 18%. As already mentioned, the total RMSE values given here should be taken with care since they depend on the dataset distribution. For comparison, when the retrieval is implemented on the full dataset, i.e., without the subsampling step, the total RMSE drops to 40 g m^{-2}. The RMSE is here again rather homogeneous across the range of LWP values (Fig. 3.5d); however, there is a small bias of around 20 g m^{-2} for low LWP values (visible in Fig. 3.5f), which are slightly overestimated, while there is an underestimation of large LWP (> 800 g m^{-2}), with a negative bias down to -100 g m^{-2}. Both biases result from an effect of regression towards the mean, which is intrinsic to statistical algorithms. The significant negative bias for large LWP values is enhanced by the lack of data in this range. It is likely acceptable because it would correspond mostly to rain cases (light to moderate), which the retrieval does not aim to capture; yet this highlights once again that those cases are out of the algorithm scope and that retrievals with high LWP would not be quantitatively trustworthy.

The analysis of the importance of higher-order terms in the case of LWP retrieval shows that the best results are obtained by using T_B polynomials up to the fourth order (see Fig. 3.8),

and this does not significantly affect the sensitivity of the retrieval to errors in T_B. In the LWP retrieval results shown here and further, "T_B" implies that T_B polynomials up to the fourth order are used.
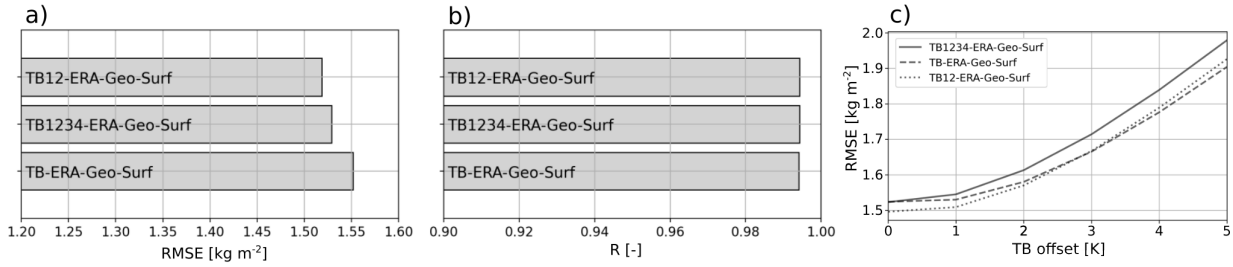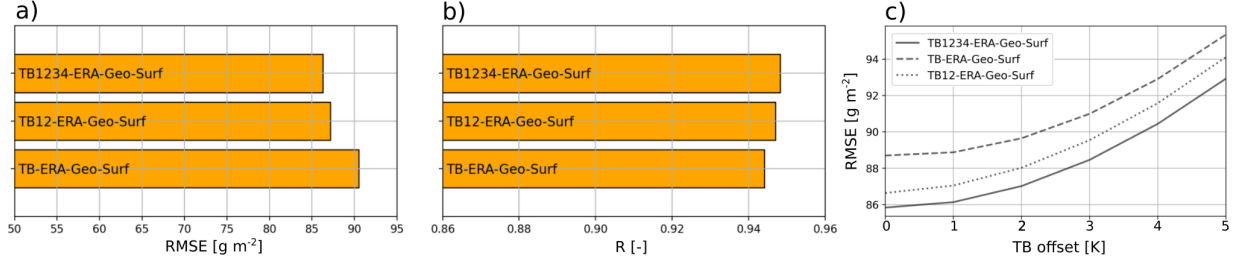

Figure 3.8: Effect of higher-order T_B polynomials on the LWP retrieval, through (a) RMSE and (b) R on the testing set. (c) Change in RMSE when a constant T_B offset is added to the testing input, simulating a miscalibration of the radiometer.

Figure 3.6c and Fig. 3.6d show that for the LWP retrieval, input features other than T_B only bring second-order improvements, while they were shown to be crucial in the IWV retrieval. For instance, the addition of reanalysis data significantly improves the IWV retrieval, but only in a relatively minor way does it increase LWP accuracy. In contrast, excluding T_B from the input features leads to an RMSE near 200 g m^{-2} and $R < 0.7$, i.e., to values that make the retrieval virtually non-relevant. This confirms that while environmental descriptors are well correlated with IWV, they are not sufficient to provide a reasonable estimate of LWP, for which microwave radiometer measurements are necessary. An additional reason for this high dependence on T_B is that LWP at a given location can have large temporal variability due to cloud dynamics in the atmospheric column, which might not always be captured in the time series of surface atmospheric variables, nor by ERA5 reanalyses, which have a comparatively low spatial and temporal resolution.

Still, the accuracy of the algorithm drops severely when no features are considered other than brightness temperature (RMSE = 140 g m^{-2}). This suggests that, although of second-order importance when taken individually and somehow redundant when all used together, the secondary input features are efficient in incorporating statistical trends and climatological information into the retrieval during the training phase.

Adding IWV prediction as an input feature to the LWP retrieval has a very minor impact. For clarity, it was only included in Fig. 3.6c in the best-case scenario and not for every other combination of input features. This is not surprising, since it is itself the output of an algorithm that relies on essentially the same input features. However, the slight improvement that is seen can be understood by recalling that the IWV retrieval algorithm was trained on a much larger dataset, which includes in particular a larger number of clear-sky cases (see Sect. 3.4).

3.6.2 Sensitivity to instrument calibration

In order to assess the robustness of the algorithm with respect to potential radiometer miscalibration or calibration drift, T_B offsets were added to the testing dataset before implementing the retrieval. Figure 3.9 illustrates the behavior of the algorithm when such a miscalibration with a constant offset is present (varying from 0 to 5 K). Figure 3.9a shows that a 5 K offset in T_B results in a 30% increase in RMSE for the IWV estimations, which is non-negligible. Ensuring proper radiometer calibration thus seems crucial in constraining the error of this retrieval. For comparison, the 89 GHz radiometer presented in *Küchler et al.* (2017) has a nominal accuracy of 0.5 K after calibration. If the calibration cannot be ensured and if there is no means to correct for miscalibration (of > 3 K), it is preferable for the IWV retrieval to use the algorithm that does not rely on T_B, shown with the black dashed line.
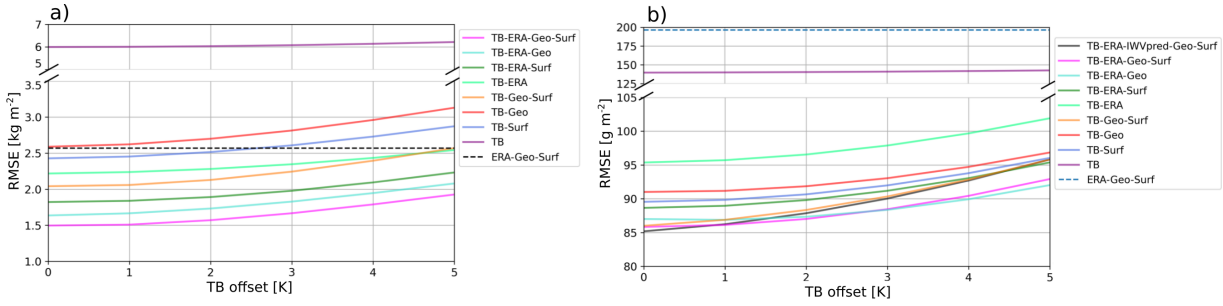
Figure 3.9: RMSE on the testing set of the different versions of the (a) IWV and (b) LWP retrieval, after addition of a constant T_B offset in the input. Dashed lines show the retrievals without T_B in the input features.

In terms of relative impact, the LWP algorithm is less affected (Fig. 3.9b) with an increase in the RMSE of less than 10% for an offset of 5 K in T_B, which makes it reasonably stable to inaccuracy of T_B measurements. The different versions are affected in a similar way by T_B offsets. However, the algorithm that includes the prediction of IWV in the input features diverges faster than the others. This is understandable because the error in T_B propagates through the "IWVpred" input feature, in addition to the T_B features themselves. Therefore, in the case of uncertain calibration, more robust results would be obtained without including this feature.

3.6.3 Geographical distribution of the error

One of the motivations of this study was to design an algorithm that could be used across the globe with a constrained uncertainty. Figure 3.10 illustrates the geographical distribution of the error for LWP and IWV retrievals, using the synthetic radiosounding dataset. Two approaches were used to assess this error: first, RMSE values were calculated on all data available for each location, excluding LWP greater than $1000 \, \mathrm{g \, m^{-2}}$. Second, the RMSE was normalized by the mean value of LWP (IWV) for each site, excluding low values (LWP $< 20 \, \mathrm{g \, m^{-2}}$, i.e., using a conservative threshold to exclude clear-sky cases). This normalized error is different from the relative error; rather, it gives an idea of how large the RMSE of the retrieval is, compared to the average values observed at a given location.
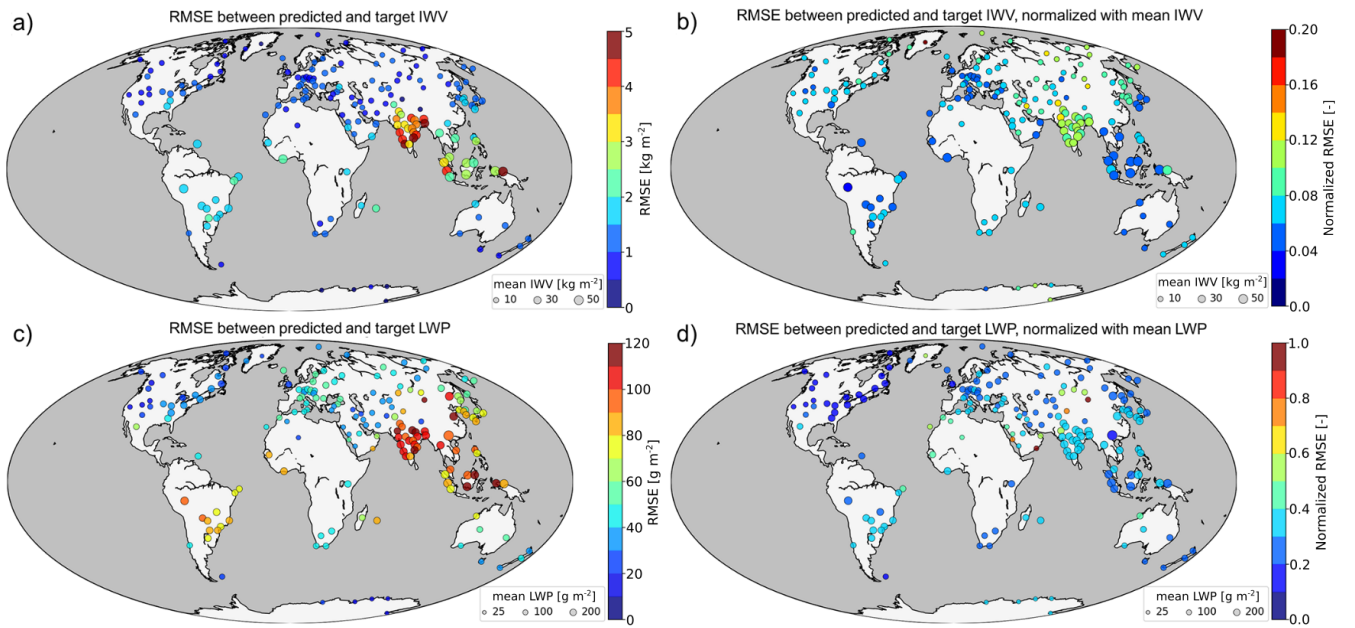
Figure 3.10: Geographical distribution of the error on the synthetic dataset. (a) Total RMSE on IWV. (b) Normalized error (defined in the text) on IWV. (c) Total RMSE on LWP. (d) Normalized error on LWP. For (c) and (d), clear-sky as well as strong rainy cases are removed (LWP $< 20 \, \mathrm{g \, m^{-2}}$ and LWP $> 1000 \, \mathrm{g \, m^{-2}}$). The size of the disks represents the mean value of IWV or LWP at each site, while the color codes for the error of the retrieval.

From the non-normalized error (left panels in Fig. 3.10), it comes across that most high-latitude and midlatitude locations have a constrained RMSE (around 20–$60 \, \mathrm{g \, m^{-2}}$ on LWP), while tropical sites are not as well captured, with RMSE exceeding $120 \, \mathrm{g \, m^{-2}}$ (on LWP) in some locations. The temperature and humidity conditions, as well as the intense precipitation that typically occurs in those regions, are probably responsible for this discrepancy. Cases with high LWP are more common under such climatic conditions, and it was observed in Sect. 3.6.1 that the accuracy of the algorithm decreases in that range. Furthermore, tropical climates are underrepresented in the dataset as fewer data are available from these regions in comparison with midlatitudes: their specificity might therefore not be fully captured during the learning

stage of the algorithm. This accounts at least partly for the enhanced error over the Indian peninsula and southeastern Asian islands.

The normalized error (Fig. 3.10b and d) shows that the error is, overall, of the same order of magnitude across the globe. A few regions do stand out from this analysis, which correspond to arid climates: the stations of Dalanzadgad (Mongolia), Salalah (Oman), Minfeng (China, north of Tibet), and Jeddah (Saudi Arabia) all have a normalized error in LWP higher than 0.7 and are in the desert. Similarly, the IWV retrieval performs poorly, in terms of normalized error, in cold environments where the absolute humidity is low, such as in Sermersooq (Greenland). In such regions, our algorithm is not sensitive enough to accurately capture the fine variations of atmospheric vapor and liquid water content; if detailed studies of those areas were to be conducted, more than one radiometer frequency would likely be necessary, along with specific training sets on which to perform the statistical learning, as was done in the Arctic by *Cadeddu et al.* (2009).

3.7 Evaluation on two contrasted datasets

As a further step in the validation process, the algorithm was applied to data from two campaigns involving WProf: first in Payerne, Switzerland, then near Pyeongchang, South Korea (see Sect. 3.3 for the full description of the datasets). In both cases, the output of the retrieval is compared against values estimated through other methods, either a multi-channel radiometer or, in the case of IWV, radiosonde data.

3.7.1 Payerne 2017

IWV retrieval

The results of the new IWV retrieval algorithm are compared to those from the MeteoSwiss operational radiometer HATPRO and to radiosonde-derived values. From Figs. 3.11a and c it appears that the IWV retrieval has relatively limited spread but has a constant bias ($-1.8\,\mathrm{kg\,m^{-2}}$), visible in both the comparison against HATPRO (Fig. 3.11a) and radiosonde-derived measurements (Fig. 3.11c). This might be due to a bias in ERA5 IWV data during this timeframe over the region ($-4.1\,\mathrm{kg\,m^{-2}}$), which is visible in ERA5 records during the entire campaign (not shown) and the investigation of which is beyond the scope of this study. This bias points to one of the drawbacks of the IWV retrieval algorithm, which is sensitive not only to radiometer miscalibration but also to possible biases in other input variables; these can be difficult to detect and monitor, as in the case of ERA5 values in Payerne. In spite of this, the top panels in Fig. 3.12 (error vs. HATPRO measurements) and Fig. 3.13 (error vs. value derived from radiosounding) show that, overall, the implementation of the different versions of the algorithm on the Payerne dataset agrees with the conclusions from the testing set results: more features lead to an enhanced precision of the retrieval. The accuracy drops when only one or two groups of input features are included, but no single group of features seems to increase

the accuracy alone. One notable difference exists between Fig. 3.12b and Fig. 3.13b: in the latter, higher R (and similar RMSE) is actually obtained from the algorithm that does not use T_B in input than with the full set of input features. This may be surprising at first, but can be understood by taking a closer look at the results: the algorithm without T_B leads to IWV values that are smoother and less sensitive to short-time variations. Such fluctuations are not reflected in the comparison against radiosonde data, for which a 30 min averaging was implemented. When variations over short time frames are considered, the inclusion of T_B improves the retrieval (Figs. 3.12a, b).
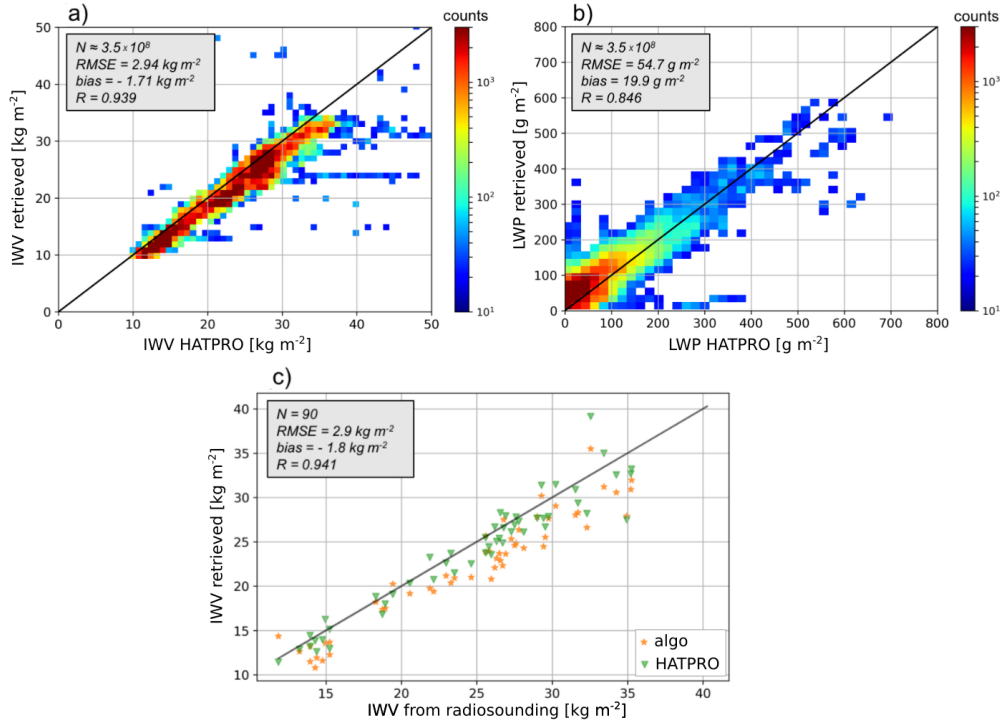
Figure 3.11: Comparison of (a) IWV and (b) LWP retrieved over Payerne with the new algorithm, using the full set of input features, against the HATPRO retrieval. (c) IWV retrieved from the new algorithm and from HATPRO vs. radiosonde measurements; a 30-minute time averaging is used for the radiometer measurements. The size of the dataset (N) is indicated, as well as relevant error metrics (RMSE, mean bias, R).

LWP retrieval

Figure 3.11b shows that LWP values retrieved with the new algorithm are in overall agreement with those obtained with HATPRO, although a larger spread is observed than in the IWV retrieval. A saturation effect can be seen near precipitation onset when LWP values from HATPRO exceed 600 g m^{-2}. Additionally, outliers are visible as vertical and horizontal bars close to the axes, for which two hypotheses are considered. One is that the distance between the two instruments was big enough that in some cases a liquid water cloud would overpass one of the two instruments but not the other. Hence, HATPRO would measure a nonzero LWP,

while WProf would indicate a clear sky or vice versa. Secondly, measurement artifacts also cannot be excluded, e.g., due to the persistence of a liquid water film on the radome of either radiometer after precipitation or due to condensation.
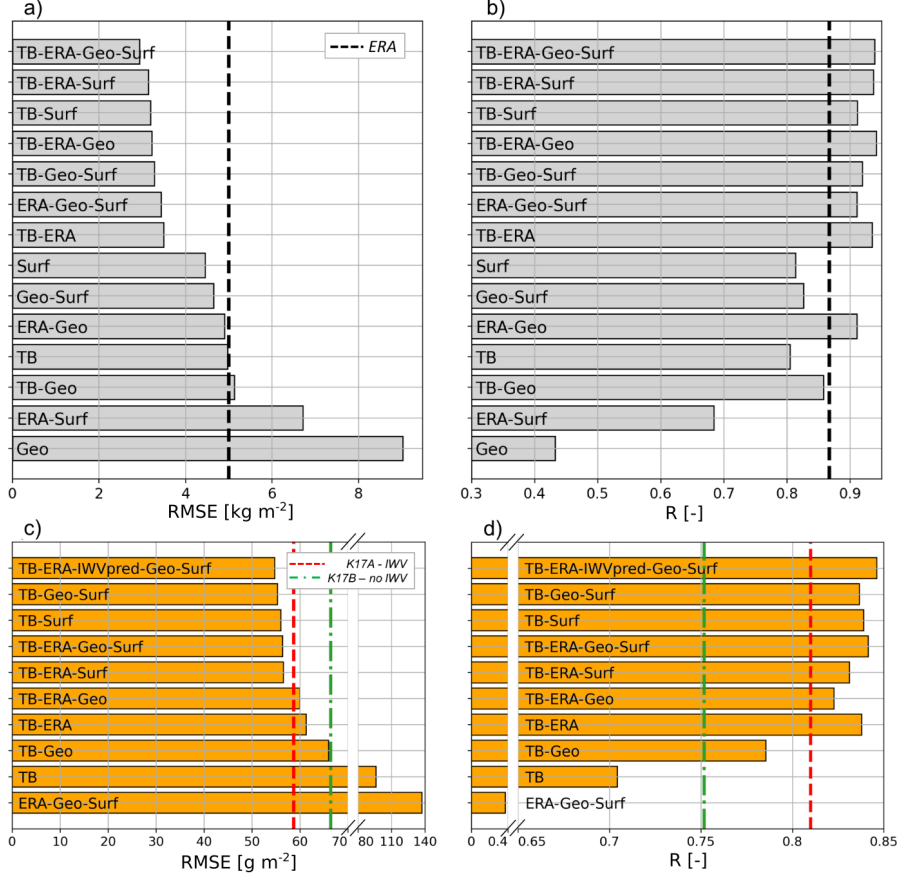
Figure 3.12: Error of the new retrieval algorithms over Payerne compared to HATPRO retrievals. (a) RMSE and (b) R of retrieved IWV. (c) RMSE and (d) R of retrieved LWP. Each bar shows the result of a version whose input features are specified in the label. In (a), (b), the black dashed line shows the error of ERA5 IWV. In (c), (d), the dashed lines show the results of K17A and K17B, as defined in the text.

For comparison, the method described in *Küchler et al.* (2017) was implemented (hereafter referred to as K17) by performing a quadratic regression on a dataset consisting solely of radiosonde profiles collected in Payerne, and constructed with the same steps as described in Sect. 3.4. A first version proposed by the authors (K17A) relies on a measurement vector consisting of T_B, T_B^2, and the IWV estimate from reanalysis data IWV_{ERA5} and IWV_{ERA5}^2. Another version (K17B) includes only T_B and T_B^2. RMSEs of those quadratic regressions, computed on the Payerne synthetic dataset (19720 profiles) are of 21 and 43 g m^{-2}, respectively, similar to the values obtained by the authors using radiosonde data from De Bilt (the Netherlands), i.e., 15 and 44 g m^{-2}.

K17A and K17B were applied to the Payerne campaign dataset, and their results are compared to those of our algorithm in Fig. 3.12. The error metrics are calculated using HATPRO values

as a reference. The algorithms perform in a similar way, with slightly better results for the new algorithm when at least one of the secondary input features is included. We recall that K17A and K17B were specifically tuned on Payerne data, while the new algorithm was trained globally on a dataset that did not comprise any radiosonde profile from Payerne.
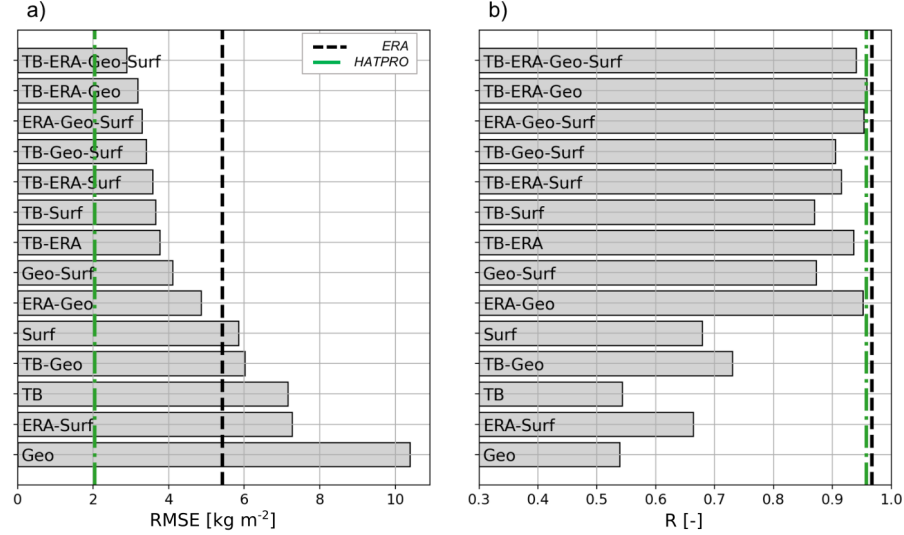
Figure 3.13: Results of the IWV retrieval in Payerne compared to radiosonde measurements. (a) RMSE; (b) R. The radiometer measurements are averaged over 30 minutes. For comparison, the dashed lines illustrate the error of HATPRO (green) and ERA5 (black) vs. radiosonde-derived IWV.

3.7.2   ICE-POP 2018

As detailed in Sect. 3.3, the South Korean deployment of WProf in 2017–2018 also offers an opportunity to compare results from the IWV retrieval to IWV from radiosonde measurements.

The analysis of the T_{B} time series showed that a miscalibration of the radiometer led to unrealistic—negative—values for which a correction had to be implemented, through the addition of a constant offset to T_{B} measurements. The value of this offset (20 K) was determined by computing theoretical brightness temperatures from clear-sky radiosonde profiles during the campaign and comparing them to measured T_{B}s, following the approach of *Ebell et al.* (2017). This is only a first-order correction whose output should be taken with care, especially after the analysis in Sect. 3.6.2, which underlined the importance of T_{B} accuracy for our IWV retrieval.

After this correction, the IWV retrieval gives consistent results (Fig. 3.14), with a total RMSE that is slightly lower than that obtained from the testing dataset (1.25 kg m^{-2}). Better results are obtained when more secondary input features are used, as was the case with the results on the synthetic dataset in Sect. 3.6. The algorithm largely relies on non-radiometric features, and even more so in cold and dry environments like that of ICE-POP, where IWV is low. In fact, slightly better results are surprisingly obtained with all input features except brightness

temperature. The miscalibration of the radiometer, which may not have been perfectly corrected by the addition of a constant offset, might emphasize this error. Note that this also corresponds to what was noted in Payerne: when the results are averaged over 30 minutes, brightness temperature brings little, if any, improvement to the results. T_B is relevant when a higher temporal resolution is considered (see Sect. 3.7.1)—for which no comparison was available during ICE-POP—or when ERA5 data are significantly off. In ICE-POP, however, the algorithm is consistently outperformed by ERA5 products (Fig. 3.14), which have both a lower RMSE and a higher R, making the algorithm less relevant for the study of IWV in this specific campaign. The high accuracy of ERA5 during ICE-POP also explains the high correlation coefficient R of the retrieval that uses ERA5 and geographical input features: since the geographical parameters are constant, the temporal variability is that of the reanalysis data, and therefore the correlation coefficient of the retrieval is close to that of ERA5 data alone. Let us highlight that although reanalysis data outperform the retrieval for ICE-POP, this was not the case in Payerne nor in the full radiosonde dataset, for which the algorithm has a higher accuracy than ERA5 values. Possibly, the dry and cold weather that was observed during the ICE-POP campaign featured little short-term variability and was associated with stable atmospheric conditions that were particularly well captured in ERA5 reanalyses.
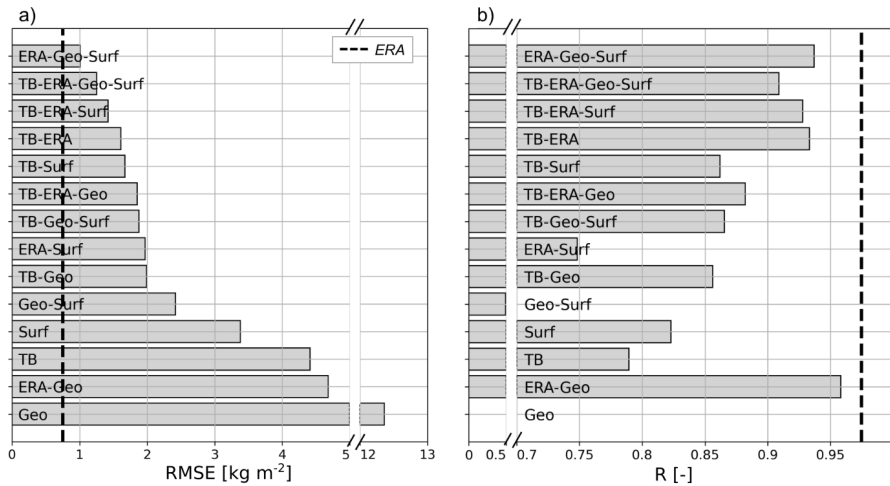
Figure 3.14: Error of the IWV retrieval during the ICE-POP campaign with different versions of the algorithm. (a) RMSE; (b) R. The error metrics are computed against IWV from radiosonde profiles, after 30 minutes of temporal averaging in the radiometer data. The dashed line shows the error of IWV from ERA5 reanalysis data.

Snowfall events during the campaign, as well as occasional fog, can also bias the retrieval by enhancing brightness temperature. The analysis of the ICE-POP data was taken a step further to explore this point; it reveals that the IWV retrieval is most reliable in non-precipitating or cold conditions. To visualize this, periods with no precipitation are identified in WProf radar measurements as time steps with low radar reflectivity (Z_e <-10 dBZ) in all the lower gates (first kilometer above the radar). Temperature time series are provided by the weather station coupled to WProf. Figure 3.15 shows the scatter plot of the error, for the algorithm that includes all input features, with the following convention to differentiate dry from pre-

cipitating conditions: black triangles correspond to dry time steps and circles to time steps labeled as precipitation, with color indicating surface temperature. As expected (Sect. 3.4), the algorithm yields a larger bias in rain—i.e., when precipitation is identified and $T > 0°$C—but also during snowfall events with relatively warm temperatures close to $0°$C. Changes in the dielectric properties of snowflakes during the melting process can explain this increased error; additionally, as described by *Kneifel et al.* (2010) and recalled in Sect. 3.4, large snow particles (such as aggregates forming at relatively mild temperatures) could have a non-negligible contribution to brightness temperature, which might explain the enhanced error in those cases.
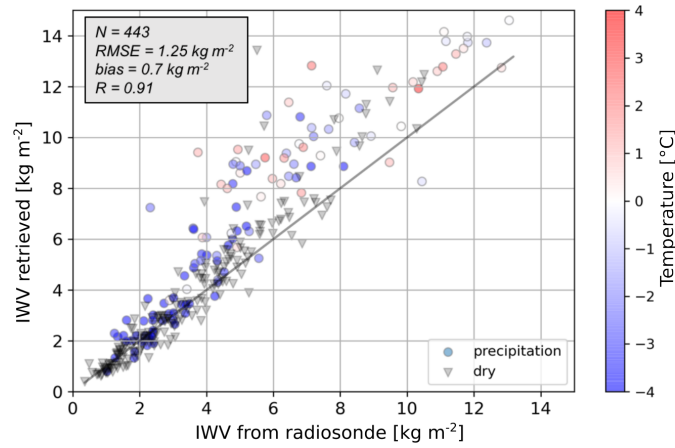
Figure 3.15: Scatter plot of retrieved IWV vs. IWV computed from radiosonde profiles. The algorithm used for the retrieval is the one with the full set of input features. Dry conditions are identified with W-band Z_e in the first kilometer above the radar (with a -10 dBZ threshold), and are coded as black triangles; precipitating conditions are denoted with circles. The color indicates the surface temperature.

3.8   Conclusions

A new site-independent method was designed for the retrieval of LWP and IWV. In addition to 89 GHz brightness temperature, additional input features are used for the retrieval, such as surface atmospheric variables (temperature, pressure, and humidity) and information on the geographical location and season. The retrieval framework relies on a neural network architecture, which was trained and tested on a synthetic dataset built from radiosonde profiles worldwide. The geographical distribution of the error shows that the algorithm performs better in midlatitudes and regions with a moderate climate than in areas with extreme climates (either arid or very moist), which include both tropical and polar regions that are not well represented in the training dataset due to lack of available data. Also, the forward model that was used should most likely be revised in order to finely capture the atmospheric conditions in such specific environments.

The algorithm was then applied to two contrasting datasets, one reflecting summertime weather conditions in Switzerland and the other winter conditions in South Korea. For this

application, measurements from the RPG cloud radar–radiometer system were used. In Payerne, the new LWP retrieval was found to perform slightly better than the method proposed by *Küchler et al.* (2017) for the same instrument, although the latter algorithm was specifically trained using radiosonde data from Payerne. When compared to radiosonde measurements of IWV, the IWV retrieval was found to be less accurate than that of a state-of-the-art multi-channel radiometer (HATPRO), although both instruments yield errors within the same order of magnitude. In the South Korean winter dataset, the IWV retrieval proved relatively robust in spite of a slight bias during some snowfall events that could be related to the scattering properties of snow particles, which were not taken into account in the forward model. In the case of ICE-POP, reanalysis data were actually more accurate than the IWV retrieval when compared with radiosonde measurements, but their temporal resolution remains low, which makes the use of the algorithm still relevant for retrievals for which a high temporal resolution is desired.

Further steps in the improvement of the current algorithm would include coupling information from the radar and the radiometer channel (*Ebell et al.*, 2010; *Cadeddu et al.*, 2020). The detection of clear-sky cases with radar (*Mätzler and Morland*, 2009) could help monitor the calibration of the radiometer and introduce T_B offsets for correction when necessary (*Ebell et al.*, 2017). If available through a separate sensor such as a GPS receiver, independent IWV measurements could be included in the algorithm, possibly leading to an enhanced precision of the LWP retrieval. Radar moments could be used to distinguish cloudy from drizzling or rainy cases, similar to the approach used by *Cadeddu et al.* (2020), and to select appropriate DSDs for each case to account for non-Rayleigh scattering by precipitating droplets. However, forward modeling of radar data requires further assumptions on microphysical properties and atmospheric conditions, for which generalization to a global geographical scale is a real challenge.

Overall, the LWP and IWV retrieval methods that were designed within this study were shown to be robust when applied to both synthetic and real datasets, although their performance is inevitably lower than that of multi-channel radiometers specifically designed for LWP and IWV retrievals. The accuracy is improved by including surface and geographical information, as well as reanalysis data if available, among the input features. The new algorithms should be seen as a valuable tool to monitor atmospheric liquid water and vapor in the context of radar–radiometer studies. They are non-site-specific and thus do not require further tuning before use at a new site, which makes them easy to implement, and their accuracy is well characterized. In the context of this thesis, further chapters will leverage the LWP retrieval in the framework of both quantitative and qualitative snowfall studies.

4 Dual-frequency spectral radar retrieval of snowfall microphysical properties: a physics-driven deep learning inversion framework

This chapter introduces a deep learning framework for the retrieval of snowfall microphysical properties from dual-frequency Doppler spectra. It is based on Sections 1–4 and Appendices of the article:

The study was designed by Anne-Claire Billault-Roux and Alexis Berne, with input from Gionata Ghiggi. The radar data were prepared by Audrey Martini, Nicolas Viltard and Anne-Claire Billault-Roux.

4.1 Summary

The use of meteorological radars to study snowfall microphysical properties and processes is well established, in particular via a few distinct techniques: the use of radar polarimetry, of multi-frequency radar measurements and of the radar Doppler spectra. We propose a novel approach to retrieve snowfall properties by combining the latter two techniques, while relaxing assumptions on, e.g., beam alignment and non-turbulent atmosphere. The method relies on a two-step deep learning framework inspired from data compression techniques: an *encoder* model maps a high-dimensional signal to a lower-dimensional *latent* space, while the *decoder* reconstructs the original signal from this latent space. Here, Doppler spectrograms at two frequencies constitute the high-dimensional input, while the latent features are constrained to represent the snowfall properties of interest. The decoder network is first trained to emulate Doppler spectra from a set of microphysical variables, using simulations from the radiative

transfer model PAMTRA as training data. In a second step, the encoder network learns the inverse mapping, from real measured dual-frequency spectrograms to the microphysical latent space; in doing so, it leverages with a convolutional structure the spatial consistency of the measurements to mitigate the ill-posedness of the problem.

4.2   Introduction

In recent years, retrievals of snowfall microphysical properties from radar measurements have been successfully conducted via a few distinct techniques. On the one hand, multi-frequency measurements have been extensively explored, combining measurements from a shorter and a longer wavelength radar (e.g., W- and X-band). The dual-frequency ratio of radar equivalent reflectivity factors (DFR = $DFR_{X,W} = Z_{e,X} - Z_{e,W}$, [dB]) can be used to identify populations of snow particles with a larger size, or with a higher degree of riming, thus indicating regions of enhanced snowfall growth (see Chapter 1, Sect. 1.3.5 and e.g., *Matrosov et al.*, 1992; *Matrosov*, 1998; *Szyrmer and Zawadzki*, 2014; *Liao et al.*, 2016; *Battaglia et al.*, 2020). In a triple-frequency space, studies were able to identify distinct signatures for riming and aggregation and to even retrieve estimates of fractal dimension during parts of snowfall events (e.g., *Kneifel et al.*, 2011; *Kulie et al.*, 2014; *Leinonen et al.*, 2018), which were later confirmed through comparison with in-situ airborne data (*Chase et al.*, 2018; *Nguyen et al.*, 2022). Similar retrievals, focusing on snow particle bulk density, were achieved using only two frequencies, but leveraging information contained in the mean Doppler velocity in addition to radar reflectivity (*Mason et al.*, 2018). Bringing this a step further, *Mróz et al.* (2021a) retrieved IWC, mean mass-weighted diameter, and riming degree from triple-frequency reflectivity and Doppler velocity measurements. In the case of scanning radars, additional polarimetric information can be included, for a more refined geometrical characterization of snow particles (e.g., *Bukovčić et al.*, 2018; *Matrosov et al.*, 2020 or *Tetoni et al.*, 2022; *Oue et al.*, 2021, where polarimetric and multi-frequency measurements are combined).

On the other hand, studies have been conducted relying not solely on radar moments but on the full Doppler spectrum, which encloses more information on microphysical properties and the particle size distribution (PSD) than scalar moments (e.g., for rainfall and cloud retrievals, *Atlas et al.*, 1973; *Gossard*, 1994; *Gossard et al.*, 1997; *Babb et al.*, 1999; *Williams et al.*, 2016). In a qualitative perspective, by observing wider, more skewed, or even multi-modal spectra, signatures of specific microphysical processes such as riming or aggregation can be identified (e.g., *Shupe et al.*, 2004; *Verlinde et al.*, 2013; *Kalesse et al.*, 2016).

The combination of multi-frequency and Doppler spectral techniques for snowfall microphysical retrievals was investigated by *Kneifel et al.* (2016) and *Barrett et al.* (2019) (see Chapter 1, Sect. 1.3.5). In practice, substantial difficulties arise from imperfect measurements or contamination by turbulent broadening (see Chapter 1, Sect. 1.3.4); as a result, direct inversions using traditional methods like *Barrett et al.* (2019) are only rarely possible. In this chapter, we introduce a physics-driven deep learning framework to retrieve snowfall microphysics

from dual-frequency Doppler spectra, while partly relaxing constraints on turbulence or beam alignment, as well as reducing the number of prior assumptions on snowfall microphysical properties in comparison with the cited studies.

A general overview of the retrieval framework and its theoretical foundation is presented in Sect. 4.3. Section 4.4 describes the synthetic and real datasets used to train the neural networks in the inversion model. In Sect. 4.5, we detail the technical implementation of the framework and verify its convergence. Chapter 5 is then dedicated to the implementation of the proposed framework on the ICE GENESIS dataset, for validation against aircraft in situ measurements, and for a statistical characterization of snowfall microphysics during the campaign.

4.3 Theoretical framework

This section introduces the theoretical components required to understand the proposed retrieval framework and provides an overview of its general structure.

4.3.1 Doppler spectra: forward model

As detailed in Chapter 1, the shape of the Doppler spectrum measured by a vertically pointing profiler in snowfall results from a combination of several factors (e.g., *Doviak and Zrnić*, 1993; *Kollias et al.*, 2002; *Luke and Kollias*, 2013; *Kneifel et al.*, 2016). It is primarily defined by the snowfall PSD and the microphysical properties of the snow particles which determine their backscattering cross-section and terminal velocity; this microphysical spectrum is additionally affected by atmospheric dynamic conditions (turbulence, horizontal wind, and vertical wind) in a way that depends on the settings and parameters of the radar itself (e.g., sensitivity and beam width). The true measured spectrum is further perturbed by instrument noise. Understanding how those parameters (microphysical, environmental, instrument-related) translate into a measured Doppler spectrum is delicate: it involves complex radiative transfer models to compute the radar backscatter of snow particles, and it also requires an understanding of snowfall aerodynamic properties for e.g., the parameterization of velocity–size relations. In this work, we use the radiative transfer code PAMTRA (*Mech et al.*, 2020) as a forward model, as it is particularly suited to simulate full Doppler spectra and provides an implementation of several scattering models, such as the SSRGA (see Chapter 1, Sect. 1.3.5). Details on how PAMTRA is used and parameterized in this study are presented in Section 4.4.1.

4.3.2 Approach to the inverse problem

Assuming a forward model, denoted f, is known—which, given a set of properties $\boldsymbol{x}$, outputs realistic Doppler spectra $\boldsymbol{y}$—the aim of the retrieval is to solve the following inverse problem: from real observed spectra $\boldsymbol{y_r}$, estimate the underlying microphysical properties $\boldsymbol{x_r}$ (see, e.g., *Maahn et al.*, 2020, for a discussion on inverse problems). Here the subscript "r" denotes real

values as opposed to synthetic or modeled quantities.

In a mathematical language, solving the inverse problem means estimating $g = f^{-1}$. This is, in general, not possible, as f is usually not an invertible mapping. Workarounds can be developed, for example through lookup tables (e.g., *Leinonen et al.*, 2018). Alternatively, one can seek $\boldsymbol{x_r}$ as the minimizing argument of a cost function (such as the squared error $||\boldsymbol{y_r} - f(\boldsymbol{x})||^2$), which can also include a regularization term (e.g., *Mason et al.*, 2018); this boils down to a minimization problem which can then be solved iteratively with, for instance, a gradient descent algorithm. From a Bayesian perspective and under additional assumptions (Gaussian probability distributions), this corresponds to the popular optimal estimation framework (*Rodgers*, 2000; *Maahn et al.*, 2020), which is widely used across atmospheric science to solve moderately linear inverse problems. Although this alleviates some requirements of f, it can only be implemented if f is differentiable, and if the computation of its gradient is tractable, either analytically or numerically. This classical Bayesian approach faces some further limitations, which include but are not limited to, the need to linearize the forward operator in order to compute its Jacobian or to explicitly assume prior values for $\boldsymbol{x}$.

Machine learning techniques offer the possibility to tackle inverse problems in a different way, with a statistical rather than an analytical approach. Note that, as pointed out by *Geer* (2021), the overarching framework in both cases ultimately remains that of Bayesian probabilities, viewed through different prisms. The typical machine learning route to solve an inverse problem (e.g., *Chase et al.*, 2021) has the following structure: the available forward model is first used to create a large synthetic dataset $\{(\boldsymbol{x_{s,k}}; \boldsymbol{y_{s,k}} = f(\boldsymbol{x_{s,k}})), k = 1..N\}$, with the "$s$" subscript denoting synthetic values and N the size of the dataset. Then, a machine learning model is trained on this dataset to learn a statistical relation between $\boldsymbol{y}$ and $\boldsymbol{x}$, i.e., an approximation of the inverse mapping $\tilde{g}$. Ultimately, this produces a gate-to-gate inversion of the problem which can be implemented on real data. This approach has been successfully used for atmospheric retrievals, for example by *Piontek et al.* (2021) to detect volcanic ash clouds, by *Vogl et al.* (2022) to estimate riming occurrences from radar measurements, or by *Chase et al.* (2021) to retrieve snowfall properties from airborne or satellite radars. The LWP retrieval algorithm introduced in Chapter 3 also falls within this category. One major limitation of this direct gate-to-gate method is when the problem itself is ill-posed, e.g., when several values of $\boldsymbol{x}$ may yield similar outputs $\boldsymbol{y}$ (f is not injective): in such cases, the retrieval may yield arbitrary outputs.

The proposed approach, illustrated in Fig. 4.1, partly mitigates this issue. It is inspired by auto-encoder architectures (sometimes referred to as a non-linear variant of principal component analysis, *Kramer*, 1991; *Hinton and Salakhutdinov*, 2006), which use neural networks (NN) to perform a powerful nonlinear dimension reduction: an *encoder* NN maps a high-dimension signal to a low-dimension *latent* space, while the *decoder* NN learns to reconstruct an approximation of the original signal from the latent space. Such tools are relevant for atmospheric sciences and in particular in the context of climate studies, which handle complex, high-dimensional signals (*Behrens et al.*, 2022). In our case, dual-frequency Doppler spectrograms constitute the high-dimensional signal, and the aim is to constrain the dimensions of the

latent space to contain microphysical descriptors of snowfall. One original aspect of the approach presented here is that it incorporates physical knowledge by using a physics-informed decoder.

- In a first step, the decoder is designed to reconstruct dual-frequency Doppler spectrograms given snowfall descriptors. In practice, a neural network is trained on a synthetic dataset of $(x_s; y_s = f(x_s))$. Instead of learning an inverse mapping, it simply learns to emulate the forward model: taking microphysical and atmospheric variables (x_s) as input, it outputs Doppler spectra (y_s). This model, which we refer to as the decoder and denote as $\tilde{f}$, is thus a differentiable emulator of PAMTRA. When applied not to a single set of microphysical descriptors but to a stack (of multiple range gates) at once, it is denoted with uppercase $\tilde{F}$. The synthetic dataset on which the decoder is trained should include a wide range of realistic parameters, to not induce bias in the further steps.

- The encoder is trained in a second step: it ingests the radar data (dual-frequency Doppler spectrograms), and is optimized to retrieve the latent snowfall properties which, when passed through the decoder, minimize the reconstruction error with respect to the input data. For this step, we shift our attention to a real (i.e., not synthetic) dataset of full dual-frequency Doppler spectrograms Y_r; the aim is to retrieve the underlying profiles of latent variables X_r. The capital letter denotes that e.g., Y_r is a vertical stack of y_r. The encoder NN, $\tilde{G}$, is trained on this real dataset: it takes as input the Doppler spectrograms Y_r, and its output $X = \tilde{G}(Y_r)$ has the same dimension as the number of latent features, times the number of range gates. X is passed on to the decoder $\tilde{F}$, which outputs a reconstructed spectrogram Y. Training is performed by optimizing $\tilde{G}$ in order to minimize the reconstruction error $||Y - Y_r||^2$.

At the end of the training, i.e., when the pipeline has converged, $\tilde{F} \circ \tilde{G}(Y_r) \approx Y_r$ and the output of the encoder $\tilde{X}_r = \tilde{G}(Y_r)$ should be close to the true profile of microphysical descriptors X_r.

The architecture of the decoder and encoder will be detailed in the following (Sect. 4.5), but one key property should already be underlined. The retrieval operates on the full dual-frequency Doppler spectrograms at once, rather than on each gate independently: the idea is to synergistically make use of the spatial structure of the measurements to reduce the ill-posedness of the inverse problem. By "spatial structure", or "spatial consistency", we refer to the fact that the spectrogram might be continuous, smooth (i.e., spectra at nearby ranges are similar), or on the contrary have some abrupt changes (e.g., in the case of high shear, where neighboring spectra might be very different). By constraining the retrieval to output a profile of microphysical variables with a similar spatial structure, we restrain the number of degrees of freedom. This is handled by the architecture of the encoder NN, which contains convolution kernels: thanks to this feature, the model can capture the vertical structure of the Doppler spectrograms, and propagate this information in a way that the output profiles are themselves spatially consistent. Note that while the issue of ill-posedness is mitigated, it is not entirely

resolved, as there may remain an intrinsic under-determination. Nevertheless, we believe that this implicit use of the measurement spatial features in the retrieval is a key contribution of this work. To support this, a brief discussion of alternative methods is proposed in Appendix B.

To conclude this overview of the framework, we highlight that while it was presented for the specific case of Doppler spectrograms and snowfall microphysics, its structure is generic and could potentially be applied to other retrieval problems with similar properties: a complex forward model that is not directly invertible, with slightly ill-posed features that hamper point-wise retrievals. One intrinsic limitation which should be already underlined is that the method is trained on the data of interest and cannot be directly used on any given measurements.
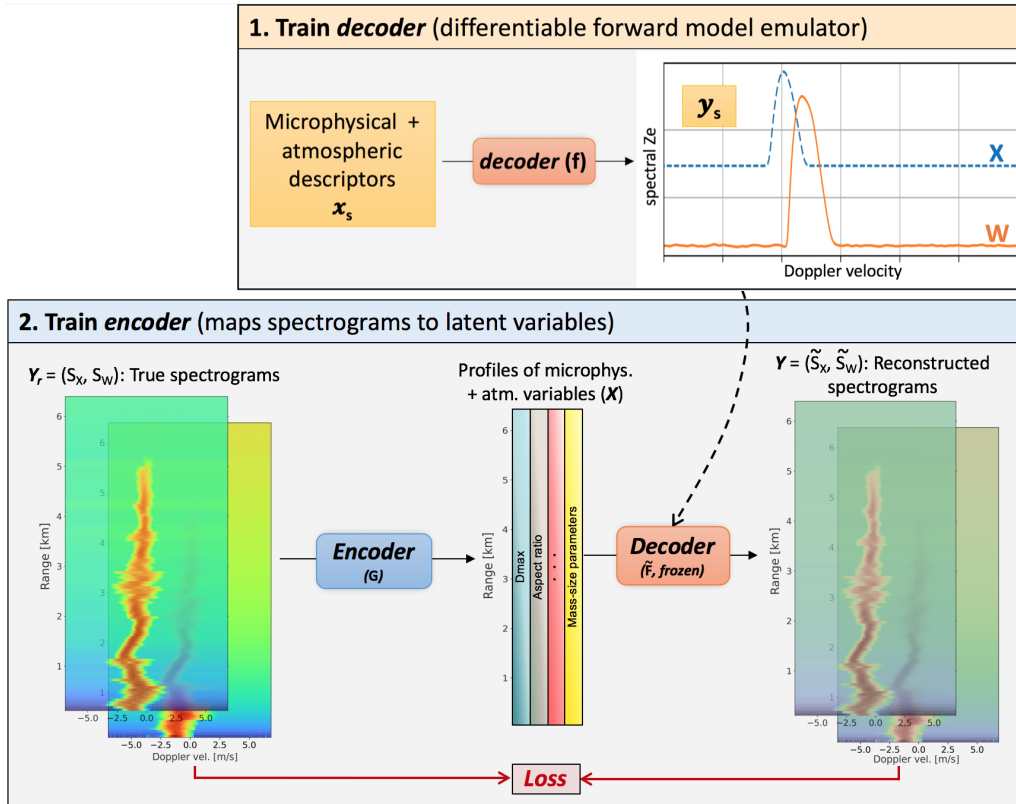
Figure 4.1: Schematic illustration of the method. The notations are those of Sect. 4.3. The upper right box illustrates that the decoder NN is trained to emulate a forward radiative transfer model. The lower box shows the full pipeline where the pretrained decoder is used to reconstruct full spectrograms based on the microphysical properties output by the encoder NN.

4.4 Data

4.4.1 Synthetic dataset

As mentioned above, the first step of the framework consists in training a decoder NN on a synthetic dataset containing sets of microphysical and atmospheric variables and the corresponding spectra. The focus of this section is the generation of this dataset.

Forward model assumptions

To build this synthetic dataset, PAMTRA is run by prescribing snowfall microphysics through several parameters. These parameters are the snowfall properties that the algorithm will then learn to retrieve.

The definitions of the microphysical descriptors are summarized in Table 4.1. The PSD is assumed to be a negative exponential distribution ($N(D) = N_0 \exp(-D/D_0)$, see Chapter 1, Eq. 1.1), whose size parameter D_0 is prescribed; we recall that, as in the rest of this thesis, the size or diameter of a particle is defined as its maximum dimension, $D = D_{max}$. For an exponential PSD, D_0 is equal to the number-concentration-weighted mean diameter (shortened as "mean diameter"); the effective diameter (ratio of the third to the second moment of the PSD), often relevant for radiative transfer models, is $D_{eff} = 3D_0$. The choice of an exponential shape for the PSD was made to restrict the degrees of freedom of the retrieval and keep the computational expense tractable; it is nonetheless a strong underlying hypothesis of the framework in its current version (discussed in Sect. 5.6.4). Mass–size and area–size relations are considered to be power laws, whose prefactors and exponents are prescribed as in Chapter 1, Sect. 1.2.5: $m = a_m D^{b_m}$, $A = \alpha_a D^{\beta_a}$. The velocity parameterization is the one proposed by *Heymsfield and Westbrook* (2010), and relies on these mass– and area–size relations. The aspect ratio A_r is then specified, defined here as equal to the particle dimension along the direction of the radar beam (here, vertical) divided by maximum dimension (*Ori et al.*, 2021), which implies $A_r \leq 1$ for both oblate and prolate particles. Particles are considered to be oriented with their maximum dimension in the horizontal plane. The ice water content (IWC) is finally assigned. Note that the total number concentration is implicitly prescribed through the definition of IWC, D_0, and a_m and b_m. In addition, the noise level (or sensitivity) is specified, since it is required to simulate realistic Doppler spectra; in practice, it only depends on the range and on the radar properties and is not related to other microphysical or atmospheric quantities.

Individual spectra are simulated through PAMTRA for an altitude of 1000 m ASL, using a standard (PAMTRA default) atmospheric profile with a temperature randomly chosen in [-20°C, 1°C]. Spectra are then simulated at X- and W-band independently. The radar settings for these simulations (frequency, beamwidth, velocity resolution, velocity range, sensitivity) should have the same values as those of the radars on which the retrieval is implemented (Sect. 4.4.2). In the current version of the algorithm, attenuation is not taken into account in

Table 4.1: Microphysical, atmospheric and radar parameters

Name	Description
IWC	Ice water content
D_0	Mean diameter (assuming exponential PSD)
b_m	Exponent of the mass–size power law
a_m	Pre-factor of the mass–size power law
β_a	Exponent of the area–size power law
α_a	Pre-factor of the area–size power law
A_r	Aspect ratio (see Sect. 4.4.1)
$TurbX$	Broadening X-band
$TurbW$	Broadening W-band
$WindX$	Radial wind X-band
$WindW$	Radial wind W-band
$LnoiseX$	Noise level at X-band
$LnoiseW$	Noise level at W-band

the PAMTRA simulations.

Scattering calculations are performed using the SSRGA, using the coefficients made available by *Ori et al.* (2021) through the SnowScatt model. These parameters were grouped by types of particles in order to match the four main categories used to sample the training set: planar crystals, columnar crystals, aggregates, and graupel. The SSRGA in general, and here the simulations of *Ori et al.* (2021), are mostly targeted on aggregates, so it was decided to include e.g., columnar aggregates in the columnar category, with the reasoning that when the size regime is that of columnar crystals, the scattering properties would approach those of the individual particles. While this rationale could be debated, it would most likely not trigger diverging results since the SSRGA collapses to the Rayleigh approximation for small particles, meaning the exact values of coefficients then have little impact. After grouping the particles into the different categories, the coefficients κ_{SSRGA} and β_{SSRGA} are then averaged within each group, for each size bin, as shown with the black lines in Fig. 4.2.

These assumptions on scattering properties are not flawless, and constitute a bottleneck in our method, as in virtually any attempt at radar-based retrievals. In particular, the current implementation of PAMTRA (28/01/2023) allows for the parameterization of only two coefficients of the SSRGA (κ_{SSRGA}, β_{SSRGA}), while current literature suggests that more coefficients should be used (γ_{SSRGA} and ζ_{SSRGA}; see *Hogan et al.*, 2017, for detail on the coefficients); furthermore, the variability of the scattering parameters shown, for instance, in *Ori et al.* (2021) or in Fig. 5 of *Leinonen et al.* (2018), was neglected when the parameters were sampled (black lines vs. colored lines in Fig. 4.2). Strictly speaking, it is also not valid to assume a single set of scattering coefficients in SSRGA computations for an entire particle size distribution, since the coefficients are size-dependent. However, as underlined in *Ori et al.* (2021), the coefficients do not change significantly for large particles, while for small particles, as mentioned earlier,

the SSRGA simplifies to Rayleigh scattering regardless of the coefficient values, which makes this assumption altogether reasonable. It should also be kept in mind that the SSRGA would fail to represent large graupel particles, although *Ori et al.* (2021) suggests that its validity extends to particles with a relatively high riming degree. All in all, these assumptions can thus naturally be questioned. We, however, believe that it was reasonable to use the simplest possible parameterization for the initial development of the method and, in particular, to use a common SSRGA framework for all scattering calculations, leaving possible improvements of the forward model to future work.
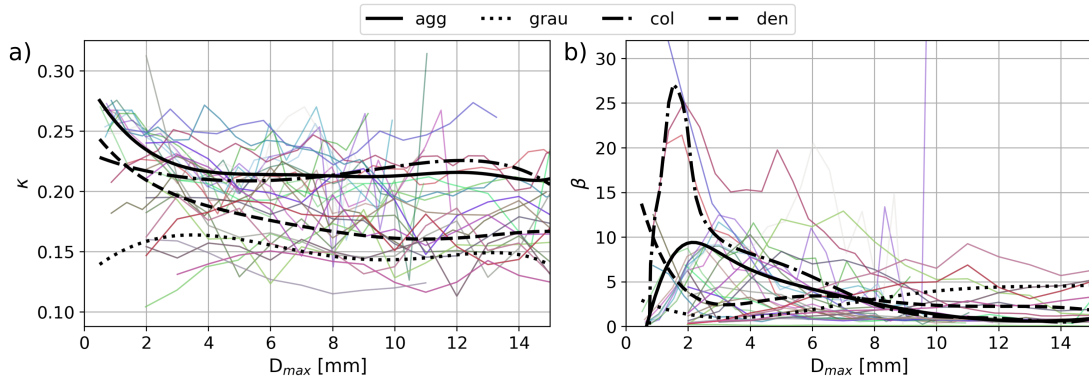
Figure 4.2: Colored lines: SSRGA coefficient computed in *Ori et al.* (2021) for a given particle type (as a function of D_{max}) for (a) κ_{SSRGA} and (b) β_{SSRGA}. Black lines: average coefficient when grouping by particle type, used for sampling the training set.

Sampling the forward model inputs

When generating the synthetic training set, a trade-off has to be defined: if the dataset is too narrow, that is, if it does not cover a large enough range of values and combinations for the microphysical descriptors, this will cause a bias in the retrieval; conversely, if the range of values is much too large, this will hamper the training process, for it will include unrealistic values. To meet this trade-off, it was chosen to parameterize PAMTRA by sampling the microphysical properties using a large observational dataset collected using the MASC during 10 field deployments. These data were organized into a database, MASCDB, by *Grazioli et al.* (2022). We follow the method presented by the authors (*Grazioli et al.*, 2022, Sect. "Technical Validation") to derive, from the database, the microphysical parameters required in the forward model (Sect. 4.4.1, Table 4.1). For each category of particle (aggregates, planar crystals, columnar crystals, and graupel) and for each microphysical parameter, a skewnorm distribution is fitted to the empirical histogram calculated from the database, shown in Figs. 4.3 and 4.6. When generating the training set, the microphysical properties are then randomly sampled from those distributions. Note that in practice, the PSD should also be truncated to a realistic size range; the minimum size is taken to be 10 μm and the maximum size is the largest diameter in MASCDB for a given particle type.
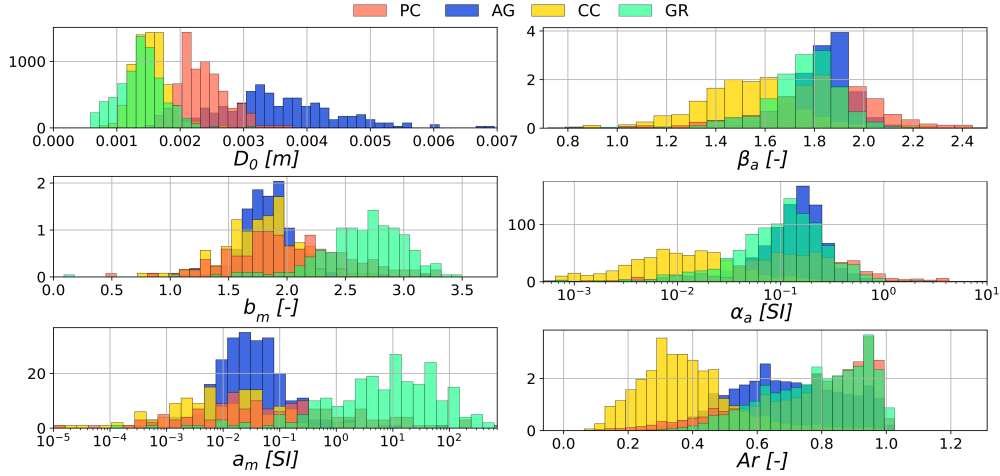
Figure 4.3: Histograms of the microphysical parameters in the MASC database. PC: planar crystals, AG: aggregates, CC: columnar crystals, GR: graupel

This way, all parameters are sampled independently, with the exception of a_m and α_a for which we applied a different method. As pointed out in *Grazioli et al.* (2022), a strong correlation exists between a_m and b_m, and between α_a and β_a; thus, empirical fits are used from which a_m (resp. α_a) is sampled for a given b_m (resp. β_a), with the addition of randomness using the RMSE of the fit (Figs. 4.4 and 4.5). In doing so, we avoid including completely unrealistic (a_m, b_m) or (α_a, β_a) pairs in the synthetic dataset, which would be detrimental to the overall framework.
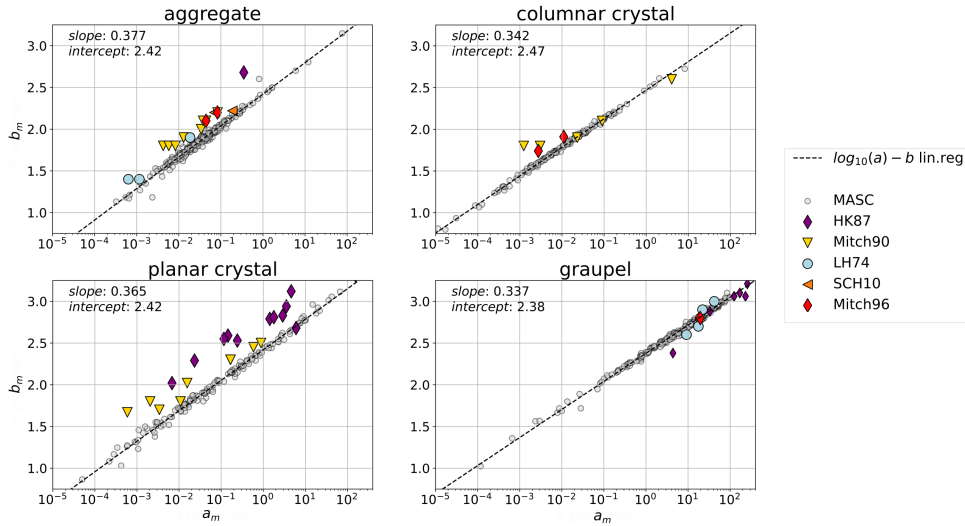
Figure 4.4: Relation between exponent and prefactor of mass–size relations for different particle types, computed using MASCDB. Literature values are added for comparison. HK87: *Heymsfield and Kajikawa* (1987); Mitch90: *Mitchell et al.* (1990), LH74: *Locatelli and Hobbs* (1974); SCH10: *Schmitt and Heymsfield* (2010); Mitch96: *Mitchell* (1996).
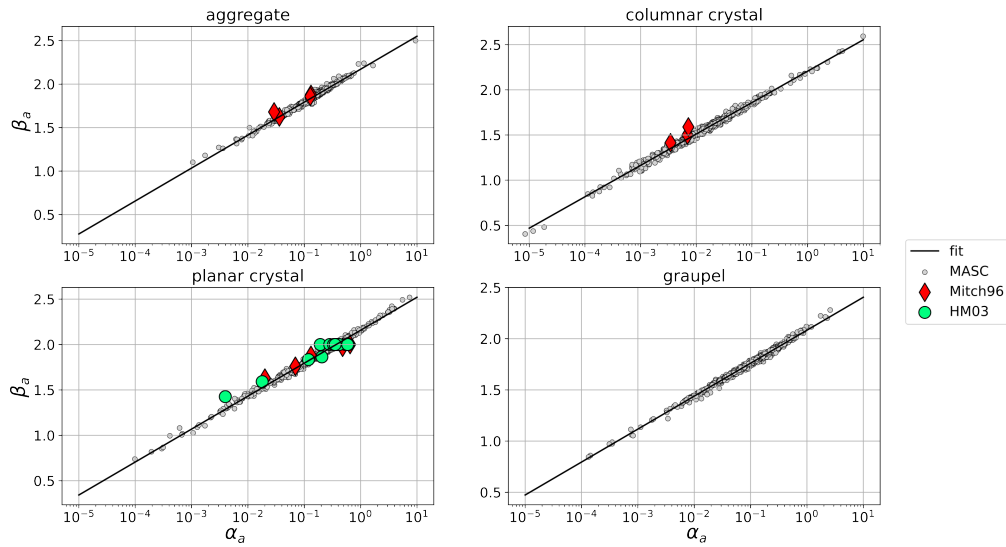
Figure 4.5: Same as 4.4 but for area–size relation. Literature values are added for comparison. Mitch96: *Mitchell* (1996); HM03: *Heymsfield and Miloshevich* (2003).

The definition of aspect ratio A_r is slightly different between the MASC dataset and the SSRGA parameterization: in the former, it is equal to the ratio of minor axis length to major axis length (*Garrett et al.*, 2015), while the latter—as mentioned earlier—defines it as particle dimension along the direction of the radar beam, divided by maximum dimension. After some empirical exploration, it was decided to use nonetheless the histograms from MASCDB, given that the distributions were quite broad, indicating that this difference in definition should not bias the retrieval. This is also consistent with the fact that particles are modeled in PAMTRA with their larger dimension aligned with the horizontal axis. IWC is the only microphysical quantity of Table 4.1 for which MASCDB does not provide estimates. It was decided, based on the literature (*Noh et al.*, 2013) and preliminary analyses of aircraft in situ measurements during ICE GENESIS, to sample it from a negative exponential distribution with a mean of $0.5 \, \mathrm{g \, m^{-3}}$.

Generation of the training set

Each item of the dataset is generated through the following procedure.

1. A particle type is randomly sampled among the four aforementioned types. Given the large variety that exists within the aggregate category, as observed in MASCDB, it is given more weight in the sampling procedure (aggregates: 40%; planar crystals: 20%; graupel: 20%; columnar crystals: 20 %).

2. Microphysical descriptors are randomly sampled using the MASC-based distributions.

3. PAMTRA is run on these descriptors, under the previously stated assumptions. The corresponding Doppler spectra are computed for 9.48 and 94 GHz (frequency of the radars used in this study, see Sect. 4.4.2), with 512 bins and a Nyquist velocity of $6.92 \, \mathrm{m \, s^{-1}}$.

4. Then, turbulent broadening and spectrum shift due to radial wind are added, with randomly sampled values, different for X- and for W-band. Including these variables will allow the retrieval to handle possible velocity offsets in the X- and W-band spectra caused by beam misalignment, or differences in spectral broadening due to the different beam widths. While these could be computed directly in PAMTRA, it was more computationally efficient to implement them in post-processing in a vectorized way.

   - The radial wind parameter accounts for the velocity shift of the spectrum that could be caused by vertical wind and beam misalignment. It is randomly sampled within [-2, +2] m s^{-1}, i.e., in the typical range of vertical wind in non-convective precipitation.

   - The broadening parameter is the size of the Gaussian broadening kernel which includes the effect of turbulent eddies and other possible causes of symmetrical broadening (e.g., horizontal wind, beam width). It is computed by randomly sampling a value of atmospheric turbulence, represented by the eddy dissipation rate (sampled from a negative exponential distribution with 10^{-3} m^2 s^{-3} mean, consistent with literature standards, e.g., *Sharman et al.*, 2014). The resulting broadening is derived following *Shupe et al.* (2008, Eq. 4); the radar settings (e.g., beam width) used in these equations are those of the W- and X-band radars used in this study, described in Sect. 4.4.2.

5. Finally, for computational reasons, X- and W-band spectra are both reduced to 256 points through bin averaging.

Ultimately, each item of the synthetic dataset contains an input vector with 13 dimensions (see Table 4.1) and the corresponding simulated Doppler spectra (X- and W-band) with 256 bins each. Figure 4.6 illustrates the distribution of the non-microphysical input features (i.e., other than those shown in Fig. 4.3) in the synthetic dataset. We underline that this dataset contains information only at the scale of the simulated radar sampling volume at a given range gate—not full spectrograms.
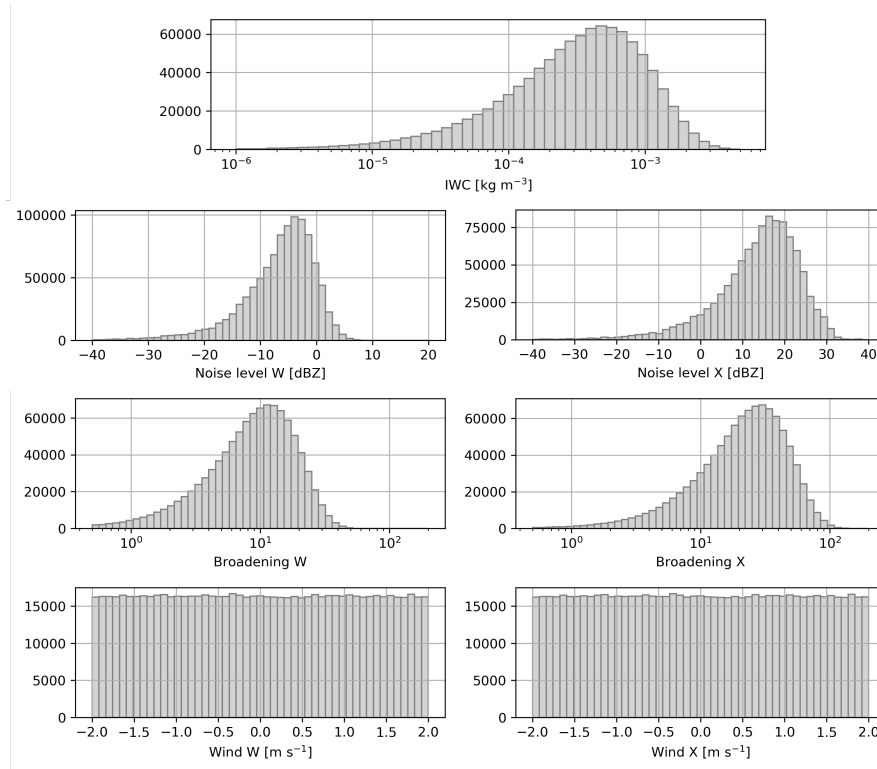
Figure 4.6: Same as Fig. 4.3, for the other descriptors (not from MASCDB) in the synthetic dataset.

4.4.2 X- and W-band Doppler spectrograms

In this section, we present the experimental dataset used in the second part of the pipeline, for the training of the encoder. Data from the X- and W-band vertically-pointing Doppler radars ROXI and WProf are used, which were located at les Éplatures airport, in la Chaux-de-Fonds, during the ICE GENESIS campaign (see Chapter 2). The properties and settings of both radars are recalled in Table 4.2. As an important pre-processing step, the radars were cross-calibrated and an attenuation correction was implemented at W-band (similarly to *Kneifel et al.*, 2015), as detailed here.

Table 4.2: Properties and parameters of WProf and ROXI during ICE GENESIS. WProf uses three chirps, with ranges as follows: chirp 0: 104-998 m, chirp 1: 1008-3496 m, chirp 2: 3512-8683 m; when applicable, the properties for each chirp are separated by "/". The maximum range of ROXI is 6.4 km.

	WProf	ROXI
Frequency (GHz)	94	9.4
Transmission	FMCW, simultaneous transmit/receive	pulsed
3-dB beam width (°)	0.53	1.8
Sensitivity (dBZ) [at range (km)]	-45 [0.5] / -41 [2] / -39 [5]	-19 [2]
Time resolution (s)	5	3
Range resolution (m)	7.5 / 16 / 32	50
Nyquist velocity (m s^{-1})	10.8 / 6.92 / 3.3	11
Velocity resolution (m s^{-1})	0.02 / 0.014 / 0.013	0.1

X-band calibration drift

An issue was encountered with the calibration of ROXI, which was found to be fluctuating in time, for a reason that is not fully clarified yet. We believe that it could be related to a hardware artifact causing the output power or received secondary wave trains to fluctuate; the investigation of this issue is beyond the scope of this work. In addition to these calibration variations, the occasional presence of wet snow on the antenna was found to affect the measurements, despite frequent manual removal. In order to correct for this, we used Z_H profiles of MXPol (extracted from RHIs remapped to a Cartesian grid, at the horizontal distance corresponding to the location of ROXI) as a reference. Although these are collected at a lower time resolution, they were sufficient to correct for the calibration fluctuations and wet snow antenna attenuation.

W-band attenuation correction

Once the X-band data is considered reliable enough, we focus on the correction of W-band attenuation by following the method described in *Kneifel et al.* (2015):

- Gaseous attenuation: atmospheric profiles are taken from hourly COSMO-1 analyses (*Consortium for Small-scale Modeling*, 2017, run with a 1-km horizontal grid resolution), and the corresponding profile of gaseous attenuation is computed using PAMTRA.

- Snowfall attenuation: We use a baseline $Z_{e,X}$–IWC relation (IWC $= 0.015\, Z_{e,X}^{0.44}$, *Kneifel et al.*, 2015; *Boudala et al.*, 2006, with $Z_{e,X}$ in linear units) to estimate the profile of snow and ice content, and the corresponding attenuation profile is obtained considering that ice attenuates around 0.9 dB km^{-1} (g m^{-3})$^{-1}$ (*Nemarich et al.*, 1988).

- SLW attenuation: this is likely the most crucial and the most error-prone step, considering that no measurements of the LWC profile are available. We make use of LWP estimates retrieved from measurements of the 89 GHz radiometer coupled to WProf (Chapter 3), and, for lack of more refined information, we assume a uniform LWC profile in the cloud/precipitation column, identified as all range gates with $Z_{e,W} > -30$ dBZ. The corresponding attenuation profile is then computed with PAMTRA, using the COSMO atmospheric profile and assuming a monodisperse cloud drop size distribution with a diameter of 20 μm. As for the brightness temperature simulations of Chapter 3, there is little to no sensitivity to this choice of distribution as long as the liquid drops are can be approximated as Rayleigh scatterers, which is the case for cloud droplets.

The mean two-way path-integrated attenuation (PIA) for each of these categories is respectively 0.3, 0.4 and 1.7 dB, on the entire dataset used. Additional details are provided in Appendix A to verify the self-consistency of this approach. W-band reflectivity and Doppler spectrograms are then corrected using the cumulative attenuation profiles. In a final step, as in *Dias Neto et al.* (2019), the reflectivity values at X- and W-band are cross-corrected by

selecting areas close to cloud top and with low reflectivity, and correcting WProf with the mean reflectivity offset in these regions (regions within 1 km of cloud top and $Z_{e,X} < -3$ dBZ were used; if a lower $Z_{e,X}$ threshold is used, too few points are available). This relies on the assumption that near cloud top, small ice crystals (with low reflectivity) are approximated by Rayleigh scattering at both frequencies, for which the DFR is 0 dB.

A further note should be added regarding one event in the dataset (22 January) which featured rain at ground level during a few hours before a transition to snowfall in the evening. Here, step 3 of the method described could not be implemented because the LWP retrieval is contaminated by low-level rain. The other steps were performed similarly, and only data above the melting layer was used for the retrieval. Overall, this mitigates attenuation-related issues but cannot eliminate them. In particular, the presence and amount of SLW is difficult to assess and correct accurately.

Data remapping

After these post-processing steps, the spectrograms of both radars are remapped to a common grid, by averaging in time (with a resolution of 20 s), interpolating in range (resolution of 50 m), and average-binning the velocity to the same bins as the synthetic dataset, with 256 bins and a velocity cutoff $v_{Nyq} = 6.92$ m s^{-1}. Only time frames with detectable signal in both frequencies are used, leading to a total of ~ 9000 profiles, corresponding to around 45 hours of measurements, collected between 22 January and 28 January.

4.5 Deep learning inversion framework

This section details the implementation of the two-step framework outlined in Sect. 4.3. For designing and training both the decoder and the encoder NNs, the PyTorch library is used (*Paszke et al.*, 2019).

4.5.1 The decoder: a differentiable emulator of PAMTRA

The first part of the framework consists in developing a differentiable emulator of PAMTRA by designing a deep learning model and training it on the synthetic dataset (Sect. 4.4.1). If viewed in perspective with the technique of auto-encoders, this means learning the "decoder", which maps the latent space—containing the physical variables—to the high-dimensional measurement space—the spectra. It was chosen to train the X- and W-band decoders separately rather than use a single NN emulating both simultaneously; indeed, the two frequencies may have slightly different smoothness or amplitude features, which justifies the use of distinct architectures. Each decoder takes as input a vector of dimension 10 containing IWC, D_0, b_m, a_m, β_a, α_a, A_r, $Turb_v$, $Wind_v$ and $Lnoise_v$, where v is either X or W. They output Doppler spectra with 256 points.

Decoder architecture

The decoder model, whose architecture is illustrated in Fig. 4.7a, is designed as a NN with a first part composed of fully-connected layers and a second part composed of convolutional layers. More precisely, since the aim of this decoder is to increase dimensionality (from 10 to 256), we use one-dimensional transposed convolutions which are well suited for this purpose (*Zeiler et al.*, 2010). Since transposed convolutions alone can create artifacts, they are combined with linear upsampling layers and standard convolutions, which ensure a smooth output. In order to improve the training of the model, residual blocks (*He et al.*, 2016) are used, which contain skip connections and batch normalization steps (*Ioffe and Szegedy*, 2015). In a nutshell, these techniques help mitigate issues caused by the depth of the model: they do not per se improve the expressiveness of the NN, but they facilitate the training process. For instance, the skip connections (illustrated in Fig. 4.7) allow to propagate information from earlier layers to further stages of the neural network, and this reduces the risk of gradients vanishing to zero during training (*Balduzzi et al.*, 2017).

Decoder training

The synthetic dataset described in Sect. 4.4.1 is split into training, validation and testing sets (80%–10%–10%). The input features are normalized using the statistics of the training dataset, with the mean and standard deviation of each variable. For certain variables, the natural logarithm is used instead of the original value, in order to have more homogeneously spread distributions: this is the case for IWC, a_m and α_a. The network is trained using the Adam optimizer (*Kingma and Ba*, 2015), with mean square error (MSE) as a loss metric, and with Xavier normal initialization of weights and biases (*Glorot and Bengio*, 2010). In addition, the learning rate is periodically decreased with a scheduler. The network and training hyperparameters are summarized in Table 4.3. It was observed that the spectra output by the NN could have a tendency to slightly underestimate the peak values, because of a flattening effect common in methods that use MSE as a loss metric. To counterbalance this, we add to the main loss a secondary loss calculated as the MSE on the part of the spectrum close to its peak (above 50% of its amplitude).

4.5.2 The encoder: retrieving a profile of latent variables

In the second part of the framework, another deep neural network, the encoder, learns the inverse mapping. Taking as input dual-frequency spectrograms (i.e., an array of shape $N_{rg} \times 256 \times 2$, with N_{rg} the number of range gates), it outputs vectors in the latent space, of shape $N_{rg} \times 13$, 13 being the total number of latent dimensions retrieved, as detailed in Table 4.1. In this section, we refer to the first dimension as the *range* dimension, to the second one as the *feature* dimension, and to the last one as the *channel* dimension.
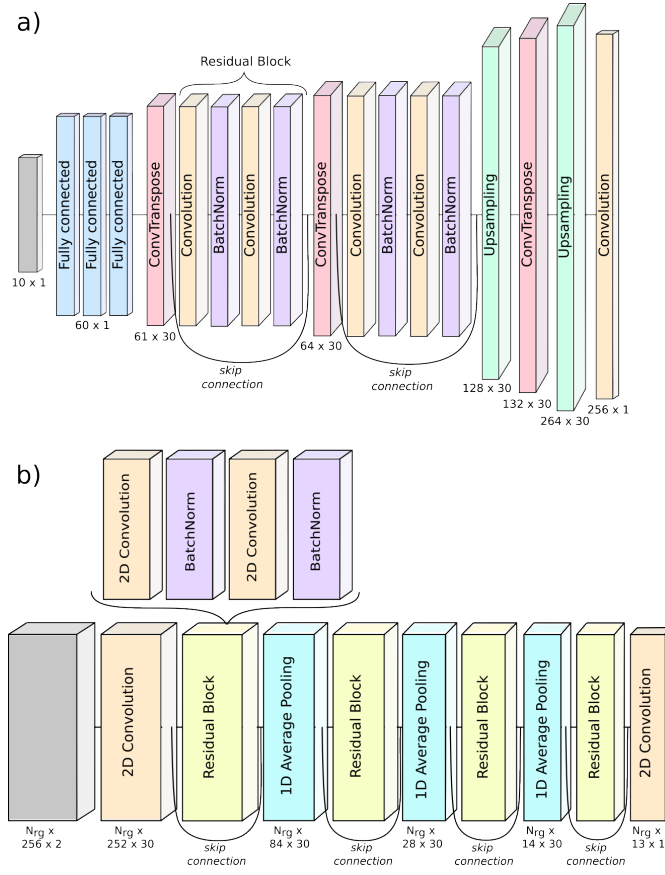
Figure 4.7: Architecture of (a) decoder and (b) encoder neural networks. In (a), the architecture of the W-band decoder is shown; that of X-band is extremely similar with only slightly different kernel widths. Skip connections indicate that the output of a given layer is kept and added further on to the output of a residual block. Color coding indicates the type of each layer. The size of each layer, defined as the dimension of its output, is indicated; when not stated, the layer is the same size as the previous one (to the left). Note that for display reasons the velocity dimension is represented in the vertical in panel (a) and along the horizontal direction in panel (b). The activation function is applied after each layer, except before batch normalization.

Encoder architecture

The neural network designed for this part uses two-dimensional convolutions, which allow reducing the feature dimension from 256 to 13. In order to keep the range dimension constant (equal to N_{rg}), padding is used, which means artificially increasing the size of the array, by replicating the items in the first and last position along the range dimension, before performing the convolution. Similar to the decoder architecture, residual blocks with skip connections and batch normalization steps are used. Additionally, average pooling along the feature dimension is performed after each residual block. The size of the convolution kernels along the range dimension gives a sense of the scale at which we can expect meaningful spatial correlation, both in the latent space and in the measured spectrograms. It is, however, not directly interpretable: as the NN contains stacks of convolution layers, the field of view

progressively increases with the model's depth; the output of the NN at a given range gate is influenced not only by its closest neighbors but also by range gates which are further away. The full architecture of the encoder is displayed in Fig. 4.7b.

Encoder training

The encoder is trained using the radar data presented in Sect. 4.4.2. The spectrograms are normalized using the same statistics as in the decoder part (means and standard deviations of the synthetic training set spectra). Rather than using the entire Doppler spectrograms ($N_{rg} = 100$) as one training item, chunks of the spectrograms are used with $N_{rg} = 25$, and are sampled in the following way: the first chunk corresponds to $i_{rg} = 0..24$, the second chunk to $i_{rg} = 5..29$, the third to $i_{rg} = 10..34$, etc., with i_{rg} being the range gate index. The dataset is then randomly shuffled at each epoch during training. Rearranging the dataset in this way makes training both more tractable, thanks to the smaller size of each item, and more robust, due to the data augmentation, which helps avoid local minima during the training process. During training, the encoder output is passed as input to the X- and W-band decoders, which output reconstructed spectrograms. The reconstruction loss is the MSE between the reconstructed ($\tilde{S}_W, \tilde{S}_X$) and the original spectrograms (S_W, S_X): $Loss = (\tilde{S}_X - S_X)^2 + (\tilde{S}_W - S_W)^2$. The encoder parameters are then updated at each step to minimize this loss, here with the Adam optimizer (*Kingma and Ba*, 2015). Training parameters are reviewed in Table 4.3. It is important to note that the decoder parameters are frozen at this step: only the encoder is being learned; this differs from classical auto-encoder models, for which the decoder and encoder are learned simultaneously.

Table 4.3: Hyperparameters of the encoder and decoder neural networks.

Hyperparameter	Decoder	Encoder
Activation	ReLU	ReLU
Range of kernel sizes (range dim. × vel. dim)	$1 \times (2 - 7)$	$3 \times (3 - 7)$
Number of input channels	1	2
Number of inner channels	30	30
Number of linear layers	3	0
Number of neurons in linear layers	60	-
Total number of parameters	35000	150000
Padding mode	replicate	replicate
Loss	MSE	MSE
Optimizer	Adam	Adam
Batch size	250	15
Number of epochs	3	200
Learning rate (initial)	1e-3	1e-3
Optimizer epsilon	1e-8	1e-6
Scheduler step / rate	0.6 / 0.2	90 / 0.5
Parameter initialization	Xavier	Xavier

Estimates of the latent features are then obtained from the output of the encoder, after inverse normalization and exponential transform for those variables whose logarithm was used as input to the decoder (see Sect. 4.5.1). To prevent occasional convergence toward unrealistic values in the latent space (e.g., $D_0 < 0$ mm), an additional constraint was incorporated into the loss term to penalize latent values outside of a manually defined range; for a given feature x with realistic bounds x_{min} and x_{max}, this secondary loss reads: $L_{sec}(x) = \mathbb{1}_{(x<x_{min})} \times (x - x_{min})^2 + \mathbb{1}_{(x>x_{max})} \times (x - x_{max})^2$. [*]

4.5.3 Ensemble approach for uncertainty quantification

In order to estimate the uncertainty of the retrieval, an ensemble approach is used: several runs are performed for both the decoders and the encoder, each trained independently with random weight and bias initialization (*Glorot and Bengio*, 2010). In the end, a total of 50 runs are used to compute mean values and standard deviations for each retrieved latent variable. This is an important point, as it both ensures a greater robustness of the retrieved values, which are less likely to reflect local minima, and provides an uncertainty estimate for the retrieval. This is especially relevant given the under-determination of the problem: with this ensemble approach, we can illustrate the uncertainty related to the remaining intrinsic ill-posedness of the model. On the downside, this implies a lengthier process since training is a computationally demanding task that typically takes a few hours on a standard GPU.

4.6 Results: training convergence and accuracy

This section is dedicated to the evaluation of the pipeline and the verification of its convergence, which is a necessary step before examining the retrieved latent variables themselves.

4.6.1 Decoder

The training of the decoder networks was successful, with the loss function decreasing with the number of batches perused until it plateaus. It was verified that increasing the training set size did not result in a change of this plateau value, meaning that the training dataset was large enough for the chosen NN complexity. Since the loss function (MSE on normalized spectra), is not easily interpretable to assess the performance of the model, another metric was defined to quantify the overlap of two spectra (Eq. 4.1). $O(S, \tilde{S})$ is equal to 1 (100%) when the spectra are identical, and to 0 when they are completely disjoint. Figure 4.8 can be helpful to understand this definition.

$$O(S, \tilde{S}) = 0.5 \left[\frac{\int_{-v_{NYQ}}^{v_{NYQ}} \min[S^*(v), \tilde{S}^*(v)] dv}{\int_{-v_{NYQ}}^{v_{NYQ}} S^*(v) dv} + \frac{\int_{-v_{NYQ}}^{v_{NYQ}} \min[S^*(v), \tilde{S}^*(v)] dv}{\int_{-v_{NYQ}}^{v_{NYQ}} \tilde{S}^*(v) dv} \right] \tag{4.1}$$

---

[*]$\mathbb{1}_{(x<x_{min})}$ is equal to 1 when $x < x_{min}$ and to 0 otherwise.

- Here, S is the reference spectrum (target), and $\tilde{S}$ is the model output (whose quality we want to assess).

- S and $\tilde{S}$ are offset as $S^* = S - \min(S)$ and $\tilde{S}^* = \tilde{S} - \min(S)$, where $\min(S)$ is the global minimum of S; i.e., we substract $\min(S)$ to both S and $\tilde{S}$. S^* and $\tilde{S}^*$ are introduced to bring the base level of the target spectrum to 0, otherwise, the integrals would be dominated by the noise rather than the signal. Note that both spectra are offset with the same value ($\min(S)$), which allows to identify discrepancies in the absolute reflectivity.

- The first term of the sum in $O(S, \tilde{S})$ is the hatched area divided by the blue area (Fig. 4.8); the second term is the hatched area divided by the pink area. Both terms are needed to account for cases when $\tilde{S}$ would be broader than S (i.e., when $\tilde{S}$ would overlap S completely), and when $\tilde{S}$ would be narrower than S (i.e., $\tilde{S}$ overlapped by S).
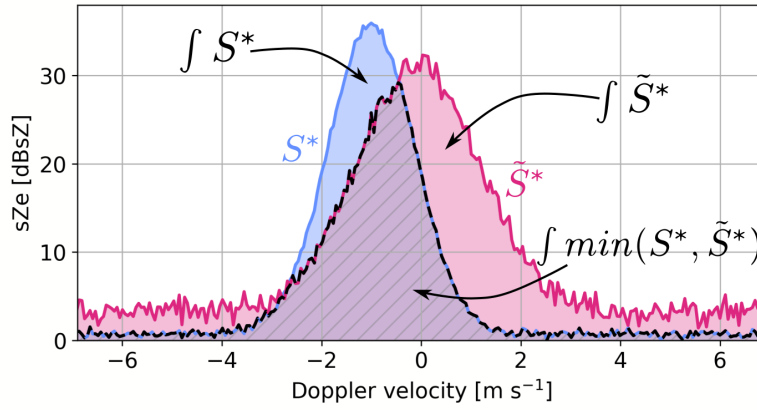
Figure 4.8: Illustration of the overlap metric. The spectra were created for illustration purposes and are not part of the dataset. In this example, the value of the overlap metric is 0.65 (65%).

Examples of model outputs on the synthetic testing set are shown in Fig. 4.9. On the synthetic testing set, the overlap for X-band (resp. W-band) is of 90.7% (resp. 94.8%), as an average over five different runs with random initialization. This reflects a good, although not perfect, performance of the algorithm. Looking at a few examples of individual spectra, it comes across that the model has a slight tendency to underestimate the peak of the spectrum (see, for example, the X-band spectrum chosen in Fig. 4.9b), despite the secondary loss that was used; however, the rather good overall agreement between target and output spectra suggests this is not a critical issue. Additionally, we observe that performance is slightly worse for X- than for W-band spectra, in spite of some efforts to adjust the neural network architectures independently to improve the accuracy of each model. This could be related to the fact that W-band spectra have a lower noise level, meaning the actual signal (the peak) occupies a larger part of the spectrum than for X-band, which could in turn facilitate learning.
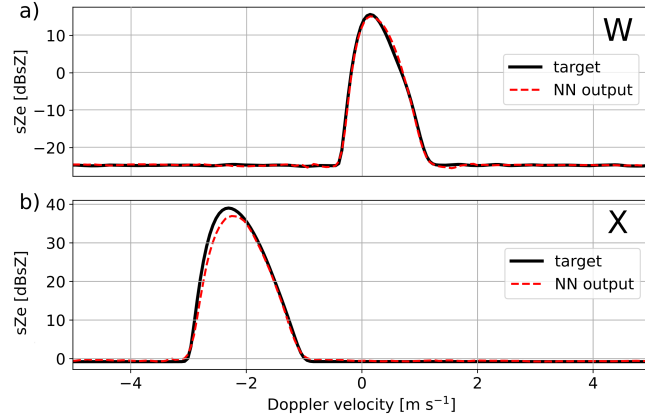
Figure 4.9: Examples of results on the synthetic testing set of the decoders, showing the decoder output (dashed red) and the target PAMTRA-generated spectrum (black line) at (a) W- and (b) X-band. The examples were chosen to reflect some of the typical behaviors and possible artifacts that were observed; the X- and W-band examples do not correspond to the same microphysical properties.

4.6.2 Encoder

Training of the encoder is also successful: the full pipeline is able to reconstruct original spectrograms in a satisfactory manner, as is visible in Figure 4.10. Only W-band spectrograms are shown but results are visually very similar at X-band. The overlap metrics are slightly below the ones of the decoder alone (86% and 91% for X- and W-band spectrograms, respectively). This slight decrease can be expected for several reasons: first, the real spectrograms include high-shear regions with significant turbulent broadening (which can be visually identified as regions with suddenly much wider spectra, along with variable velocity, e.g., in Fig. 4.10 below 500 m), which the model cannot be expected to resolve perfectly. Then, some time steps include bimodal spectra (e.g., 2.5 km–3.5 km) which the pipeline in its current state is not able to replicate. When looking only at spectrograms with moderate apparent turbulence (e.g., 0.5 km–1.5 km), and strict unimodality, the overlap metrics are similar to the decoder. Finally, it is also empirically observed that in some cases (Fig. 4.10e) the model can slightly underestimate the peak of the spectrograms, which is a propagation of the decoder behavior. As an important safety check, it is also verified that running PAMTRA on the latent variables also leads to spectrograms close to the original ones (Fig. 4.10c).

Let us point out at this stage that, unlike most machine learning models, which are trained on a dedicated dataset and then implemented on independent data, the encoder is here trained directly on the data of interest. Indeed, the aim is not to create a generic model that can be used to retrieve microphysical variables from any dual-frequency spectrogram: rather, the aim is to find the latent variables which minimize the reconstruction error on specific measurements. The encoder can learn any relevant feature from the input data to achieve this goal. In that sense, overfitting the data, which can be an issue in usual machine learning problems, is not a concern when training the encoder. It is, however, preferable to train the
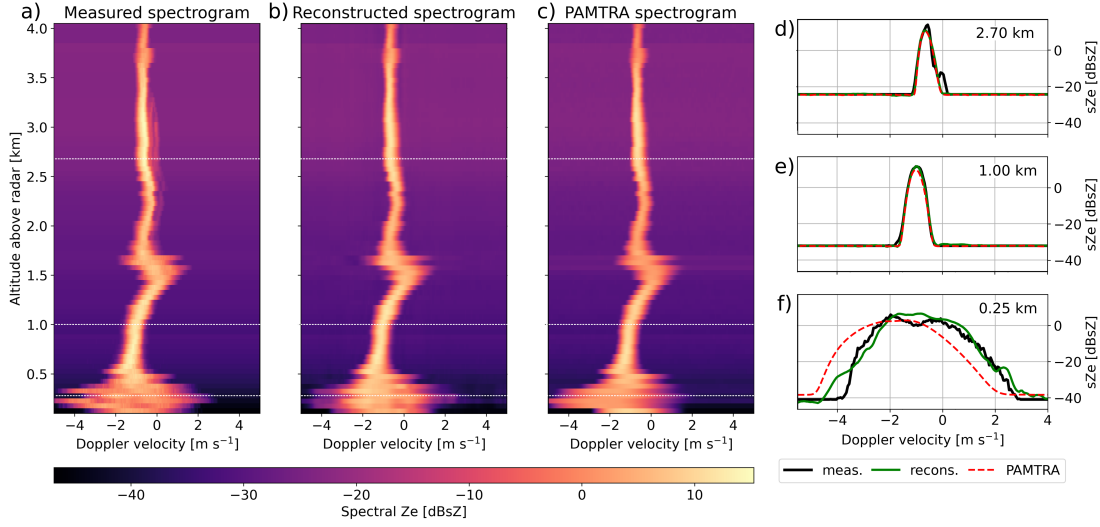
Figure 4.10: Examples of W-band spectrograms: (a) measured, (b) reconstructed through the pipeline, and (c) reconstructed in PAMTRA from the learned latent features. Corresponding spectra from selected altitudes are displayed in (d), (e), and (f); they are indicated with dashed white lines in the spectrograms. The reconstruction of X-band spectrograms (not shown) is of similar quality.

model on a large enough dataset rather than just a few spectrograms: this reduces the risk of converging toward local minima that would correspond to non-physical combinations of microphysical parameters.

4.7 Conclusions

In this chapter, we introduced a new method for the retrieval of seven microphysical properties of snowfall from dual-frequency Doppler radar spectrograms. The approach relies on a two-step deep learning framework: a *decoder* network serves as a differentiable gate-to-gate emulator of a known radiative transfer model, while the *encoder* network learns to map the Doppler spectrograms to full profiles of microphysical variables. To our knowledge, no previous method allows for the joint retrieval of these descriptors with this high spatial and temporal resolution. In addition, the proposed method allows, through its design, to overcome some usual challenges of Doppler spectral retrievals, like the need for perfectly vertical beam alignment, or the requirement of very low turbulence.

This chapter was dedicated to setting up the theoretical framework and detailing the deep learning models. It was then verified that the decoder and encoder networks converge and have reasonable accuracy. The next chapter will assess the quality of the framework by focusing on the accuracy of the retrieved microphysical variables themselves. For this purpose, we will make use of the multi-sensor measurements in the ICE GENESIS dataset.

5 Dual-frequency spectral radar retrieval of snowfall microphysical properties: implementation and evaluation on the ICE GENESIS dataset

In close connection with Chapter 4, this chapter focuses on the implementation of the proposed deep learning microphysical retrieval framework on the ICE GENESIS dataset. The text is adapted from Sections 5–7 of the published article:

- **Anne-Claire Billault-Roux**, Gionata Ghiggi, Louis Jaffeux, Audrey Martini, Nicolas Viltard and Alexis Berne (2023): Dual-frequency spectral radar retrieval of snowfall microphysics: a physics-driven deep-learning approach. *Atmospheric Measurement Techniques*, 16(4), 911–940, doi: 10.5194/amt-16-911-2023.

The implementation of the retrieval on the dataset, the comparisons of retrieved to in situ values, and the sensitivity analyses, were conducted by Anne-Claire Billault-Roux with input and supervision from Alexis Berne. Aircraft in situ data were processed by Louis Jaffeux.

5.1 Summary

The retrieval framework presented in Chapter 4 is implemented on X- and W-band data from the ICE GENESIS campaign. The accuracy of the retrieval is assessed through comparisons with collocated aircraft in situ measurements during three precipitation events. An overall good agreement is found with, however, a bias in retrieved D_0 values. The main limitations of the method are discussed, together with its sensitivity to the underlying assumptions.

Statistics of retrieved snowfall microphysical properties during ICE GENESIS are then presented and analyzed. Overall, the proposed framework opens up possibilities for a detailed characterization of snowfall microphysics on larger datasets, with the seven retrieved microphysical descriptors of snow particles providing relevant insights into snowfall processes.

5.2 Introduction

In the previous chapter, a new deep-learning-based framework was introduced to retrieve microphysical properties of snowfall from dual-frequency Doppler spectrograms. It relies on a two-step architecture inspired from auto-encoder neural networks. The microphysical descriptors are viewed as the dimensions of a latent space to which the spectrograms can be mapped. The decoder neural network emulates a physical radiative transfer model, which generates Doppler spectra from a set of snowfall properties. The encoder NN ingests dual-frequency spectrograms and maps them to the latent space, from which the pre-trained decoder produces reconstructed spectrograms; the encoder is trained by minimizing the reconstruction error. It was verified that both the decoder and the encoder neural networks were trained adequately. The former was trained, validated, and tested on a synthetic dataset; it reproduces accurately the spectra generated with a physical scattering model (PAMTRA). The training of the encoder also converges, and the spectrograms reconstructed by the pipeline are a reasonably good approximation of the original measurements.

ICE GENESIS (Chapter 2), with its multi-sensor, ground-based and airborne suite of in situ and remote sensing instruments, provides a rare opportunity to validate the approach more thoroughly and assess the accuracy of its underlying assumptions. In this chapter, we discuss the implementation of the algorithm on the ICE GENESIS dataset in a qualitative and quantitative way, using data presented in Sect. 5.3. Comparisons of retrieved properties against reference measurements are conducted in Sect. 5.4 and 5.5; in Sect. 5.6, we identify the main limitations of the framework in its current state. We finally illustrate (Sect. 5.7) its results on 45 hours of cloud and precipitation measurements during ICE GENESIS, and provide some statistical perspectives on the snowfall microphysics that were sampled during the campaign.

5.3 Data for model evaluation

In this section, we detail the components of the ICE GENESIS dataset that are used for the assessment of the retrieval. They include ground-based and airborne radar products, as well as in situ aircraft measurements.

5.3.1 Polarimetric radar

The polarimetric X-band scanning radar MXPol (*Schneebeli et al.*, 2013), deployed 4.8 km away from the main site, performed routine range-height indicator (RHI) scans in direction of ROXI and WProf. Hydrometeor classification with demixing (*Besic et al.*, 2016, 2018) was implemented on these measurements to estimate the proportions of hydrometeor types in the sampled volume. From the RHIs, remapped to a Cartesian grid, profiles are extracted over the main site with a horizontal resolution $\delta x = \pm 500$ m, using only elevation angles below 45 degrees. The time series of hydrometeor classification extracted in this manner will be used qualitatively as an independent tool to assess the performance of our microphysical retrieval.

5.3.2 Aircraft in situ measurements

The airborne in situ data are particularly valuable for the quantitative evaluation of the retrieval. In this work, we use airborne measurements from three flights of the Safire ATR 42 (22, 23, and 27 January), with data from several probes (see Chapter 2). First, the CVI provides a measurement of TWC, and the CDP-2 measures LWC; from those quantities, an estimate of IWC is obtained as IWC = TWC − LWC. Two imaging probes are also used, the 2D-S and the PIP, sampling respectively from 10 μm to 1.28 mm and 100 μm to 6.4 mm. From these images, the method of *Leroy et al.* (2016) is used to compute the PSD and derive the following microphysical descriptors: mean aspect ratio[*], mass–size power law coefficients, and area–size power law coefficients. In order to estimate the D_0 parameter, an exponential distribution is fitted to the PSD (leaving out small particles with D_{max}< 800 μm, since it was empirically noted that these did not always follow this exponential behavior). This approach was chosen rather than computing moments from the in situ PSDs, as those could potentially be affected by the size cutoff at 6.4 mm, while the slope of the distribution is expected to be a more robust indicator. For the mass–size parameters, in addition to the CVI closure method of *Leroy et al.* (2016), another method is used for particle-by-particle mass reconstruction based on *Baker and Lawson* (2006); the methods are respectively denoted as "*CVI*" and "*BL*". All aircraft-based microphysical descriptors are computed using 5-second running averages of the measurements.

5.3.3 Airborne radar retrieval

The aircraft was also equipped with an upward-looking W-band radar, RASTA, from which values of IWC are derived following *Delanoë et al.* (2007), and hereafter denoted with the "*RASTA*" subscript. In order to compare IWC$_{RASTA}$ to in situ measurements, the closest valid radar gates are used, which correspond to a vertical distance of 150 to 250 m above the aircraft. For the comparison between airborne RASTA retrievals and our inversion model, only time steps when the aircraft overpasses the ground site are used, i.e., when the aircraft is within a 1 km horizontal distance to the ground site (distance chosen to allow for a sufficient number of points in the comparison).

---

[*]The aircraft in situ aspect ratio is defined as the ratio of minor axis length to maximum dimension of the particle's 2D projection.

5.4 Qualitative assessment of the retrieval

5.4.1 Microphysical parameters

This section presents a qualitative perspective on the retrieval results, based on a snowfall event that took place on 23 January 2021. Figure 5.1 features height–time plots of selected radar variables (left column) and retrieved microphysical descriptors (right). The radar data include $Z_{e,X}$, DFR, MDV_W and SW_W, as well as the hydrometeor classification from MXPol. It is noteworthy that the latter classification, derived from polarimetric variables, is fully independent from WProf and ROXI spectrograms. The microphysical variables included in the right panels are IWC, D_0, b_m, β_a, and A_r. The variables a_m and α_a, not shown, are highly correlated with respectively b_m and β_a (see e.g., Fig. 5.6).
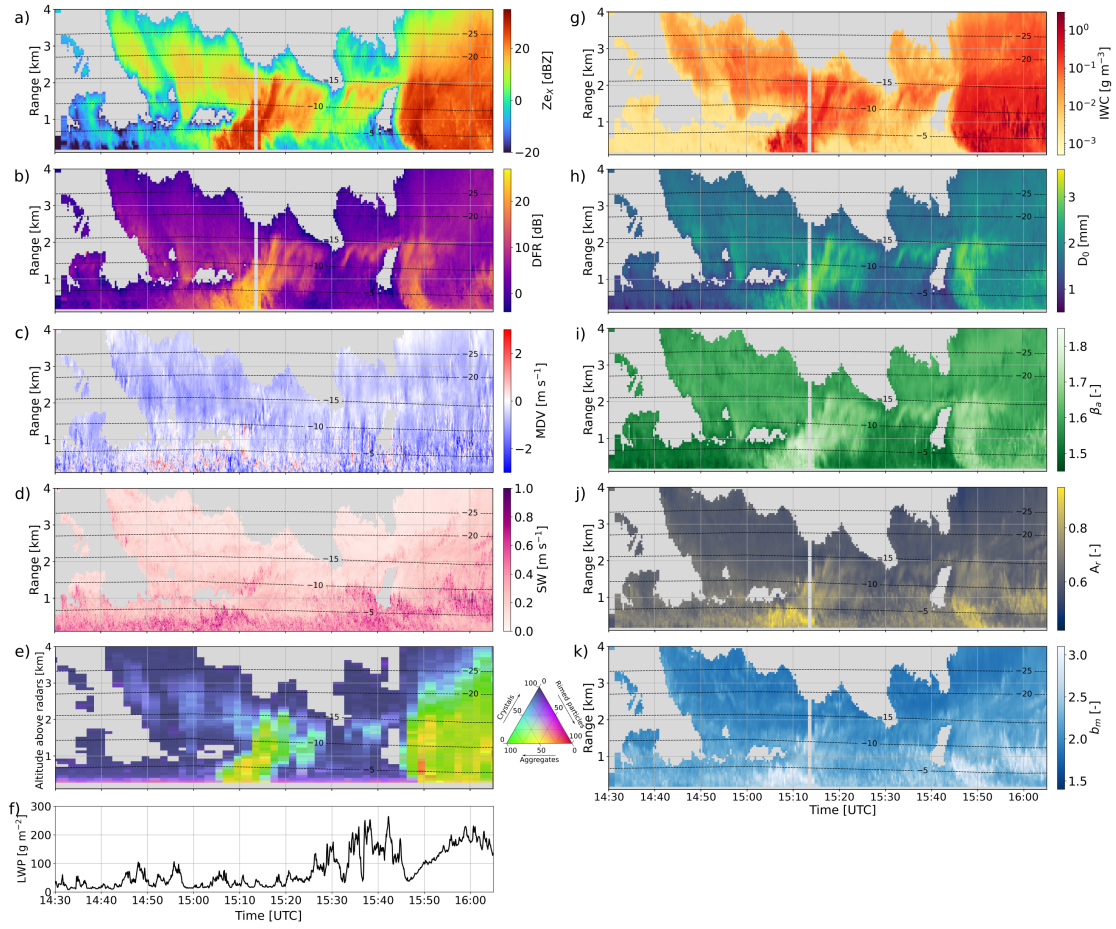
Figure 5.1: Height–time plots of radar measurements and microphysical retrievals. The left panels contain radar data: (a) $Z_{e,X}$; (b) DFR; (c) W-band MDV; (d) W-band SW; (e) MXPol hydrometeor classification with demixing showing the proportion of the three main particle types identified: here aggregates, rimed particles and crystals; (f) time series of retrieved LWP (Chapter 3). The right panels feature microphysical retrievals: (g) Ice water content; (h) Size parameter D_0; (i) Area–size exponent β_a; (j) Aspect ratio A_r; (k) Mass–size exponent b_m. The temperature contours are from COSMO-1 hourly analyses.

A first general observation is the persistence of spatiotemporal structures visible in the radar data, like the fall streaks, in the microphysical fields. While the pipeline implicitly took into account the spatial consistency of the measurements (through the use of convolutions), the temporal features are never used in the training of the model. It is thus reassuring that the full spatiotemporal features are well captured by the retrieval.

The retrieved values are also fairly consistent with the physical interpretation that stems from the radar measurements. IWC correlates quite strongly with $Z_{e,X}$ values, i.e., large IWC values are retrieved for high reflectivity measurements (e.g., around 15:10 and 15:50 UTC). The size parameter D_0 also matches the intuition, with small diameters near cloud top, and some localized pockets with large values such as around 15:10 between 1 and 2 km range, which correspond to regions of large DFR. The D_0 time series also agrees seemingly well with the hydrometeor classification that tends to identify aggregates in regions where D_0 is larger (with, for example, the same fall streak around 15:10 UTC).

The β_a exponent of the area–size relation is smaller when $Z_{e,X}$ and DFR are low, which is compatible with small non-disk-like particles such as columnar crystals, while larger values could indicate aggregates or rimed snowflakes.

Somewhat more noisy are the mass–size exponent b_m and the aspect ratio A_r, although their values and spatial trends still seem reasonable. They are rather correlated, which is not unrealistic: particles with an aspect ratio near 1 are rounder and thus closer to spheres, which in turn, have a b_m close to 3. Indications of riming in the hydrometeor classification (visible as yellowish-red regions) roughly correspond to regions with larger A_r and b_m, as expected from rimed particles (e.g., 15:10 between 0.5 and 1 km, 15:50 between 0 and 1.5 km, 16:00 around 1 km). Additionally, small values of b_m and A_r are retrieved near cloud top, consistent with pristine crystals, while fall streaks where high D_0 values point to aggregation (15:00 to 15:20) also have medium-high b_m and A_r. A few time steps stand out with large values of A_r and b_m, coinciding with regions where large SW and variable MDV suggest strong turbulence (16:00, 1 km). In such high-turbulence cases, the retrieval cannot be expected to perform perfectly as the shape of the spectra is then largely dominated by turbulent broadening.

Let us add a few words about correlations between certain variables. As mentioned before, some expected consistent behaviors are observed in the retrieval like the apparent correlation between b_m and A_r, or between D_0 and β_a. This is not in any way enforced by the pipeline, since those variables are prescribed independently when generating the training set. The situation is different with the correlations between a_m and b_m (and α_a and β_a), which are also expected: when building the training set (see Sect. 4.4.1), these variables were sampled in a correlated way—with some noise included—to avoid completely unrealistic combinations, and this may therefore influence the retrieval. However, the correlation between these variables is not explicitly enforced during the training of the encoder: it is therefore reassuring to see that the model output still follows the expected behavior.

5.4.2 Other retrieved variables

In addition to the microphysical descriptors, the latent features comprise other quantities which are required by the pipeline in order to reconstruct the spectrograms (Table 4.1). These are not designed to serve a proper physical interpretation, but their behavior should still be assessed. The noise level is only related to instrument properties and range, and not to microphysical or atmospheric processes. As visible in Figs. 5.2a and b, the noise level estimates are exactly what could be expected and reflect the evolution of the radar sensitivity with range. At W-band, the abrupt change of sensitivity around 900 m range is due to the change of chirp. Some artifacts are visible (Fig. 5.2b, 16:00 at 1 km), in the same regions of Fig. 5.1 where the other retrieved values visually also appeared less reliable. This is likely related to the presence of strong turbulence in these areas, which can be expected to affect the retrieval accuracy.
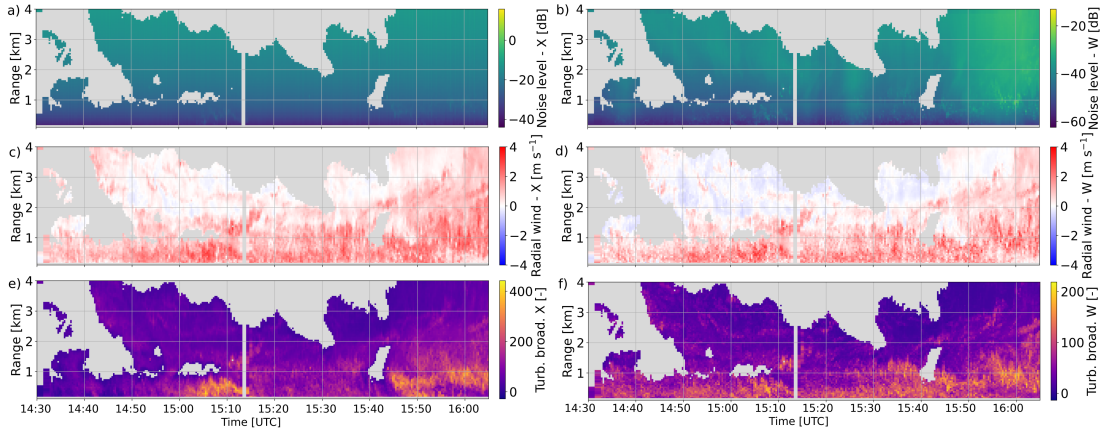
Figure 5.2: Height–time plot of additional retrieved variables: Noise level at (a) X- and (b) W-band; Radial wind at (c) X- and (d) W-band; Broadening at (e) X- and (f) W-band. Note that different colorbars are used in panels (a) and (b), and in panels (e) and (f).

The radial wind estimates serve to artificially correct for shifts of the Doppler spectra caused either by vertical wind (up- or downdrafts), by contamination due to horizontal wind in the case of imperfectly vertical radar beams, or by biases in the velocity–size relation of the forward model. Their interpretation as a physical atmospheric quantity should be avoided. However, it is rather reassuring to see in Fig. 5.2c and d that the X- and W-band radial winds have a satisfactory cofluctuation: the opposite would be a problem since the MDV time series of both radars are rather similar (not shown). Likewise, the broadening parameters are similar in X- and W-band, and also somewhat follow SW (Fig. 5.1d). We recall that the broadening parameters are not expressed in physical units, but as the size of the Gaussian kernel that results in the observed broadening; they include all the broadening causes (not just turbulence, but also e.g., horizontal wind) and are rather a side product of our retrieval than descriptors of actual atmospheric dynamics. Nonetheless, a reasonable agreement is found (not shown) when comparing these values to broadening estimates derived through classical methods (*Borque et al.*, 2016; *Shupe et al.*, 2008), which rely on the temporal variations of MDV and on wind profiles.

5.5 Comparison to in situ data

In this section, we take a step further in the evaluation of the retrieval by performing quantitative comparisons with airborne in situ measurements.

5.5.1 Ice water content

Figure 5.3 illustrates the retrieval results of ice water content in comparison with in situ estimates. The IWC time series are displayed, first as a height–time plot to which the aircraft trajectory is added (Fig. 5.3a), then along the aircraft trajectory to which retrieval outputs are overlaid at time steps of overpasses (Fig. 5.3b). The comparison is overall good, with satisfactory cofluctuations as well as reasonable quantitative agreement. For reference, we also display IWC_{RASTA} (*Delanoë et al.*, 2007, see Sect. 5.3), which appears to fluctuate slightly more.
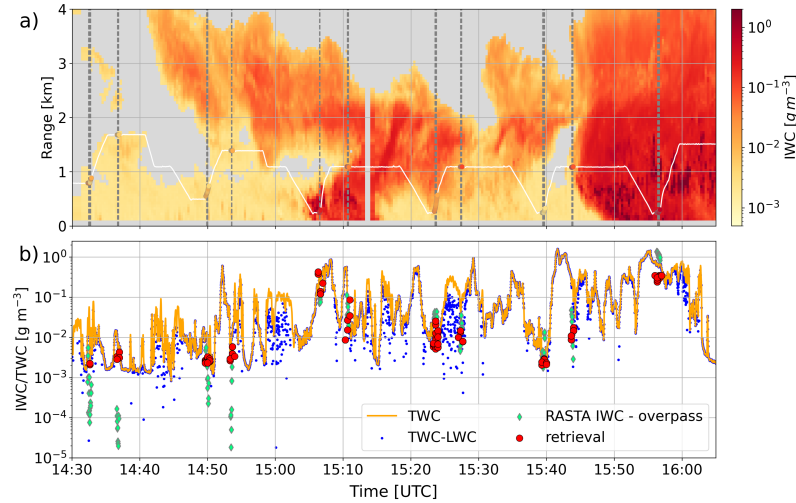
Figure 5.3: (a) Height–time plot of IWC retrieval, to which the aircraft trajectory is overlaid (altitude as a function of time); aircraft IWC values at time steps of aircraft overpasses (horizontal distance smaller than 1 km) are shown as scattered points with the same colormap. Dashed vertical lines indicate when the aircraft is within 500 m of horizontal distance to the radars. (b) Time series of water content measured by the aircraft (TWC and TWC − LWC) and overlaid radar retrieval.

In Fig. 5.4a, the scatterplot of retrieved vs. measured IWC combines the results from the three flights; the points are color-coded with $Z_{e,X}$ to illustrate that large IWC corresponds to large reflectivity, as expected and already noted in the qualitative analysis. The error bars illustrate the ensemble spread (standard deviation) of the retrieval realizations as described in Sect. 4.5.3. This scatterplot confirms the robustness of the retrieval results and their good correlation to the measured IWC ($R = 0.87$ in logarithmic scale), with, however, the existence of a slight bias toward low values (-0.19 in logarithmic scale). Surely, the spread of the values remains substantial, but it should be kept in mind that, even at times of overpasses, the aircraft is not perfectly collocated with the radar measurements, and that the sampled volumes are

not identical: the radar resolution volume is of the order of $10^3 - 10^4$ m^3, while the aircraft sampling volume is around 10^{-2} m^3.
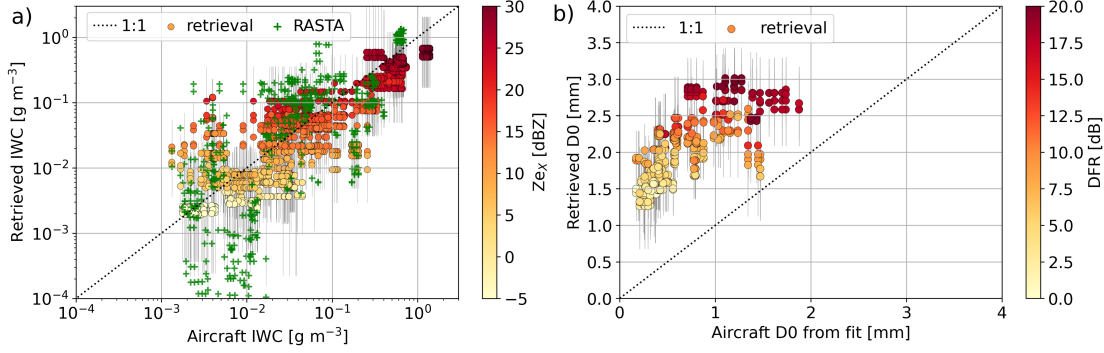
Figure 5.4: Scatter plots of retrieved vs. aircraft measurement of (a) IWC and (b) size parameter D_0. Each point corresponds to a time step when the aircraft is within 1 km horizontal distance to the radars. Three flights are used (22, 23, and 27 January). The color indicates corresponding (a) $Z_{e,X}$ and (b) DFR. The black vertical lines indicate the standard deviation of the retrieval ensemble.

5.5.2   Size parameter D_0

Aircraft measurements do not provide a variable that can directly be compared to the D_0 retrieved through our method. Hence, we use the values of D_0 derived from the exponential fit of the in situ PSDs (Sect. 5.3). In order to monitor the validity of this approach, the correlation coefficients of the fits are also included in the time series, and are typically very high (often $R^2 > 0.9$, Fig. 5.5b). Our retrieval is superimposed to the time series in Fig. 5.5, and compared to the in situ values in Fig. 5.4b using all available flights. While this was not perceptible in the qualitative analysis, D_0 retrievals actually show a strong bias (+1.3 mm) when compared to aircraft measurements, leading to an overestimation of particle size. Possible causes for this behavior are investigated in Section 5.6. This being noted, the cofluctuation between retrieved and in situ D_0 is nonetheless good (R = 0.74), which gives confidence that the retrieval is still appropriate for process-oriented studies: there, even more than the actual values, the changes and evolution of particle size can indicate the occurrence of specific snowfall growth or decay mechanisms.
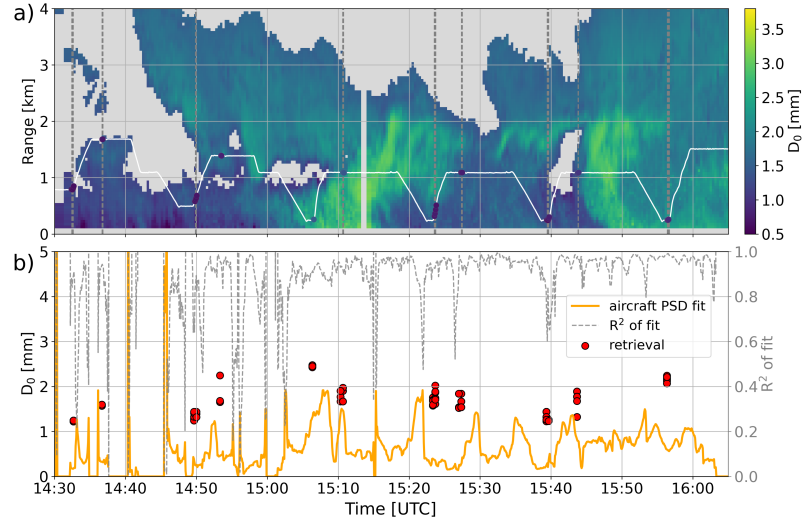
Figure 5.5: As for 5.3, but for D_0. (b) also includes R^2 from the exponential fit to the aircraft PSD.

5.5.3   Mass–size and area–size relations

Mass–size and area–size power law coefficients are explicitly computed from the aircraft measurements and can therefore be compared to our retrieval. However, the time series of these aircraft quantities are highly noisy and thus point-to-point comparisons did not appear meaningful; it was therefore preferred to perform a statistical analysis. We thus compare the histogram of b_m (resp. β_a) estimated from aircraft observations during each flight (except for the part of the flight to and from the campaign location), to the histogram of retrieved b_m (resp. β_a) above the radars, during the time frame of the flights and in the altitude range sampled by the aircraft, which excludes, for instance, regions near cloud top.
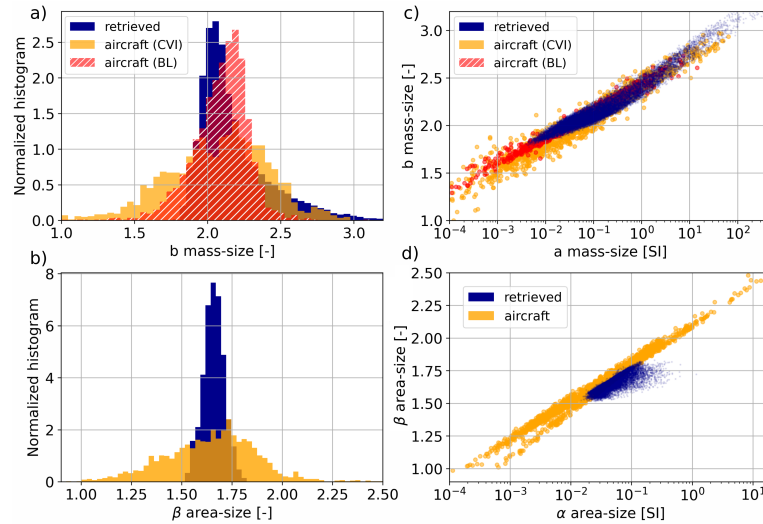
Figure 5.6: Histograms of (a) mass–size and (b) area–size exponents. Scatter plots of (c) mass–size and (d) area–size exponent to prefactor, from retrieval and aircraft measurements (Sect. 5.3)

The histograms of b_m agree rather well (Fig. 5.6a), with a similar mode around 2.2, although fewer values below 2 are retrieved from the radar measurements. In Fig. 5.6b, the histograms again have relatively close peak values (around 1.6 for the retrieval and 1.7 for the aircraft). There however, and for b_m to a lesser extent, the histogram of retrieved values is much narrower than the aircraft one. This is not too surprising, given the noisiness of the aircraft measurements and considering that the volume sampled by the PIP and 2D-S probes is much smaller than the radar volume—which automatically increases the variability and flattens the distribution. With this in mind, these histograms support a rather good consistency of the retrieval with the aircraft measurements. In addition, we verify that the relations between a_m and b_m (resp. α_a–β_a), retrieved and measured, are consistent: this is visible in Fig. 5.6c (resp. d), where the scatter plots of a_m vs. b_m (resp. α_a vs. β_a) are overlaid. Although not perfect, the match is reasonable. Let us highlight that once again, retrieved β_a values are narrower, consistent with the histograms.

5.5.4 Aspect ratio

The last microphysical variable for which we can perform a comparison is the mean aspect ratio: similarly to the mass–size exponent, Fig. 5.7a displays the histogram of retrieved and aircraft values. A significant difference is visible in the modes, with the aircraft values around 0.45 and the retrieval mode around 0.6; this, however, is consistent with the difference in the definitions of aspect ratio in each case. We recall that the aspect ratio retrieved through our pipeline is $A_{r,v}$ defined as the ratio of particle dimension along the vertical to maximum dimension, whereas the aircraft measurement is $A_{r,\perp}$, the ratio of minor axis length to maximum dimension. Relating both quantities is not directly possible without having additional information on particle orientation, but an intuition can be gained from Fig. 5.7b, where the relation between $A_{r,v}$ and $A_{r,\perp}$ is shown for particles randomly oriented within a certain angle (90° corresponds to completely random orientation). Using the relations of Fig. 5.7b, a transformed histogram is included in Fig. 5.7a, showing the equivalent aircraft $A_{r,v}$ assuming ellipsoidal particles with random orientation within 75°: it fits rather well with the retrieval. While this is not per se rigorous, it gives a qualitative understanding of the observed discrepancy.
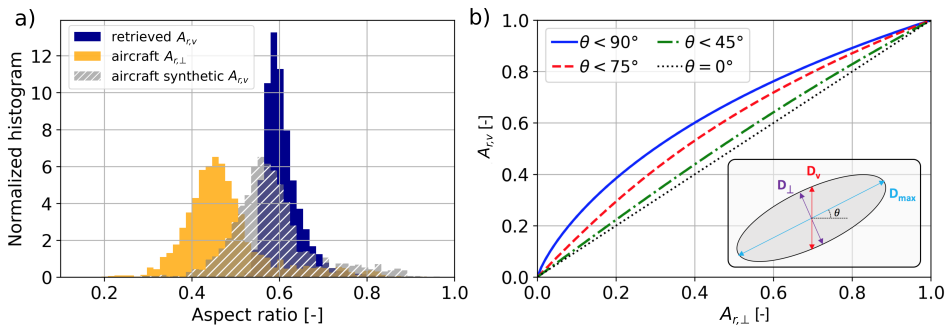
Figure 5.7: (a) Histogram of retrieved and aircraft-measured aspect ratio. (b) Illustration of the relation between $A_{r,\perp}$ and $A_{r,v}$ for particles with random orientation within a given angle θ; the various quantities are sketched in the bottom right of panel (b).

Note that the aspect ratio values derived from the in situ images are themselves bias-prone, due to the projection of three-dimensional particles in a two-dimensional space (*Jiang et al.*, 2017). This bias would, however, be opposite to what is observed here, and is likely not dominant in our study. Another element to consider is that aspect ratio is assumed to be the same across the particle size distribution, which may well be an oversimplification; in particular, smaller particles may have smaller aspect ratios than aggregates, which would affect the aircraft-derived quantity differently than the radar-based estimate.

5.6 Discussion

While the results are overall encouraging, the previous section highlighted some points that call for further discussion. This section investigates the sensitivity of the pipeline to certain key hypotheses and, in particular, identifies possible causes for the D_0 bias.

5.6.1 Sensitivity to miscalibration and differential attenuation

One limitation of our framework is that it requires a good calibration of the radars, both absolute and relative, as well as an independent correction of attenuation. As detailed in Sect. 4.4.2, the issue of attenuation was tackled by implementing a correction of W-band reflectivity based on estimates of gaseous, snowfall and liquid water attenuation. This correction method is, however, error-prone, and we cannot exclude that reflectivity biases are present in the data. The presence of supercooled liquid water cloud layers or wet snow can be particularly difficult to identify and quantify, while attenuating strongly millimeter-wavelength signal (with e.g., path-integrated attenuation up to 5 dB for a liquid water path of 500 g m^{-2}, *Kneifel et al.*, 2015). To assess the possible impact of inaccurate calibration or attenuation correction on the retrieval, we investigate its sensitivity to reflectivity offsets, both absolute and relative.

Fig. 5.8 shows the mean bias of retrieved IWC and D_0, computed as the mean difference between retrieved values and aircraft measurements, when a constant offset in reflectivity is added to the input X- and W-band spectrograms. The following behavior is observed, in accordance with previous qualitative observations: IWC is especially sensitive to X-band reflectivity (as illustrated in Fig. 5.8b and by the rather horizontal color gradient in Fig. 5.8a). Rather, D_0 is more sensitive to differential offset, i.e., to changes in DFR (as illustrated in Fig. 5.8d and by the rather diagonal color gradient in Fig. 5.8c).

While this Z_e calibration is undoubtedly a key factor in the uncertainty of the algorithm, it does not appear to cause extreme divergence in the retrieval: the changes in D_0 and IWC shown in Fig. 5.8, while not negligible, are also not massive. In particular, Z_e miscalibration solely could not explain the observed D_0 discrepancy: changing the DFR of -6 dB only brings down the bias from 1.3 mm to around 1.0 mm.
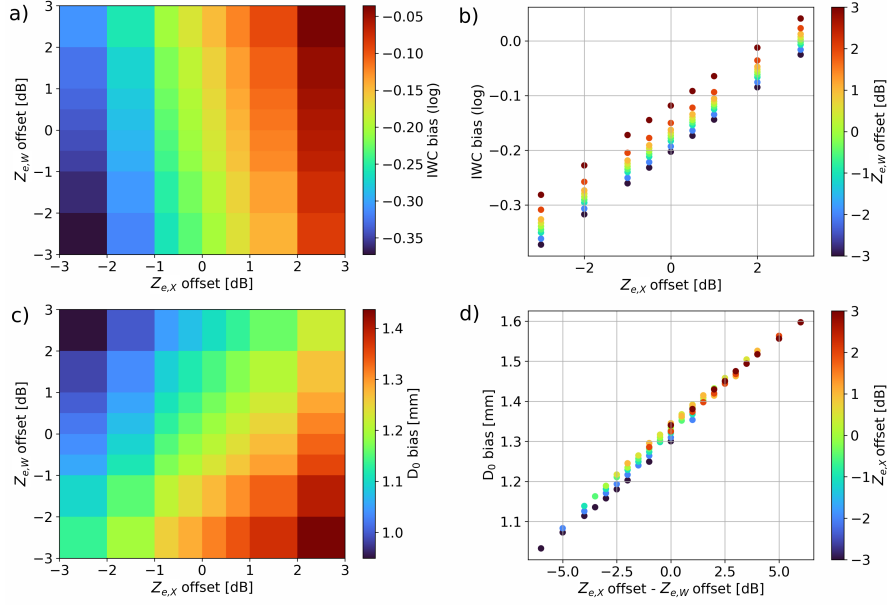
Figure 5.8: (a) Heat map of IWC bias as a function of X- and W-band Z_e offset; the bias is computed using the aircraft values as reference. (b) Different visualization showing IWC bias as a function of $Z_{e,X}$ offset. (c) As for panel (a) but for D_0. (d) As for panel (b) but for D_0 bias as a function of DFR offset.

We note (not shown) that shifting the spectra by constant or relative velocity offsets, to mimic one of the effects of radar mispointing, only minimally affects the retrieval of microphysical properties, and mostly translates into changes in the retrieved radial wind.

5.6.2 Training set limitations

Another aspect of our framework that could cause a bias in the retrieval is if the training set is too narrow. While special attention was paid to this potential issue as the microphysical parameters were sampled from the MASC database, there is likely still room for improvement. In particular, the size cutoff for good-quality images in the MASC is quite high and very few particles with a diameter below 0.5 mm are accurately captured. For reference, Fig. 5.9 illustrates the histogram of D_0 derived from MASC measurements (*Grazioli et al.*, 2022) and by the aircraft 2D-S and PIP probes during the ICE GENESIS campaign. The limitation is apparent: the aircraft is able to capture much smaller particles, but not beyond a certain size, while the MASC can detect large snowflakes but very few small particles. Along the same line, we underline that the MASC can only provide observations of precipitating particles at the ground level; although the instrument was deployed in numerous locations and temperature ranges, it may not be sufficient to capture the full spectrum of in-cloud microphysical properties. The framework would thus probably benefit from training the decoder on a larger dataset, that includes a better representation of this smaller particle range. It is yet unlikely that this will entirely resolve the size bias, for there is still an overlap between the aircraft-measured size range and that on which the model was trained.
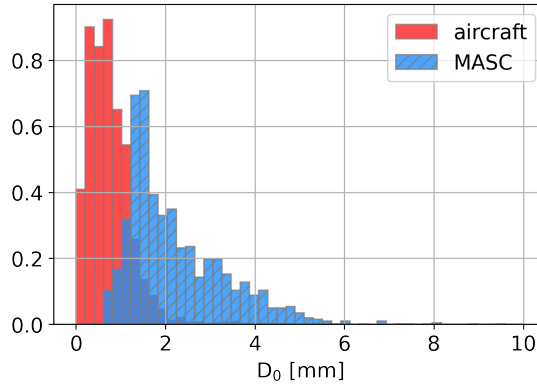
Figure 5.9: Histogram of D_0 from aircraft measurements during ICE GENESIS (red) and from MASC measurements (MASCDB).

5.6.3 Scattering model

Surely one of the strongest hypotheses on which the pipeline was built is the parameterization of the scattering model in forward simulations. As explained in Sect. 4.4.1, the default version of PAMTRA was used which to this date (28/01/2023) assumes constant values for certain parameters of the SSRGA, and allows changing two coefficients (κ_{SSRGA} and β_{SSRGA}, see *Hogan and Westbrook*, 2014 and online documentation, *Mech et al.*, 2015). Several studies suggest that more parameters are in fact needed and that their values can vary significantly (e.g., *Leinonen et al.*, 2018; *Ori et al.*, 2021) depending on particle type and shape, among others.

To get an empirical sense of how this could affect the retrieval, the approach described hereafter was followed. First, a few time and range gates were randomly selected from the dataset. The corresponding retrieved values were then modified by adding a D_0 offset ranging from -1.5 to +2 mm, and PAMTRA simulations were run on the microphysical parameters obtained (using the same settings as in Sect. 4.4.1). Parallel to that, the PAMTRA code was slightly adjusted to allow for modification of the four literature coefficients of the self-similar Rayleigh–Gans approximation (κ_{SSRGA}, β_{SSRGA}, γ_{SSRGA}, ζ_{SSRGA}); new simulations were run for the selected time and range gates, keeping the retrieved microphysics unchanged but randomly changing the SSRGA parameters within ±10% of their original values. As seen in Sect. 4.4.1, this is well within the typical variability of the coefficients calculated from simulating various types of particles. The influence of modifications of (i) D_0 and (ii) SRRGA coefficients was measured by the change in the (total) dual-frequency ratio. The obtained results are illustrated in Fig. 5.10 (see details in the caption): they suggest that moderate changes in the SSRGA parameters could have an impact similar to varying the size parameter by approximately 1 mm (-0.6 to +1.5 mm), which is a significant change. Taking this investigation a step further, the influence of each of the four parameters can be computed independently by following the same steps but modifying only one coefficient: it appears that the output is most sensitive to β_{SSRGA} and γ_{SSRGA}, which each cause amplitude changes corresponding to ΔD_0 of at least

±0.4 mm. Obviously, this empirical analysis cannot be directly translated into a quantitative interpretation, yet it highlights that the scattering model can have a substantial influence on the retrieval. This leads us to believe that the D_0 bias observed when comparing our retrieval to aircraft measurements is partly caused by an inaccurate or insufficient parameterization of the radiative transfer model. In order to remedy this effect, a forward model with a more subtle parameterization is likely required when designing the decoder training set; a more accurate description could be obtained by using, for instance, pre-computed databases of scattering properties calculated based on the DDA (e.g., *Kuo et al.*, 2016; *Lu et al.*, 2016).
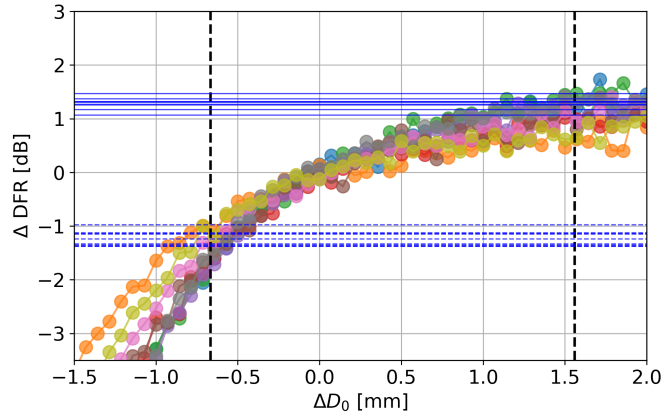
Figure 5.10: Colored lines with scattered points: ΔDFR caused by adding a diameter offset ΔD_0 on microphysical descriptors of selected (time, range) gates. Horizontal lines: for each of these (time,range) gates, maximum ΔDFR (positive and negative) caused by a modification of the SSRGA coefficients within ±10%. For each selected (time,range) gates, the intersection of the horizontal and colored lines gives a ΔD_0 value which causes the same change in DFR as a change in SSRGA coefficients (worst case). Dashed vertical lines show the mean of these ΔD_0 values.

5.6.4   Shape of the particle size distribution

Another underlying hypothesis that was made when designing the pipeline and defining the set of microphysical descriptors was to consider only exponential PSDs. This choice was made to keep a minimal number of retrieved parameters at this stage. Yet, it is known that multi-frequency signatures, on the one hand, and Doppler spectra, on the other hand, are both affected by PSD shape (e.g., *Mason et al.*, 2019; *Barrett et al.*, 2019, respectively). Here, we conduct a similar analysis as in the previous subsection: this time, since changes in the PSD shape mostly influence the shape of the spectrum, we focus on the skewness of the W-band spectrum (instead of the DFR) as a metric to understand how modifying the shape of the PSD could influence the retrieval. A gamma distribution was assumed ($N(D) = N_0 D^\mu \exp(-D/D_1)$, e.g., *Petty and Huang*, 2011), constraining D_1 by keeping the effective diameter constant ($D_{eff} = 3D_0$) and varying the shape parameter μ in the range [-2, +5] as observed in snowfall (*Mason et al.*, 2019). Figure 5.11 illustrates that changes in the PSD shape may have a similar effect on W-band spectrum skewness as varying D_0 of approximately 1 mm (-0.9 to +1.5 mm). Here again, this observation is mainly qualitative and cannot be directly used to quantify the

influence of PSD shape on the retrieved microphysical descriptors, but it does underline that considering more complex distributions would be necessary to further refine the framework, and that the assumption of an exponential behavior may also have a role in the observed D_0 bias.
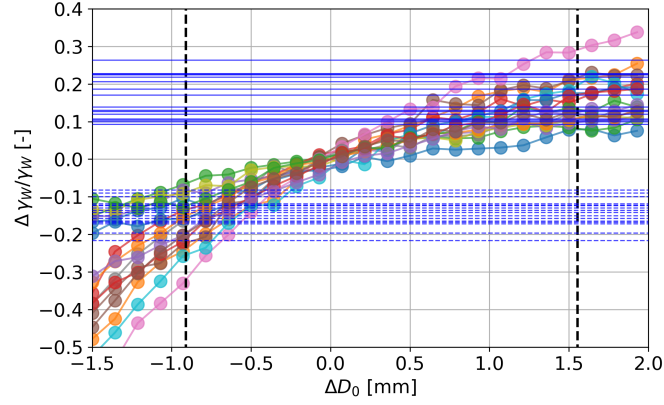
Figure 5.11: Colored lines with scattered points: relative change in W-band skewness γ_W ($\Delta\gamma_W/\gamma_W$) caused by adding a diameter offset ΔD_0 on microphysical descriptors of selected (time, range) gates, if assuming an exponential PSD. Horizontal lines: for each of these (time,range) gates, maximum relative change in γ_W caused by a modification of the PSD shape (assumed a gamma distribution, μ in the range [-2, +5]); the maximum relative increase (resp. decrease) in skewness, in full line (resp. dashed) is consistently obtained for $\mu = 5$ (resp. $\mu = -2$). For each selected (time,range) gate, the intersection of the horizontal and colored lines gives a ΔD_0 value which causes the same relative change in γ_W as a change in PSD shape (worst case). Dashed vertical lines show the mean of these ΔD_0 values.

In addition to these important hypotheses—SSRGA scattering model and assumption of exponential size distributions—we recall that other modeling choices were made during the design of the synthetic dataset and the underlying physical framework, such as assumptions on particle orientation and velocity–size relation, among others (see Sect. 4.4.1). These are inevitably a simplification of the physical reality and may thus also influence the retrieval. Another point should be briefly mentioned regarding small particles, which are Rayleigh scatterers at both X- and W-band. This means that, if a population is composed entirely of small particles, the influence of particle size and number concentration is hardly distinguishable in the spectrograms. The ill-posedness of the problem is reinforced and the retrieval could be expected to have a reduced accuracy, even if the training set and scattering model were improved.

5.7 Snowfall microphysical properties during ICE GENESIS

Having in mind the encouraging results as well as the limitations of the retrieval, and being aware of how its output may be affected by residual underlying assumptions, we now focus on the results obtained on the ICE GENESIS dataset. Specifically, we take a closer look at the microphysical properties retrieved during the ~45 hours of available spectral dual-frequency measurements in precipitation (from 22 to 27 January). Note that the estimation of snowfall microphysical properties from cloud to ground, thanks to this radar-based retrieval, was relevant to the ICE GENESIS project as it complements the more detailed, but much sparser, aircraft in situ measurements. Figure 5.12 illustrates the time series on which the algorithm is run and the retrieved IWC. As detailed in Chapter 2, a succession of precipitation events were observed, with varying intensity (visible in $Z_{e,X}$), duration (widespread precipitation or showers), and vertical structure (with echo top ranging from ~1 km to 5 km above ground).
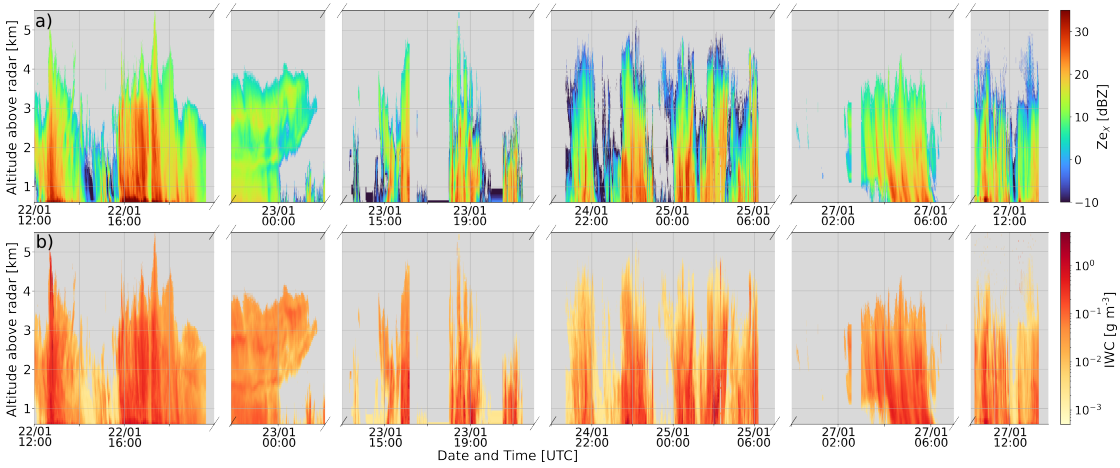
Figure 5.12: Height–time plots of (a) $Z_{e,X}$ and (b) retrieved IWC during the precipitation events on which the retrieval was implemented.

In Fig. 5.13, we analyze in bulk the retrieved microphysical descriptors, first by considering their distribution in altitude (panels a–e), then as a function of temperature T (panels f–j). For the latter, temperature profiles over la Chaux-de-Fonds were extracted from COSMO-1 analyses run by MeteoSwiss at an hourly resolution. The 2-dimensional histograms shown in these plots rely on all the available retrieved values (corresponding to the time series of Fig. 5.12). For consistency with expected values, D_0 was corrected using the bias computed from the comparisons with in situ measurements (1.3 mm, Sect. 5.5); this is mainly for illustrative purposes. We highlight that this statistical analysis of microphysical properties during ICE GENESIS can only point to some basic trends; in reality, these properties result from production, growth and decay processes that depend on the large-scale and mesoscale features of the precipitating system (such as the vertical extent and structure of the cloud, the moisture level, the availability of SLW, among others), which may vary significantly between events as seen in Fig. 5.12. The lowest range gates (500 m above ground) were excluded, as frequently contaminated by enhanced near-ground turbulent broadening.
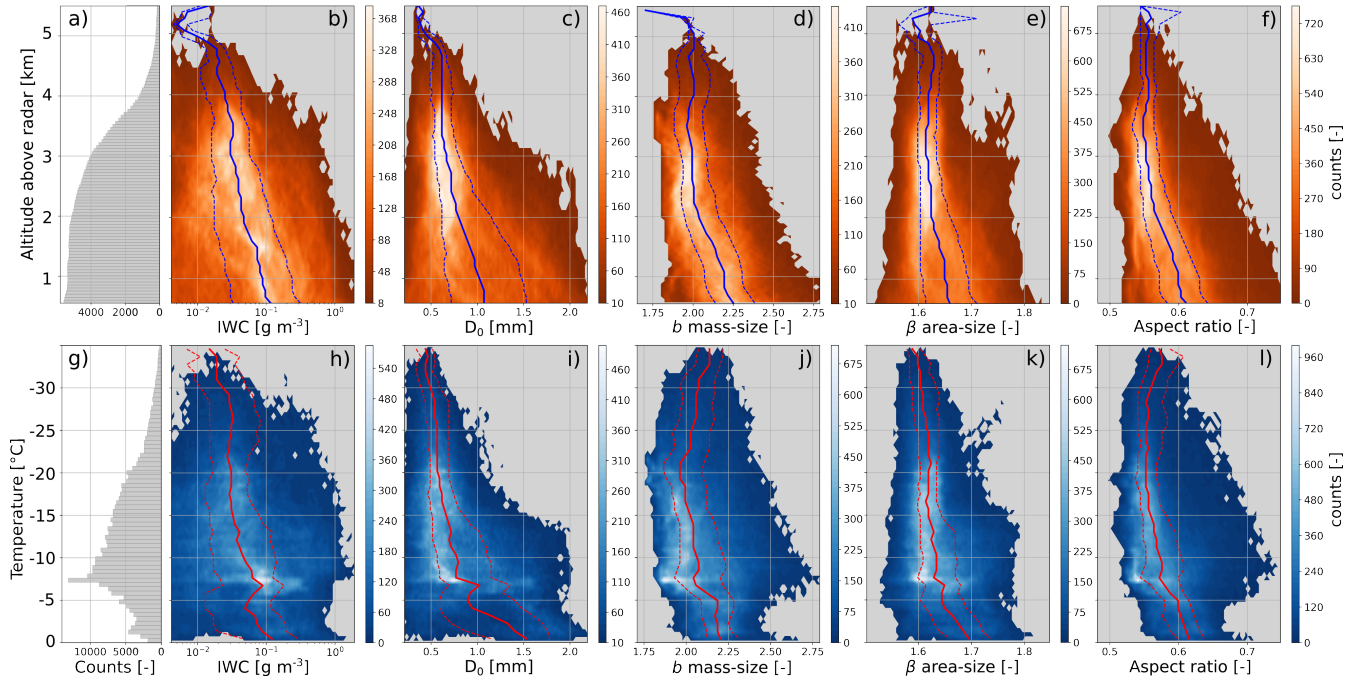
Figure 5.13: (a) Distribution of range gates with valid precipitation signal in the dataset; (g) Distribution of temperatures in the range gates with precipitation signal. Statistics of retrieved microphysical properties, in the form of 2-dimensional density plots; (b)–(f), as a function of range; (h)–(l), as a function of temperature (values from COSMO-1 analyses). Full lines indicate the median values in a given altitude or temperature bin; dashed lines show the 25% and 75% quantiles. D_0 values were corrected with a 1.3 mm offset.

In terms of general behavior, we note a smooth increase of IWC downwards (Fig. 5.13b), which reflects the expected growth of snow particles as they settle, either by vapor deposition or riming. Although sublimation is possible during snowfall events, it is unlikely to always take place at the same altitude (at least in terrains like the Jura) and thus would not be visible in those statistics. In terms of temperature, a similar trend is observed, with IWC increasing quite regularly with T; note that the irregular feature around -7°C, also visible in other variables, is related to the distribution of temperatures in the (time, range) gates studied (Fig. 5.13g), and does not reflect a microphysical mechanism.

The characteristic size D_0 also has a trend that increases downward (Fig. 5.13c), again compatible with the classic snowfall growth processes, although less smoothly than IWC. Comparing density plots of IWC and D_0 as a function of temperature (Fig. 5.13h and i) may give some intuition on this point. While IWC increases relatively smoothly with temperature, D_0 grows only slightly at low temperatures, with a more significant enhancement around -15°C. This is especially visible in the interquartile range and in the 75% quantile (which increases from 0.75 mm around -17°C to 1.25 mm around -13°C) and in the heat map itself, where large values around 2 mm are only present below the -15°C isotherm. We suggest that this effect is related to dendritic growth occurring around these temperatures (in saturated conditions), which is in turn favorable for the formation of aggregates (see Chapter 1). Aggregation alone does not

lead to an augmentation of IWC, but of the particle sizes; this could explain the significant increase of D_0, with only mild gain in IWC, in this temperature range. Another rapid increase of D_0 occurs at temperatures above -5°C, which can again be attributed to the highly efficient aggregation in this warmer range (*Hobbs et al.*, 1974).

When taking a closer look at the other variables, one can see that the fractal dimension b_m has a relatively low dependence on temperature, but still tends to increase with increasing temperature, and more visibly with decreasing altitude, especially below 2 km above ground (Fig. 5.13d, j). The aspect ratio behaves similarly, in a slightly more correlated way with altitude and temperature, with rounder particles retrieved at lower altitudes (higher temperatures), which is compatible with aggregation and riming processes (Fig. 5.13f, l). The latter, while not strictly confined to a precise temperature range, is mostly expected at relatively mild temperatures, where mixed-phase conditions are more frequent (e.g., LWC inflexion around -18°C in *Korolev et al.*, 2003; < 10% of clouds containing liquid droplets for T< −20°C in *Hogan and Kew*, 2005). Riming might be responsible for a minor inflexion of b_m and A_r around -20°C (Fig. 5.13h and j); another increase slightly above -15°C, and again around -5°C, could be due to aggregation. It is not certain that the slightly decreasing trend of b_m (and to a lesser extent of A_r) from -35 to -20°C is statistically significant, given that fewer data come from this temperature range. Nonetheless, pure depositional growth may result in such a signature: at very cold temperatures, vapor deposition is not very efficient (cf. slow increase of D_0), leading to particles which are less elongated—if growing in a columnar direction—and less extended in the planar directions—if they grow as planar crystals—than at warmer temperatures, and therefore more sphere-like (higher b_m). As temperature increases, a possibly higher atmospheric vapor content allows for more active depositional growth of crystals into oblate or prolate shapes, depending on the growth direction.

Finally, the behavior of the area–size exponent β_a with altitude and temperature can be summarized as follows (Fig. 5.13e, k): it is relatively constant and shows little spread at low temperatures (high altitudes); a slight increase is noted for $T > −20$°C which may correspond to occasional riming, and another enhancement is visible at the aggregation temperatures (-15 and -5°C levels).

Note that these interpretations are based solely on a few snowfall events of the time-restricted ICE GENESIS dataset and should therefore not be directly generalized. The implementation of the algorithm on lengthier and possibly more diverse datasets would eventually allow to support this analysis in a more robust way.

5.8 Conclusions

The algorithm introduced in Chapter 4 could be assessed thoroughly by confronting the retrieved quantities to in situ aircraft measurements which were conducted during the 2021 ICE GENESIS campaign. Overall, the comparisons with in situ data are highly encouraging and support the validity of the framework, as good cofluctuations and similar statistics are reported. Certain discrepancies were nonetheless observed: in particular, the retrieved values of the size parameters are affected by a bias (+1.3 mm), for which possible explanations were proposed. They point to limitations in the training set itself (in which small particles are under-represented) and to assumptions in the scattering model (which relies on the SSRGA) or the parameterization of the PSD (as an exponential distribution). These analyses open up for possible improvements of the retrieval, particularly along the line of radiative transfer modeling.

Meanwhile, in spite of these limitations, the method can provide relevant insights into snowfall properties from the perspective of process-oriented studies whose focus is typically the relative spatial and temporal evolution of microphysical variables, rather than their exact numerical values. Building up on this, we analyzed the results of the retrieval on 45 hours of precipitation collected during ICE GENESIS. Rough trends were described that are consistent with the occurrence of distinct snowfall growth processes (depositional growth, riming, aggregation) in certain altitude or temperature ranges during the campaign.

The approach could potentially be extended to retrieve other variables and further alleviate the baseline microphysical assumptions. For instance, the restrictive hypothesis of exponential PSDs, whose limitations were discussed in Sect. 5.6.4, could be relaxed by considering gamma or modified gamma distributions and retrieving their additional shape parameter(s). A retrieval of the scattering coefficients themselves could eventually be considered; alternatively, more accurate scattering calculations based on the DDA may be used when building the training dataset. We also recalled that one drawback of the algorithm in its current state is that it relies on attenuation-corrected data. Future improvements of the method could include the retrieval of an attenuation profile, used to correct the spectrograms within the pipeline itself in a recursive way.

It should be kept in mind that the addition of new parameters increases the computational cost of the algorithm but also its ill-posedness, and that two-frequency Doppler spectrograms may not be sufficient to resolve it. Given the convincing results obtained recently with triple-frequency data (such as the retrieval of snowfall properties from triple-frequency radar moments proposed in *Mróz et al.* (2021a), or studies of *Mróz et al.* (2021b), and *von Terzi et al.* (2022) where triple-frequency spectra are used to study the melting and dendritic growth layers, respectively), it is likely that our method would gain in robustness and precision were a third frequency to be included. Further extensions could also incorporate spectral polarimetric variables, which could help retrieve more accurately certain geometrical properties of the hydrometeors.

The theoretical pipeline itself is an important contribution of this work, for it can be implemented in other settings and for different types of inverse problems. One fundamental difficulty of such problems is often their ill-posedness: several combinations of physical parameters can yield similar observations. The proposed approach mitigates this by learning information from the spatial structure of the data thanks to convolutional neural networks.

6 Distinct secondary ice production processes observed in radar Doppler spectra: insights from a case study

This chapter presents a case study of the ICE GENESIS campaign, where signs of secondary ice production are analyzed with Doppler spectral and dual-frequency radar measurements. The text is adapted from the submitted manuscript:

- **Anne-Claire Billault-Roux**, Paraskevi Georgakaki, Josué Gehring, Louis Jaffeux, Alfons Schwarzenboeck, Pierre Coutris, Athanasios Nenes, Alexis Berne (2023): Distinct secondary ice production processes observed in radar Doppler spectra: insights from a case study. *Under review for Atmospheric Chemistry and Physics*, doi: 10.5194/egusphere-2023-478.

The processing and analysis of the radar measurements were performed by Anne-Claire Billault-Roux with input and supervision from Alexis Berne. Josué Gehring provided valuable insights in the analysis of the synoptic context. Paraskevi Georgakaki conducted the WRF simulations with input from Athanasios Nenes. Louis Jaffeux, Pierre Coutris and Alfons Schwarzenboeck processed and analyzed the aircraft observations.

6.1 Summary

Secondary ice production (SIP), particularly within mixed-phase clouds, has an essential role in cloud and precipitation microphysics and has been the subject of active research in recent years. Substantial insights were gained by combining experimental, modeling, and observational approaches. Remote sensing instruments, and among them meteorological radars, offer the possibility to study clouds and precipitation in extended areas over long time periods, and are highly valuable to understand the spatio-temporal structure of microphysical processes. Multi-modal Doppler spectra measured by vertically-pointing radars reveal the coexistence, within a radar resolution volume, of hydrometeor populations with distinct properties; as such, they can provide decisive insight into precipitation microphysics. This chapter

leverages polarimetric radar Doppler spectra as a tool to study the microphysical processes that took place during a snowfall event on 27 January 2021, in the Swiss Jura Mountains, during the ICE GENESIS campaign. A multi-layered cloud system was present, with ice particles sedimenting through a supercooled liquid water (SLW) layer in a seeder-feeder configuration. Building on a Doppler peak detection algorithm, we implement a peak labeling procedure to identify the particle type(s) that may be present within a radar resolution volume. With this approach, we can visualize spatio-temporal features in the radar time series that point to the occurrence of distinct mechanisms at different stages of the event. By focusing on three 30-minute phases of the case study, and by using the detailed information contained in the Doppler spectra, together with dual-frequency radar measurements, aircraft in-situ images, and simulated profiles of atmospheric variables, we narrow down the possible processes which can be responsible for the observed signatures. Depending on the availability of SLW and the droplet sizes, on the temperature range, and on the interaction between the liquid and ice particles, various SIP processes are identified as plausible, with distinct fingerprints in the radar Doppler spectra. A simple modeling approach suggests that the ice crystal number concentrations likely exceed typical concentrations of ice nucleating particles by one to four orders of magnitude. While a robust proof of occurrence of a given SIP mechanism cannot be easily established, the multi-sensor data provides various independent elements each supporting the proposed interpretations.

6.2   Introduction

Mixed-phase clouds (MPCs), in which ice crystals and snow particles coexist with supercooled liquid water (SLW) droplets, have a key role in the atmosphere both in terms of their impact on the Earth's radiation budget (*McCoy et al.*, 2016; *Matus and L'Ecuyer*, 2017) and on precipitation processes (*Mülmenstädt et al.*, 2015). MPCs are intrinsically unstable structures: without a sustained source of SLW, the liquid phase tends to be depleted through the Wegener-Bergeron-Findeisen process or riming (*Korolev et al.*, 2017), leading to a full glaciation of the cloud. They are, however, very frequently observed (e.g., in the Arctic, *Intrieri et al.*, 2002, or in orographic terrain, *Lohmann et al.*, 2016) and there exist several means by which the liquid water content is sustained: frontal or orographic lifting of the air masses, for instance, are associated with vertical velocities sufficient to maintain supersaturation with respect to liquid water (*Korolev and Field*, 2008; *Georgakaki et al.*, 2021); small-scale vertical motion caused by turbulence (*Field et al.*, 2014), as well as cloud top radiative cooling (*Morrison et al.*, 2012), also enable the formation of supercooled cloud droplets.

Among the processes that occur in the mixed phase, the production of ice through secondary processes has received substantial attention in recent years. Secondary ice production (SIP) is thought to increase the ice crystal number concentration (ICNC) by up to several orders of magnitude, which impacts the phase partitioning in MPCs (*Atlas et al.*, 2020) and the resulting overall radiation budget (*Sun and Shine*, 1994; *Young et al.*, 2019) and precipitation (*Dedekind et al.*, 2021, 2023). Chapter 1, Sect. 1.2.4 listed the known SIP processes (*Field et al.*,

2016; *Korolev and Leisner*, 2020), among which three are considered as dominant: Hallett-Mossop (HM) rime splintering (*Hallett and Mossop*, 1974) active between -8°C and -3°C; droplet shattering upon freezing (*Takahashi and Yamashita*, 1977; *Phillips et al.*, 2018), which requires at least drizzle-size drops (*Wildeman et al.*, 2017; *Lauber et al.*, 2018; *Keinert et al.*, 2020; *Kleinheins et al.*, 2021); collisional breakup, facilitated in turbulent regions and in the presence of rimed particles (*Vardiman*, 1978; *Takahashi et al.*, 1995; *Schwarzenboeck et al.*, 2009; *Phillips et al.*, 2017a,b).

Proof of SIP mostly stems from in situ observations showing that measured ICNCs considerably exceed values that would result from primary ice nucleation, controlled by the concentration of active INPs (*Mossop et al.*, 1970; *Hobbs and Rangno*, 1985; *Lloyd et al.*, 2015; *Pasquier et al.*, 2022). Additional evidence was obtained in refined setups, which could verify that some snow crystals did not contain an INP (*Mignani et al.*, 2019), and must have been generated through SIP. Such measurements remain sparse and these approaches are difficult to implement for a statistical characterization of SIP processes and their spatial and temporal dynamics. By contrast, remote sensing observations, although indirect, provide invaluable complementary insight into processes occurring in the entire atmospheric column. As seen in Chapter 3 of this thesis, microwave radiometers allow estimating integrated quantities like the LWP, which is relevant to monitor the formation and evolution of MPCs (e.g., *Ramelli et al.*, 2021). Time series of radar moments can convey further information on snowfall growth and decay—through the reflectivity, Z_e—or the on occurrence of riming, visible through enhanced mean Doppler velocity (MDV). As discussed in the previous chapters, radar Doppler spectra from vertically-pointing profilers allow separating the contribution of fast- and slow-falling particles in the radar echo (e.g., *Kollias et al.*, 2002; *Luke and Kollias*, 2013; *Kneifel et al.*, 2016). Multi-modal Doppler spectra are the sign that hydrometeor populations with different microphysical properties are present in the same radar volume (*Zawadzki et al.*, 2001; *Shupe et al.*, 2004; *Kalesse et al.*, 2016). Depending on the properties of each peak (e.g., reflectivity and Doppler velocity), they may indicate that SLW droplets are present (*Kalesse et al.*, 2016), or that new ice is formed. Additional information can be leveraged, when available, from spectral polarimetric measurements through the spectral linear depolarization ratio (LDR, e.g., *Oue et al.*, 2018; *Luke et al.*, 2021). While radar measurements alone are not sufficient to actually demonstrate the occurrence of SIP, some signatures can be identified that reasonably suggest such processes (*Lauber et al.*, 2021; *Luke et al.*, 2021; *Li et al.*, 2021b).

In this study, we focus on a snowfall event that took place during the ICE GENESIS campaign on 27 January 2021, during the passage of a warm front. A seeder-feeder configuration was observed, whereby ice particles sedimented through a SLW-containing cloud layer. Doppler spectra with persistent multi-modalities extending over several kilometers were recorded, pointing to the occurrence of complex microphysical processes. This is further supported by in situ aircraft observations of ice and snow particles. An in-depth analysis of signatures in the multi-sensor data and of atmospheric profiles obtained with high-resolution numerical modeling suggests that SIP was possibly taking place through different mechanisms. The data and instrumentation are presented in Sect. 6.3, and the methods used for the analysis

of the multi-modal spectra are detailed in Sect. 6.4. An overview of the event is provided in Sect. 6.5 with the synoptic context and an outline of the main observations. We then focus (Sect. 6.6) on three time frames where different signatures are observed, for which we propose interpretations.

6.3   Data and instrumentation

In this work, multi-sensor measurements are used to investigate microphysical processes during a snowfall event of the ICE GENESIS campaign, which was presented in Chapter 2 (*Billault-Roux et al.*, 2023a). We recall that the deployment took place in La Chaux-de-Fonds (LCDF), at an altitude of 1020 m ASL which will be hereafter used as a reference: unless specified otherwise, altitudes will be expressed as a range, i.e., in m or km above ground level.

6.3.1   Ground-based remote sensing

The central instrument used in this study is the dual-polarization W-band cloud profiler WProf (see Chapter 2), whose settings were recalled in Table 4.2, Chapter 4. First moments (radar equivalent reflectivity factor $Z_{e,W}$ and mean Doppler velocity MDV) are used as well as full Doppler reflectivity spectra. The spectral slanted linear depolarization ratio (SLDR) is computed from the Doppler spectra measured in horizontal and vertical polarization and the covariance spectrum (*Galletti et al.*, 2014; *Myagkov et al.*, 2016). Note that the spectral SLDR measurements are only valid if the cross-polar component of the received signal exceeds the noise level in the corresponding channel (*Matrosov and Kropfli*, 1993; *Radenz et al.*, 2019). Attenuation due to water or snow accumulating on the radome is not considered an issue, as blowers were active during the entire measurement period, keeping the surface of the radome dry and snow-free. For this study, the W-band data that we use are otherwise not corrected for path attenuation (see further on, Sect. 6.6). In addition to the radar variables, WProf allows retrieving estimates of LWP through the brightness temperature measured by a joint 89-GHz radiometer (*Küchler et al.*, 2017; Chapter 3). As discussed in Chapter 3, the error on retrieved LWP (~18%) increases during snowfall due to the radiative contribution of snow particles to the measured brightness temperature, but general trends in LWP are nevertheless considered reliable.

In this study, we also use data from the X-band zenith profiler ROXI (*Viltard et al.*, 2019). A cross-calibration of the radars was performed using independent measurements from the scanning X-band radar MXPol, which had absolute calibration during the campaign (see Chapter 4, Sect.4.4.2, or *Billault-Roux et al.*, 2023b). X-band reflectivity ($Z_{e,X}$) values are interpolated to the time and range resolution of WProf and used for computation of the dual-frequency ratio of reflectivity (DFR).

6.3.2   In situ aircraft measurements

In situ measurements were conducted at various altitude levels by the scientific aircraft SAFIRE-ATR42, equipped with an extensive set of probes as listed in Chapter 2 and, in particular, three different optical array probes which are used in this work. The high-volume precipitation spectrometer (HVPS) (resp. precipitation imaging probe, PIP, and 2D-Stereo, 2D-S) collected images of particles with diameters ranging from 150 μm to 1.92 cm (resp. 100 μm to 6.4 mm, 10 μm to 1.28 mm). An automatic classification algorithm (*Jaffeux et al.*, 2022) allows identifying particle habits from 2D-S and PIP images. In addition, cloud liquid water content (LWC) is estimated with a cloud droplet probe (CDP-2, *Faber et al.*, 2018), which samples droplets up to 50 μm.

6.3.3   WRF model runs

Simulations of the case study were run with the Weather Research and Forecasting (WRF) model, version 4.0.1. Three two-way nested domains were used in a downscaling approach, with a horizontal resolution of respectively 12, 3, and 1 km (Fig. 6.1). The initial conditions and lateral forcing were obtained from the 6-hourly National Centers for Environmental Prediction (NCEP) Global Final Analysis (FNL) dataset at 1° × 1° grid resolution. Other static fields were obtained from default WRF pre-processing system datasets at a resolution of 30-arc-seconds for both the topography and the land use fields. A grid spacing of 97 vertical eta levels was used, with a refined resolution of ~100 m up to mid-troposphere, following *Vignon et al.* (2021).
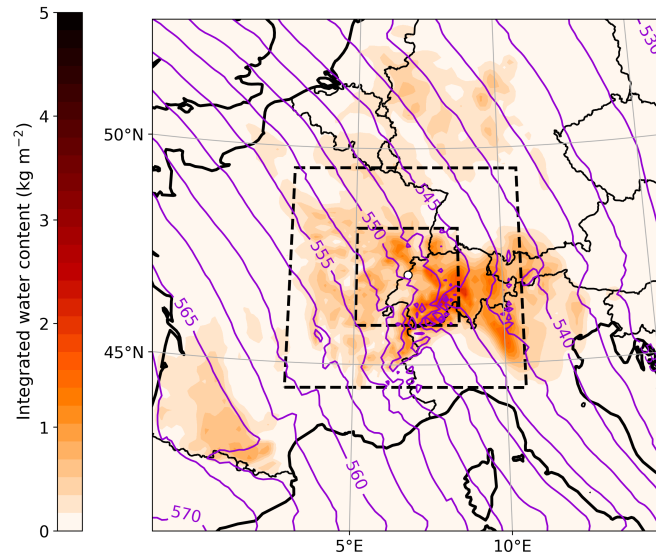
Figure 6.1: WRF simulations of vertically-integrated water content, with geopotential height at 500 hPa (contours; unit: dam) at 12 UTC on 27 January. The white dot indicates LCDF. The dashed boxes show the nested domains.

The double-moment microphysical scheme of *Morrison et al.* (2005) (M05) was employed, following the implementation of *Georgakaki et al.* (2022) (control run in the latter study). As the cloud droplets are represented with a single-moment approach in the M05 scheme, a constant droplet number concentration has to be considered. Here we set it to 50 cm^{-3}, consistent which CDP-2 measurements during the case study of interest. Additional physics options include the implementation of the Quasi-Normal Scale Elimination (QNSE) planetary boundary layer scheme (*Sukoriansky et al.*, 2005), the Noah land surface scheme and the Rapid Radiative Transfer Model for General Circulation Models (RRTMG) radiation scheme to model the shortwave and longwave radiative transfer. The Kain-Fritsch cumulus parameterization is also activated in the 12-km resolution domain. Atmospheric variables in the innermost domain were output with a 5-min time resolution, starting on 25 January at 12 UTC, allowing for a sufficient spin-up time before the onset of precipitation at the ground site in the early morning hours of 27 January. It was verified that the simulated WRF surface meteorological variables agreed reasonably well with weather station measurements (Fig. 6.2). The WRF simulations are used in this study to provide high-resolution temperature, wind and humidity profiles, to gain an understanding of the mesoscale processes and how they may contribute to snowfall microphysics over LCDF.
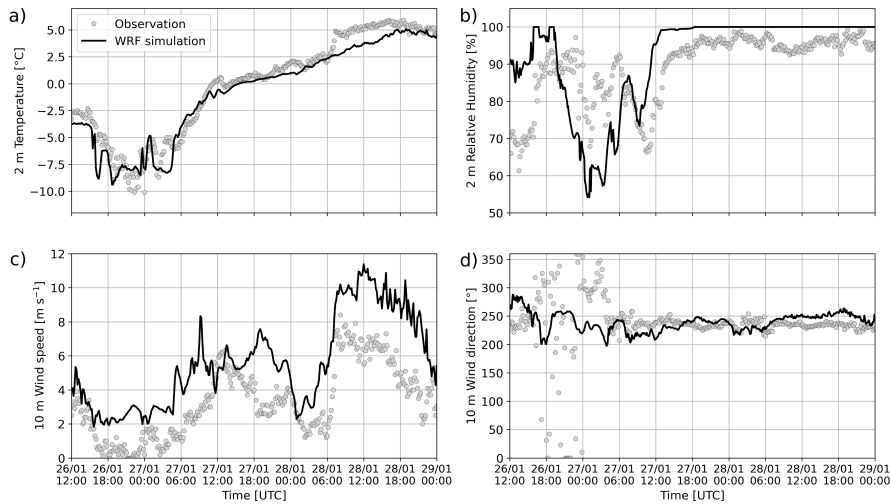
Figure 6.2: WRF simulations and observations (source: MeteoSwiss) of surface meteorological variables: (a) 2 m temperature; (b) 2 m relative humidity; (c) 10 m wind speed; (d) 10 m wind direction.

6.4   Methods

6.4.1   Doppler spectra peak finding algorithm

In order to perform a systematic identification of multi-modalities in Doppler spectra, an automatic peak identification routine was implemented. The *pyPEAKO* code (*Kalesse et al.*, 2019) was used after adjustment to our dataset. The algorithm is trained on a manually-labeled dataset, consisting of 300 WProf spectra for each chirp (no improvement was noted when including more spectra), randomly sampled from 27 January 2021 (12 UTC to 23 UTC).

pyPEAKO was then trained on these data, leading to the following optimal values for the parameters detailed in *Vogl and Radenz* (2022): a time averaging window of size 1, a height averaging window of size 1, a smoothing span of 0.5, a minimum peak width of 0.1 m s^{-1} and a prominence threshold of 0.75 dBZ. After this training step, the algorithm was run on the entire event to label peaks at all (time, range) gates. It was verified that the algorithm yielded similar results as an alternative method where sums of Gaussian-shaped peaks are fitted to the Doppler spectra (*Gehring et al.*, 2022). In addition to the location of each peak, *pyPEAKO* determines its edges; this way, moments (Z_e, MDV) can be computed for each identified mode, as well as the SLDR and the signal-to-noise ratio (SNR). Peaks with a low SNR (< -15 dB) are discarded from our analysis. Eventually, for each time and range gate, a number of valid peaks is estimated, for which the radar variables are stored.

6.4.2 Identification of hydrometeor types in multi-modal spectra

To refine the interpretation of multi-modal Doppler spectra, an approach similar to the one of *Luke et al.* (2021) is implemented. The purpose is to classify the secondary modes when two or more peaks are identified in the spectra. Here and further, the *primary mode*, sometimes referred to as the *rimer*, denotes the peak with the largest Doppler velocity, while the *secondary modes* are all the slower-falling modes; this distinction between primary and secondary peaks is purely velocity-based and independent of reflectivity values. To identify the type of particles that cause a Doppler spectral mode, the spectral LDR, or spectral SLDR, is highly relevant. As pointed out in e.g., *Oue et al.* (2015); *Luke et al.* (2021), high (S)LDR values in zenith-pointing measurements imply either the presence of prolate (needle-like or columnar) crystals, or, when visible only in a restricted altitude range, of melting particles (*Ryzhkov and Zrnic*, 2019). Conversely, extremely low, or even below-noise-floor (S)LDR values reflect the presence of particles that are symmetrical with respect to the electromagnetic propagation direction, i.e., "disk-like" in the radar view, such as liquid water droplets or planar crystals (*Ryzhkov and Zrnic*, 2019). Note, however, that the latter are usually associated with slightly higher (S)LDR values. Other types of snow particles such as aggregate snowflakes or rimed particles may lead to medium-low values of (S)LDR depending on their composition and geometry. By examining not only (S)LDR but also the other radar variables, additional insights can be gained. For instance, cloud droplets are often identified by their signature in the form of a narrow, low-reflectivity peak with Doppler velocity close to zero (*Li and Moisseev*, 2019; *Li et al.*, 2021b; *von Terzi et al.*, 2022).

The proposed approach aims to combine the information contained in spectral variables (MDV$_m$, $Z_{e,m}$, SLDR$_m$ of the secondary peaks, where the subscript "m" indicates that the quantities correspond to a single spectral mode) in a comprehensive manner, to facilitate the visualization and interpretation of spatio-temporal features of Doppler modes. When at least two peaks are detected, the following decision tree is applied to the *secondary peaks* to classify them into a particle type (we recall that only peaks with SNR$_m$ > -15 dB are considered):

- SLDR_m > -20 dB: *columnar crystals.*

- SLDR_m < -28 dB and $Z_{e,m}$ < -18 dBZ and MDV_m > -0.6 m s^{-1}: *cloud liquid water droplets.*

- SLDR_m < -25 dB and not classified as cloud liquid water: *disk-like particle*, a category which may include planar crystals (pristine or rimed) or large droplets.

- Secondary mode not classified in the prior categories: *other*. This may include, for instance, aggregates or other rimed particles.

The threshold values were chosen based on the literature (e.g., for SLDR: *Oue et al.*, 2018; *Luke et al.*, 2021, for Z_e: *Kogan et al.*, 2005, for MDV: *Li and Moisseev*, 2019; *von Terzi et al.*, 2022) after adjustments based on a few individual spectra from our case study. In particular, for Doppler velocity, using a stricter threshold led to discarding some profiles that were affected by radial air motion (e.g., downdrafts). The SLDR threshold used to detect columnar crystals is also rather low compared to studies where values up to -16 dB are sometimes used (*Oue et al.*, 2018); this choice was made to improve the spatial consistency of the detection. Note that possible attenuation of W-band reflectivity caused for instance by liquid water cloud layers may affect minimally the output of this classification, in the identification of cloud liquid droplets vs. disk-like particles. However, the results of the classification show overall little sensitivity to the selected threshold values: only the exact spatial and temporal extent of the regions identified as containing one type of particles are affected by these thresholds, but not per se the existence of these regions, their general behavior, or their approximate location.

Figure 6.3 shows an example of secondary mode labeling where two main categories are identified: columnar crystals and cloud liquid droplets. This time step was chosen as it corresponds to an overpass of the aircraft above the ground site and offers the opportunity to validate the proposed classification. In general, a single spectrogram should not be interpreted as the trajectory or history of a particle population: the particles in the lower layers do not necessarily originate from the upper layers, and this can be misleading in heterogeneous or non-stationary systems. In periods with reasonable temporal homogeneity as is the case here, however, one can still look for signatures of processes in Doppler spectrograms. Alternatively, fall streak tracking can be implemented (e.g., *Kalesse et al.*, 2016; *Pfitzenmaier et al.*, 2017). This method can also have shortcomings, as it relies on wind profiles estimated from model data or interpolated radiosoundings; it also requires to neglect directional wind shear, which, in this case study, seemed an overly strong assumption (with the presence of at least one layer of significant directional shear, not shown).

In the reflectivity spectrogram (Fig. 6.3a) one can identify the rimer, precipitating from higher regions and progressively reaching high fall velocities ($|\text{MDV}_{rimer}|$ > 2 m s^{-1}). As it accelerates between 3 and 2 km, it coexists with a population of hydrometeors whose signature is a narrow mode with low reflectivity, negligible fall velocity, and a low, even below noise level, SLDR (Fig. 6.3b) : this is a likely signature of SLW, and the fact that the primary mode accelerates at the same time, suggesting riming, supports this interpretation. Below 1.8 km, a secondary mode with much higher reflectivity, spectral width, and most strikingly high SLDR is visible:

this would correspond to columnar or needle-like crystals and is labeled as such by our classification routine. Simultaneous aircraft measurements at 1700 m support this reading: in the HVPS images (Fig. 6.3c), a few large heavily rimed or graupel particles can be seen, as well as numerous columnar particles and aggregates of needles or columns. The independent PIP-based morphological classification (for particles larger than 2 mm, *Jaffeux et al.*, 2022) shown in Fig. 6.3d also confirms this partitioning, with 18% of rimed particles (graupel and rimed aggregates), 36% of columnar crystals and 42% of aggregates which are labeled as either made of columns and needles or as fragile, i.e., made of weakly bounded crystals).
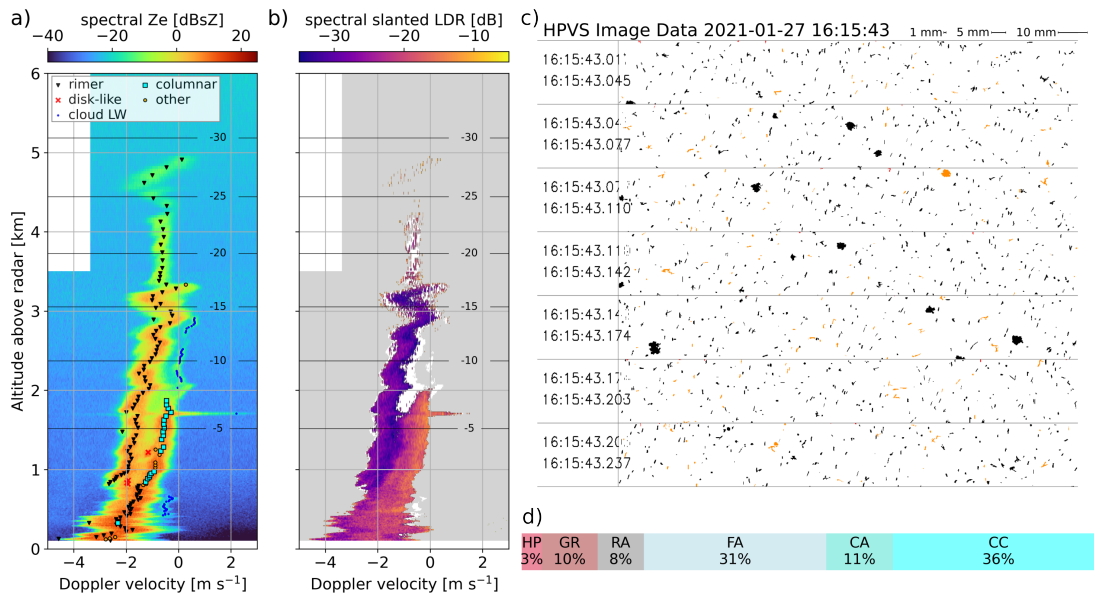
Figure 6.3: (a) Doppler spectrogram with peak labeling. (b) Corresponding SLDR spectrogram; the white area is where the cross-polar signal is below the noise level, but where the co-polar signal is strong enough that a SLDR higher than -18 dB would be detected; the gray area is where both the cross-polar signal is below noise level and the co-polar signal is too low for a SLDR up to -18 dB to be measurable. In (a) and (b), the temperature contours are interpolated from WRF simulations. (c) HVPS image from the time step when the aircraft overpasses the radar, at 1700 m AGL; orange particles are flagged by the built-in probe software as possibly shattered. (d) Habit classification from PIP images at the same time step. HP: hexagonal planar crystals; GR: graupel; RA: rimed aggregates, FA: fragile aggregates, CA: aggregates of columns, CC: columnar crystals.

6.5   Overview of the case study

The synoptic situation on 27 January 2021 is described in Chapter 2, Sect. 2.4, and illustrated with the corresponding charts in Fig. 2.6. During this event, a warm front associated with a deep low-pressure system over the North Atlantic (Figure 2.6a) led to stratiform precipitation in LCDF, in a northwesterly flow configuration. At the surface, an increase of temperatures was observed in two stages, first in the morning of 27 January, then on 28 January at 06 UTC (see for instance, Fig. 6.2). Between these two time frames, the surface temperature was roughly around or slightly above 0°C; snowfall was observed at the ground until 21 UTC on 27 January.

6.5.1 Radar time series

Height–time plots of WProf reflectivity and mean Doppler velocity are displayed in Fig. 6.4. Here we point out a few distinct features visible in these time series. A low-level cloud layer persists throughout the event around 800–1000 m above ground, visible at first (before 10:30 UTC) in the $Z_{e,W}$ and MDV fields (panels a and b), then as a persistent layer with multi-modal spectra through which ice particles from higher levels sediment (panel c). Collocated zenith-pointing lidar measurements available between 11 and 12 UTC (panel d) confirm the presence of cloud liquid water droplets in this region, identified as a layer with strong lidar backscatter above which the signal is extinct. Around a similar altitude, and slightly later, a layer of enhanced reflectivity can sometimes be observed (∼12:30, ∼15:30–16:15, ∼19:10–19:50 UTC). This reveals the presence of a partial melting layer related to the onset of the warm front, during which a warm air mass with slightly positive temperature overlays, then replaces, a cooler air mass with negative temperature (e.g., *Emory et al.*, 2014). This temperature inversion is confirmed by aircraft measurements of air temperature (see Chapter 2).
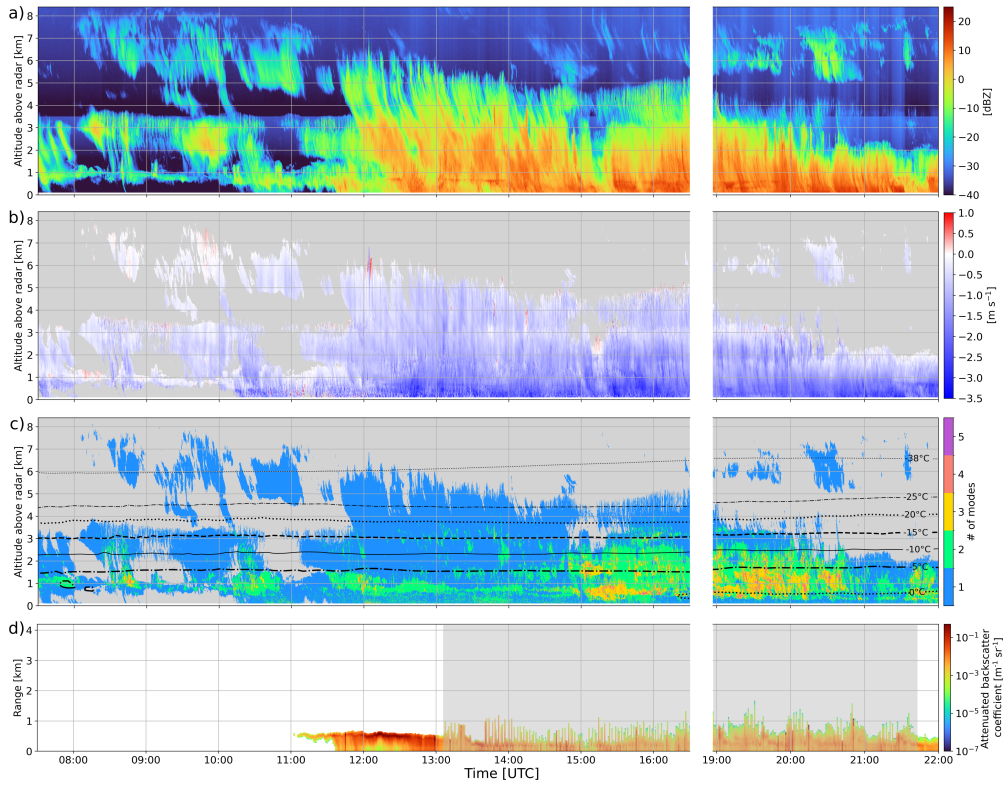
Figure 6.4: Time series of WProf radar moments on 27 January. (a) Z_e; (b) MDV; (c) number of modes detected with pyPEAKO (*Kalesse et al.*, 2019), with overlaid temperature contours (WRF simulations). (d) Height-time plot of lidar backscatter (note that the extent of y-axis is smaller than (a)–(c); after 13:30 UTC (gray zone), the lidar was performing hemispherical RHI scans, i.e., the range does not correspond to height above ground. An SNR threshold (-8 dB) is applied in panels (b) and (c). Data collection was interrupted from 16:30 UTC to 18:57 UTC due to a power outage; the later stage of the event, after 19:00 UTC, is included to show the persistence and eventual decay of the cloud system.

Another noticeable feature that comes across from the radar time series is the presence of multiple—at least three—cloud layers, which are first distinct in the hours before 12 UTC, and then merge in the radar signature as particles precipitate from the higher clouds through the lower ones, in a seeder/feeder configuration. This is particularly visible in the time frame 11:40 to 12:05 UTC, between 3 and 5 km above ground: snow particles formed in the overlaying cloud (4–6 km) precipitate above a feeder cloud (extending from 2 to 3 km), which they reach around 11:55 UTC causing a reflectivity enhancement. The enhancement at this altitude continues to be observed after this, which leads to believe that the seeding mechanism persists, as external or possibly in-cloud seeding (*Proske et al.*, 2021). This interpretation is reinforced by the analyses conducted in the following sections.

One of the most striking observations is the persistent Doppler spectral multimodality which has a significant extent in both height (2 to 3 km) and time (from 14:50 to at least 21:00 UTC, assuming that there is a degree of continuity during the time period where data are missing). The rest of the investigation will focus on the multi-modal features during this time frame.

The results of the labeling procedure described in Sect. 6.4.2 are shown in Fig. 6.5, focusing on a shorter time frame. In Fig. 6.5a, (time, range) gates where a secondary population is labeled as one of the four types (*columnar, cloud LW, disk-like, other*) are visualized as semi-transparent colored layers: this way, the spatial and temporal signatures of the different hydrometeor populations and their coexistence can be analyzed. One noticeable feature in this time series is the lower-level liquid cloud (sometimes labeled as disk-like particles), which corresponds to the pre-existing low-level cloud already visible from ~08:00 UTC. The presence of liquid water does not seem restricted to this layer, as cloud liquid is detected between 1.5 and 3 km from ~14:45 to ~16:30 UTC, which confirms the existence of a high-level feeder layer. Another striking observation is the detection of columnar crystals, at first in a restricted altitude range around 1.5 km (~13:15 to 15:00 UTC), then in most range gates below 1.8 km (15:00 to 20:30 UTC). One can observe other spatially and temporally consistent structures which are labeled as a certain particle type. For instance, a disk-like mode is identified either in restricted altitude ranges (e.g., 15:00 UTC, ~2 km) or in vertically-extended but short-lasting cells (e.g., 16:20 UTC). In what follows, we focus our analysis on specific time frames where different signatures are observed and seem to reveal different microphysical processes.

6.6   Insights into microphysical processes

From the inspection of Fig. 6.5, it was decided to focus on the signatures observed during three time frames: 14:50–15:20 UTC, 15:25–15:45 UTC, and 16:05–16:30 UTC. By investigating more precisely the radar and in situ measurements during those phases, we narrow down possible interpretations for these microphysical fingerprints.
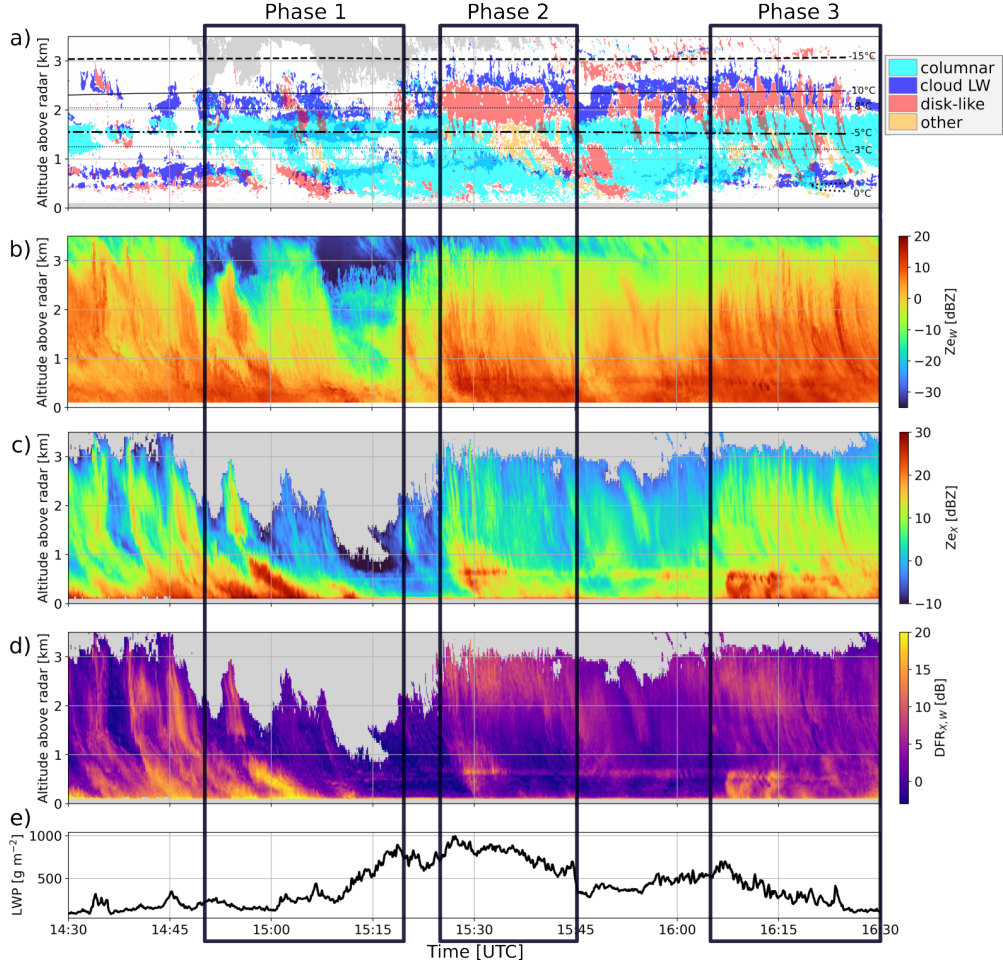
Figure 6.5: Time series covering a subset of the event where the multi-modal features are the most visible. (a) Secondary mode labeling visualized in the following way: for each of the four types considered, a boolean array is defined which is *true* at (time, range) pixels where a secondary mode is classified as this type; these four layers are then superimposed as semi-transparent layers with different colors. Temperature contours from WRF simulations. To reduce the noisiness, a pixel is colored if at least two of its neighbors are labeled with the same type. Height–time plots of (b) $Z_{e,W}$, (c), $Z_{e,X}$ and (d) DFR. (e) LWP time series. The dark boxes indicate the three time frames on which Sect. 6.6 focuses.

6.6.1 Phase 1, 14:50–15:20 UTC: Rime splintering

The first time frame stands out by the presence of a rimer population, a supercooled liquid cloud layer, and a population of columnar crystals, as visible in the time series of Fig. 6.5a. Figure 6.6 summarizes these features through the statistics (median and interquartile range IQR) of $Z_{e,W}$ (a) and MDV (b) of each mode during this time frame, together with the number of peaks (c). Figure 6.6d–e illustrate an example of Doppler spectrogram (respectively sZ_e and spectral SLDR) where the most representative features were visible at once. The range dimension is restricted to the region between 1 and 4 km to focus on the area of interest. From Fig. 6.6a–b it can be seen that the SLW mode (denoted CLW1) has, as expected, both low reflectivity (< -20 dBZ) and low Doppler velocity (between -0.3 and 0.1 m s^{-1}). In the upper

130

levels, the primary mode (R1) has a faint signature, with low reflectivity (-30 to -20 dBZ), which decreases from ~4 to ~3 km; this may reflect sublimation within a drier layer underneath a seeder region, confirmed by the profile of relative humidity with respect to ice simulated with WRF (not shown). $Z_{e,R1}$ (the subscript refers to the hydrometeor population detected) then increases downwards below 3 km (-15°C), while MDV_{R1} increases only slightly (of ~0.5 m s^{-1}). This may correspond to a region of planar depositional growth, consistent with the temperature range. When R1 reaches the CLW1 layer around 2.4 km (-10°C), $Z_{e,R1}$ continues to increase and MDV_{R1} accelerates up to ~-1.5 m s^{-1}, which indicates riming (*Kneifel and Moisseev*, 2020), consistent with the interpretation of CLW1 as liquid droplets. Further down, the columnar mode (CC1) is detected, roughly below 2 km. In Fig. 6.6c, the median of the number of peaks is shown; it illustrates that the three modes (rimer, supercooled droplets, column/needle-like crystals) indeed coexist and do not correspond to different time steps. Collocated in situ observations are available during an overpass of the ATR42 at 15:05 UTC, 1400 m: 2D-S and HVPS images (Fig. 6.7a) reveal large graupel particles as well as column- or needle-like crystals, while the CDP-2 confirms the presence of supercooled cloud droplets, with an LWC around 0.1 g m^{-3}. These observations support the interpretation of the types of particles corresponding to each mode (heavily rimed R1, pristine CC1, and droplets CLW1).
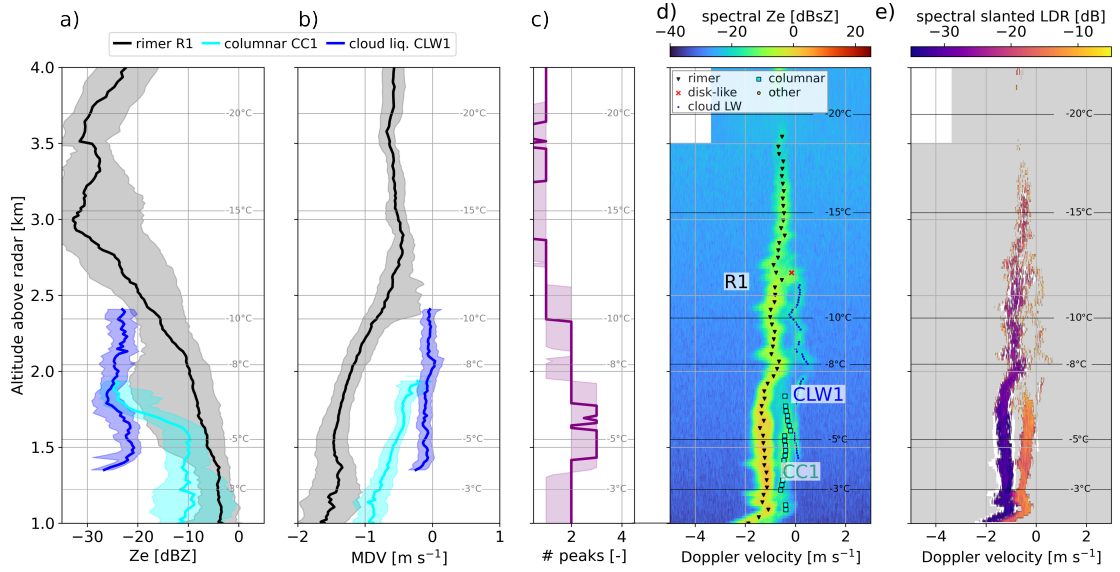
Figure 6.6: (a) Z_e, (b) MDV median profiles (with IQR in shaded area) of the different mode types labeled following Sect. 6.4.2, during the time frame 14:50–15:20 UTC. Range gates where the modes were detected less than 25% of the time are discarded. (c) Median profile (and IQR) of the number of peaks identified with *pyPEAKO*. (d) (resp. (e)) Example of reflectivity (resp. SLDR) spectrogram collected during this time frame (15:01:06 UTC), with the modes found and labeled through the methods of Sect. 6.4. Temperature contours from WRF simulations.

These signatures and the temperature range in which they are observed (slightly above -8°C) suggest that SIP through rime splintering (HM process) may be active: CC1 would result from the splinters produced during the riming of CLW1 onto R1 when temperature exceeds -8°C. It is likely that the HM process is active during most of the event after ~14:30 UTC, as suggested

by the persistence of a columnar mode exactly below the -8°C isotherm during this phase (Fig. 6.5). We chose to focus specifically on the 14:50–15:20 UTC time frame to analyze this mechanism since the signatures in the rest of the event are entangled with other processes, as will be discussed further.

Hypothesis of secondary ice production

Radar measurements are not sufficient for an unequivocal identification of SIP occurrence, since those can only be proven through a comparison of ICNC and INP concentrations close to cloud top, obtained with in situ aerosol measurements (e.g., *Järvinen et al.*, 2022) or with Raman lidars (*Wieder et al.*, 2022). In regions where the atmospheric conditions are typically pristine and INP concentrations quite low, the reflectivity of secondary spectral modes can be used to identify SIP: this is the approach of *Luke et al.* (2021) where a reflectivity threshold is used (-21 dBsZ), above which the authors consider that the ICNC must be high enough that only ice multiplication processes can account for it. In our case, these thresholds are well exceeded, with the spectral reflectivity of the secondary mode reaching -10 dBsZ in Fig. 6.6d and exceeding 0 dBsZ at other time steps. However, for a more quantitative approach, we follow the generic method of *Li et al.* (2021b), hereafter LI21, to assess whether we can support the hypothesis that the secondary mode indeed originates in SIP.

The goal is to demonstrate that, if this mode were generated through primary ice production (heterogeneous nucleation, since temperatures are greater than -38°C), it would require INP concentrations that exceed the expected ones. The steps are as follows (the detail of the equations is provided in Appendix C):

1. Identification of a region as the source of the new ice population: we suppose that it is generated at altitudes slightly above the upper limit of the detected radar signal (here, between 1850 and 2050 m).

2. Simulate the growth by vapor deposition of crystals generated in this region, assuming saturation with respect to liquid water. In this step, particle mass (m), size (maximum dimension D), and terminal velocity (v_t) are modeled using equations of diffusional growth (e.g., *Hall and Pruppacher*, 1976 or *Pruppacher and Klett*, 2010, Chapter 13). We assess the accuracy of this modeling step by verifying that the obtained terminal velocity v_t agrees with that of CC1 (Appendix Sect. C.2). Assuming columnar growth, we obtain (Appendix Fig. C.1a–c) a crystal mass of 0.90 to 2.4 μg corresponding to $D \sim 0.12$–0.33 mm, at 1.6 km above ground ($v_t \sim 0.29$–0.46 m s^{-1}). This range of values is obtained by varying the generation height (see step 1) and the aspect ratio of the particles.

3. Estimate the ice water content (IWC) of the secondary mode using literature Z_e–IWC relations (e.g., IWC = 0.137 $z_e^{0.643}$ after *Liu and Illingworth*, 2000, with z_e in mm^{6}m^{-3} [such that $Z_e = 10 \log_{10}(z_e)$] and IWC in g m^{-3}). Using the 25% and 75% quantiles of the Z_e profile (-16 to -8 dBZ), this gives an IWC of 0.012 to 0.042 g m^{-3} at 1.6 km. Similar results are obtained with the relations of *Aydin and Tang* (1997); *Boudala et al.* (2006).

Note that such Z_e–IWC relations are, however, associated with rather high uncertainty (e.g., -50% to +100% errors reported in *Liu and Illingworth*, 2000).

4. A rough estimate of the resulting ICNC is then obtained as ICNC = $\frac{\text{IWC}}{m}$, i.e., here ICNC~ 7–50 L^{-1} at 1.6 km, using the IQR of IWC and the mass estimate obtained earlier.

5. This estimate is compared to typical INP concentrations at the temperature range where the ice particles were assumed to be generated (here, -8 to -10°C). For this, statistics of INP concentrations measured at the high altitude Jungfraujoch (JFJ) measurement site (3580 m ASL, approximately 100 km southeast of LCDF) in free tropospheric conditions are taken from *Conen et al.* (2022). During two years of measurements, *Conen et al.* (2022) observed concentrations of active INPs at -10°C and -15°C ranging from 1.0×10^{-3} L^{-1} to 1.6×10^{-2} L^{-1}. While no INP measurements are directly available for the event of interest, measurements of the total aerosol number concentration indicate a low aerosol loading on this day (below the lower 10% quantile of the 2020-2021 winter, compiled from condensation particle counter data available through *Tørseth et al.*, 2012, at http://ebas-data.nilu.no/, last access: 7 March 2023): the concentration of active INP on 27 January are thus unlikely to be significantly outside of the statistical bounds of *Conen et al.* (2022). An other estimate of INP concentrations may be derived from the temperature-dependent relation mentioned in *DeMott et al.* (2010), which gives values of 0.3 to 0.4 L^{-1} at -8 to -10°C. As underlined by *DeMott et al.* (2010), this relation has a large uncertainty, and is presumably less trustworthy than the INP statistics at JFJ.

This approach gives ICNC estimates higher by one to four orders of magnitude compared to expected INP concentrations, which supports the SIP hypothesis. While these estimates are valuable, they are prone to a quite high error as several hypotheses are involved in each step of the method, such as where the ice particles are generated, the mass-dimensional relations used, geometrical description, ventilation coefficients, to list a few (see Appendix C). We can also note that possible riming of the crystals (after they have grown to a sufficient size) would not be adequately modeled by this approach, which considers exclusively depositional growth. All these hypotheses inevitably contribute to an uncertainty propagation which it is both challenging to quantify and to reduce. Without further information on INP concentrations during this specific event, it remains difficult to make strict assertions on the occurrence of SIP through the HM process, although it appears as a reasonable hypothesis in view of the observed signatures and results of the LI21 method.
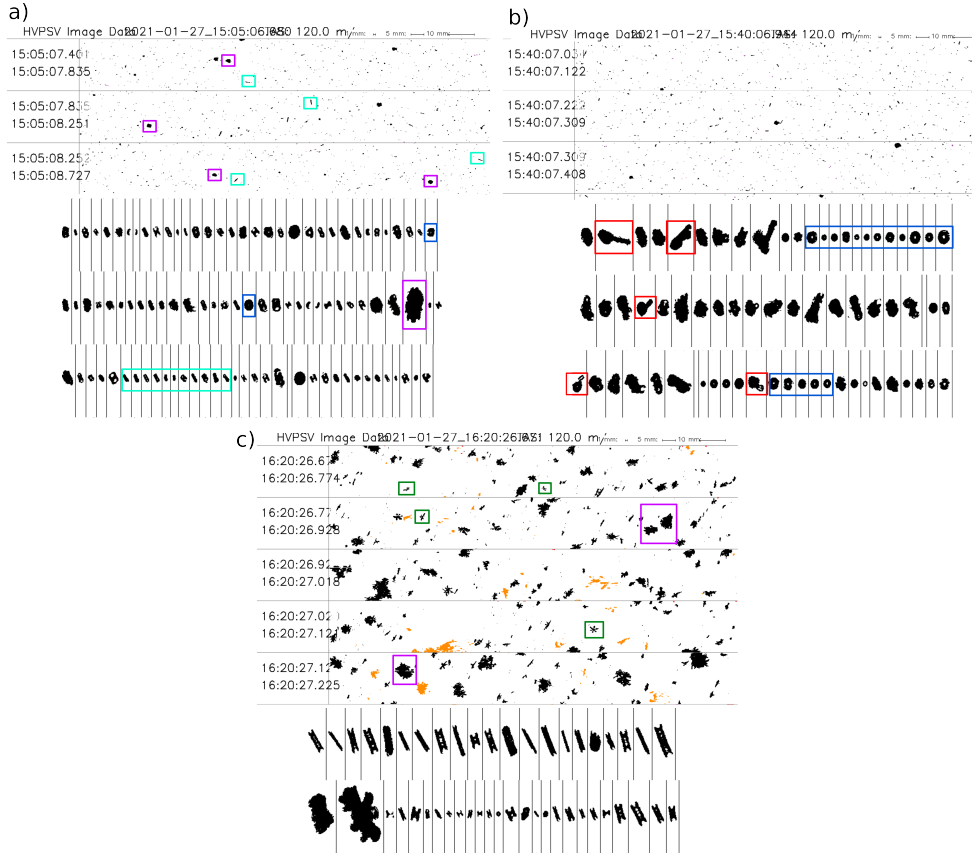
Figure 6.7: HVPS and 2D-S images for the three time frames: (a) 15:05 (b) 15:40 and (c) 16:20 UTC. Panels (a) and (b) correspond to overpasses over the radar. The scale of the HVPS images is indicated at the top. The vertical bar in the 2D-S images corresponds to 1.28 mm. The orange particles were flagged by the HVPS built-in software as possibly affected by shattering within the probe. Circled are examples of particles discussed in the text: liquid droplets/drops (blue), heavily rimed particles (purple), spicules (red), (fragments of) pristine dendritic crystals (green).

6.6.2 Phase 2, 15:25–15:45 UTC: New ice production in high-LWC region

From 15:25 to 15:45 UTC, a mode labeled as "disk-like" (DL2) is persistently identified between 1.8 and 2.2 km. Figure 6.5, from a time series perspective, and Fig. 6.8a–b from a statistical summary perspective, suggest that DL2 is below a layer of SLW droplets, and above a population with higher SLDR (labeled either as "columnar" or as "other"). Following the rationale of Sect. 6.4.2, the low SLDR$_{DL2}$ (< -25 dB) together with relatively high reflectivity ($Z_{e,DL2}$ >-10 dBZ, Fig. 6.8) and MDV$_{DL2}$ (down to -0.5 m s^{-1}) of this peak suggests that it is composed of either planar crystals or larger supercooled droplets (drizzle). Fully resolving this question is challenging, but a few steps can be achieved to improve the understanding of these microphysical signatures.
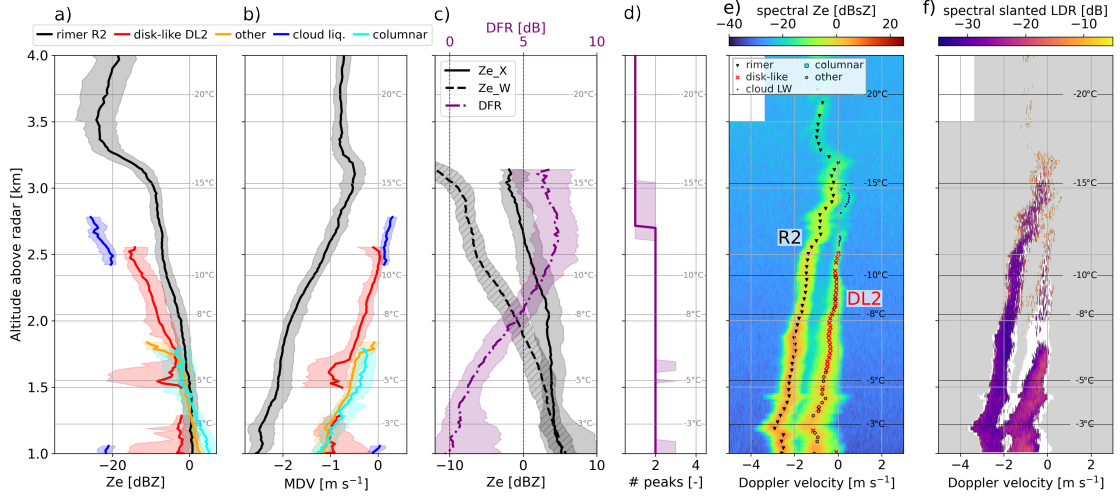
Figure 6.8: (a) Z_e, (b) MDV median profiles (with IQR in shaded area) of the different mode types labeled following Sect. 6.4.2, during the time frame 15:25–15:45 UTC. Range gates where the modes were detected less than 25% of the time are discarded. (c) Black lines (values on bottom x-axis): profiles of $Z_{e,X}$ (full) and $Z_{e,W}$ (dashed); purple line (values on upper x-axis): DFR profile. (d) Profile of the number of peaks identified with *pyPEAKO*. (e) (resp. (f)) Example of reflectivity (resp. SLDR) spectrogram collected during this time frame (15:36:28 UTC), with the modes found and labeled through the methods of Sect. 6.4. Temperature contours from WRF simulations.

Presence of liquid droplets

Several independent observations point to the presence of liquid water in this region, suggesting that the secondary mode DL2 is at least partly caused by liquid water droplets. The first element is the increase in fall velocity of the rimer mode (R2), from 1 to 2 m s^{-1} between 2.5 and 2 km. This increase already begins in the region of the cloud droplet mode (2.5 - 2.8 km), but continues below. Fall velocities of this order (e.g., larger than 1.5 m s^{-1}) typically indicate riming (*Kneifel and Moisseev*, 2020) and consequently suggest the presence of supercooled droplets. Secondly, the LWP time series (Fig. 6.5e) reaches remarkably large (> 800 g m^{-2}) values during this time frame. While the LWP retrieval does not inform on the altitude of the liquid cloud layers, it does confirm the presence of SLW in this period. Lastly, we can leverage the collocated X-band measurements, shown in Fig. 6.5 with both $Z_{e,X}$ (panel c) and DFR (panel d). DFR is often used in radar-based studies of snowfall microphysics as a proxy for particle size (as mentioned in earlier chapters of this dissertation), but it can also serve as a way to quantify W-band attenuation (*Hogan et al.*, 2005; *Tridon et al.*, 2020). In the time frame on which this subsection focuses, high DFR (>10 dB) coinciding with relatively low $Z_{e,X}$ (~5 dBZ) are observed up to echo top, while low DFR values are expected in such regions where crystals are usually in an early growth phase. This suggests that the enhanced DFR is not related to the presence of large particles but rather to an abrupt attenuation of the W-band signal, caused by a layer with significant LWC. Fig. 6.8c illustrates the median DFR profile between 15:25 and 15:45 UTC and confirms what was observed in the time series, with a DFR that increases in the region where DL2 is present, and does not decrease to 0 dB near echo

top, suggesting that the increase is related to W-band attenuation. As DFR values are low in the bottom part of the profile, little to no attenuation is expected in this region, meaning that most of the SLW droplets would be in the region of DL2.

These elements are evidence that a population of liquid water droplets is at least partly responsible for the DL2 signature. The question is then, whether we can quantify the properties of the liquid droplets in this region. For this, we can combine the information from 1/ $Z_{e,DL2}$ and MDV_{DL2}, both of which would be related to the size of the drops (assuming DL2 consists only of liquid water), and 2/ the attenuation caused by DL2, which reflects the total LWC (if all droplets are small enough to be within the Rayleigh scattering approximation). We use the radiative transfer model PAMTRA (*Mech et al.*, 2020) to simulate the attenuation and reflectivity of a cloud/drizzle population as a function of the LWC and the drop size distribution. A gamma distribution is assumed, with a shape parameter μ taken in the range -0.5 to 5 (*Bringi et al.*, 2003). Simulations are run by varying μ as well as the LWC and the effective diameter D_{eff}, which is the ratio of the third to the second moment of the PSD. The median volume diameter* D_v can be inferred from the effective diameter as in e.g., *Straka* (2009); *Ulbrich and Atlas* (1998). Absorption and scattering coefficients are calculated with Mie theory, with the liquid water refractive index following *Turner et al.* (2016). Then, attenuation due to hydrometeors as well as radar reflectivity at W-band are modeled for a temperature of -10°C. Figure 6.9 illustrates the results.
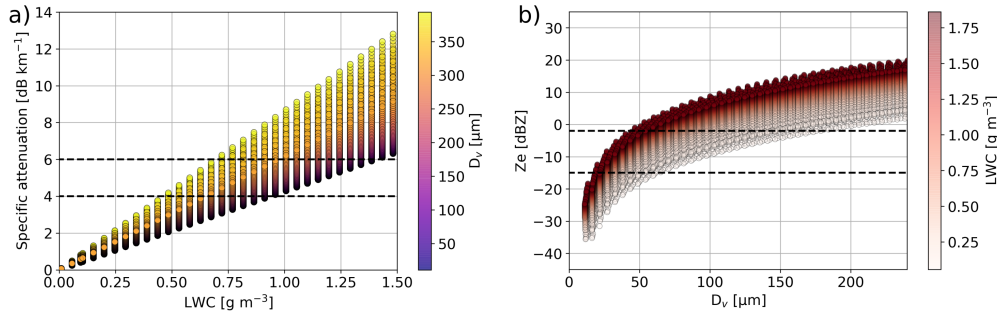
Figure 6.9: PAMTRA simulations of a gamma distribution of liquid droplets with varying parameters (μ = -0.5..5, D_{eff} = 10..300 μm, LWC = 0.01..2 g m^{-3}). (a) Specific attenuation due to liquid water vs. LWC, color-coded with D_v, (b) $Z_{e,W}$ vs. D_v, color-coded with LWC. The black dashed lines indicate the bounds of DL2.

We then rely on the measurements of DL2 as constraints on reflectivity (between -15 and -2 dBZ), attenuation (between 4 and 6 dB km^{-1}) and mean Doppler velocity (0.15 m s^{-1} < |MDV| < 0.5 m s^{-1}). With a simple look-up table approach, this translates into bounds on LWC and D_v: 0.9 g m^{-3} < LWC < 1.4 g m^{-3}, and 35 μm < D_v < 70 μm. These bounds are quite rough, in particular since we considered that only liquid droplets (i.e., no ice crystals) contributed to $Z_{e,DL2}$. They do, nonetheless, highlight the presence of significant LWC and likely of large (> 50 μm) droplets, although this is not sufficient to claim that DL2 consists solely of liquid drops.

---

*such that half of the volume of water is contained in droplets smaller than D_v

New ice formation

In fact, some signs suggest that the "disk-like" DL2 mode may also contain non-liquid particles. Although they are relatively large and with non-negligible fall velocity, the liquid drops do not precipitate to the ground, or else the attenuation would occur at lower altitudes: hence the liquid content is somehow depleted. Riming is likely not the only process through which this happens, as the DL2 mode does not vanish away in the lower regions, but slowly evolves into a higher-SLDR (> -25 dB) mode (pointing to aggregate or column-like snow particles). This implies that some ice crystals are formed within this "disk-like" region, and coexist with liquid droplets.

To support this, in Fig. 6.10, we look at an individual time step instead of global statistics. There, DFR increases only toward the upper part of DL2: this suggests that, at this time step, the LWC of the lower region is only moderate, and that SLW drops are not the only population contributing to the reflectivity.
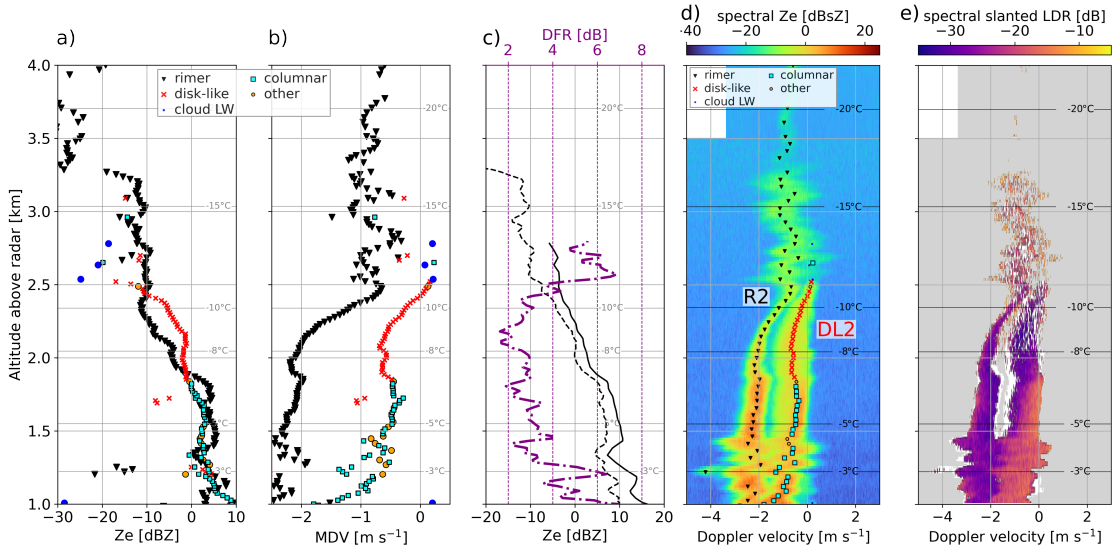
Figure 6.10: (a) Z_e, (b) MDV profiles of the different mode types labeled following Sect. 6.4.2, at 15:27:53 UTC. (c) Black lines (values on bottom axis): profiles of $Z_{e,X}$ (full) and $Z_{e,W}$ (dashed); purple line, with values on upper x-axis: DFR profile. (d) (resp. (e)) Reflectivity (resp. SLDR) spectrogram collected at the same time step, with the modes found and labeled through the methods of Sect. 6.4. Temperature contours from WRF simulations.

These elements point to the production of non-columnar ice crystals between 1.8 and 2.5 km, i.e., -7 to -12°C, through heterogeneous freezing of the cloud droplets and/or by SIP. Among the supposedly prominent SIP mechanisms, rime splintering would be unlikely because of the cold temperatures at the top of DL2; given that drizzle-size drops (> 50 μm) might be present, droplet shattering appears as a possible mechanism, although collisional breakup cannot be excluded altogether.

Unfortunately, no aircraft overpasses took place directly in this region (1500 m– 2500 m), but

one overpass at 15:40 UTC at 1100 m is still instructive (Fig. 6.7b). In the 2D-S images, one can identify (red frames) columnar crystals that grew onto rather large spherical or semi-spherical particles. These are likely frozen drops or fragments of frozen drops, which were formed within the DL2 region: they then served as germs for crystal growth by vapor deposition, with temperatures just above -10°C favoring columnar growth. Similar structures were reported by *Korolev et al.* (2020) in conditions where droplet shattering was suspected. Such shapes could also explain the only moderately high SLDR values measured in the region of columnar growth. In addition to these spicules with "lollipop" shapes, a few images of large drops are collected by the 2D-S (blue frames in Fig. 6.7b); a precise estimate of droplet size is difficult to make based on these images due to possible diffraction by out-of-focus drops (*Korolev*, 2007b; *Vaillant De Guélis et al.*, 2019). These in situ images are compatible with the analysis, that drizzle-size liquid droplets are involved in the formation of new ice particles in the region of the DL2 mode. They also suggest that collisional breakup would not be the dominant process, as no signs of fragments of crystals are apparent (*Ramelli et al.*, 2021).

Overall, the above elements suggest droplet shattering as a possibly active mechanism given 1/ the high LWC reflected by W-band attenuation (detected through high DFR values), 2/ the presence of large droplets inferred from the enhanced reflectivity and increase in Doppler velocity of the secondary mode, 3/ the signs of ice formation within this DL2 mode, 4/ the in situ observations which reveal (fragments of) frozen droplets upon which crystalline growth occurred, 5/ the temperature range, which is compatible with droplet shattering but not HM.

However, because the liquid droplet and new ice signatures are intertwined in DL2, it is very challenging to disentangle them further to reliably narrow down the dominant microphysical process—primary or secondary ice production. We employ the LI21 method as in Sect. 6.6.1, to get a rough estimate of the potential discrepancy between INP and ICNC. Assuming the formation of ice particles around 2450 to 2500 m and subsequent growth by vapor deposition and sedimentation (see Appendix C, Fig. C.1d–f), at an altitude of 2200 m the particles would have grown to a mass of $2.9 - 26\,\mu$g (maximum dimension 0.37 to 2.5 mm, terminal velocity 0.31 to 0.42 m s^{-1}). The IWC retrieved from $Z_{e,DL2}$ values (-15 to -7.7 dBZ, assuming this time that $Z_{e,DL2}$ is dominated by ice crystals) would range from .019 to 0.054 g m^{-3}, which in the end leads to an estimation of ICNC in the order of 0.7 to 20 L^{-1}. The spread is significant due to the uncertainties in modeling particle habit in this temperature range (-12 to -9°C), where the dominant growth mode shifts from planar to columnar; for this reason, both habits were considered in the simulations leading to a large spread in the modeled masses and sizes. The retrieved ICNC are here again above the typical active INP concentrations in this temperature range measured at JFJ (*Conen et al.*, 2022), although the discrepancy is slightly less obvious than in the first case (still one to four orders of magnitude higher than JFJ statistics, but within zeros to two orders of magnitude compared to the temperature-based estimate). We highlight that the reflectivity values used here are affected by significant attenuation; in that sense, the ICNC estimates that we give are rather conservative. If Z_e values are corrected from 4 dB of attenuation (see Sect. 6.6.2), slightly higher ICNC are obtained ranging from 1 to 30 L^{-1}. However, it was now assumed that the $Z_{e,DL2}$ values are dominated by ice crystals rather than

liquid droplets (by contrast with the previous paragraph): overall, these results do not allow for a clear-cut demonstration of SIP occurrence. It is possible that droplet freezing (upon INP immersion, or collision with ice crystals), and not necessarily shattering, is at least partly responsible for DL2.

If droplet shattering were taking place, it might, in any case, not be highly efficient in the production of secondary ice crystals. Indeed, *Korolev and Leisner* (2020) and studies mentioned therein (e.g., *Lauber et al.*, 2018) suggest that the efficiency of droplet shattering upon freezing increases as the supercooled drops become larger. Our analysis, although it does point to the possible presence of droplets with a diameter sufficient to cause shattering of the droplets upon freezing, does not provide evidence that very large drops (e.g., $> 300\ \mu$m) are present. In these conditions, droplet shattering might only be moderately efficient in the sense that only a few fragments would be generated per freezing drop, leading to a modest enhancement of ICNC through SIP, consistent with the retrieved estimates.

Formation of large droplets

The seeder-feeder configuration, involving a SLW feeding cloud layer with top around 3 km, seems to be an essential driver of the microphysical signatures discussed up to now. Even though the persistence of mixed-phase system is frequently acknowledged in the literature (*Lohmann et al.*, 2016), it is instructive to investigate the mechanisms behind the maintenance of the supersaturation over liquid water in the feeder cloud, and the occasional formation of drizzle-sized drops as discussed above. For this purpose, the WRF simulations of the event provide relevant insights into the origin of the air masses and the supercooled liquid clouds. A cross-section along the main wind direction (315°) at 15:20 UTC is shown in Fig. 6.11, together with a time series of simulated ice and liquid water content. One first observation from the time series is its rather good agreement with the radar measurements and some of the baseline interpretations that were proposed (Sect. 6.5.1): the presence of a warm nose as a sign of the warm front onset, visible in the converging contours of potential temperatures slightly below 1 km (especially clear before 12 UTC), and the corresponding low-level liquid water cloud which persists around 1 km with a slowly decreasing altitude (see Sect. 6.5.1). More specifically, the time series also indicates the presence of a higher-level supercooled cloud (with a top at 3 km), which act as a feeding layer for ice crystals precipitating from above. This SLW cloud is present in the WRF simulation starting around 12:00 UTC and decaying in strength after 16:00 UTC. LWC is highest around 15:00 UTC with values exceeding 0.5 g m^{-3} around 2.5 km, which is compatible with the radar-based interpretations conducted above (although with a slight temporal shift).

The cross-section (Fig. 6.11b–d) helps us understand the origin of the enhanced LWC. It appears related to a combination of large-scale moisture supply—associated with the warm front extending from the Northern Atlantic—with a local enhancement due to orographic lifting over the Jura, efficient since the northwesterly flow is approximately orthogonal to the mountain range. This is confirmed by the vertical velocity field (Fig. 6.11c), with updrafts

visible in upsloping areas, and in the cross-section of the liquid water mixing ratio (Fig. 6.11b) which is enhanced above the ridge of the Jura around 3.5 km ASL (2.5 km above ground).

In Fig. 6.11d, the moist Richardson number (Ri, which is the ratio of buoyancy to wind shear, is used to characterize atmospheric stability, *Hogan et al.*, 2002) at this location indicates a slight dynamic instability (Ri ~0.6) near cloud top; this low-Ri region seems to cover a large spatial extent and roughly corresponds to the upper cap of the mesoscale cloud (i.e., windward of the Jura). While these values are not strictly speaking descriptive of a strong dynamic instability (for which a typical threshold is Ri ≤ 0.25), they suggest that shear-driven turbulence and/or isobaric mixing may be present and contribute to sustaining the LWC of the cloud, and possibly inducing the formation of larger droplets (*Korolev and Isaac*, 2000; *Pobanz et al.*, 1994; *Grabowski and Abade*, 2017). Overall, the WRF analysis shows that the saturation over liquid water and formation of cloud droplets is triggered by a combination of orographic and frontal lifting, with a possible contribution from shear-induced mixing that favors the formation of larger drops between 15:00 and 15:30 UTC, as modeled in WRF and observed in our analysis.
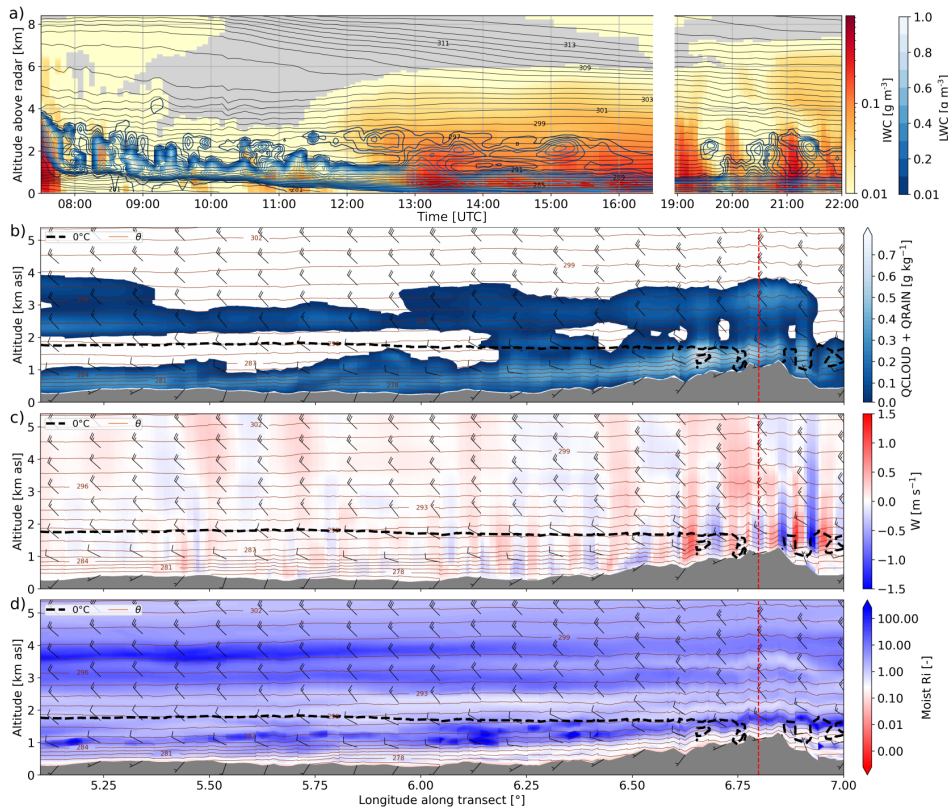
Figure 6.11: (a) Time series of IWC simulated in WRF over LCDF (includes ice, snow, and graupel), with LWC in blue contours. (b) (resp. c, d) 15:15 UTC cross-section in direction of the main wind (315°) with cloud and rain content (resp. vertical wind, moist Richardson number). In all panels, the brown contours indicate the potential temperature; in (b), (c), (d) wind barbs indicate wind speed and direction following standard conventions (in knots) and the black dashed line corresponds to the 0°C isotherm. The vertical dashed red line indicates the location of LCDF.

6.6.3   Phase 3, 16:05–16:30 UTC: New ice production in turbulent regions

From 16:05 to 16:30 UTC, another type of process appears to be happening. In Fig. 6.5, instead of being confined to a fixed altitude range like DL2, the mode labeled as "disk-like" during this time (DL3) seems to be generated at distinct time steps and at specific heights (between 2.5 and 3 km), and then precipitate to lower altitudes. Such spatio-temporal structures are also visible in the later stage of the event between 19:00 and 20:00 UTC. This creates *fall streak* structures, which can be seen in both the classification and the reflectivity time series of Fig. 6.5. As DL3 precipitates, it coexists with other modes (e.g., columnar crystals or liquid cloud droplets) while remaining well separated from these. In the supplementary material (available at https://egusphere.copernicus.org/preprints/2023/egusphere-2023-478/egusphere-2023-478-supplement.zip), a video is included showing the evolution of the Doppler spectra during these fall streak time steps; for comparison, similar animations of phases 1 and 2 are also included. It clearly illustrates that DL3 is generated in a region of atmospheric turbulence and updrafts; its formation stops when the turbulence and updraft cease, and the hydrometeor population that was formed then settles downwards.

This is summarized through the statistics and the sample spectrum shown in Fig. 6.12. There, the statistics are computed on the entire time frame (16:05 to 16:30 UTC), except for DL3 from which we specifically extracted the fall streak patterns, identified as regions when $Z_{e,DL3} >$ -10 dBZ. To identify turbulent regions, an estimate of the turbulence eddy dissipation rate (EDR) was derived following *Shupe et al.* (2008), which combines the variance of the MDV (here, of the *rimer* mode, MDV_{R3}) with information on horizontal wind and wind shear (here, from WRF simulations). Fig. 6.12b illustrates that DL3 is detected just below a region of updraft (seen in a reduction of the rimer MDV) and turbulence (visible in the EDR), between 2.8 and 3.1 km. In the upper region of DL3 (2.7 km), the mode sometimes coexists with SLW droplets, while lower down it is present along with columnar crystals (Fig. 6.12a, b, d). While these are not the main focus of this subsection, we can hypothesize that they are formed through rime splintering at temperatures warmer than -8°C, similar to Sect. 6.6.1.

In terms of radar variables, DL3 combines low $SLDR_{DL3}$ values (< -25 dB) with relatively high $Z_{e,DL3}$ (up to 5 dBZ when looking at individual fall streaks), and MDV_{DL3} around -0.5 to -1 m s^{-1}. This suggests that it is composed of planar ice crystals (or such low-depolarization ice particles) rather than liquid droplets, which would be expected, for instance, to have larger fall velocities for this level of reflectivity (e.g., Z_e-V relations for identification of drizzle *Luke et al.*, 2021, and their Supplementary Material). The temperature range in the region where this mode is formed (-15 to -12°C) is compatible with planar growth of crystals by vapor deposition. It is worth noting that the DL3 signature differs from the ones typically observed in the dendritic growth layer, in which a small updraft, an increase in reflectivity, and a persistent spectral bimodality are often reported (*von Terzi et al.*, 2022), and which is occasionally observed during this case study (see for instance, Fig. 6.4, around -15°C between 15:00 and 16:30 UTC, or the spectrogram in Fig. 6.12 around 3.1 km). By contrast, DL3 is generated in stronger and more localized updrafts (e.g., 2.8 km in Fig. 6.12e). We note that a

similar interpretation emerges when examining the Doppler spectrograms along slanted fall streaks—rather than the vertical stack of spectra at a single time step— obtained by following *Kalesse et al.* (2016) (not shown).
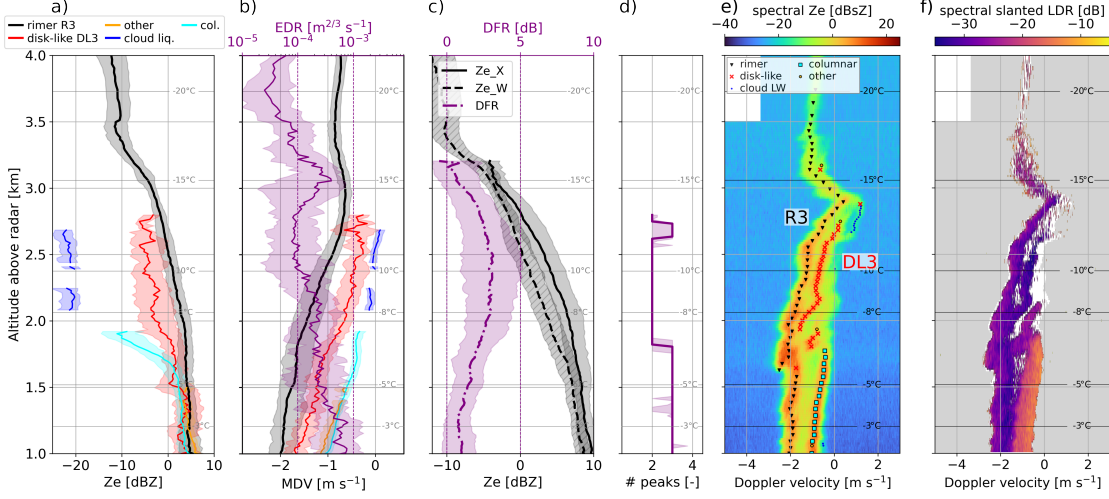
Figure 6.12: (a) Z_e median profiles (with IQR in shaded area) of the different mode types labeled following Sect. 6.4.2, during the time frame 16:05–16:30 UTC. Range gates where the modes are detected less than 25% of the time are discarded. (b) Same with MDV (on the bottom x-axis); the turbulent EDR estimated from the rimer mode (*Shupe et al.*, 2008) is shown with the purple line (median and IQR; values on the top x-axis). (c) Black lines, with values on bottom x-axis: median profiles of $Z_{e,X}$ (full) and $Z_{e,W}$ (dashed); purple line, with values on upper x-axis: median DFR profile (and IQR). (d) Median profile (and IQR) of the number of peaks identified with *pyPEAKO*. (e) (resp. (f)) Example of reflectivity (resp. SLDR) spectrogram collected during this time frame (16:18:08 UTC), with the modes found and labeled through the methods of Sect. 6.4. Temperature contours from WRF simulations.

An unambiguous identification of the microphysical process(es) leading to the formation of this mode is once again difficult. SIP is possibly responsible for DL3: the high reflectivity of the new ice mode, only a few range gates below it is formed, indicates a relatively high concentration of ice crystals which would exceed typical values of INP concentrations in this temperature range. This concurs with previous observations of ice multiplication occurring within generating cells leading to fall streak structures (*Ramelli et al.*, 2021). With the LI21 approach, we focus here on a single DL3 fall streak (16:17–16:20 UTC) and consider that particles are formed between 2.7 and 2.85 km (see Appendix C Fig. C.1g–i). At a height of 2.5 km, they would have grown (assuming plate-like or dendritic crystals) to a mass of 9.5 to 35 μg (D ~0.82 to 2.8 mm); the IWC estimate from $Z_{e,DL3}$ values (-4.1 to 1.4 dBZ) ranges from 0.074 to 0.17 g m^{-3} and the resulting ICNC = 2 to 20 L^{-1} once again exceeds the typical active INP concentration (1.0–16×10^{-3} L^{-1} following *Conen et al.*, 2022, 0.5 to 0.6 L^{-1} with the temperature-only relation of *DeMott et al.*, 2010). As in phase 2, the attenuated reflectivity values are used here, so this would rather underestimate the true ICNC. Similar to the previous sections, these values are subject to uncertainty and should be taken with care, but nonetheless, support the hypothesis that DL3 originates in SIP.

The updrafts and turbulence which contribute to the formation of DL3 also generate SLW

droplets: this is seen, for instance, in Fig. 6.12e, and in the LWP time series (Fig. 6.5e) where peaks in LWP occur when the DL3 cells/fall streaks are formed. However, the LWC in this region does not cause significant W-band attenuation like was observed in Sect. 6.6.2 and must therefore be lower. This is especially true when looking at the end of the time frame of interest, after 16:15 UTC in Fig. 6.5: there is then no DFR increase toward cloud top. Additionally, when the liquid cloud droplets generated by these updrafts are visible as a distinct mode—which is not always the case, since strong turbulence can broaden the spectra to a point where several peaks are merged into one—like in Fig. 6.12e, it is rather narrow and has a low reflectivity (~-20 dBZ), which is rather a sign of small cloud droplets than of drizzle-size drops. With these elements in mind, droplet shattering upon freezing does not seem the most likely process for the DL3 signatures.

On the contrary, ice multiplication through collisional breakup might be a plausible explanation. In the turbulent updraft region, supercooled droplets may form, onto which the primary population can start riming; meanwhile, in these turbulent eddies, collisions of these newly rimed particles would be favored (*Pruppacher and Klett*, 2010, Chapter 14; *Sheikh et al.*, 2022) either with one another or with the still pristine ones (*Phillips et al.*, 2017b), leading to the formation of DL3 particles. These fragments would subsequently grow by vapor deposition (efficient because of the supersaturated conditions), by aggregation, and/or eventually by riming if they reach large enough sizes (~100 μm, e.g., *Pruppacher and Klett*, 2010, Chapter 14). R3 and DL3 would then separate in the Doppler spectra below the turbulent region due to their different settling velocities (e.g., *Ramelli et al.*, 2021).

The ATR42, unfortunately, did not overpass the radars at a time step when DL3 fall streaks are observed, and we must therefore make cautious interpretations of the in situ observations during this time frame. HVPS images at 16:20 UTC at 1700 m (Fig. 6.7c) reveal a population of slightly rimed particles, together with a few still pristine dendrites and fragments of dendrites, a clear sign to invoke the presence of the collisional breakup mechanism. The latter two might correspond to the DL3 population (either as pristine dendrites that grew onto small fragments, or directly as fragments generated during breakup), and thus endorse the proposed interpretation, also considering that there are no signs of shattered drops. Yet, we underline again that the link between the in situ and radar observations remains hypothetical, as they are not collocated.

6.7 Conclusions

In this work, we investigated snowfall microphysical processes during the passage of a warm front in the Swiss Jura Mountains, involving a multi-layer, mixed-phase cloud system. The analyses were primarily based on the measurements of a W-band spectral profiler, together with in situ observations from the ATR42 aircraft which performed overpasses above the ground site, as well as LWP and dual-frequency radar measurements (X- and W-band) to quantify atmospheric liquid water. Multi-peak Doppler spectra were observed for several hours

and over several kilometers in height above ground, suggesting the occurrence of a number of microphysical processes involving different hydrometeor populations. We proposed a labeling method that allows for the systematic identification of certain hydrometeor types in these Doppler spectra, making use of the spectral polarimetric variables. Specifically, supercooled cloud droplets were distinguished from columnar crystals, and from disk-like particles that may include drizzle-size drops or planar crystals. This way, it became apparent that various hydrometeor habits were causing the multi-modality at different heights and time steps of the event. Three time periods stood out, during which the multi-modality was attributed to distinct processes. In each case, secondary ice production appeared as a likely cause for the formation of the new spectral peak(s). Looking into the Doppler spectra in more detail, we proposed interpretations of the mechanisms during the different time frames.
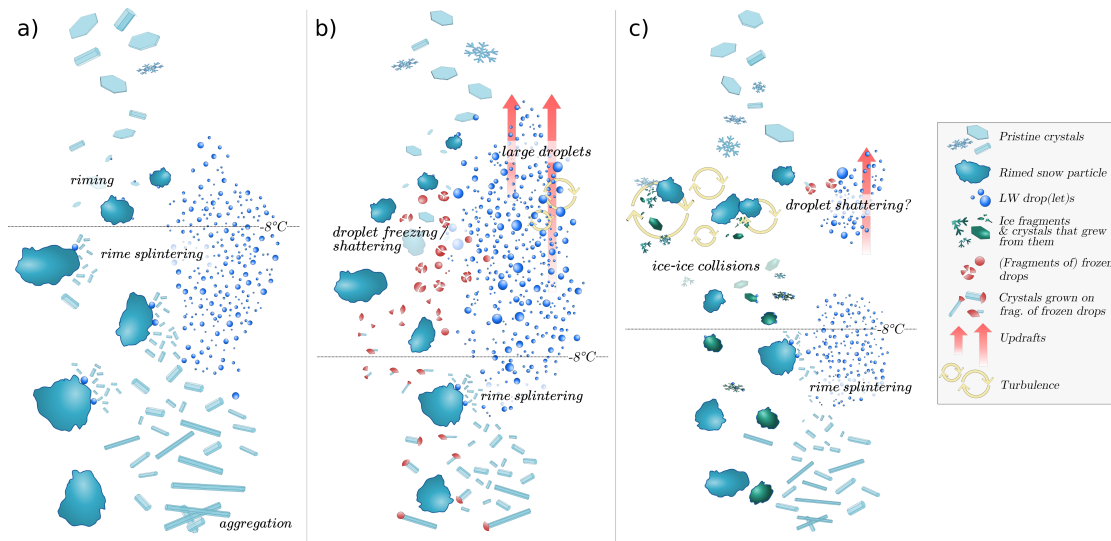
Figure 6.13: Conceptual sketch of the proposed interpretations for the microphysical signatures during the different time frames: (a) 14:50–15:20 UTC, (b) 15:25–15:45 UTC, (c) 16:05–16:30 UTC. Note that HM is also indicated in the lower layers in (b) and (c), as it is suspected to occur throughout the event (see Sect. 6.6.1).

The presence of a seeder-feeder configuration seemed to play an essential role in the microphysics of the event. During the three phases, ice crystals precipitated through a SLW layer around 2-3 km above ground, whose presence was identified through cloud radar Doppler spectra, confirmed by WRF simulations and consistent with LWP estimates. In the first phase, the interaction between the rimer and the SLW cloud led to the formation of columnar ice particles at temperatures warmer than -8°C, pointing to HM rime splintering (Fig. 6.13a), while no new ice formation was detected at colder temperatures during this time frame. The second phase (Fig. 6.13b) was associated with an enhancement of the SLW layer, in terms of both LWC and droplet sizes, with the formation of drizzle-size drops. In these conditions, droplet freezing—either through INP immersion, or upon collision of a drop with an ice crystal—and/or shattering may have been active, and involved in the emergence of a new spectral mode below $-10°C$. Lastly, new ice formation was observed at cold temperatures ($\lesssim -12°C$),

toward the top of the SLW cloud region, in localized generating cells associated with strong updrafts and turbulence; these ingredients would favor the riming of the seeding population, and SIP through ice-ice collisions between these newly rimed particles (Fig. 6.13c). The resulting signatures are rather complex, and were narrowed down by combining dual-frequency, Doppler spectral radar measurements, and in situ images.

A simple modeling method following *Li et al.* (2021b) (detailed in Sect. 6.6.1 and Appendix C) was implemented for each of these phases and suggested that primary ice production through heterogeneous nucleation could not explain alone these signatures (especially phases 1 and 3), with ICNC estimates exceeding expected INP concentrations by one to four orders of magnitude, hence supporting the SIP hypothesis. This discrepancy is in agreement with previous observations in orographic clouds, especially under seeder-feeder configurations (e.g., *Lloyd et al.*, 2015; *Georgakaki et al.*, 2022). Uncertainties related to this modeling are, however, substantial: it involves assumptions on ice microphysical properties such as geometry, mass–dimensional or velocity–size relations, on Z_e-IWC relations, and on INP concentrations, which may vary significantly.

All in all, the interpretation of these processes remains hypothetical: an unambiguous demonstration of the occurrence of SIP via a specific process is a challenge that would require more in-situ measurements across scales, to get a full picture of INP availability and of the interactions between ice (and liquid) particles. Additionally, the information derived from zenith-pointing instruments remains insufficient to grasp the horizontal variability within the precipitating system; it is, for instance, challenging to fully characterize the impact of the orographic terrain in the observations. What remains clear is that different signatures were visible in the remote sensing measurements, calling for distinct interpretations of their possible causes. This also demonstrates the relevance of radar and, in particular, of high-sensitivity Doppler spectral measurements, to investigate in a detailed way the microphysics of clouds and precipitation. Further studies could include, on the one hand, more involved multi-sensor approaches to confirm the occurrence of SIP, and on the other hand, a generalization of the methods introduced here to gain insights into how frequently such microphysical processes are observed at a given location.

7 Conclusions

7.1 Summary and discussion of the results

Snowfall is an essential weather and climate variable, which is at the root of most precipitation on Earth and hence a key component of hydrological resources. Understanding what takes place at the microscale in the solid phase of clouds and precipitation is a necessary step to take to model snowfall and precipitation, as well as quantify accurately how clouds affect the Earth's radiative budget. At the same time, snow particles can take on an extraordinary variety of geometries, sizes, or internal structures, and they undergo diverse production and growth mechanisms depending on the way they interact with one another and on the atmospheric conditions. Because of this heterogeneity, many unknowns remain tied to snowfall microphysics.

This thesis focused on leveraging multi-frequency and Doppler spectral measurements from zenith-pointing radars to improve the characterization of snowfall microphysics, both from the angle of microphysical properties and from that of snow particle growth, decay, and production processes. In the following, we recall the main results from the different chapters and summarize how they each contributed to this overarching goal.

- **ICE GENESIS: a multi-sensor snowfall dataset**

The ICE GENESIS campaign, presented in Chapter 2, took place in the Swiss Jura in January 2021 and was designed to collect observations of snowfall at temperatures between -10° C and +2° C. It included a ground-based set-up, with meteorological radars operating at different frequencies, and an airborne instrumented platform sampling in situ measurements at various altitudes over the ground site.

The ICE GENESIS field campaign is a data-oriented contribution on the route to an improved characterization of snowfall microphysics. With its diverse suite of ground-based and airborne remote sensing and in situ probes, it paves the way for studies of snowfall across scales. The in situ imaging instruments, whether airborne or ground-based, inform on detailed geometrical properties of individual snow particles. Conversely, the meteorological radars reveal statistical

information on the microphysics of snow particle populations in the entire atmospheric column. The synergy between ground-based remote sensing and airborne in situ instruments is one of the highlights of the campaign: it allows for bridging the gap between the indirect but spatially extended measurements of the former, and the refined but spatially restricted observations collected by the latter.

In the context of this thesis, the ICE GENESIS dataset fueled the research conducted in Chapters 4 to 6, by providing not only radar measurements, the starting point of our investigations, but also in situ measurements against which to validate the retrieved estimates of snowfall properties (Chapter 5) or the proposed microphysical interpretations (Chapter 6).

- **Liquid water path retrieval from radiometer measurements**

Chapter 3 introduces a simple deep learning method to retrieve LWP and IWV from 89 GHz radiometer measurements complemented with additional features, including surface meteorological variables, geographical information and, when available, reanalysis data. Through this approach, the retrieval algorithm can be implemented on measurements from diverse locations with a well-characterized uncertainty (18%).

Readily available estimates of LWP are valuable to cloud scientists, for whom the monitoring of MPCs, and the modeling of processes that drive their formation, persistence, and decay are important questions. Besides these cloud-focused applications, characterizing atmospheric liquid water is a necessary detour to take to study snowfall microphysics, for several reasons.

A first way in which the monitoring of column-integrated liquid water during snowfall pertains to snowfall microphysical studies is for the detection of riming, which significantly modifies the microphysical properties of individual snow particles, by making them more sphere-like, and by increasing their mass and terminal velocity. Secondly, and along the same direction, SLW and/or rimed snow particles are involved in the dominant known SIP mechanisms, which in turn may affect precipitation patterns and amounts as well as cloud radiative properties (*Young et al.*, 2019; *Luke et al.*, 2021), and are the subject of active research.

Lastly, monitoring cloud liquid water is important to radar meteorologists working with millimeter-wavelength instruments, as it is a significant source of signal attenuation in these frequency bands. LWP estimates allow for a quantification of uncertainty in reflectivity-based radar products (*Tridon and Battaglia*, 2015); this is indispensable for further interpretations of radar measurements and even more so for quantitative retrieval-oriented works. This aspect is leveraged in Chapter 4, where we use the LWP estimates to correct for W-band liquid water attenuation, also detailed in Appendix A.

- **Retrieval of snowfall microphysical properties: framework design and evaluation**

In Chapter 4, a novel deep learning framework is introduced to retrieve snowfall microphysical properties from dual-frequency Doppler spectrograms. The algorithm is implemented (Chapter 5) on the ICE GENESIS dataset and evaluated against in situ measurements, showing promising results in spite of discrepancies in the retrieval of size descriptors, for which likely causes are discussed.

The potential of multi-frequency radar measurements, on the one hand, and of radar Doppler spectra, on the other hand, for snowfall studies, has long been recognized (*Matrosov et al.*, 1992; *Shupe et al.*, 2004; *Luke and Kollias*, 2013). When attempting to combine both approaches for actually retrieving snowfall properties from dual-frequency (e.g., X- and W-band) Doppler spectra, substantial challenges are faced due to the conjunction of measurement errors, differential attenuation, and atmospheric dynamic effects, which make the inverse problem a highly ill-posed one.

The deep-learning based perspective which we bring on this problem helps relieve some of these fundamental difficulties and mitigate the ill-posedness. The proposed approach can be implemented on radars with different beam widths and imperfect vertical alignment in conditions of (moderate) atmospheric turbulence: this is a novelty compared to previous studies, where retrievals were conducted on selected events with low, if not zero, turbulence (e.g., *Barrett et al.*, 2019). Extending the conditions where snowfall properties are retrieved from dual-frequency Doppler spectra means that a more diverse range of atmospheric conditions can be sampled, leading to possibly less biased and consequently more robust characterizations of microphysical properties.

Our method additionally relaxes a number of microphysical assumptions on snowfall properties, in comparison with existing retrievals (e.g., *Szyrmer and Zawadzki*, 2014; *Liao et al.*, 2016; *Barrett et al.*, 2019; *Tetoni et al.*, 2022; *Mróz et al.*, 2021a), and a total of seven different statistical descriptors of microphysical properties are estimated. One important premise which is largely relieved, is the prior assumption on a mass-dimensional relation, previously often assumed constant (e.g., *Barrett et al.*, 2019; *Tetoni et al.*, 2022). Given the broad variety of habits that snow particles can take on, capturing this mass-related information within a retrieval is crucial. Certain hypotheses remain and the comparisons with in situ measurements indicate that certain biases in the retrieved variables are present, as discussed in detail in Chapter 5.

In spite of these biases, and after having constrained them, the proposed framework could be used to derive basic statistics on how snowfall properties are distributed in the atmospheric column. In that sense, the implementation of the retrieval on the ICE GENESIS dataset, at the end of Chapter 5, gives a flavor of what could be obtained if the method were to be used on larger datasets. Within the framework of the ICE GENESIS project, this statistical characterization was combined with detailed in situ quantification of the snow particle geometrical properties, for a both precise and spatially distributed description of snowfall microphysics.

- **Gaining insights into snowfall microphysical processes from a case study**

In Chapter 6, possible signatures of different secondary ice production processes are identified during a case study of the ICE GENESIS campaign, where a seeder-feeder configuration prevailed. The analysis relies primarily on dual-polarization W-band Doppler spectra, complemented with X-band reflectivity as well as in situ aircraft observations and profiles of atmospheric variables from WRF simulations.

A quantitative characterization of snowfall microphysical *properties*, as explored in Chapters 4 and 5, is essential, but not sufficient to capture a full picture of snowfall microphysics as it does not address the question of the *processes* through which snow particles are formed, grow or decay. By focusing on a specific case study, Chapter 6 illustrates how radar observations can be used to study complex, entangled microphysical processes. The retrieval of snowfall properties designed in Chapter 4 could not be directly implemented on this event because of the strong multi-modalities in the Doppler spectra which are, to this stage, not captured by the retrieval framework. Nonetheless, dual-frequency and spectral radar measurements were decisive in identifying possible microphysical processes, as they provided a comprehensive spatio-temporal view into the precipitating system.

It is found that within short time intervals, distinct mechanisms of ice production took place, as evidenced by different fingerprints in the observations. The varying strength of the liquid water supply, controlled by synoptic and terrain-related features, was a likely driver of these microphysical processes. In phases with rather modest LWC, HM rime splintering was probably occurring at temperatures warmer than -8°C; when the LWC was greater and associated with larger-sized droplets, signatures could be explained by droplet freezing and/or shattering upon freezing, at colder temperatures. Finally, unstable atmospheric conditions with localized turbulent updrafts favored yet another type of microphysical fingerprint which might be attributed to SIP through collisional breakup.

Summary of the contributions

Figure 7.1 summarizes how the different chapters contribute to addressing the overarching theme of snowfall microphysics, and specifically our central question: how can remote sensing, in particular dual-frequency and Doppler spectral radar measurements, be used to characterize snowfall properties and processes?

The first aspect is the dataset collected during ICE GENESIS, shared with the scientific community, and which opens up new possibilities for snowfall microphysical studies. Then, the novel microphysical retrieval framework that we developed allows for a **quantitative description of snowfall properties** in the entire atmospheric column, and paves the way for an advanced characterization of how these properties are distributed in altitude or depending on atmospheric conditions. Lastly, we demonstrate the possibility to gain **insights into snowfall microphysical processes**, and in particular into the diversity of ice production mechanisms, through the analysis of Doppler spectral and dual-frequency radar measurements. The re-

trieval of LWP is an important milestone that contributes both to the correction of radar measurements prior to retrieving snowfall properties, and to the identification of mixed-phase conditions from a process-oriented perspective.
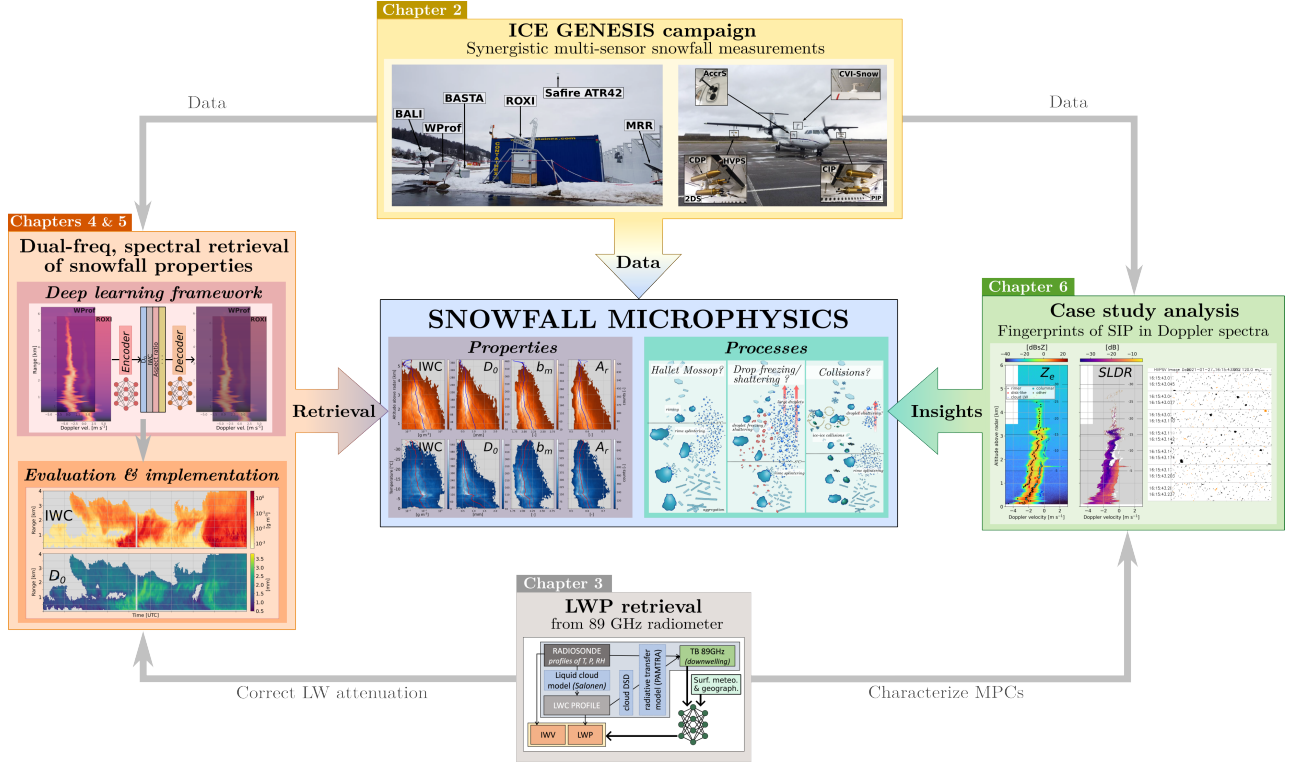
Figure 7.1: Overview of the different projects conducted during this thesis, organized as chapters. Gray arrows indicate how methods or data from one project are used in other chapters. The figures are taken from the different chapters to recall the main results and/or methodological developments.

7.2 Open questions and perspectives

In this last section, we discuss the main limitations of the studies conducted during this thesis, along with perspectives for future work, ranging from technical extensions of our work to more open questions.

- **Spectral radar retrieval of snowfall properties: improvements and extensions**

The shortcomings of the deep-learning-based snowfall retrieval were discussed in length in Chapter 5. A few directions were identified for future improvements of the framework; they include an extension of the training set and a more refined parameterization of the forward model, which would take into account diverse PSD shapes and more accurate scattering calculations.

Beyond these technical considerations, other avenues may be explored in further developments of the retrieval. Using Doppler spectrograms at a third frequency (e.g., Ka-band), would

likely be helpful to capture information on bulk density and PSD shape (*Leinonen et al.*, 2018; *Mason et al.*, 2019; *Mróz et al.*, 2021a). Relevant extensions would also enable the framework to ingest multi-modal Doppler spectra, and accordingly retrieve microphysical properties of several coexisting populations of snow particles. Note that this comes with certain challenges, as spectral peaks may not be well separated in the measurements of both radars due to differential beam broadening; an increase in computational costs could become an additional concern requiring non-trivial optimizations.

A natural further step to take would be implementing the retrieval, possibly with some of the afore-mentioned adjustments, on a larger dataset of multi-frequency Doppler spectrograms. For this purpose, longer time frames should be considered than that of ICE GENESIS. Including data collected at diverse geographical locations would also enable a more statistically-relevant characterization of snowfall properties. One possibility would be to complement the ICE GENESIS dataset, which reflects snowfall in mild orography, with data from flatland regions (e.g., *Dias Neto et al.*, 2019), and possibly high-latitude environments (e.g., *Petäjä et al.*, 2016), to capture the diversity of snowfall properties. Along the line of the preliminary statistics derived on the ICE GENESIS dataset at the end of Chapter 5, an extended implementation of the retrieval would allow addressing a number of scientific questions, for example: how frequently and under what conditions do aggregation, riming, or dendritic growth occur— identified through D_0, mass–size coefficients and/or aspect ratio, and temperature profile information.

Another direction which could yield promising results, is the implementation of the two-step deep learning framework, not on full Doppler spectrograms, but on time series of multi-frequency radar moments. This entails letting go of the detailed information contained in the spectra, and possibly reducing the number of retrieved variables; in return, it would allow for snowfall retrievals on much broader datasets. Collecting full Doppler spectra comes with high storage costs, and is mostly done during restrained campaigns, while radar moments are more widely used and may be available in more diverse settings. Fruitful comparisons of our framework to existing moment-based retrievals (*Chase et al.*, 2021) may open up directions for improvements with, further down the road, possible applications also for satellite retrievals of precipitation microphysics.

- **Improving the quantification of liquid water in the atmospheric column**

Although snowfall is the primary focus of this thesis, supercooled liquid water and mixed phase clouds are recurrently mentioned throughout this dissertation. The microphysical processes of snowfall are tightly linked to the presence of supercooled water droplets, whose quantification is thus of prominent importance.

The vertically-integrated information provided by the LWP is coarse, and does not provide detail on the structure of SLW cloud layers in the atmospheric column. The fact that the validity of our LWP retrieval drops in raining conditions is also a drawback, as it implies that it cannot be used to study snowfall processes above the melting layer in cases of cold stratiform

rainfall. To overcome these limitations, retrieving information on the full vertical profile of liquid water content would be beneficial. It would greatly improve the correction of W-band attenuation, resulting in higher accuracy of subsequent snowfall retrievals (Chapters 4 and 5). From a process-oriented perspective, a detailed LWC profile would be a robust help to detect the onset of riming and/or of SIP.

Full LWC profiles can be obtained with multi-frequency radiometers (*Rose et al.*, 2005), but these are not always available, and in particular, were not part of the ICE GENESIS setup. With the instrumental configuration used in this dissertation, a possibility would be to revisit the dual-frequency spectral radar retrieval to obtain an additional estimate of attenuation and/or LWC profiles. The latent space would contain, as new dimensions, LWC and/or attenuation values at each range gate, from which a cumulative attenuation profile would be computed to correct W-band spectrograms within the pipeline itself; meanwhile, the single-channel LWP retrieval would serve as a constraint on the vertical integral of LWC. Information on the detailed structure of the liquid cloud layers may also be obtained from the spectra through independent methods such as the machine-learning based algorithm proposed by *Schimmel et al.* (2022).

- **Systematic studies of SIP processes**

The analysis conducted in Chapter 6 illustrates how signatures of complex microphysical processes can be disentangled by making use of the rich information in Doppler spectral and multi-frequency radar measurements. In addition to the detailed analysis of a few short time frames, we also proposed tools to study the coexistence of different hydrometeor populations in radar volumes—specifically, with a four-class labeling method based on the spectral moments and (S)LDR of individual Doppler peaks. *Luke et al.* (2021) laid the ground for systematic studies of SIP using radar Doppler spectra in the Arctic, and showed the importance of studying not only the better-known HM process but also other SIP processes, as they notably found a frequent occurrence of droplet shattering. One limitation of their study was to identify secondary ice particles primarily through high spectral LDR values: this disregards SIP processes occurring at temperatures colder than the columnar growth regime, which would generate low-LDR crystals. Implementing more detailed peak classification routines, such as that introduced in Chapter 6, could be relevant to characterize SIP occurrence in more diverse atmospheric conditions (*Korolev et al.*, 2020, 2022).

Further work would also investigate whether the various signatures identified in this individual case study are statistically significant. Possible questions to be addressed are: Is the signature which we attributed to HM *always* observed, when a rimer population falls through a SLW layer at temperatures above -8°C? Under what circumstances do localized updrafts / generating cells produce a secondary mode, as observed in the later stages of our case study, and what causes these updrafts? What is the impact of these processes on the depletion of cloud liquid water, and on surface precipitation fluxes? What role does the orography play in the emergence of such seeder-feeder configurations?

- **Bringing together properties and processes**

Taking a few steps back, we open up the discussion to broader perspectives and examine how radar-based studies of snowfall microphysics may contribute to the more general objective of improving the parameterization of ice/ mixed-phase clouds and snowfall in weather and climate models. Modelers are interested both in the quantitative description of snow particles, and in the physical mechanisms that drive their evolution along their fall trajectory. Quantitative precipitation forecasting is a good example, where knowledge of e.g., snowfall PSD and bulk density, and of the processes by which they are modified, are required to lay down the physical equations predicting snow- or rainfall rate at the ground and the spatial distribution of precipitation.

Bridging the gap between quantitative retrievals and qualitative process-oriented studies is not easily done. As illustrated in Chapter 6 with the implementation of the LI21 SIP identification method, combining a physical modeling of snowfall processes with radar measurements comes with uncertainties that propagate across the model and are difficult to constrain. This highlights the interest of possible future work in this direction, to develop mathematical frameworks that would facilitate the integration of physics-based modeling and observations.

Meanwhile, novel insights may stem from high-resolution numerical modeling, which can help bring together remote sensing studies of snowfall properties and processes (e.g., *Vignon et al.*, 2019; *Oue et al.*, 2020; *Vignon et al.*, 2021; *Gehring et al.*, 2022). By defining hypotheses on the physical processes that take place, putting them into equations, and resolving them numerically, one can compare the simulated physical quantities to those retrieved from measurements, and thus validate or rule out the underlying initial hypotheses. Conversely, statistics may be derived from remote sensing retrievals to describe, for instance, how microphysical properties depend on e.g., temperature, humidity, altitude, or how they are correlated with each other. These can then serve for model verification, to endorse hypotheses or parameterizations, or on the contrary, point to discrepancies and loopholes in numerical models (*Ori et al.*, 2020; *Trömel et al.*, 2021; *Shrestha et al.*, 2022). Ultimately, knowledge gained from remote sensing approaches—possibly combined with in situ observations and even laboratory experiments—fosters the development of more accurate microphysical parameterizations of numerical weather models, which in turn serve an improved understanding of observations at all scales.

- **Deep learning for clouds and precipitation**

Finally, a few words may be added to emphasize the role of machine-learning-based techniques in future work on snowfall microphysics and more generally, on clouds and precipitation. We pointed out in Chapters 4 and 5 that, besides the retrieval of snowfall properties that it enables, the framework that we proposed may be of interest to a broader audience, as it could be transposed to other inversion problems. This also highlights the relevance of deep learning as a tool in atmospheric sciences as a whole. On a first level, machine learning offers an undeniable potential to perform efficient non-linear approximations, as in the LWP

retrieval of Chapter 3. Beyond this, it also opens up new ways to address problems which are difficult to solve with classical methods, either because of their underdetermination, or due to their high-dimensionality (*Behrens et al.*, 2022), the large size of the datasets, and the resulting computational costs.

Deep learning methods come with shortcomings. They commonly raise skepticism because of their lack of interpretability, and their incapacity to assimilate physical constraints. Nonetheless, thriving research in recent years has shown many ways in which these obstacles can be mitigated, either by improving model stability and explainability (*Brenowitz et al.*, 2020; *White et al.*, 2022) or by incorporating physical knowledge into the models (*Beucler et al.*, 2021). Substantial efforts are devoted to bringing together machine learning and physical knowledge, by designing new models and new frameworks, with promising outlooks (*McGovern and Broccoli*, 2022). Atmospheric remote sensing, whether ground- or satellite-based, with the abundant data it makes available, will likely participate to and benefit from the development of such data-driven frameworks.

A Consistency of the attenuation correction

In this Appendix section, we come back on the attenuation correction of WProf measurements which was implemented in Chapter 4, to verify its consistency. Specifically, we consider two possible attenuation correction methods: the first approach (Method 1) is the one described in Chapter 4, Sect. 4.4.2, which follows *Kneifel et al.* (2015); an alternative approach is also tested as detailed below (Method 2), relying solely on COSMO-1 analyses.

Method 1

- Gaseous attenuation: atmospheric profiles are taken from hourly COSMO-1 analyses (*Consortium for Small-scale Modeling*, 2017), and the corresponding profile of gaseous attenuation is computed using PAMTRA.

- Snowfall attenuation: a baseline $Z_{e,X}$–IWC relation (IWC = 0.015 $Z_{e,X}^{0.44}$, *Kneifel et al.*, 2015; *Boudala et al.*, 2006, with Z_e in mm^6 m^{-3}) is used to estimate the profile of snow and ice content; the corresponding attenuation profile is obtained considering that ice attenuates around 0.9 dB km^{-1}(g m^{-3})$^{-1}$ (*Nemarich et al.*, 1988).

- Liquid water attenuation: we use the LWP retrieved from 89 GHz radiometer measurements (following Chapter 3), and assume a uniform LWC profile in the cloud/precipitation column (range gates with $Z_{e,W} > -30$ dBZ). The corresponding attenuation profile is then computed with PAMTRA using the COSMO-1 profiles of standar atmospheric variables.

Method 2

- Gaseous attenuation: atmospheric profiles are taken from hourly COSMO-1 analyses, and the corresponding profiles of gaseous attenuation are computed using PAMTRA.

- Snowfall attenuation: profiles of ice, snow and graupel mixing ratio are also taken from COSMO-1 analyses; the corresponding attenuation profile is modeled with PAMTRA using Mie scattering, with a constant mass–size relation (a_m = 0.0185 g m$^{-1.9}$, b_m = 1.9) and a single exponential PSD with D_0 = 0.5 mm; there is little sensitivity to this choice as attenuation by ice particles is typically small in comparison with liquid water.

- Liquid water attenuation: profiles of cloud water mixing ratio from COSMO-1 analyses are used. The corresponding attenuation profile is computed with PAMTRA under the same assumptions as Method 1 (namely, monodisperse cloud drop size distribution with a diameter of 20 μm).

To verify the consistency of the attenuation correction, the profiles of atmospheric variables as well as snow and liquid water content derived in Methods 1 and 2 are input to PAMTRA to simulate brightness temperature at 89 GHz. The agreement between simulated and measured T_B is a sanity check that the total path-integrated attenuation (PIA) is appropriately modeled: indeed, as attenuating targets are also emitters, T_B and PIA are intrinsically related. We underline that this check does not allow to assess the quality of the modeled attenuation profile, but only provides column-integrated information.
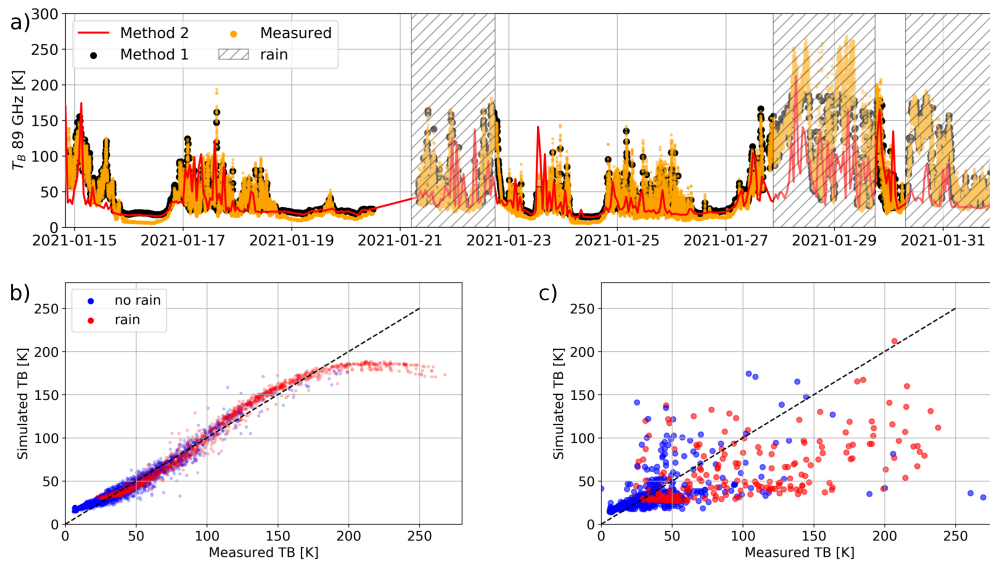
Figure A.1: Comparison of measured and simulated T_B at 89 GHz using the profiles of Methods 1 and 2. (a) Timeseries of T_B; time frames where rain was observed at the ground are indicated as hatched gray zones. (b) Scatter plot of T_B simulated with Method 1 vs. measured. (c) Scatter plot of T_B simulated with Method 2 vs. measured (a 10-minute temporal average of the measurements is used in panel (c) to account for possible timing inconsistencies; no significant difference is visible when using instantaneous values).

Figure A.1a shows the time series of measured and simulated T_B (with the profiles reconstructed through Methods 1 and 2), and the corresponding density plots (Fig. A.1b and c). Method 1 yields an RMSE of 10 K ($R = 0.98$, scatter plot of Fig. A.1b), while lower accuracy results from Method 2 (RMSE = 43 K, $R = 0.6$, Fig. A.1c). This is likely due to the high temporal variability of T_B, which is difficult to capture from COSMO-1 hourly data. Note that even with Method 1, the accuracy decreases in rainy cases with high T_B; this was anticipated as both the LWP retrieval and the T_B modeling used here only consider cloud profiles, and their validity drops in rain.

Naturally, in the case of Method 1, the LWP estimate itself depends on measured brightness temperature, so the agreement is expected, but this self-consistency is reassuring. This overall supports the choice of the first method over the second: even though the COSMO-based approach allows for a refined LWC profile instead of a uniform one, it does not result in sufficiently reliable total attenuation / brightness temperature simulations to be considered preferable.

As a side remark, to further exploit the link between microwave emission and absorption, we note that T_B may directly be used to estimate the PIA. This is in essence similar to the results of *Tridon and Battaglia* (2015), who found that W-band PIA was closely related to the LWP retrieved with an independent microwave radiometer. We use the COSMO-1 profiles, through which we simulate both PIA (through Method 2) and T_B: Fig. A.2 shows the good (quadratic) correlation between the two quantities. The parameterization of this relationship is likely dependent on the geographical location and atmospheric profile, but the correlation obtained on the time frame of ICE GENESIS data where WProf was deployed (330 hours) is high ($R = 0.996$ with a quadratic fit): this indicates a good robustness of this relationship even within relatively diverse wintertime atmospheric conditions in La Chaux-de-Fonds. This relation may thus be used to obtain a rough estimate of the PIA, directly computed from T_B, in order to assess the importance of attenuation during a given snowfall event. It does not, however, inform on how attenuation is distributed in the atmospheric column.
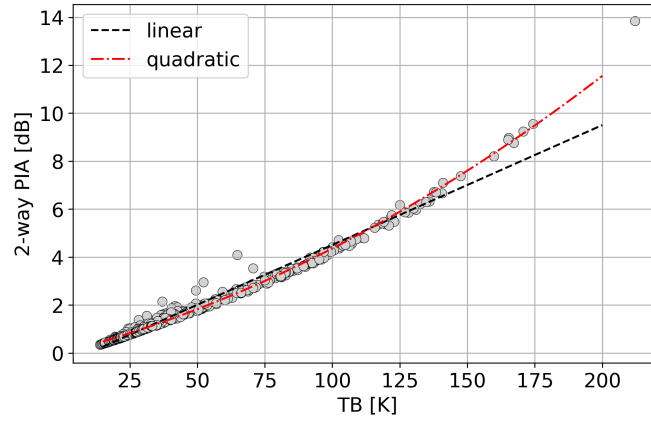
Figure A.2: 2-way PIA and T_B simulated with PAMTRA using COSMO-1 profiles at an hourly resolution (14 - 31 January 2021) over la Chaux-de-Fonds. The linear fit is $PIA_{2-way} = 0.04994\,T_B - 0.4841$, with an RMSE of 0.25 dB and $R = 0.987$; the quadratic fit is $PIA_{2-way} = 0.0001421\,T_B^2 + 0.02933\,T_B + 0.00766$ (RMSE = 0.15 dB, $R = 0.996$).

B Comparison of the snowfall retrieval to other frameworks

In this Appendix, we discuss the microphysical retrieval pipeline that was developed in Chapter 4 in comparison with other possible approaches. It is adapted from the Appendix of the article:

- **Anne-Claire Billault-Roux**, Gionata Ghiggi, Louis Jaffeux, Audrey Martini, Nicolas Viltard and Alexis Berne (2023): Dual-frequency spectral radar retrieval of snowfall microphysics: a physics-driven deep-learning approach. *Atmospheric Measurement Techniques*, 16(4), 911–940, doi: 10.5194/amt-16-911-2023.

B.1   Gate-to-gate deep learning inversion

One of the motivations to use the architecture proposed in Chapter 4 is the ill-posedness of the problem, which is an obstacle to direct inversion methods that would take as input Doppler spectra at a given range and output corresponding microphysical properties. We believe that the framework we introduced partly mitigates this underdetermination by ingesting the full spectrograms (in a convolutional neural network), instead of operating on individual spectra. To support this, we also implemented a "gate-to-gate" inversion, through a deep learning framework trained on the same synthetic dataset as the one used to train the decoder. It essentially consists in learning the inverse of our decoder, similar to the approach of *Chase et al.* (2021), i.e., directly fitting an approximation of the inverse mapping, $\tilde{g}$. The notations used here are those of Chapter 4, Sect. 4.3.

This time, the input consists of dual-frequency spectra, and the output is the set of microphysical and atmospheric descriptors (same as Table 4.1). The architecture, illustrated in Fig. B.1, is virtually the same as the encoder (Fig 4.7b), except that 2-dimensional convolutions are now 1-D: the neural network is not trained on full spectrograms but on single-gate spectra, thus the range dimension is equal to 1.

After training and tuning, the model is applied to the ICE GENESIS dataset. Figure B.2 shows the same variables as in the left panels of Fig. 5.1, retrieved through this *direct* inversion.
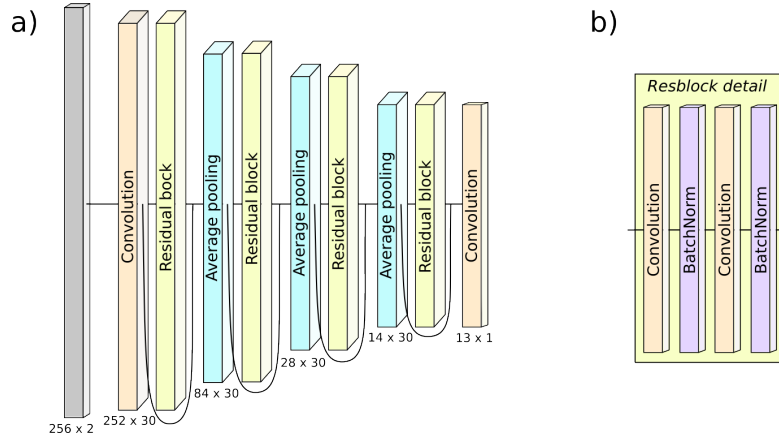
Figure B.1: (a) Architecture of the gate-to-gate deep learning retrieval. (b) Detail of the residual block composition. The notations are those of Chapter 4.

Overall, the order of magnitude of the variables is similar to that obtained with the new pipeline, and the very general spatio-temporal structure is also visible. This is reassuring since it suggests that the training dataset was appropriate and indeed captured the scope of possibly observed spectra. However, it is also apparent that the retrieved variables are substantially noisier than through our method, reflecting the ill-posedness issue. When comparing these retrieved results with aircraft in-situ measurements, as done in Section 5.3, we obtain for example R = 0.59 for IWC (instead of R = 0.87). Some variables also reach unrealistic values, e.g., negative values of D_0.
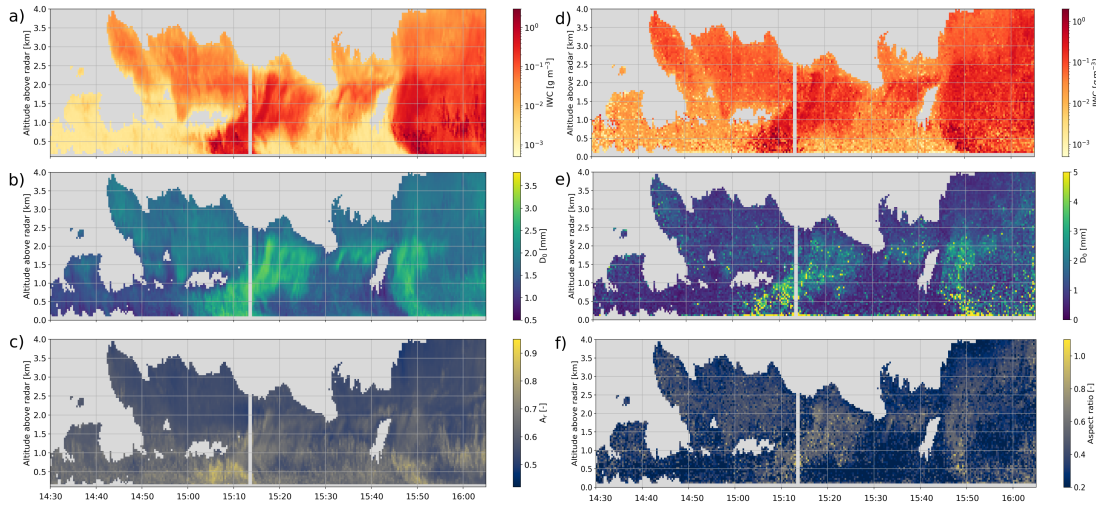
Figure B.2: Comparison of timeseries for three examples of variables (IWC, D_0 and A_r) retrieved through the proposed framework (left panels) or a direct deep-learning retrieval (right panels). Note that the colorbars may differ (adjusted to reflect at best the variability in each field).

B.2 Alternative approach

We briefly mention an alternative approach that could be used, which lies halfway between classical Bayesian optimal estimation and the framework we introduced. If a differentiable approximation of the forward model is known ($\tilde{f}$), another way to look for $\boldsymbol{X_r}$ is to find the minimizing argument of $||\tilde{F}(\boldsymbol{X}) - \boldsymbol{Y_r}||^2$ using gradient descent; a regularizing term can be added to ensure, for instance, the spatial continuity of $\boldsymbol{X}$ or to enforce some degree of spatiotemporal smoothness. This requires only one deep learning model instead of two, and could thus seem more appealing, but the approach of Chapter 4 was preferred. Indeed, by actually learning an approximation of the inverse mapping $\tilde{G}$ and doing so on a large dataset, the risk of reaching a local minimum in $\boldsymbol{X}$ is reduced. Our method also does not require any explicit prior assumption on $\boldsymbol{X}$, or on any property of the latent space, like spatial smoothness; rather, it is constrained by the spatial structure of the observed signal itself.

C Details on the implementation of LI21

In this Appendix, we detail the equations used in Chapter 6 with the implementation of the SIP identification method proposed by *Li et al.* (2021b). The text is adapted from the Appendix of the submitted manuscript:

- **Anne-Claire Billault-Roux**, Paraskevi Georgakaki, Josué Gehring, Louis Jaffeux, Alfons Schwarzenboeck, Pierre Coutris, Athanasios Nenes, Alexis Berne (2023): Distinct secondary ice production processes observed in radar Doppler spectra: insights from a case study. *Under review for Atmospheric Chemistry and Physics*, doi: 10.5194/egusphere-2023-478.

C.1 Diffusional growth model

To model the growth of ice crystals by vapor deposition, we implement the ventilated diffusion growth model presented in *Pruppacher and Klett* (2010), Ch. 13, following e.g., *Hall and Pruppacher* (1976), relying on the following equation:

$$\frac{dm}{dt} = \frac{4\pi C S_i f_v}{(\frac{L_s}{R_v T} - 1)\frac{L_s}{K_{air}T} + \frac{R_v T}{e_{s,ice}\mathscr{D}_v}} \tag{C.1}$$

Here and below, all values are given in SI units unless specified otherwise. T is the air temperature, S_i is the supersaturation over ice; assuming conditions of saturation with respect to liquid water, it is equal to:

$$S_i = (e_{s,liq}(T) - e_{s,ice}(T))/e_{s,ice}(T) \tag{C.2}$$

where $e_{s,liq}(T)$ and $e_{s,ice}(T)$ are respectively the saturation vapor pressure over liquid water and over ice (e.g., *Huang*, 2018). L_s is the latent heat of sublimation (*Yau and Rogers*, 1989):

$$L_s = (2834.1 - 0.29(T - 273.15) - 0.004(T - 273.15)^2) \times 10^3 \tag{C.3}$$

165

K_{air} is the thermal conductivity of air, R_v is the gas constant of water vapor and $\mathcal{D}_v$ is the molecular diffusion coefficient of water vapor in air (*Pruppacher and Klett*, 2010, Ch. 13), with P denoting the pressure, $T_0 = 273.15$ K and $P_0 = 1013.25$ hPa:

$$\mathcal{D}_v = 0.211 \times 10^{-4} \left(\frac{T}{T_0} \right)^{1.94} \frac{P_0}{P} \tag{C.4}$$

f_v is the ventilation coefficient, which depends on particle habit: in this study we used the equations of *Pruppacher and Klett* (2010), Ch. 13, and *Ji and Wang* (1999) for columnar (CC), plate-like (PLATE) and dendritic (DEN) crystals:

$$f_{v,CC} = 1 - 0.00668 \left(\frac{X}{4} \right) + 2.39402 \left(\frac{X}{4} \right)^2 + 0.73409 \left(\frac{X}{4} \right)^3 - 0.73911 \left(\frac{X}{4} \right)^4 \tag{C.5}$$

$$f_{v,PLATE} = 1 - 0.6042 \left(\frac{X}{10} \right) + 2.79820 \left(\frac{X}{10} \right)^2 + 0.31933 \left(\frac{X}{10} \right)^3 - 0.06247 \left(\frac{X}{10} \right)^4 \tag{C.6}$$

$$f_{v,DEN} = 1 + 0.35463 \left(\frac{X}{10} \right) + 3.55333 \left(\frac{X}{10} \right)^2 \tag{C.7}$$

where $X = Sc^{\frac{1}{3}} Re^{\frac{1}{2}}$ depends on the Schmidt number $Sc = 0.632$ and the Reynolds number $Re = \frac{\rho_a L_* v}{\mu_a}$ with ρ_a and μ_a the density and dynamic viscosity of air. Re in turn relies on a spheroidal model of the ice crystals (prolate for needle-like particles, oblate for planar particles) with L_* the effective aerodynamic size defined as the ratio of the spheroid total surface area Ω_{sph} to the perimeter P_{sph} of its projection normal to the flow:

$$L_* = \frac{\Omega_{sph}}{P_{sph}} \tag{C.8}$$

$$\Omega_{sph,obl} = \frac{\pi}{2} D^2 + \frac{\pi}{4} \frac{A_r^2 D^2}{e} \ln \left(\frac{1+e}{1-e} \right) \tag{C.9}$$

$$\Omega_{sph,prol} = \frac{\pi}{2} \frac{D^2}{A_r^2} \left(1 + A_r \frac{\arcsin(e)}{e} \right) \tag{C.10}$$

$$P_{sph,obl} = \pi D \tag{C.11}$$

$$P_{sph,prol} = \pi D (1 - \frac{1}{4} e^2 - \frac{3}{64} e^4 - \frac{5}{256} e^6 - \frac{89}{8192} e^8 - \frac{231}{32768} e^{10}) \tag{C.12}$$

where $e^2 = 1 - A_r^2$ for oblate spheroids and $e^2 = 1 - \frac{1}{A_r^2}$ for prolate spheroids, D is the particle maximum diameter, A_r is the aspect ratio ($A_r > 1$ for prolate, $A_r < 1$ for oblate spheroids).

The capacitance C is also a function of particle geometry, for which we again followed *Prup-*

pacher and Klett (2010), Ch. 13:

$$C_{obl} = \frac{D\sqrt{1-A_r^2}}{\arcsin(\sqrt{1-A_r^2})} \tag{C.13}$$

$$C_{prol} = \frac{D}{A_r} \frac{\sqrt{A_r^2-1}}{\ln(A_r + \sqrt{A_r^2-1})} \tag{C.14}$$

We additionally use parameterizations of mass–size and velocity–size relations to propagate Eq. C.1 and model the growth of the ice crystals during their fall:

$$v = a_{v,m} \, m^{b_{v,m}} \left(\frac{P_1}{P}\right)^{0.35} \tag{C.15}$$

$$v = a_{v,d} \, D^{b_{v,d}} \left(\frac{P_0}{P}\right)^{0.35} \tag{C.16}$$

$$m = a_m D^{b_m} \tag{C.17}$$

where $P_1 = 8.8 \times 10^4$ Pa, and $a_{v,m}$, $b_{v,m}$, $a_{v,d}$, $b_{v,d}$, a_m, b_m are geometry-dependent coefficients listed in Table C.1. For columnar crystals: Eq. C.15 and the coefficients are from *Kajikawa* (1976); for planar crystals (plates and dendrites), Eq. C.16 and coefficients from *Heymsfield and Kajikawa* (1987).

Crystal type	A_r	a_v	b_v	$a_{v,d}$	$b_{v,d}$	a_m	b_m
COL2	2	107	0.271	-	-	0.00929	1.8
COL4	4	162	0.302	-	-	0.0185	1.9
COL8	8	66	0.271	-	-	0.00427	1.8
DEN	0.1	-	-	5.01	0.48	0.0232	2.29
DEN2	0.1	-	-	3.29	0.11	0.242	2.53
PLATE	0.2	-	-	29.5	0.68	1.78	2.81

Table C.1: Coefficients of the velocity–size ($v = a_{v,m} \, m^{b_{v,m}}$ or $v = a_{v,d} \, D^{b_{v,d}}$) and mass–size ($m = a_m D^{b_m}$) relations, where m is the mass of the crystal, D its maximum dimension and v its terminal velocity. SI units are used.

C.2   Comparison of modeled and estimated terminal velocity

The adequacy of the growth model and microphysical parameterization is verified by comparing the modeled terminal velocity to an estimate of the true one (v_t), shown in Fig. C.1. In the first implementation of the LI21 method in Sect. 6.6.1, this is done by considering as in *Li et al.* (2021b) that cloud SLW droplets are passive air motion tracers; the settling velocity of the ice particles is then estimated as $v_{t,CC1} = MDV_{CC1} - MDV_{CLW1}$. In the case of Sect. 6.6.2, there is no detected cloud SLW mode that would be fully separated from DL2; to correct for the possible effect of vertical air motion on MDV, we follow *Luke et al.* (2021) and use the velocity

at the edge of the spectrum, corrected with 0.2 m s^{-1} as a rough estimate of typical turbulent spread (the resulting velocity correction is v_a). In the last phase, the significant air motion and absence of a consistently detected SLW mode make the estimation of v_t much more difficult; Fig. C.1i illustrates the large difference between MDV$_{DL3}$ and $v_{t,DL3}$ =MDV$_{DL3}$ − v_a. The estimation of air motion as in *Luke et al.* (2021) used here to compute v_a is less reliable due to the greater spectral broadening in this turbulent region; as a result, the comparison of modeled vs. estimated v_t cannot be conclusive (Fig. C.1i). Note that possible riming of the crystals having grown to a sufficient size would not be adequately modeled by this approach, which considers exclusively depositional growth, and would also influence significantly the terminal velocity of the particles.
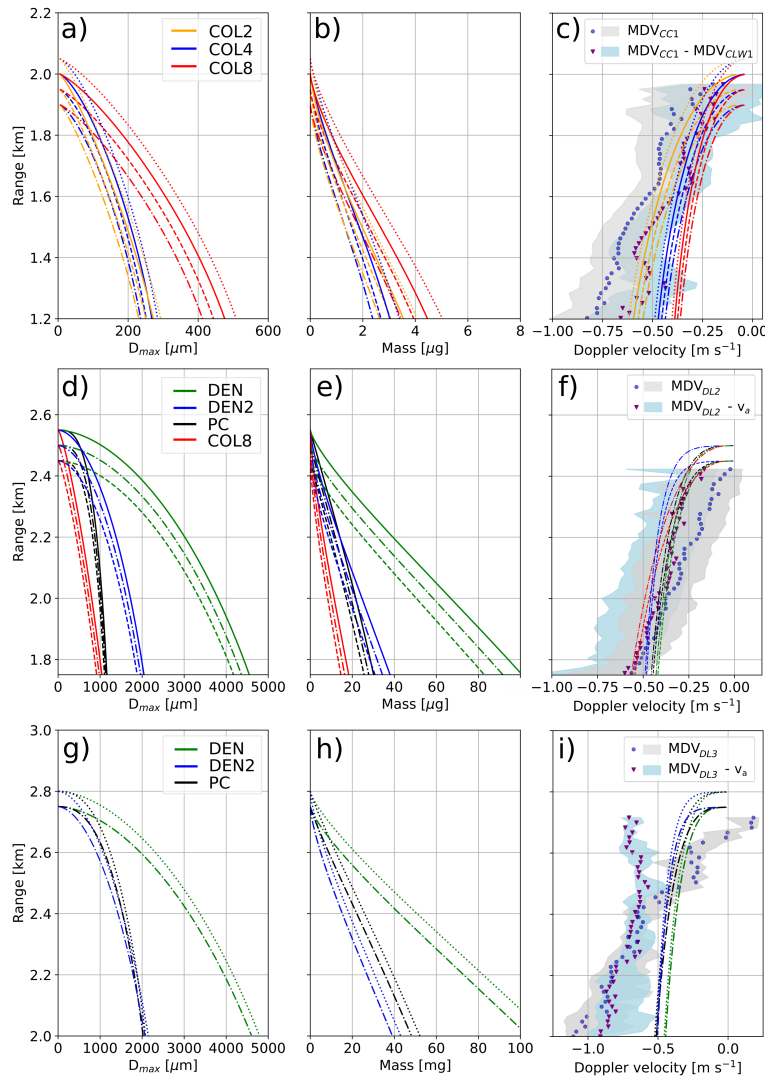
Figure C.1: Diffusional growth and terminal velocity modeled with the LI21 approach for the various phases (phase 1: (a)–(c), phase 2: (d)–(f), phase 3: (g)–(i)). Panels (a), (d), (g): modeled crystal maximum dimension; panels (b), (e), (h): modeled crystal mass (cf. Sect. C.1); panels (c), (f), (i): modeled v_t, with measured MDV and estimated v_t (cf. Sect. C.2, median and interquartile range are shown).

Bibliography

Acquistapace, C., S. Kneifel, U. Löhnert, P. Kollias, M. Maahn, and M. Bauer-Pfundstein (2017), Optimizing observations of drizzle onset with millimeter-wavelength radars, *Atmospheric Measurement Techniques*, *10*(5), 1783–1802, doi: 10.5194/amt-10-1783-2017.

Aguilar, B., K. Köbschall, L. Reitter, P. Trontin, F. Dezitter, J. Breitenbach, I. Roisman, O. Rouzaud, and P. Villedieu (2021), Experimental and numerical investigations of snow accretion, in *AIAA Aviation and Aeronautics Forum and Exposition, AIAA AVIATION Forum 2021*, American Institute of Aeronautics and Astronautics, Virtual event, doi: 10.2514/6.2021-2684.

Anderson, T. L., D. S. Covert, and R. J. Charlson (1994), Cloud droplet number studies with a counterflow virtual impactor, *Journal of Geophysical Research*, *99*(D4), 8249–8256, doi: 10.1029/93JD03522.

Andrić, J., M. R. Kumjian, D. S. Zrnić, J. M. Straka, and V. M. Melnikov (2013), Polarimetric Signatures above the Melting Layer in Winter Storms: An Observational and Modeling Study, *Journal of Applied Meteorology and Climatology*, *52*(3), 682–700, doi: 10.1175/JAMC-D-12-028.1.

Arias, P., et al. (2021), Climate Change 2021: The Physical Science Basis. Contribution of Working Group I to the Sixth Assessment Report of the Intergovernmental Panel on Climate Change; Technical Summary, in *The Intergovernmental Panel on Climate Change AR6*, edited by V. Masson-Delmotte, P. Zhai, A. Pirani, S. L. Conners, C. Péan, S. Berger, N. Caud, Y. Chen, L. Goldfarb, M. I. Gomis, M. Huang, K. Leitzell, E. Lonnoy, J. B. R. Matthews, T. K. Maycock, T. Waterfield, O. Yelek, R. Yu, and B. Zhou, doi: 10.1017/9781009157896.002.

Atlas, D., R. C. Srivastava, and R. S. Sekhon (1973), Doppler radar characteristics of precipitation at vertical incidence, *Reviews of Geophysics*, *11*(1), 1–35, doi: 10.1029/RG011i001p00001.

Atlas, R. L., C. S. Bretherton, P. N. Blossey, A. Gettelman, C. Bardeen, P. Lin, and Y. Ming (2020), How Well Do Large-Eddy Simulations and Global Climate Models Represent Observed Boundary Layer Structures and Low Clouds Over the Summertime Southern Ocean?, *Journal of Advances in Modeling Earth Systems*, *12*(11), 1–25, doi: 10.1029/2020MS002205.

Aydin, K., and C. Tang (1997), Relationships between IWC and polarimetric radar measurands at 94 and 220 GHz for hexagonal columns and plates, *Journal of Atmospheric and Oceanic Technology*, *14*(5), 1055–1063, doi: 10.1175/1520-0426(1997)014<1055:RBIAPR>2.0.CO;2.

Bibliography

Babb, D. M., J. Verlinde, and B. A. Albrecht (1999), Retrieval of Cloud Microphysical Parameters from 94-GHz Radar Doppler Power Spectra, *Journal of Atmospheric and Oceanic Technology*, *16*(5), 489–503, doi: 10.1175/1520-0426(1999)016<0489:ROCMPF>2.0.CO;2.

Bacon, N. J., B. D. Swanson, M. B. Baker, and E. J. Davis (1998), Breakup of levitated frost particles, *Journal of Geophysical Research: Atmospheres*, *103*(D12), 13,763–13,775, doi: 10.1029/98JD01162.

Baker, B., and R. P. Lawson (2006), Improvement in Determination of Ice Water Content from Two-Dimensional Particle Imagery. Part I: Image-to-Mass Relationships, *Journal of Applied Meteorology and Climatology*, *45*(9), 1282–1290, doi: 10.1175/JAM2398.1.

Balduzzi, D., M. Frean, L. Leary, J. Lewis, K. Wan-Duo Ma, and B. Mcwilliams (2017), Shattered Gradients, in *Proceedings of the 34th International Conference on Machine Learning*, pp. 342–350, Sydney, Australia, doi: 10.48550/arXiv.1702.08591.

Barrett, A., C. Westbrook, J. Nicol, and T. Stein (2019), Rapid ice aggregation process revealed through triple-wavelength Doppler spectra radar analysis, *Atmospheric Chemistry and Physics*, *19*(8), 5753–5769, doi: 10.5194/acp-2018-836.

Barthazy, E., W. Henrich, and A. Waldvogel (1998), Size distribution of hydrometeors through the melting layer, *Atmospheric Research*, *47-48*, 193–208, doi: 10.1016/S0169-8095(98)00065-9.

Battaglia, A., S. Tanelli, F. Tridon, S. Kneifel, J. Leinonen, and P. Kollias (2020), Triple-Frequency Radar Retrievals, in *Satellite Precipitation Measurement: Volume 1*, edited by V. Levizzani, C. Kidd, D. B. Kirschbaum, C. D. Kummerow, K. Nakamura, and F. J. Turk, chap. 13, pp. 211–229, Springer International Publishing, Cham, doi: 10.1007/978-3-030-24568-9.

Bauer, P., P. D. Dueben, T. Hoefler, T. Quintino, T. C. Schulthess, and N. P. Wedi (2021), The digital revolution of Earth-system science, *Nature Computational Science*, *1*(2), 104–113, doi: 10.1038/s43588-021-00023-0.

Baumgardner, D., et al. (2017), Cloud Ice Properties: In Situ Measurement Challenges, *Meteorological Monographs*, *58*, 1–9, doi: 10.1175/amsmonographs-d-16-0011.1.

Behrens, G., T. Beucler, P. Gentine, F. Iglesias-Suarez, M. Pritchard, and V. Eyring (2022), Non-Linear Dimensionality Reduction With a Variational Encoder Decoder to Understand Convective Processes in Climate Models, *Journal of Advances in Modeling Earth Systems*, *14*(8), e2022MS003,130, doi: 10.1029/2022MS003130.

Bellon, A., I. Zawadzki, and F. Fabry (1997), Measurements of melting layer attenuation at X-band frequencies, *European Journal of Radiology*, *32*(3), 943–955, doi: 10.1029/97RS00492.

Bergeron, T. (1935), On the physics of clouds and precipitation, in *Procès verbaux de l'Association de Météorologie, International Union of Geodesy and Geophysics*, pp. 156–178, Lisbon, Portugal.

Besic, N., J. Figueras i Ventura, J. Grazioli, M. Gabella, U. Germann, and A. Berne (2016), Hydrometeor classification through statistical clustering of polarimetric radar measurements: A semi-supervised approach, *Atmospheric Measurement Techniques*, *9*(9), 4425–4445, doi: 10.5194/amt-9-4425-2016.

Besic, N., J. Gehring, C. Praz, J. Figueras i Ventura, J. Grazioli, M. Gabella, U. Germann, and A. Berne (2018), Unraveling hydrometeor mixtures in polarimetric radar measurements, *Atmospheric Measurement Techniques*, *11*(8), 4847–4866, doi: 10.5194/amt-11-4847-2018.

Beucler, T., M. Pritchard, S. Rasp, J. Ott, P. Baldi, and P. Gentine (2021), Enforcing Analytic Constraints in Neural Networks Emulating Physical Systems, *Physical Review Letters*, *126*(9), 098,302, doi: 10.1103/PhysRevLett.126.098302.

Bevis, M., S. Businger, S. Chiswell, T. A. Herring, R. A. Anthes, C. Rocken, and R. Ware (1994), GPS Meteorology: Mapping Zenith Wet Delays onto Precipitable Water, *Journal of Applied Meteorology*, *33*, 379–386, doi: 10.1175/1520-0450(1994)033<0379:GMMZWD>2.0.CO;2.

Billault-Roux, A. C., and A. Berne (2021), Integrated water vapor and liquid water path retrieval using a single-channel radiometer, *Atmospheric Measurement Techniques*, *14*(4), 2749–2769, doi: 10.5194/amt-14-2749-2021.

Billault-Roux, A.-C., et al. (2023a), ICE GENESIS: Synergetic Aircraft and Ground-Based Remote Sensing and In Situ Measurements of Snowfall Microphysical Properties, *Bulletin of the American Meteorological Society*, *104*(2), E367–E388, doi: 10.1175/BAMS-D-21-0184.1.

Billault-Roux, A.-C., G. Ghiggi, L. Jaffeux, A. Martini, N. Viltard, and A. Berne (2023b), Dual-frequency spectral radar retrieval of snowfall microphysics: a physics-driven deep-learning approach, *Atmospheric Measurement Techniques*, *16*(4), 911–940, doi: 10.5194/amt-16-911-2023.

Borque, P., E. Luke, and P. Kollias (2016), On the unified estimation of turbulence eddy dissipation rate using Doppler cloud radars and lidars, *Journal of Geophysical Research: Atmospheres*, *120*, 5972–5989, doi: 10.1002/2015JD024543.

Boucher, O., C. G. France, C. H. Germany, and A. J. Uk (2013), Clouds and Aerosols, in *Climate Change 2013: The Physical Science Basis. Contribution of Working Group I to the Fifth Assessment Report of the Intergovernmental Panel on Climate Change*, edited by T. Stocker, D. Qin, G. K. Plattner, M. Tignor, S. K. Allen, J. Boschung, A. Nauels, Y. Xia, V. Bex, and P. M. Midgley, pp. 571–658, Cambridge University Press, Cambridge, United Kingdom and New York, NY, USA, doi: 10.1017/CBO9781107415324.016.

Boudala, F. S., G. A. Isaac, and D. Hudak (2006), Ice water content and precipitation rate as a function of equivalent radar reflectivity and temperature based on in situ observations, *Journal of Geophysical Research: Atmospheres*, *111*(11), 1–13, doi: 10.1029/2005JD006499.

Bibliography

Bousquet, O., et al. (2015), Multifrequency Radar Observations Collected in Southern France during HyMeX-SOP1, *Bulletin of the American Meteorological Society*, *96*(2), 267–282, doi: 10.1175/BAMS-D-13-00076.1.

Bousquet, O., J. Delanoë, and S. Bielli (2016), Evaluation of 3D wind observations inferred from the analysis of airborne and ground-based radars during HyMeX SOP-1, *Quarterly Journal of the Royal Meteorological Society*, *142*(8), 86–94, doi: 10.1002/qj.2710.

Brenowitz, N. D., T. Beucler, M. Pritchard, and C. S. Bretherton (2020), Interpreting and Stabilizing Machine-Learning Parametrizations of Convection, *Journal of the Atmospheric Sciences*, *77*(12), 4357–4375, doi: 10.1175/JAS-D-20-0082.1.

Bringi, V. N., V. Chandrasekar, J. Hubbert, E. Gorgucci, W. L. Randeu, and M. Schoenhuber (2003), Raindrop Size Distribution in Different Climatic Regimes from Disdrometer and Dual-Polarized Radar Analysis, *Journal of the Atmospheric Sciences*, *60*(2), 354–365, doi: 10.1175/1520-0469(2003)060<0354:RSDIDC>2.0.CO;2.

Brown, P. R., and P. N. Francis (1995), Improved Measurements of the Ice Water Content in Cirrus Using a Total-Water Probe, *Journal of Atmospheric and Oceanic Technology*, *12*(2), 410–414, doi: 10.1175/1520-0426(1995)012<0410:IMOTIW>2.0.CO;2.

Bukovčić, P., A. Ryzhkov, D. Zrnić, and G. Zhang (2018), Polarimetric Radar Relations for Quantification of Snow Based on Disdrometer Data, *Journal of Applied Meteorology and Climatology*, *57*(1), 103–120, doi: 10.1175/JAMC-D-17-0090.1.

Cadeddu, M. P., D. D. Turner, and J. C. Liljegren (2009), A Neural Network for Real-Time Retrievals of PWV and LWP From Arctic Millimeter-Wave Ground-Based Observations, *IEEE Transactions on Geoscience and Remote Sensing*, *47*(7), 1887–1900, doi: 10.1109/TGRS.2009.2013205.

Cadeddu, M. P., J. C. Liljegren, and D. D. Turner (2013), The Atmospheric Radiation Measurement (ARM) Program Network of Microwave Radiometers: Instrumentation, Data, and Retrievals, *Atmospheric Measurement Techniques*, *6*(9), 2359–2372, doi: 10.5194/amt-6-2359-2013.

Cadeddu, M. P., R. Marchand, E. Orlandi, D. D. Turner, and M. Mech (2017), Microwave Passive Ground-Based Retrievals of Cloud and Rain Liquid Water Path in Drizzling Clouds: Challenges and Possibilities, *IEEE Transactions on Geoscience and Remote Sensing*, *55*(11), 6468–6481, doi: 10.1109/TGRS.2017.2728699.

Cadeddu, M. P., V. P. Ghate, and M. Mech (2020), Ground-based observations of cloud and drizzle liquid water path in stratocumulus clouds, *Atmospheric Measurement Techniques*, *13*(3), 1485–1499, doi: 10.5194/amt-13-1485-2020.

Cao, Y., W. Tan, and Z. Wu (2018), Aircraft icing: An ongoing threat to aviation safety, *Aerospace Science and Technology*, *75*, 353–385, doi: 10.1016/j.ast.2017.12.028.

Chantry, M., H. Christensen, P. Dueben, and T. Palmer (2021), Opportunities and challenges for machine learning in weather and climate modelling: Hard, medium and soft AI, *Philosophical Transactions of the Royal Society A: Mathematical, Physical and Engineering Sciences*, *379*(2194), doi: 10.1098/rsta.2020.0083.

Chase, R. J., J. A. Finlon, P. Borque, G. M. McFarquhar, S. W. Nesbitt, S. Tanelli, O. O. Sy, S. L. Durden, and M. R. Poellot (2018), Evaluation of Triple-Frequency Radar Retrieval of Snowfall Properties Using Coincident Airborne In Situ Observations During OLYMPEX, *Geophysical Research Letters*, *45*(11), 5752–5760, doi: 10.1029/2018GL077997.

Chase, R. J., S. W. Nesbitt, and G. M. McFarquhar (2021), A Dual-Frequency Radar Retrieval of Two Parameters of the Snowfall Particle Size Distribution Using a Neural Network, *Journal of Applied Meteorology and Climatology*, *60*(3), 341–359, doi: 10.1175/JAMC-D-20-0177.1.

Chase, R. J., D. R. Harrison, A. Burke, G. M. Lackmann, and A. McGovern (2022a), A Machine Learning Tutorial for Operational Meteorology. Part I: Traditional Machine Learning, *Weather and Forecasting*, *37*(8), 1509–1529, doi: 10.1175/WAF-D-22-0070.1.

Chase, R. J., D. R. Harrison, G. Lackmann, and A. McGovern (2022b), A Machine Learning Tutorial for Operational Meteorology, Part II: Neural Networks and Deep Learning, pp. 1–23, doi: 10.48550/arXiv.2211.00147.

Chollet, F. (2015), Keras, https://keras.io (last access: 15 February 2023).

Chollet, F. (2017), *Deep learning with Python*, Manning Publications Company.

Choularton, T. W., and S. J. Perry (1986), A model of the orographic enhancement of snowfall by the seeder-feeder mechanism, *Quarterly Journal of the Royal Meteorological Society*, *112*(472), 335–345, doi: 10.1002/qj.49711247204.

Chow, F. K., S. F. De Wekker, and B. J. Snyder (2013), *Mountain Weather Research and Forecasting*, Springer Atmospheric Sciences, Springer Netherlands, Dordrecht, doi: 10.1007/978-94-007-4098-3.

Conen, F., A. Einbock, C. Mignani, and C. Hüglin (2022), Measurement report: Ice-nucleating particles active $\geq -15\,°C$ in free tropospheric air over western Europe, *Atmospheric Chemistry and Physics*, *22*(5), 3433–3444, doi: 10.5194/acp-22-3433-2022.

Connolly, P. J., C. Emersic, and P. R. Field (2012), A laboratory investigation into the aggregation efficiency of small ice crystals, *Atmospheric Chemistry and Physics*, *12*(4), 2055–2076, doi: 10.5194/acp-12-2055-2012.

Consortium for Small-scale Modeling (2017), COSMO, http://cosmo-model.org/ (last access: 15 January 2023).

Copernicus Climate Change Service (2020), ERA5: Fifth generation of ECMWF atmospheric reanalyses of the global climate, https://cds.climate.copernicus.eu (last access: 14 February 2023).

Bibliography

Currier, W. R., T. Thorsona, and J. D. Lundquist (2017), Independent evaluation of frozen precipitation from WRF and PRISM in the Olympic Mountains, *Journal of Hydrometeorology*, *18*(10), 2681–2703, doi: 10.1175/JHM-D-17-0026.1.

Curry, J. A., J. L. Schramm, W. B. Rossow, and D. Randall (1996), Overview of Artic Cloud and Radiation Characteristics, *Journal of Climate*, *9*(8), 1731–1764, doi: 10.1175/1520-0442(1996) 009<1731:OOACAR>2.0.CO;2.

Dedekind, Z., A. Lauber, S. Ferrachat, and U. Lohmann (2021), Sensitivity of precipitation formation to secondary ice production in winter orographic mixed-phase clouds, *Atmospheric Chemistry and Physics*, *21*(19), 15,115–15,134, doi: 10.5194/acp-21-15115-2021.

Dedekind, Z., J. Grazioli, P. H. Austin, and U. Lohmann (2023), Heavy snowfall event over the Swiss Alps : Did wind shear impact secondary ice production?, *Atmospheric Chemistry and Physics*, *23*(4), 2345–2364, doi: 10.5194/acp-23-2345-2023.

Delanoë, J., A. Protat, D. Bouniol, A. Heymsfield, A. Bansemer, and P. Brown (2007), The Characterization of Ice Cloud Properties from Doppler Radar Measurements, *Journal of Applied Meteorology and Climatology*, *46*(10), 1682–1698, doi: 10.1175/JAM2543.1.

Delanoë, J., A. Protat, O. Jourdan, J. Pelon, M. Papazzoni, R. Dupuy, J.-F. Gayet, and C. Jouan (2013), Comparison of Airborne In Situ, Airborne Radar–Lidar, and Spaceborne Radar–Lidar Retrievals of Polar Ice Cloud Properties Sampled during the POLARCAT Campaign, *Journal of Atmospheric and Oceanic Technology*, *30*(1), 57–73, doi: 10.1175/JTECH-D-11-00200.1.

Delanoë, J., et al. (2016), BASTA: A 95-GHz FMCW Doppler Radar for Cloud and Fog Studies, *Journal of Atmospheric and Oceanic Technology*, *33*(5), 1023–1038, doi: 10.1175/ JTECH-D-15-0104.1.

DeMott, P. J., A. J. Prenni, X. Liu, S. M. Kreidenweis, M. D. Petters, C. H. Twohy, M. S. Richardson, T. Eidhammer, and D. C. Rogers (2010), Predicting global atmospheric ice nuclei distributions and their impacts on climate, *Proceedings of the National Academy of Sciences of the United States of America*, *107*(25), 11,217–11,222, doi: 10.1073/pnas.0910818107.

Descartes, R. (1637), *Les Météores*.

DeWalle, D. R., and A. Rango (2008), Snow climatology and snow distribution, in *Principles of Snow Hydrology*, chap. 2, pp. 20–47, Cambridge University Press, doi: 10.1017/ CBO9780511535673.

Dias Neto, J., et al. (2019), The TRIple-frequency and Polarimetric radar Experiment for improving process observations of winter precipitation, *Earth System Science Data*, *11*(2), 845–863, doi: 10.5194/essd-11-845-2019.

Doviak, R. J., and D. S. Zrnić (1993), Doppler spectra of weather signals, in *Doppler Radar and Weather Observations*, edited by N. Y. Mineola, chap. 5, pp. 106–115, Dover pulications, Inc., doi: 10.1016/B978-0-12-221422-6.50010-3.

Draine, B. T., and P. J. Flatau (1994), Discrete-Dipole Approximation For Scattering Calculations, *Journal of the Optical Society of America A: Optics, Image Science, and Vision*, *11*(4), 1491–1499, doi: 10.1364/JOSAA.11.001491.

Ebell, K., U. Löhnert, S. Crewell, and D. D. Turner (2010), On characterizing the error in a remotely sensed liquid water content profile, *Atmospheric Research*, *98*(1), 57–68, doi: 10.1016/j.atmosres.2010.06.002.

Ebell, K., U. Löhnert, E. Päschke, E. Orlandi, J. H. Schween, and S. Crewell (2017), A 1-D variational retrieval of temperature, humidity, and liquid cloud properties: Performance under idealized and real conditions, *Journal of Geophysical Research: Atmospheres*, *122*(3), 1746–1766, doi: 10.1002/2016JD025945.

Ellison, W. J. (2007), Permittivity of pure water, at standard atmospheric pressure, over the frequency range 0-25 THz and the temperature range 0-100°C, *Journal of Physical and Chemical Reference Data*, *36*(1), 1–18, doi: 10.1063/1.2360986.

Emory, A. E., B. Demoz, K. Vermeesch, and M. Hicks (2014), Double bright band observations with high-resolution vertically pointing radar, lidar, and profilers, *Journal of Geophysical Research: Atmospheres*, *119*, 8201–8211, doi: 10.1002/2013JD020063.

Faber, S., J. R. French, and R. Jackson (2018), Laboratory and in-flight evaluation of measurement uncertainties from a commercial Cloud Droplet Probe (CDP), *Atmospheric Measurement Techniques*, *11*(6), 3645–3659, doi: 10.5194/amt-11-3645-2018.

Fabry, F. (1995), Long-Term Radar Observations of the Melting Layer of Precipitation and Their Interpretation, *Journal of the Atmospheric Sciences*, *52*(7), 838–851, doi: 10.1175/1520-0469(1995)052<0838:LTROOT>2.0.CO;2.

Fabry, F. (2015), *Radar Meteorology: Principles and Practice*, Cambridge University Press, doi: 10.1017/CBO9781107707405.

Ferrone, A., and A. Berne (2020), Dynamic Differential Reflectivity Calibration Using Vertical Profiles in Rain and Snow, *Remote Sensing*, *13*(1), 8, doi: 10.3390/rs13010008.

Ferrone, A., A.-C. Billault-Roux, and A. Berne (2022), ERUO: a spectral processing routine for the Micro Rain Radar PRO (MRR-PRO), *Atmospheric Measurement Techniques*, *15*(11), 3569–3592, doi: 10.5194/amt-15-3569-2022.

Field, P. R., and A. J. Heymsfield (2015), Importance of snow to global precipitation, *Geophysical Research Letters*, *42*(21), 9512–9520, doi: 10.1002/2015GL065497.

Field, P. R., A. A. Hill, K. Furtado, and A. Korolev (2014), Mixed-phase clouds in a turbulent environment. Part 2: Analytic treatment, *Quarterly Journal of the Royal Meteorological Society*, *140*(680), 870–880, doi: 10.1002/qj.2175.

Bibliography

Field, P. R., et al. (2016), Chapter 7. Secondary Ice Production - current state of the science and recommendations for the future, *Meteorological Monographs*, pp. 16–0014, doi: 10.1175/ AMSMONOGRAPHS-D-16-0014.1.

Findeisen, Z. (1938), Kolloid-meteorologische Vorgänge bei Neiderschlags-bildung, *Meteorologische Zeitschrift*, *55*, 121.

Foresti, L., I. V. Sideris, L. Panziera, D. Nerini, and U. Germann (2018), A 10-year radar-based analysis of orographic precipitation growth and decay patterns over the Swiss Alpine region, *Quarterly Journal of the Royal Meteorological Society*, *144*(716), 2277–2301, doi: 10.1002/qj. 3364.

Fujiyoshi, Y. (2023), Underlying microphysical processes in the melting layer during moderate precipitation: Evidence from ground-based data, *Journal of the Atmospheric Sciences*, doi: 10.1175/JAS-D-22-0183.1.

Furukawa, Y., M. Yamamoto, and T. Kuroda (1987), Ellipsometric study of the transition layer on the surface of an ice crystal, *Journal of Crystal Growth*, *82*(4), 665–677, doi: 10.1016/ S0022-0248(87)80012-X.

Galletti, M., D. Huang, and P. Kollias (2014), Zenith/Nadir pointing mm-wave radars: Linear or circular polarization?, *IEEE Transactions on Geoscience and Remote Sensing*, *52*(1), 628–639, doi: 10.1109/TGRS.2013.2243155.

Garrett, T. J., and S. E. Yuter (2014), Observed influence of riming, temperature, and turbulence on the fallspeed of solid precipitation, *Geophysical Research Letters*, *41*(18), 6515–6522, doi: 10.1002/2014GL061016.

Garrett, T. J., C. Fallgatter, K. Shkurko, and D. Howlett (2012), Fall speed measurement and high-resolution multi-angle photography of hydrometeors in free fall, *Atmospheric Measurement Techniques*, *5*(11), 2625–2633, doi: 10.5194/amt-5-2625-2012.

Garrett, T. J., S. E. Yuter, C. Fallgatter, K. Shkurko, S. R. Rhodes, and J. L. Endries (2015), Orientations and aspect ratios of falling snow, *Geophysical Research Letters*, *42*(11), 4617–4622, doi: 10.1002/2015GL064040.

Gaussiat, N., R. J. Hogan, and A. J. Illingworth (2007), Accurate Liquid Water Path Retrieval from Low-Cost Microwave Radiometers Using Additional Information from a Lidar Ceilometer and Operational Forecast Models, *Journal of Atmospheric and Oceanic Technology*, *24*(9), 1562–1575, doi: 10.1175/JTECH2053.1.

Geer, A. J. (2021), Learning earth system models from observations: machine learning or data assimilation?, *Philosophical Transactions of the Royal Society A: Mathematical, Physical and Engineering Sciences*, *379*(2194), 20200,089, doi: 10.1098/rsta.2020.0089.

Gehring, J., A. Ferrone, A.-C. Billault-Roux, N. Besic, K. D. Ahn, G. Lee, and A. Berne (2021), Radar and ground-level measurements of precipitation collected by the École Polytechnique

Fédérale de Lausanne during the International Collaborative Experiments for PyeongChang 2018 Olympic and Paralympic winter games, *Earth System Science Data, 13*(2), 417–433, doi: 10.5194/essd-13-417-2021.

Gehring, J., É. Vignon, A. C. Billault-Roux, A. Ferrone, A. Protat, S. P. Alexander, and A. Berne (2022), Orographic Flow Influence on Precipitation During an Atmospheric River Event at Davis, Antarctica, *Journal of Geophysical Research: Atmospheres, 127*(2), 1–23, doi: 10.1029/2021JD035210.

Georgakaki, P., et al. (2021), On the drivers of droplet variability in alpine mixed-phase clouds, *Atmospheric Chemistry and Physics, 21*(14), 10,993–11,012, doi: 10.5194/acp-21-10993-2021.

Georgakaki, P., G. Sotiropoulou, É. Vignon, A.-C. Billault-Roux, A. Berne, and A. Nenes (2022), Secondary ice production processes in wintertime alpine mixed-phase clouds, *Atmospheric Chemistry and Physics, 22*(3), 1965–1988, doi: 10.5194/acp-22-1965-2022.

Giangrande, S. E., T. Toto, A. Bansemer, M. R. Kumjian, S. Mishra, and A. V. Ryzhkov (2016), Insights into riming and aggregation processes as revealed by aircraft, radar, and disdrometer observations for a 27 April 2011 widespread precipitation event, *Journal of Geophysical Research: Atmospheres, 121*, 5846–5863, doi: 10.1002/2015JD024537.

Glorot, X., and Y. Bengio (2010), Understanding the difficulty of training deep feedforward neural networks, in *Proceedings of the Thirteenth International Conference on Artificial Intelligence and Statistics, Proceedings of Machine Learning Research*, vol. 9, edited by Y. W. Teh and M. Titterington, pp. 249–256, PMLR, Sardinia, Italy.

Gossard, E. E. (1994), Measurement of Cloud Droplet Size Spectra by Doppler Radar, *Journal of Atmospheric and Oceanic Technology, 11*(3), 712–726, doi: 10.1175/1520-0426(1994)011<0712:MOCDSS>2.0.CO;2.

Gossard, E. E., J. B. Snider, E. E. Clothiaux, B. Martner, J. S. Gibson, R. A. Kropfli, and A. S. Frisch (1997), The Potential of 8-mm Radars for Remotely Sensing Cloud Drop Size Distributions, *Journal of Atmospheric and Oceanic Technology, 14*(1), 76–87, doi: 10.1175/1520-0426(1997)014<0076:TPOMRF>2.0.CO;2.

Goujon, A., A. Etemadi, and M. Unser (2022), The Role of Depth, Width, and Activation Complexity in the Number of Linear Regions of Neural Networks, doi: 10.48550/arXiv.2206.08615.

Grabowski, W. W., and G. C. Abade (2017), Broadening of Cloud Droplet Spectra through Eddy Hopping: Turbulent Adiabatic Parcel Simulations, *Journal of the Atmospheric Sciences, 74*(5), 1485–1493, doi: 10.1175/JAS-D-17-0043.1.

Grabowski, W. W., H. Morrison, S.-I. Shima, G. C. Abade, P. Dziekan, and H. Pawlowska (2019), Modeling of Cloud Microphysics: Can We Do Better?, *Bulletin of the American Meteorological Society, 100*(4), 655–672, doi: 10.1175/BAMS-D-18-0005.1.

Bibliography

Grandin, A., J.-M. Merle, M. Weber, J. Strapp, A. Protat, and P. King (2014), AIRBUS Flight Tests in High Total Water Content Regions, in *6th AIAA Atmospheric and Space Environments Conference*, American Institute of Aeronautics and Astronautics, Atlanta, GA, USA, doi: 10.2514/6.2014-2753.

Grazioli, J., G. Lloyd, L. Panziera, C. R. Hoyle, P. J. Connolly, J. Henneberger, and A. Berne (2015), Polarimetric radar and in situ observations of riming and snowfall microphysics during CLACE 2014, *Atmospheric Chemistry and Physics*, *15*(23), 13,787–13,802, doi: 10.5194/acp-15-13787-2015.

Grazioli, J., J. B. Madeleine, H. Gallée, R. M. Forbes, C. Genthon, G. Krinner, and A. Berne (2017), Katabatic winds diminish precipitation contribution to the Antarctic ice mass balance, *Proceedings of the National Academy of Sciences of the United States of America*, *114*(41), 10,858–10,863, doi: 10.1073/pnas.1707633114.

Grazioli, J., G. Ghiggi, A.-C. Billault-Roux, and A. Berne (2022), MASCDB, a database of images, descriptors and microphysical properties of individual snowflakes in free fall, *Scientific Data*, *9*, 186, doi: 10.1038/s41597-022-01269-7.

Haggerty, J., et al. (2019), Detecting Clouds Associated with Jet Engine Ice Crystal Icing, *Bulletin of the American Meteorological Society*, *100*(1), 31–40, doi: 10.1175/BAMS-D-17-0252.1.

Hall, W. D., and H. R. Pruppacher (1976), The Survival of Ice Particles Falling from Cirrus Clouds in Subsaturated Air, *Journal of the Atmospheric Sciences*, *33*(10), 1995–2006, doi: 10.1175/1520-0469(1976)033<1995:TSOIPF>2.0.CO;2.

Hallett, J., and G. A. Isaac (2008), Aircraft Icing in Glaciated and Mixed Phase Clouds, *Journal of Aircraft*, *45*(6), 2120–2130, doi: 10.2514/1.37596.

Hallett, J., and S. C. Mossop (1974), Production of secondary ice particles during the riming process, *Nature*, *249*(5452), 26–28, doi: 10.1038/249026a0.

Hallett, J., B. J. Mason, and J. D. Bernal (1958), The influence of temperature and super-saturation on the habit of ice crystals grown from the vapour, *Proceedings of the Royal Society of London. Series A. Mathematical and Physical Sciences*, *247*(1251), 440–453, doi: 10.1098/rspa.1958.0199.

He, K., X. Zhang, S. Ren, and J. Sun (2016), Deep Residual Learning for Image Recognition, in *Proceedings of the IEEE Conference on Computer Vision and Pattern Recognition (CVPR)*, pp. 1951–1954, IEEE, Las Vegas, NV, USA, doi: 10.1109/CVPR.2016.90.

Heffernan, E., and J. Marwitz (1996), The Front Range Blizzard of 1990. Part II: Melting Effects in a Convective Band, *Monthly Weather Review*, *124*(11), 2469–2482, doi: 10.1175/1520-0493(1996)124<2469:TFRBOP>2.0.CO;2.

Hersbach, H., et al. (2020), The ERA5 global reanalysis, *Quarterly Journal of the Royal Meteorological Society*, *146*(730), 1999–2049, doi: 10.1002/qj.3803.

Heymsfield, A. J. (1986), Ice Particle Evolution in the Anvil of a Severe Thunderstorm during CCOPE, *Journal of the Atmospheric Sciences*, *43*(21), 2463–2478, doi: 10.1175/1520-0469(1986)043<2463:IPEITA>2.0.CO;2.

Heymsfield, A. J., and M. Kajikawa (1987), An Improved Approach to Calculating Terminal Velocities of Plate-like Crystals and Graupel, *Journal of the Atmospheric Sciences*, *44*(7), 1088–1099, doi: 10.1175/1520-0469(1987)044<1088:AIATCT>2.0.CO;2.

Heymsfield, A. J., and L. M. Miloshevich (2003), Parameterizations for the Cross-Sectional Area and Extinction of Cirrus and Stratiform Ice Cloud Particles, *Journal of the Atmospheric Sciences*, *60*(7), 936–956, doi: 10.1175/1520-0469(2003)060<0936:PFTCSA>2.0.CO;2.

Heymsfield, A. J., and C. D. Westbrook (2010), Advances in the Estimation of Ice Particle Fall Speeds Using Laboratory and Field Measurements, *Journal of the Atmospheric Sciences*, *67*(8), 2469–2482, doi: 10.1175/2010JAS3379.1.

Heymsfield, A. J., P. Field, and A. Bansemer (2008), Exponential Size Distributions for Snow, *Journal of the Atmospheric Sciences*, *65*(12), 4017–4031, doi: 10.1175/2008JAS2583.1.

Heymsfield, A. J., A. Bansemer, M. R. Poellot, and N. Wood (2015), Observations of Ice Microphysics through the Melting Layer, *Journal of the Atmospheric Sciences*, *72*(8), 2902–2928, doi: 10.1175/JAS-D-14-0363.1.

Heymsfield, A. J., C. Schmitt, C. C. J. Chen, A. Bansemer, A. Gettelman, P. R. Field, and C. Liu (2020), Contributions of the Liquid and Ice Phases to Global Surface Precipitation: Observations and Global Climate Modeling, *Journal of the Atmospheric Sciences*, *77*(8), 2629–2648, doi: 10.1175/JAS-D-19-0352.1.

Hinton, G. E., and R. R. Salakhutdinov (2006), Reducing the Dimensionality of Data with Neural Networks, *Science*, *313*(5786), 504–507, doi: 10.1126/science.1127647.

Hobbs, P. V., and A. L. Rangno (1985), Ice Particle Concentrations in Clouds, *Journal of the Atmospheric Sciences*, *42*(23), 2523–2549, doi: 10.1175/1520-0469(1985)042<2523:IPCIC>2.0.CO;2.

Hobbs, P. V., S. Chang, and J. D. Locatelli (1974), The Dimensions and Aggregation of Ice Crystals in Natural Clouds, *Journal of the Atmospheric Sciences*, *79*(15), 2199–2206, doi: 10.1175/1520-0469(1970)027<0919:tdoici>2.0.co;2.

Hogan, R. J., and S. F. Kew (2005), A 3D stochastic cloud model for investigating the radiative properties of inhomogeneous cirrus clouds, *Quarterly Journal of the Royal Meteorological Society*, *131*(611), 2585–2608, doi: 10.1256/qj.04.144.

Hogan, R. J., and C. D. Westbrook (2014), Equation for the Microwave Backscatter Cross Section of Aggregate Snowflakes Using the Self-Similar Rayleigh–Gans Approximation, *Journal of the Atmospheric Sciences*, *71*(9), 3292–3301, doi: 10.1175/JAS-D-13-0347.1.

Bibliography

Hogan, R. J., A. J. Illingworth, and H. Sauvageot (2000), Measuring Crystal Size in Cirrus Using 35- and 94-GHz Radars, *Journal of Atmospheric and Oceanic Technology, 17*(1), 27–37, doi: 10.1175/1520-0426(2000)017<0027:MCSICU>2.0.CO;2.

Hogan, R. J., P. R. Field, A. J. Illingworth, R. J. Cotton, and T. W. Choularton (2002), Properties of embedded convection in warm-frontal mixed-phase cloud from aircraft and polarimetric radar, *Quarterly Journal of the Royal Meteorological Society, 128*, 451–476, doi: 10.1256/003590002321042054.

Hogan, R. J., N. Gaussiat, and A. J. Illingworth (2005), Stratocumulus Liquid Water Content from Dual-Wavelength Radar, *Journal of Atmospheric and Oceanic Technology, 22*(8), 1207–1218, doi: 10.1175/JTECH1768.1.

Hogan, R. J., R. Honeyager, J. Tyynelä, and S. Kneifel (2017), Calculating the millimetre-wave scattering phase function of snowflakes using the self-similar Rayleigh-Gans Approximation, *Quarterly Journal of the Royal Meteorological Society, 143*(703), 834–844, doi: 10.1002/qj.2968.

Houze, R. A. (2012), Orographic effects on precipitating clouds, *Reviews of Geophysics, 50*(1), 1–47, doi: 10.1029/2011RG000365.

Houze, R. A., and S. Medina (2005), Turbulence as a Mechanism for Orographic Precipitation Enhancement, *Journal of the Atmospheric Sciences, 62*(10), 3599–3623, doi: 10.1175/JAS3555.1.

Houze, R. A., et al. (2017), The Olympic Mountains Experiment (OLYMPEX), *Bulletin of the American Meteorological Society, 98*(10), 2167–2188, doi: 10.1175/BAMS-D-16-0182.1.

Huang, J. (2018), A Simple Accurate Formula for Calculating Saturation Vapor Pressure of Water and Ice, *Journal of Applied Meteorology and Climatology, 57*(6), 1265–1272, doi: 10.1175/JAMC-D-17-0334.1.

Intrieri, J. M., M. D. Shupe, T. Uttal, and B. J. McCarty (2002), An annual cycle of Arctic cloud characteristics observed by radar and lidar at SHEBA, *Journal of Geophysical Research: Oceans, 107*(10), 8030, doi: 10.1029/2000jc000423.

Ioffe, S., and C. Szegedy (2015), Batch Normalization: Accelerating Deep Network Training by Reducing Internal Covariate Shift Sergey, in *Proceedings of the 32nd International Conference on Machine Learning*, vol. 37, edited by D. B. Francis Bach, pp. 448–456, Lille, France, doi: doi.org/10.48550/arXiv.1502.03167.

Jaffeux, L., A. Schwarzenböck, P. Coutris, and C. Duroure (2022), Ice crystal images from Optical Array Probes: Classification with convolutional neural networks, *Atmospheric Measurement Techniques, 15*(17), 5141–5157, doi: 10.5194/amt-15-5141-2022.

Jankiraman, M. (2018), *FMCW Radar Design*, Artech House.

Järvinen, E., et al. (2022), Evidence for Secondary Ice Production in Southern Ocean Maritime Boundary Layer Clouds, *Journal of Geophysical Research: Atmospheres*, *127*(16), 1–31, doi: 10.1029/2021JD036411.

Ji, W., and P. K. Wang (1999), Ventilation Coefficients for Falling Ice Crystals in the Atmosphere at Low–Intermediate Reynolds Numbers, *Journal of the Atmospheric Sciences*, *56*(6), 829–836, doi: 10.1175/1520-0469(1999)056<0829:VCFFIC>2.0.CO;2.

Jiang, Z., M. Oue, J. Verlinde, E. E. Clothiaux, K. Aydin, G. Botta, and Y. Lu (2017), What Can We Conclude about the Real Aspect Ratios of Ice Particle Aggregates from Two-Dimensional Images?, *Journal of Applied Meteorology and Climatology*, *56*(3), 725–734, doi: 10.1175/JAMC-D-16-0248.1.

Jiang, Z., J. Verlinde, E. E. Clothiaux, K. Aydin, and C. Schmitt (2019), Shapes and Fall Orientations of Ice Particle Aggregates, *Journal of the Atmospheric Sciences*, *76*(7), 1903–1916, doi: 10.1175/JAS-D-18-0251.1.

Jorquera, S., F. T. Bittner, J. Delanoë, A. Berne, A.-C. Billault-Roux, A. Schwarzenboeck, F. Dezitter, N. Viltard, and A. Martini (2023), Calibration transfer methodology for cloud radars based on ice cloud observations, *Journal of Atmospheric and Oceanic Technology*, doi: 10.1175/JTECH-D-22-0087.1.

Kajikawa, M. (1976), Observation of Falling Motion of Columnar Snow Crystals, *Journal of the Meteorological Society of Japan. Ser. II*, *54*(5), 276–284, doi: 10.2151/jmsj1965.54.5_276.

Kalesse, H., W. Szyrmer, S. Kneifel, P. Kollias, and E. Luke (2016), Fingerprints of a riming event on cloud radar Doppler spectra: Observations and modeling, *Atmospheric Chemistry and Physics*, *16*(5), 2997–3012, doi: 10.5194/acp-16-2997-2016.

Kalesse, H., T. Vogl, C. Paduraru, and E. Luke (2019), Development and validation of a supervised machine learning radar Doppler spectra peak-finding algorithm, *Atmospheric Measurement Techniques*, *12*(8), 4591–4617, doi: 10.5194/amt-12-4591-2019.

Karstens, U., C. Simmer, and E. Ruprecht (1994), Remote sensing of cloud liquid water, *Meteorology and Atmospheric Physics*, *54*(1), 157–171, doi: 10.1007/BF01030057.

Keinert, A., D. Spannagel, T. Leisner, and A. Kiselev (2020), Secondary Ice Production upon Freezing of Freely Falling Drizzle Droplets, *Journal of the Atmospheric Sciences*, *77*(8), 2959–2967, doi: 10.1175/JAS-D-20-0081.1.

Kepler, J. (1611), *De nive sexangula (On the six-cornered snowflake)*, Godfrey Tampach.

Khvorostyanov, V. I., and J. A. Curry (2002), Terminal Velocities of Droplets and Crystals: Power Laws with Continuous Parameters over the Size Spectrum, *Journal of the Atmospheric Sciences*, *59*(11), 1872–1884, doi: 10.1175/1520-0469(2002)059<1872:TVODAC>2.0.CO;2.

Bibliography

Kikuchi, K., T. Kameda, K. Higuchi, and A. Yamashita (2013), A global classification of snow crystals, ice crystals, and solid precipitation based on observations from middle latitudes to polar regions, *Atmospheric Research*, *132-133*, 460–472, doi: 10.1016/j.atmosres.2013.06.006.

King, F., G. Duffy, and C. G. Fletcher (2022a), A Centimeter-Wavelength Snowfall Retrieval Algorithm Using Machine Learning, *Journal of Applied Meteorology and Climatology*, *61*(8), 1029–1039, doi: 10.1175/JAMC-D-22-0036.1.

King, F., G. Duffy, L. Milani, C. G. Fletcher, C. Pettersen, and K. Ebell (2022b), DeepPrecip: a deep neural network for precipitation retrievals, *Atmospheric Measurement Techniques*, *15*(20), 6035–6050, doi: 10.5194/amt-15-6035-2022.

King, W. D., and N. H. Fletcher (1976a), Thermal Shock as an Ice Multiplication Mechanism. Part I. Theory, *Journal of the Atmospheric Sciences*, *33*(1), 85–96, doi: 10.1175/1520-0469(1976)033<0085:TSAAIM>2.0.CO;2.

King, W. D., and N. H. Fletcher (1976b), Thermal Shock as an Ice Multiplication Mechanism. Part II. Experimental, *Journal of the Atmospheric Sciences*, *33*(1), 97–102, doi: 10.1175/1520-0469(1976)033<0097:TSAAIM>2.0.CO;2.

Kingma, D. P., and J. L. Ba (2015), Adam: A method for stochastic optimization, in *3rd International Conference on Learning Representations, ICLR 2015 - Conference Track Proceedings*, pp. 1–15, San Diego CA, USA, doi: 10.48550/arXiv.1412.6980.

Kleinheins, J., A. Kiselev, A. Keinert, M. Kind, and T. Leisner (2021), Thermal imaging of freezing drizzle droplets: pressure release events as a source of secondary ice particles, *Journal of the Atmospheric Sciences*, *78*(5), 1703–1713, doi: 10.1175/JAS-D-20-0323.1.

Kneifel, S., and D. Moisseev (2020), Long-Term Statistics of Riming in Nonconvective Clouds Derived from Ground-Based Doppler Cloud Radar Observations, *Journal of the Atmospheric Sciences*, *77*(10), 3495–3508, doi: 10.1175/JAS-D-20-0007.1.

Kneifel, S., U. Löhnert, A. Battaglia, S. Crewell, and D. Siebler (2010), Snow scattering signals in ground-based passive microwave radiometer measurements, *Journal of Geophysical Research*, *115*(D16), 1–17, doi: 10.1029/2010JD013856.

Kneifel, S., M. S. Kulie, and R. Bennartz (2011), A triple-frequency approach to retrieve microphysical snowfall parameters, *Journal of Geophysical Research: Atmospheres*, *116*(11), 1–15, doi: 10.1029/2010JD015430.

Kneifel, S., A. Von Lerber, J. Tiira, D. Moisseev, P. Kollias, and J. Leinonen (2015), Observed relations between snowfall microphysics and triple-frequency radar measurements, *Journal of Geophysical Research*, *120*(12), 6034–6055, doi: 10.1002/2015JD023156.

Kneifel, S., P. Kollias, A. Battaglia, J. Leinonen, M. Maahn, H. Kalesse, and F. Tridon (2016), First observations of triple-frequency radar Doppler spectra in snowfall: Interpretation and applications, *Geophysical Research Letters*, *43*(5), 2225–2233, doi: 10.1002/2015GL067618.

Köbschall, K., J. Breitenbach, I. V. Roisman, C. Tropea, and J. Hussong (2023), Geometric descriptors for the prediction of snowflake drag, *Experiments in Fluids*, *64*, 4, doi: 10.1007/s00348-022-03539-x.

Kogan, Z. N., D. B. Mechem, and Y. L. Kogan (2005), Assessment of variability in continental low stratiform clouds based on observations of radar reflectivity, *Journal of Geophysical Research: Atmospheres*, *110*(18), 1–15, doi: 10.1029/2005JD006158.

Kollias, P., B. Albrecht, and F. J. Marks (2002), Why Mie?, *Bulletin of the American Meteorological Society*, *83*(10), 1471–1484, doi: 10.1175/BAMS-83-10-1471.

Korolev, A. (2007a), Limitations of the Wegener-Bergeron-Findeisen mechanism in the evolution of mixed-phase clouds, *Journal of the Atmospheric Sciences*, *64*(9), 3372–3375, doi: 10.1175/JAS4035.1.

Korolev, A. (2007b), Reconstruction of the sizes of spherical particles from their shadow images. Part I: Theoretical considerations, *Journal of Atmospheric and Oceanic Technology*, *24*(3), 376–389, doi: 10.1175/JTECH1980.1.

Korolev, A., and P. R. Field (2008), The Effect of Dynamics on Mixed-Phase Clouds: Theoretical Considerations, *Journal of the Atmospheric Sciences*, *65*(1), 66–86, doi: 10.1175/2007JAS2355.1.

Korolev, A., and T. Leisner (2020), Review of experimental studies of secondary ice production, *Atmospheric Chemistry and Physics*, *20*(20), 11,767–11,797, doi: 10.5194/acp-20-11767-2020.

Korolev, A., et al. (2017), Mixed-Phase Clouds: Progress and Challenges, *Meteorological Monographs*, *58*(1), 1–5, doi: 10.1175/amsmonographs-d-17-0001.1.

Korolev, A., I. Heckman, M. Wolde, A. S. Ackerman, A. M. Fridlind, L. A. Ladino, R. Paul Lawson, J. Milbrandt, and E. Williams (2020), A new look at the environmental conditions favorable to secondary ice production, *Atmospheric Chemistry and Physics*, *20*(3), 1391–1429, doi: 10.5194/acp-20-1391-2020.

Korolev, A., P. J. Demott, I. Heckman, M. Wolde, E. Williams, D. J. Smalley, and M. F. Donovan (2022), Observation of secondary ice production in clouds at low temperatures, *Atmospheric Chemistry and Physics*, *22*(19), 13,103–13,113, doi: 10.5194/acp-22-13103-2022.

Korolev, A. V., and G. A. Isaac (2000), Drop Growth Due to High Supersaturation Caused by Isobaric Mixing, *Journal of the Atmospheric Sciences*, *57*(10), 1675–1685, doi: 10.1175/1520-0469(2000)057<1675:DGDTHS>2.0.CO;2.

Korolev, A. V., and I. P. Mazin (2003), Supersaturation of Water Vapor in Clouds, *Journal of the Atmospheric Sciences*, *60*(24), 2957–2974, doi: 10.1175/1520-0469(2003)060<2957:SOWVIC>2.0.CO;2.

Bibliography

Korolev, A. V., G. A. Isaac, S. G. Cober, J. W. Strapp, and J. Hallett (2003), Microphysical characterization of mixed-phase clouds, *Quarterly Journal of the Royal Meteorological Society*, *129*(587), 39–65, doi: 10.1256/qj.01.204.

Kramer, M. A. (1991), Nonlinear principal component analysis using autoassociative neural networks, *AIChE Journal*, *37*(2), 233–243, doi: 10.1002/aic.690370209.

Küchler, N., S. Kneifel, U. Löhnert, P. Kollias, H. Czekala, and T. Rose (2017), A W-Band Radar–Radiometer System for Accurate and Continuous Monitoring of Clouds and Precipitation, *Journal of Atmospheric and Oceanic Technology*, *34*(11), 2375–2392, doi: 10.1175/JTECH-D-17-0019.1.

Kulie, M. S., M. J. Hiley, R. Bennartz, S. Kneifel, and S. Tanelli (2014), Triple-Frequency Radar Reflectivity Signatures of Snow: Observations and Comparisons with Theoretical Ice Particle Scattering Models, *Journal of Applied Meteorology and Climatology*, *53*(4), 1080–1098, doi: 10.1175/JAMC-D-13-066.1.

Kulie, M. S., L. Milani, N. B. Wood, S. A. Tushaus, R. Bennartz, and T. S. L'Ecuyer (2016), A shallow cumuliform snowfall census using spaceborne radar, *Journal of Hydrometeorology*, *17*(4), 1261–1279, doi: 10.1175/JHM-D-15-0123.1.

Kumjian, M. (2013a), Principles and applications of dual-polarization weather radar. Part I: Description of the polarimetric radar variables, *Journal of Operational Meteorology*, *1*(19), 226–242, doi: 10.15191/nwajom.2013.0119.

Kumjian, M. (2013b), Principles and applications of dual-polarization weather radar. Part III: Artifacts, *Journal of Operational Meteorology*, *1*(21), 265–274, doi: 10.15191/nwajom.2013.0121.

Kumjian, M. R. (2018), Weather Radars, in *Remote Sensing of Clouds and Precipitation*, edited by C. Andronache, chap. 2, pp. 15–63, Springer International Publishing, Cham, doi: 10.1007/978-3-319-72583-3.

Kuo, K.-S., et al. (2016), The Microwave Radiative Properties of Falling Snow Derived from Non-spherical Ice Particle Models. Part I: An Extensive Database of Simulated Pristine Crystals and Aggregate Particles, and Their Scattering Properties, *Journal of Applied Meteorology and Climatology*, *55*(3), 691–708, doi: 10.1175/JAMC-D-15-0130.1.

Lauber, A., A. Kiselev, T. Pander, P. Handmann, and T. Leisner (2018), Secondary Ice Formation during Freezing of Levitated Droplets, *Journal of the Atmospheric Sciences*, *75*(8), 2815–2826, doi: 10.1175/JAS-D-18-0052.1.

Lauber, A., J. Henneberger, C. Mignani, F. Ramelli, J. T. Pasquier, J. Wieder, M. Hervo, and U. Lohmann (2021), Continuous secondary-ice production initiated by updrafts through the melting layer in mountainous regions, *Atmospheric Chemistry and Physics*, *21*(5), 3855–3870, doi: 10.5194/acp-21-3855-2021.

Lazo, J. K., R. E. Morss, and J. L. Demuth (2009), 300 Billion Served, *Bulletin of the American Meteorological Society*, *90*(6), 785–798, doi: 10.1175/2008BAMS2604.1.

Lecun, Y., L. Bottou, Y. Bengio, and P. Haffner (1998), Gradient-based learning applied to document recognition, *Proceedings of the IEEE*, *86*(11), 2278–2324, doi: 10.1109/5.726791.

Leinonen, J., and W. Szyrmer (2015), Radar signatures of snowflake riming: A modeling study, *Earth and Space Science*, *2*(8), 346–358, doi: 10.1002/2015EA000102.

Leinonen, J., and A. von Lerber (2018), Snowflake Melting Simulation Using Smoothed Particle Hydrodynamics, *Journal of Geophysical Research: Atmospheres*, *123*(3), 1811–1825, doi: 10.1002/2017JD027909.

Leinonen, J., S. Kneifel, and R. J. Hogan (2018), Evaluation of the Rayleigh–Gans approximation for microwave scattering by rimed snowflakes, *Quarterly Journal of the Royal Meteorological Society*, *144*(S1), 77–88, doi: 10.1002/qj.3093.

Leinonen, J., J. Grazioli, and A. Berne (2021), Reconstruction of the mass and geometry of snowfall particles from multi-angle snowflake camera (MASC) images, *Atmospheric Measurement Techniques*, *14*(10), 6851–6866, doi: 10.5194/amt-14-6851-2021.

Lenaerts, J. T., K. Van Tricht, S. Lhermitte, and T. S. L'Ecuyer (2017), Polar clouds and radiation in satellite observations, reanalyses, and climate models, *Geophysical Research Letters*, *44*(7), 3355–3364, doi: 10.1002/2016GL072242.

Leroy, D., E. Fontaine, A. Schwarzenboeck, and J. W. Strapp (2016), Ice Crystal Sizes in High Ice Water Content Clouds. Part I: On the Computation of Median Mass Diameter from In Situ Measurements, *Journal of Atmospheric and Oceanic Technology*, *33*(11), 2461–2476, doi: 10.1175/JTECH-D-15-0151.1.

Lhermitte, R. (1987), A 94-GHz Doppler Radar for Cloud Observations, *Journal of Atmospheric and Oceanic Technology*, *4*(1), 36–48, doi: 10.1175/1520-0426(1987)004<0036:AGDRFC>2.0.CO;2.

Li, C., K. Lim, T. Berk, A. Abraham, M. Heisel, M. Guala, F. Coletti, and J. Hong (2021a), Settling and clustering of snow particles in atmospheric turbulence, *Journal of Fluid Mechanics*, *912*, A49, doi: 10.1017/jfm.2020.1153.

Li, H., and D. Moisseev (2019), Melting Layer Attenuation at Ka- and W-Bands as Derived From Multifrequency Radar Doppler Spectra Observations, *Journal of Geophysical Research: Atmospheres*, *124*(16), 9520–9533, doi: 10.1029/2019JD030316.

Li, H., A. Korolev, and D. Moisseev (2021b), Supercooled liquid water and secondary ice production in Kelvin-Helmholtz instability as revealed by radar Doppler spectra observations, *Atmospheric Chemistry and Physics*, *21*(17), 13,593–13,608, doi: 10.5194/acp-21-13593-2021.

Li, Z. X., and H. Le Treut (1992), Cloud-radiation feedbacks in a general circulation model and their dependence on cloud modelling assumptions, *Climate Dynamics*, *7*(3), 133–139, doi: 10.1007/BF00211155.

Liao, L., R. Meneghini, L. Tian, and G. M. Heymsfield (2008), Retrieval of snow and rain from combined X- And W-Band airborne radar measurements, *IEEE Transactions on Geoscience and Remote Sensing*, *46*(5), 1514–1524, doi: 10.1109/TGRS.2008.916079.

Liao, L., R. Meneghini, A. Tokay, and L. F. Bliven (2016), Retrieval of Snow Properties for Ku- and Ka-Band Dual-Frequency Radar, *Journal of Applied Meteorology and Climatology*, *55*(9), 1845–1858, doi: 10.1175/JAMC-D-15-0355.1.

Libbrecht, K. G. (2005), The physics of snow crystals, *Reports on Progress in Physics*, *68*(4), 855–895, doi: 10.1088/0034-4885/68/4/R03.

Liljegren, J. C., E. E. Clothiaux, G. G. Mace, S. Kato, and X. Dong (2001), A new retrieval for cloud liquid water path using a ground-based microwave radiometer and measurements of cloud temperature, *Journal of Geophysical Research: Atmospheres*, *106*(D13), 14,485–14,500, doi: 10.1029/2000JD900817.

Liljegren, J. C., S. Boukabara, K. Cady-Pereira, and S. A. Clough (2005), The effect of the half-width of the 22-GHz water vapor line on retrievals of temperature and water vapor profiles with a 12-channel microwave radiometer, *IEEE Transactions on Geoscience and Remote Sensing*, *43*(5), 1102–1108, doi: 10.1109/TGRS.2004.839593.

Liu, C.-L., and A. J. Illingworth (2000), Toward More Accurate Retrievals of Ice Water Content from Radar Measurements of Clouds, *Journal of Applied Meteorology*, *39*(7), 1130–1146, doi: 10.1175/1520-0450(2000)039<1130:TMAROI>2.0.CO;2.

Liu, G. (2004), Approximation of Single Scattering Properties of Ice and Snow Particles for High Microwave Frequencies, *Journal of the Atmospheric Sciences*, *61*(20), 2441–2456, doi: 10.1175/1520-0469(2004)061<2441:AOSSPO>2.0.CO;2.

Lloyd, G., et al. (2015), The origins of ice crystals measured in mixed-phase clouds at the high-alpine site Jungfraujoch, *Atmospheric Chemistry and Physics*, *15*(22), 12,953–12,969, doi: 10.5194/acp-15-12953-2015.

Locatelli, J. D., and P. V. Hobbs (1974), Fall speeds and masses of solid precipitation particles, *Journal of Geophysical Research*, *79*(15), 2185–2197, doi: 10.1029/JC079i015p02185.

Löffler-Mang, M., M. Kunz, and W. Schmid (1999), On the Performance of a Low-Cost K-Band Doppler Radar for Quantitative Rain Measurements, *Journal of Atmospheric and Oceanic Technology*, *16*(3), 379–387, doi: 10.1175/1520-0426(1999)016<0379:OTPOAL>2.0.CO;2.

Lohmann, U., F. Lüönd, and F. Mahrt (2016), Microphysical processes in cold clouds, in *An introduction to clouds: From the microscale to climate*, chap. 8, pp. 218–250, Cambridge University Press, Cambridge, doi: 10.1017/CBO9781139087513.009.

Löhnert, U., and S. Crewell (2003), Accuracy of cloud liquid water path from ground-based microwave radiometry 1. Dependency on cloud model statistics, *Radio Science*, *38*(3), 8041, doi: 10.1029/2002RS002654.

Löhnert, U., and O. Maier (2012), Operational profiling of temperature using ground-based microwave radiometry at Payerne: prospects and challenges, *Atmospheric Measurement Techniques*, *5*(5), 1121–1134, doi: 10.5194/amt-5-1121-2012.

Löhnert, U., S. Crewell, and C. Simmer (2004), An Integrated Approach toward Retrieving Physically Consistent Profiles of Temperature, Humidity, and Cloud Liquid Water, *Journal of Applied Meteorology*, *43*(9), 1295–1307, doi: 10.1175/1520-0450(2004)043<1295:AIATRP> 2.0.CO;2.

Lu, Y., Z. Jiang, K. Aydin, J. Verlinde, E. Clothiaux, and G. Botta (2016), A polarimetric scattering database for non-spherical ice particles at microwave wavelengths, *Atmospheric Measurement Techniques*, *9*(10), 5119–5134, doi: 10.5194/amt-9-5119-2016.

Luke, E. P., and P. Kollias (2013), Separating Cloud and Drizzle Radar Moments during Precipitation Onset Using Doppler Spectra, *Journal of Atmospheric and Oceanic Technology*, *30*(8), 1656–1671, doi: 10.1175/JTECH-D-11-00195.1.

Luke, E. P., F. Yang, P. Kollias, A. M. Vogelmann, and M. Maahn (2021), New insights into ice multiplication using remote-sensing observations of slightly supercooled mixed-phase clouds in the Arctic, *Proceedings of the National Academy of Sciences of the United States of America*, *118*(13), e2021387,118, doi: 10.1073/pnas.2021387118.

Lynch, D. K. (1996), Cirrus clouds: Their role in climate and global change, *Acta Astronautica*, *38*(11), 859–863, doi: 10.1016/S0094-5765(96)00098-7.

Maahn, M., and U. Löhnert (2017), Potential of Higher-Order Moments and Slopes of the Radar Doppler Spectrum for Retrieving Microphysical and Kinematic Properties of Arctic Ice Clouds, *Journal of Applied Meteorology and Climatology*, *56*(2), 263–282, doi: 10.1175/JAMC-D-16-0020.1.

Maahn, M., D. D. Turner, U. Löhnert, D. J. Posselt, K. Ebell, G. G. Mace, and J. M. Comstock (2020), Optimal Estimation Retrievals and Their Uncertainties: What Every Atmospheric Scientist Should Know, *Bulletin of the American Meteorological Society*, *101*(9), E1512–E1523, doi: 10.1175/BAMS-D-19-0027.1.

Magono, C., and C. W. Lee (1966), Meteorological Classification of Natural Snow Crystals, *Journal of the Faculty of Science, Hokkaido University. Series 7, Geophysics*, *2*(4), 321–362, doi: 10.5331/seppyo.24.33.

Mallet, C., E. Moreau, L. Casagrande, and C. Klapisz (2002), Determination of integrated cloud liquid water path and total precipitable water from SSM/I data using a neural network algorithm, *International Journal of Remote Sensing*, *23*(4), 661–674, doi: 10.1080/01431160110045959.

Bibliography

Mariage, V., et al. (2017), IAOOS microlidar-on-buoy development and first atmospheric observations obtained during 2014 and 2015 arctic drifts, *Optics Express*, *25*(4), A73, doi: 10.1364/OE.25.000A73.

Marshall, J. S., and W. M. K. Palmer (1948), The Distribution of Raindrops with Size, *Journal of Meteorology*, *5*(4), 165–166, doi: 10.1175/1520-0469(1948)005<0165:TDORWS>2.0.CO;2.

Mason, S., R. Hogan, C. Westbrook, S. Kneifel, D. Moisseev, and L. von Terzi (2019), The importance of particle size distribution and internal structure for triple-frequency radar retrievals of the morphology of snow, *Atmospheric Measurement Techniques*, *12*(9), 4993–5018, doi: 10.5194/amt-12-4993-2019.

Mason, S. L., C. J. Chiu, R. J. Hogan, D. Moisseev, and S. Kneifel (2018), Retrievals of Riming and Snow Density From Vertically Pointing Doppler Radars, *Journal of Geophysical Research: Atmospheres*, *123*(24), 13,807–13,834, doi: 10.1029/2018JD028603.

Massaro, G., I. Stiperski, B. Pospichal, and M. W. Rotach (2015), Accuracy of retrieving temperature and humidity profiles by ground-based microwave radiometry in truly complex terrain, *Atmospheric Measurement Techniques*, *8*(8), 3355–3367, doi: 10.5194/amt-8-3355-2015.

Matrosov, S. Y. (1998), A Dual-Wavelength Radar Method to Measure Snowfall Rate, *Journal of Applied Meteorology*, *37*(11), 1510–1521, doi: 10.1175/1520-0450(1998)037<1510:ADWRMT> 2.0.CO;2.

Matrosov, S. Y. (2011), Feasibility of using radar differential Doppler velocity and dual-frequency ratio for sizing particles in thick ice clouds, *Journal of Geophysical Research: Atmospheres*, *116*(D17), D17,202, doi: 10.1029/2011JD015857.

Matrosov, S. Y., and R. A. Kropfli (1993), Cirrus Cloud Studies with Elliptically Polarized Ka-band Radar Signals: A Suggested Approach, *Journal of Atmospheric and Oceanic Technology*, *10*(5), 684–692, doi: 10.1175/1520-0426(1993)010<0684:CCSWEP>2.0.CO;2.

Matrosov, S. Y., T. Uttal, J. B. Snider, and R. A. Kropfli (1992), Estimation of ice cloud parameters from ground-based infrared radiometer and radar measurements, *Journal of Geophysical Research*, *97*(D11), 11,567–11,574, doi: 10.1029/92JD00968.

Matrosov, S. Y., G. G. Mace, R. Marchand, M. D. Shupe, A. G. Hallar, and I. B. McCubbin (2012), Observations of Ice Crystal Habits with a Scanning Polarimetric W-Band Radar at Slant Linear Depolarization Ratio Mode, *Journal of Atmospheric and Oceanic Technology*, *29*(8), 989–1008, doi: 10.1175/JTECH-D-11-00131.1.

Matrosov, S. Y., A. V. Ryzhkov, M. Maahn, and G. de Boer (2020), Hydrometeor Shape Variability in Snowfall as Retrieved from Polarimetric Radar Measurements, *Journal of Applied Meteorology and Climatology*, *59*(9), 1503–1517, doi: 10.1175/JAMC-D-20-0052.1.

Mattioli, V., P. Basili, S. Bonafoni, P. Ciotti, and E. R. Westwater (2009), Analysis and improvements of cloud models for propagation studies, *Radio Science*, *44*(2), RS2005, doi: 10.1029/2008RS003876.

Matus, A. V., and T. S. L'Ecuyer (2017), The role of cloud phase in Earth's radiation budget, *Journal of Geophysical Research*, *122*(5), 2559–2578, doi: 10.1002/2016JD025951.

Mätzler, C., and J. Morland (2009), Refined Physical Retrieval of Integrated Water Vapor and Cloud Liquid for Microwave Radiometer Data, *IEEE Transactions on Geoscience and Remote Sensing*, *47*(6), 1585–1594, doi: 10.1109/TGRS.2008.2006984.

McCoy, D. T., I. Tan, D. L. Hartmann, M. D. Zelinka, and T. Storelvmo (2016), On the relationships among cloud cover, mixed-phase partioning, and planetary albedo in GCMs, *Journal of Advances in Modeling Earth Systems*, *8*, 650–668, doi: 10.1002/2015MS000589.

McFarquhar, G. M., et al. (2017), Processing of Ice Cloud In Situ Data Collected by Bulk Water, Scattering, and Imaging Probes: Fundamentals, Uncertainties, and Efforts toward Consistency, *Meteorological Monographs*, *58*, 11.1–11.33, doi: 10.1175/AMSMONOGRAPHS-D-16-0007.1.

McGovern, A., and A. J. Broccoli (2022), Editorial, *Artificial Intelligence for the Earth Systems*, *1*(1), e220,014, doi: 10.1175/aies-d-22-0014.1.

McMurdie, L. A., et al. (2022), Chasing Snowstorms: The Investigation of Microphysics and Precipitation for Atlantic Coast-Threatening Snowstorms (IMPACTS) Campaign, *Bulletin of the American Meteorological Society*, *103*(5), E1243–E1269, doi: 10.1175/BAMS-D-20-0246.1.

Mech, M., M. Maahn, D. Ori, S. Kneifel, and E. Orlandi (2015), PAMTRA documentation, https://pamtra.readthedocs.io/en/latest/ (last access: 14 February 2023).

Mech, M., M. Maahn, S. Kneifel, D. Ori, E. Orlandi, P. Kollias, V. Schemann, and S. Crewell (2020), PAMTRA 1.0: the Passive and Active Microwave radiative TRAnsfer tool for simulating radiometer and radar measurements of the cloudy atmosphere, *Geoscientific Model Development*, *13*(9), 4229–4251, doi: 10.5194/gmd-13-4229-2020.

Mignani, C., J. M. Creamean, L. Zimmermann, C. Alewell, and F. Conen (2019), New type of evidence for secondary ice formation at around -15°C in mixed-phase clouds, *Atmospheric Chemistry and Physics*, *19*(2), 877–886, doi: 10.5194/acp-19-877-2019.

Mitchell, D. L. (1996), Use of Mass- and Area-Dimensional Power Laws for Determining Precipitation Particle Terminal Velocities, *Journal of the Atmospheric Sciences*, *53*(12), 1710–1723, doi: 10.1175/1520-0469(1996)053<1710:UOMAAD>2.0.CO;2.

Mitchell, D. L., and A. J. Heymsfield (2005), Refinements in the Treatment of Ice Particle Terminal Velocities, Highlighting Aggregates, *Journal of the Atmospheric Sciences*, *62*(5), 1637–1644, doi: 10.1175/JAS3413.1.

Mitchell, D. L., R. Zhang, and R. L. Pitter (1990), Mass-Dimensional Relationships for Ice Particles and the Influence of Riming on Snowfall Rates, *Journal of Applied Meteorology*, *29*(2), 153–163, doi: 10.1175/1520-0450(1990)029<0153:MDRFIP>2.0.CO;2.

Bibliography

Mitra, S. K., O. Vohl, M. Ahr, and H. R. Pruppacher (1990), A Wind Tunnel and Theoretical Study of the Melting Behavior of Atmospheric Ice Particles. IV: Experiment and Theory for Snow Flakes, *Journal of the Atmospheric Sciences*, *47*(5), 584–591, doi: 10.1175/1520-0469(1990) 047<0584:AWTATS>2.0.CO;2.

Moisseev, D., A. von Lerber, and J. Tiira (2017), Quantifying the effect of riming on snowfall using ground-based observations, *Journal of Geophysical Research: Atmospheres*, *122*(7), 4019–4037, doi: 10.1002/2016JD026272.

Morrison, H., J. A. Curry, and V. I. Khvorostyanov (2005), A New Double-Moment Microphysics Parameterization for Application in Cloud and Climate Models. Part I: Description, *Journal of the Atmospheric Sciences*, *62*(6), 1665–1677, doi: 10.1175/JAS3446.1.

Morrison, H., G. De Boer, G. Feingold, J. Harrington, M. D. Shupe, and K. Sulia (2012), Resilience of persistent Arctic mixed-phase clouds, *Nature Geoscience*, *5*(1), 11–17, doi: 10.1038/ ngeo1332.

Morrison, H., et al. (2020), Confronting the Challenge of Modeling Cloud and Precipitation Microphysics, *Journal of Advances in Modeling Earth Systems*, *12*(8), e2019MS001,689, doi: 10.1029/2019MS001689.

Mossop, S. C., A. Ono, and E. R. Wishart (1970), Ice particles in maritime clouds near Tasmania, *Quarterly Journal of the Royal Meteorological Society*, *96*(409), 487–508, doi: 10.1002/qj. 49709640910.

Mróz, K., A. Battaglia, S. Kneifel, L. P. D'Adderio, and J. Dias Neto (2020), Triple-Frequency Doppler Retrieval of Characteristic Raindrop Size, *Earth and Space Science*, *7*(3), 1–17, doi: 10.1029/2019EA000789.

Mróz, K., A. Battaglia, C. Nguyen, A. Heymsfield, A. Protat, and M. Wolde (2021a), Triple-frequency radar retrieval of microphysical properties of snow, *Atmospheric Measurement Techniques*, *14*(11), 7243–7254, doi: 10.5194/amt-14-7243-2021.

Mróz, K., A. Battaglia, S. Kneifel, L. Von Terzi, M. Karrer, and D. Ori (2021b), Linking rain into ice microphysics across the melting layer in stratiform rain: A closure study, *Atmospheric Measurement Techniques*, *14*(1), 511–529, doi: 10.5194/amt-14-511-2021.

Mülmenstädt, J., O. Sourdeval, J. Delanoë, and J. Quaas (2015), Frequency of occurrence of rain from liquid-, mixed-, and ice-phase clouds derived from A-Train satellite retrievals, *Geophysical Research Letters*, *42*(15), 6502–6509, doi: 10.1002/2015GL064604.

Murphy, A. M., A. Ryzhkov, and P. Zhang (2020), Columnar Vertical Profile (CVP) Methodology for Validating Polarimetric Radar Retrievals in Ice Using In Situ Aircraft Measurements, *Journal of Atmospheric and Oceanic Technology*, *37*(9), 1623–1642, doi: 10.1175/ JTECH-D-20-0011.1.

Murray, B. J., K. S. Carslaw, and P. R. Field (2021), Opinion: Cloud-phase climate feedback and the importance of ice-nucleating particles, *Atmospheric Chemistry and Physics*, *21*(2), 665–679, doi: 10.5194/acp-21-665-2021.

Myagkov, A., P. Seifert, M. Bauer-Pfundstein, and U. Wandinger (2016), Cloud radar with hybrid mode towards estimation of shape and orientation of ice crystals, *Atmospheric Measurement Techniques*, *9*(2), 469–489, doi: 10.5194/amt-9-469-2016.

Nakaya, U. (1954), *Snow Crystals: Natural and Artificial*, Harvard University Press, Cambridge, MA and London, England, doi: 10.4159/harvard.9780674182769.

Nemarich, J., R. J. Wellman, and J. Lacombe (1988), Backscatter and Attenuation by Falling Snow and Rain at 96, 140, and 225 GHz, *IEEE Transactions on Geoscience and Remote Sensing*, *26*(3), 319–329, doi: 10.1109/36.3034.

Nguyen, C. M., M. Wolde, A. Battaglia, L. Nichman, N. Bliankinshtein, S. Haimov, K. Bala, and D. Schuettemeyer (2022), Coincident in situ and triple-frequency radar airborne observations in the Arctic, *Atmospheric Measurement Techniques*, *15*(3), 775–795, doi: 10.5194/amt-15-775-2022.

Noh, Y.-J., C. J. Seaman, T. H. Vonder Haar, and G. Liu (2013), In Situ Aircraft Measurements of the Vertical Distribution of Liquid and Ice Water Content in Midlatitude Mixed-Phase Clouds, *Journal of Applied Meteorology and Climatology*, *52*(1), 269–279, doi: 10.1175/JAMC-D-11-0202.1.

Oolman, L. (2020), Atmospheric Soundings, http://weather.uwyo.edu/upperair/sounding.html (last access: 15 March 2023).

Ori, D., V. Schemann, M. Karrer, J. Dias Neto, L. von Terzi, A. Seifert, and S. Kneifel (2020), Evaluation of ice particle growth in ICON using statistics of multi-frequency Doppler cloud radar observations, *Quarterly Journal of the Royal Meteorological Society*, *146*(733), 3830–3849, doi: 10.1002/qj.3875.

Ori, D., L. von Terzi, M. Karrer, and S. Kneifel (2021), snowScatt 1.0: consistent model of microphysical and scattering properties of rimed and unrimed snowflakes based on the self-similar Rayleigh–Gans approximation, *Geoscientific Model Development*, *14*(3), 1511–1531, doi: 10.5194/gmd-14-1511-2021.

Orr, B. W., and R. A. Kropfli (1999), A Method for Estimating Particle Fall Velocities from Vertically Pointing Doppler Radar, *Journal of Atmospheric and Oceanic Technology*, *16*(1), 29–37, doi: 10.1175/1520-0426(1999)016<0029:AMFEPF>2.0.CO;2.

Oue, M., M. R. Kumjian, Y. Lu, J. Verlinde, K. Aydin, and E. E. Clothiaux (2015), Linear Depolarization Ratios of Columnar Ice Crystals in a Deep Precipitating System over the Arctic Observed by Zenith-Pointing Ka-Band Doppler Radar, *Journal of Applied Meteorology and Climatology*, *54*(5), 1060–1068, doi: 10.1175/JAMC-D-15-0012.1.

Bibliography

Oue, M., P. Kollias, A. Ryzhkov, and E. P. Luke (2018), Toward Exploring the Synergy Between Cloud Radar Polarimetry and Doppler Spectral Analysis in Deep Cold Precipitating Systems in the Arctic, *Journal of Geophysical Research: Atmospheres*, *123*(5), 2797–2815, doi: 10.1002/2017JD027717.

Oue, M., A. Tatarevic, P. Kollias, D. Wang, K. Yu, and A. M. Vogelmann (2020), The Cloud-resolving model Radar SIMulator (CR-SIM) Version 3.3: description and applications of a virtual observatory, *Geoscientific Model Development*, *13*(4), 1975–1998, doi: 10.5194/gmd-13-1975-2020.

Oue, M., P. Kollias, S. Y. Matrosov, A. Battaglia, and A. V. Ryzhkov (2021), Analysis of the microphysical properties of snowfall using scanning polarimetric and vertically pointing multi-frequency Doppler radars, *Atmospheric Measurement Techniques*, *14*(7), 4893–4913, doi: 10.5194/amt-14-4893-2021.

Pasquier, J. T., et al. (2022), Conditions favorable for secondary ice production in Arctic mixed-phase clouds, *Atmospheric Chemistry and Physics*, *22*(23), 15,579–15,601, doi: 10.5194/acp-22-15579-2022.

Passarelli, R. E., and H. Boehme (1983), The Orographic Modulation of Pre-Warm-Front Precipitation in Southern New England, *Monthly Weather Review*, *111*(5), 1062–1070, doi: 10.1175/1520-0493(1983)111<1062:TOMOPW>2.0.CO;2.

Paszke, A., et al. (2019), PyTorch: An imperative style, high-performance deep learning library, in *Advances in Neural Information Processing Systems*, vol. 32, edited by H. Wallach, H. Larochelle, A. Beygelzimer, F. D'Alché-Buc, E. Fox, and R. Garnett, Curran Associates, Inc., doi: 10.48550/arXiv.1912.01703.

Petäjä, T., et al. (2016), BAECC: A Field Campaign to Elucidate the Impact of Biogenic Aerosols on Clouds and Climate, *Bulletin of the American Meteorological Society*, *97*(10), 1909–1928, doi: 10.1175/BAMS-D-14-00199.1.

Petty, G. W., and W. Huang (2011), The Modified Gamma Size Distribution Applied to Inhomogeneous and Nonspherical Particles: Key Relationships and Conversions, *Journal of the Atmospheric Sciences*, *68*(7), 1460–1473, doi: 10.1175/2011JAS3645.1.

Pfitzenmaier, L., Y. Dufournet, C. M. H. Unal, and H. W. J. Russchenberg (2017), Retrieving Fall Streaks within Cloud Systems Using Doppler Radar, *Journal of Atmospheric and Oceanic Technology*, *34*(4), 905–920, doi: 10.1175/JTECH-D-16-0117.1.

Phillips, V. T. J., M. Formenton, A. Bansemer, I. Kudzotsa, and B. Lienert (2015), A Parameterization of Sticking Efficiency for Collisions of Snow and Graupel with Ice Crystals: Theory and Comparison with Observations*, *Journal of the Atmospheric Sciences*, *72*(12), 4885–4902, doi: 10.1175/JAS-D-14-0096.1.

Phillips, V. T. J., et al. (2017a), Ice Multiplication by Breakup in Ice–Ice Collisions. Part II: Numerical Simulations, *Journal of the Atmospheric Sciences, 74*(9), 2789–2811, doi: 10.1175/JAS-D-16-0223.1.

Phillips, V. T. J., J.-I. Yano, and A. Khain (2017b), Ice Multiplication by Breakup in Ice–Ice Collisions. Part I: Theoretical Formulation, *Journal of the Atmospheric Sciences, 74*(6), 1705–1719, doi: 10.1175/JAS-D-16-0224.1.

Phillips, V. T. J., S. Patade, J. Gutierrez, and A. Bansemer (2018), Secondary Ice Production by Fragmentation of Freezing Drops: Formulation and Theory, *Journal of the Atmospheric Sciences, 75*(9), 3031–3070, doi: 10.1175/JAS-D-17-0190.1.

Pierdicca, N., L. Pulvirenti, and F. S. Marzano (2006), A model to predict cloud density from midlatitude atmospheric soundings for microwave radiative transfer applications, *Radio Science, 41*(6), RS6005, doi: 10.1029/2006RS003463.

Piontek, D., L. Bugliaro, M. Schmidl, D. K. Zhou, and C. Voigt (2021), The New Volcanic Ash Satellite Retrieval VACOS Using MSG/SEVIRI and Artificial Neural Networks: 1. Development, *Remote Sensing, 13*(16), 3112, doi: 10.3390/rs13163112.

Plana-Fattori, A., A. Protat, and J. Delanoë (2010), Observing ice clouds with a Doppler cloud radar, *Comptes Rendus Physique, 11*(1), 96–103, doi: 10.1016/j.crhy.2009.11.004.

Planat, N., J. Gehring, . E. Vignon, and A. Berne (2021), Identification of snowfall microphysical processes from Eulerian vertical gradients of polarimetric radar variables, *Atmospheric Measurement Techniques, 14*(6), 4543–4564, doi: 10.5194/amt-14-4543-2021.

Pobanz, B. M., J. D. Marwitz, and M. K. Politovich (1994), Conditions Associated with Large-Drop Regions, *Journal of Applied Meteorology, 33*(11), 1366–1372, doi: 10.1175/1520-0450(1994)033<1366:CAWLDR>2.0.CO;2.

Poots, G. (2000), Introductory Remarks (Ice and Snow Accretion on Structures), *Philosophical Transactions: Mathematical, Physical and Engineering Sciences, 358*(1776), 2803–2810, doi: 10.1098/rsta.2000.0686.

Poulida, O., M. Schwikowski, U. Baltensperger, J. Staehelin, and H. Gaeggeler (1998), Scavenging of atmospheric constituents in mixed phase clouds at the high-alpine site jungfraujoch—part II. Influence of riming on the scavenging of particulate and gaseous chemical species, *Atmospheric Environment, 32*(23), 3985–4000, doi: 10.1016/S1352-2310(98)00131-9.

Praz, C., Y. A. Roulet, and A. Berne (2017), Solid hydrometeor classification and riming degree estimation from pictures collected with a Multi-Angle Snowflake Camera, *Atmospheric Measurement Techniques, 10*(4), 1335–1357, doi: 10.5194/amt-10-1335-2017.

Proske, U., V. Bessenbacher, Z. Dedekind, U. Lohmann, and D. Neubauer (2021), How frequent is natural cloud seeding from ice cloud layers (< -35°C) over Switzerland?, *Atmospheric Chemistry and Physics, 21*(6), 5195–5216, doi: 10.5194/acp-21-5195-2021.

Bibliography

Protat, A., and C. R. Williams (2011), The Accuracy of Radar Estimates of Ice Terminal Fall Speed from Vertically Pointing Doppler Radar Measurements, *Journal of Applied Meteorology and Climatology*, *50*(10), 2120–2138, doi: 10.1175/JAMC-D-10-05031.1.

Protat, A., J. Delanoë, D. Bouniol, A. J. Heymsfield, A. Bansemer, and P. Brown (2007), Evaluation of Ice Water Content Retrievals from Cloud Radar Reflectivity and Temperature Using a Large Airborne In Situ Microphysical Database, *Journal of Applied Meteorology and Climatology*, *46*(5), 557–572, doi: 10.1175/JAM2488.1.

Protat, A., S. Rauniyar, J. Delanoë, E. Fontaine, and A. Schwarzenboeck (2019), W-Band (95 GHz) Radar Attenuation in Tropical Stratiform Ice Anvils, *Journal of Atmospheric and Oceanic Technology*, *36*(8), 1463–1476, doi: 10.1175/JTECH-D-18-0154.1.

Pruppacher, H., and J. Klett (2010), *Microphysics of Clouds and Precipitation*, 954 pp., Springer Dordrecht, doi: 10.1007/978-0-306-48100-0.

Radenz, M., J. Bühl, P. Seifert, H. Griesche, and R. Engelmann (2019), peakTree: a framework for structure-preserving radar Doppler spectra analysis, *Atmospheric Measurement Techniques*, *12*(9), 4813–4828, doi: 10.5194/amt-12-4813-2019.

Rambukkange, M. P., J. Verlinde, E. W. Eloranta, C. J. Flynn, and E. E. Clothiaux (2011), Using Doppler Spectra to Separate Hydrometeor Populations and Analyze Ice Precipitation in Multilayered Mixed-Phase Clouds, *IEEE Geoscience and Remote Sensing Letters*, *8*(1), 108–112, doi: 10.1109/LGRS.2010.2052781.

Ramelli, F., et al. (2021), Microphysical investigation of the seeder and feeder region of an Alpine mixed-phase cloud, *Atmospheric Chemistry and Physics*, *21*(9), 6681–6706, doi: 10.5194/acp-21-6681-2021.

Rasmussen, R. M., J. Vivekanandan, J. Cole, B. Myers, and C. Masters (1999), The Estimation of Snowfall Rate Using Visibility, *Journal of Applied Meteorology*, *38*(10), 1542–1563, doi: 10.1175/1520-0450(1999)038<1542:TEOSRU>2.0.CO;2.

Rasp, S., M. S. Pritchard, and P. Gentine (2018), Deep learning to represent subgrid processes in climate models, *Proceedings of the National Academy of Sciences of the United States of America*, *115*(39), 9684–9689, doi: 10.1073/pnas.1810286115.

Rees, K. N., D. K. Singh, E. R. Pardyjak, and T. J. Garrett (2021), Mass and density of individual frozen hydrometeors, *Atmospheric Chemistry and Physics*, *21*(18), 14,235–14,250, doi: 10.5194/acp-21-14235-2021.

Reeves, H. D., and Y.-L. Lin (2007), The Effects of a Mountain on the Propagation of a Preexisting Convective System for Blocked and Unblocked Flow Regimes, *Journal of the Atmospheric Sciences*, *64*(7), 2401–2421, doi: 10.1175/JAS3959.1.

Reichstein, M., G. Camps-Valls, B. Stevens, M. Jung, J. Denzler, N. Carvalhais, and Prabhat (2019), Deep learning and process understanding for data-driven Earth system science, *Nature*, *566*(7743), 195–204, doi: 10.1038/s41586-019-0912-1.

Rodgers, C. D. (2000), *Inverse Methods for Atmospheric Sounding: Theory and Practice*, vol. 2, World Scientific Publishing Co.Pte.Ltd.

Roe, G. H. (2005), Orographic precipitation, *Annual Review of Earth and Planetary Sciences, 33*, 645–671, doi: 10.1146/annurev.earth.33.092203.122541.

Rogers, D. C., P. J. DeMott, S. M. Kreidenweis, and Y. Chen (1998), Measurements of ice nucleating aerosols during SUCCESS, *Geophysical Research Letters, 25*(9), 1383–1386, doi: 10.1029/97GL03478.

Rose, T., and RPG (2018), RPG-FMCW-94-SP / DP 94 GHz W-band Cloud Doppler Radar Instrument Installation , Operation and Software, http://www.radiometer-physics.de/downloadftp/pub/pdf/cloud radar/rpg-fmcw-instrument_manual.pdf (last access: 18 january 2023).

Rose, T., S. Crewell, U. Löhnert, and C. Simmer (2005), A network suitable microwave radiometer for operational monitoring of the cloudy atmosphere, *Atmospheric Research, 75*(3), 183–200, doi: 10.1016/j.atmosres.2004.12.005.

Rosenberg, R. (2005), Why is ice slippery?, *Physics Today, 58*(12), 50–55, doi: 10.1063/1.2169444.

Rosenkranz, P. W. (1998), Water vapor microwave continuum absorption: A comparison of measurements and models, *Radio Science, 33*(4), 919–928, doi: 10.1029/98RS01182.

RPG Radiometer Physics GmbH (2014), Humidity And Temperature PROfilers, https://www.radiometer-physics.de/products/microwave-remote-sensing-instruments/radiometers/humidity-and-temperature-profilers/#tabs-container-0 (last access: 20 February 2023).

Ryzhkov, A. V., and D. S. Zrnic (2019), *Radar polarimetry for weather observations*, 486 pp., Springer Atmospheric Sciences.

Sadiku, M. N. O. (1985), Refractive index of snow at microwave frequencies, *Applied Optics, 24*(4), 572–575, doi: 10.1364/AO.24.000572.

SAFIRE (2017), The SAFIRE ATR42 offers a big scientific payload, https://www.safire.fr/en/content_page/safire-utilisateurs/latr42-2.html (last access: 2 May 2023).

Saleeby, S. M., W. R. Cotton, and J. D. Fuller (2011), The Cumulative Impact of Cloud Droplet Nucleating Aerosols on Orographic Snowfall in Colorado, *Journal of Applied Meteorology and Climatology, 50*(3), 604–625, doi: 10.1175/2010JAMC2594.1.

Salonen, E., and S. Uppala (1991), New prediction method of cloud attenuation, *Electronics Letters, 27*(12), 1106–1108, doi: 10.1049/el:19910687.

Bibliography

Saunders, C., and A. Hosseini (2001), A laboratory study of the effect of velocity on Hallett–Mossop ice crystal multiplication, *Atmospheric Research*, *59-60*, 3–14, doi: 10.1016/S0169-8095(01)00106-5.

Schimmel, W., H. Kalesse-Los, M. Maahn, T. Vogl, A. Foth, P. S. Garfias, and P. Seifert (2022), Identifying cloud droplets beyond lidar attenuation from vertically pointing cloud radar observations using artificial neural networks, *Atmospheric Measurement Techniques*, *15*(18), 5343–5366, doi: 10.5194/amt-15-5343-2022.

Schmitt, C. G., and A. J. Heymsfield (2010), The Dimensional Characteristics of Ice Crystal Aggregates from Fractal Geometry, *Journal of the Atmospheric Sciences*, *67*(5), 1605–1616, doi: 10.1175/2009JAS3187.1.

Schneebeli, M., N. Dawes, M. Lehning, and A. Berne (2013), High-Resolution Vertical Profiles of X-Band Polarimetric Radar Observables during Snowfall in the Swiss Alps, *Journal of Applied Meteorology and Climatology*, *52*(2), 378–394, doi: 10.1175/JAMC-D-12-015.1.

Schneebeli, M., J. Grazioli, and A. Berne (2014), Improved Estimation of the Specific Differential Phase Shift Using a Compilation of Kalman Filter Ensembles, *IEEE Transactions on Geoscience and Remote Sensing*, *52*(8), 5137–5149, doi: 10.1109/TGRS.2013.2287017.

Schneebeli, M., A. Leuenberger, U. Siegenthaler, and P. Wellig (2020), Testing a multistatic C-band radar with a target simulator, in *2020 21st International Radar Symposium (IRS)*, pp. 222–227, IEEE, Warsaw, Poland, doi: 10.23919/IRS48640.2020.9253811.

Schultz, M. G., C. Betancourt, B. Gong, F. Kleinert, M. Langguth, L. H. Leufen, A. Mozaffari, and S. Stadtler (2021), Can deep learning beat numerical weather prediction?, *Philosophical Transactions of the Royal Society A: Mathematical, Physical and Engineering Sciences*, *379*(2194), doi: 10.1098/rsta.2020.0097.

Schwarzenboeck, A., J. Heintzenberg, and S. Mertes (2000), Incorporation of aerosol particles between 25 and 850 nm into cloud elements: Measurements with a new complementary sampling system, *Atmospheric Research*, *52*(4), 241–260, doi: 10.1016/S0169-8095(99)00034-4.

Schwarzenboeck, A., V. Shcherbakov, R. Lefevre, J. F. Gayet, Y. Pointin, and C. Duroure (2009), Indications for stellar-crystal fragmentation in Arctic clouds, *Atmospheric Research*, *92*(2), 220–228, doi: 10.1016/j.atmosres.2008.10.002.

Sharman, R. D., L. B. Cornman, G. Meymaris, J. Pearson, and T. Farrar (2014), Description and Derived Climatologies of Automated In Situ Eddy-Dissipation-Rate Reports of Atmospheric Turbulence, *Journal of Applied Meteorology and Climatology*, *53*(6), 1416–1432, doi: 10.1175/JAMC-D-13-0329.1.

Sheikh, M. Z., K. Gustavsson, E. Lévêque, B. Mehlig, A. Pumir, and A. Naso (2022), Colliding Ice Crystals in Turbulent Clouds, *Journal of the Atmospheric Sciences*, *79*(9), 2205–2218, doi: 10.1175/JAS-D-21-0305.1.

Shi, X., Z. Gao, L. Lausen, H. Wang, D. Y. Yeung, W. K. Wong, and W. C. Woo (2017), Deep learning for precipitation nowcasting: A benchmark and a new model, in *Advances in Neural Information Processing Systems*, vol. 31, pp. 5618–5628, Long Beach, CA, USA, doi: 10.48550/arXiv.1706.03458.

Shrestha, P., J. Mendrok, V. Pejcic, S. Trömel, U. Blahak, and J. T. Carlin (2022), Evaluation of the COSMO model (v5.1) in polarimetric radar space - Impact of uncertainties in model microphysics, retrievals and forward operators, *Geoscientific Model Development*, *15*(1), 291–313, doi: 10.5194/gmd-15-291-2022.

Shupe, M. D., P. Kollias, S. Y. Matrosov, and T. L. Schneider (2004), Deriving Mixed-Phase Cloud Properties from Doppler Radar Spectra, *Journal of Atmospheric and Oceanic Technology*, *21*(4), 660–670, doi: 10.1175/1520-0426(2004)021<0660:DMCPFD>2.0.CO;2.

Shupe, M. D., P. Kollias, M. Poellot, and E. Eloranta (2008), On Deriving Vertical Air Motions from Cloud Radar Doppler Spectra, *Journal of Atmospheric and Oceanic Technology*, *25*(4), 547–557, doi: 10.1175/2007JTECHA1007.1.

Skofronick-Jackson, G., et al. (2015), Global Precipitation Measurement Cold Season Precipitation Experiment (GCPEX): For Measurement's Sake, Let It Snow, *Bulletin of the American Meteorological Society*, *96*(10), 1719–1741, doi: 10.1175/BAMS-D-13-00262.1.

Sotiropoulou, G., S. Sullivan, J. Savre, G. Lloyd, T. Lachlan-Cope, A. M. Ekman, and A. Nenes (2020), The impact of secondary ice production on Arctic stratocumulus, *Atmospheric Chemistry and Physics*, *20*(3), 1301–1316, doi: 10.5194/acp-20-1301-2020.

Sotiropoulou, G., L. Ickes, A. Nenes, and A. M. Ekman (2021), Ice multiplication from ice-ice collisions in the high Arctic: Sensitivity to ice habit, rimed fraction, ice type and uncertainties in the numerical description of the process, *Atmospheric Chemistry and Physics*, *21*(12), 9741–9760, doi: 10.5194/acp-21-9741-2021.

Stein, T. H., C. D. Westbrook, and J. C. Nicol (2015), Fractal geometry of aggregate snowflakes revealed by triple-wavelength radar measurements, *Geophysical Research Letters*, *42*(1), 176–183, doi: 10.1002/2014GL062170.

Stewart, R. E., J. M. Thériault, and W. Henson (2015), On the Characteristics of and Processes Producing Winter Precipitation Types near 0°C, *Bulletin of the American Meteorological Society*, *96*(4), 623–639, doi: 10.1175/BAMS-D-14-00032.1.

Straka, J. M. (2009), *Cloud and Precipitation Microphysics: Principles and Parameterizations*, 392 pp., Cambridge University Press, doi: 10.1017/CBO9780511581168.

Straka, J. M., D. S. Zrnić, and A. V. Ryzhkov (2000), Bulk Hydrometeor Classification and Quantification Using Polarimetric Radar Data: Synthesis of Relations, *Journal of Applied Meteorology*, *39*(8), 1341–1372, doi: 10.1175/1520-0450(2000)039<1341:BHCAQU>2.0.CO;2.

Bibliography

Strapp, J., J. D. MacLeod, and L. E. Lilie (2008), Calibration Of Ice Water Content In A Wind Tunnel/Engine Test Cell Facility, in *15th International Conference on Clouds and Precipitation*, Leipzig, Germany.

Sukoriansky, S., B. Galperin, and V. Perov (2005), Application of a New Spectral Theory of Stably Stratified Turbulence to the Atmospheric Boundary Layer over Sea Ice, *Boundary-Layer Meteorology*, *117*(2), 231–257, doi: 10.1007/s10546-004-6848-4.

Sullivan, S. C., and A. Voigt (2021), Ice microphysical processes exert a strong control on the simulated radiative energy budget in the tropics, *Communications Earth and Environment*, *2*(1), 3–10, doi: 10.1038/s43247-021-00206-7.

Sullivan, S. C., C. Hoose, A. Kiselev, T. Leisner, and A. Nenes (2018), Initiation of secondary ice production in clouds, *Atmospheric Chemistry and Physics*, *18*(3), 1593–1610, doi: 10.5194/acp-18-1593-2018.

Sun, Z., and K. P. Shine (1994), Studies of the radiative properties of ice and mixed-phase clouds, *Quarterly Journal of the Royal Meteorological Society*, *120*(515), 111–137, doi: 10.1002/qj.49712051508.

Szyrmer, W., and I. Zawadzki (1999), Modeling of the melting layer. Part I: Dynamics and microphysics, *Journal of the Atmospheric Sciences*, *56*(20), 3573–3592, doi: 10.1175/1520-0469(1999)056<3573:MOTMLP>2.0.CO;2.

Szyrmer, W., and I. Zawadzki (2014), Snow studies. Part IV: Ensemble retrieval of snow microphysics from dual-wavelength vertically pointing radars, *Journal of the Atmospheric Sciences*, *71*(3), 1171–1186, doi: 10.1175/JAS-D-12-0286.1.

Takahashi, C., and A. Yamashita (1977), Production of Ice Splinters by the Freezing of Water Drops in Free Fall, *Journal of the Meteorological Society of Japan. Ser. II*, *55*(1), 139–141, doi: 10.2151/jmsj1965.55.1_139.

Takahashi, T., Y. Nagao, and Y. Kushiyama (1995), Possible High Ice Particle Production during Graupel–Graupel Collisions, *Journal of the Atmospheric Sciences*, *52*(24), 4523–4527, doi: 10.1175/1520-0469(1995)052<4523:PHIPPD>2.0.CO;2.

Tanelli, S., E. Im, S. L. Durden, L. Facheris, and D. Giuli (2002), The Effects of Nonuniform Beam Filling on Vertical Rainfall Velocity Measurements with a Spaceborne Doppler Radar, *Journal of Atmospheric and Oceanic Technology*, *19*(7), 1019 – 1034, doi: 10.1175/1520-0426(2002) 019<1019:TEONBF>2.0.CO;2.

Taszarek, M., S. Kendzierski, and N. Pilguj (2020), Hazardous weather affecting European airports: Climatological estimates of situations with limited visibility, thunderstorm, low-level wind shear and snowfall from ERA5, *Weather and Climate Extremes*, *28*, 100,243, doi: 10.1016/j.wace.2020.100243.

Tetoni, E., F. Ewald, M. Hagen, G. Köcher, T. Zinner, and S. Groß (2022), Retrievals of ice microphysical properties using dual-wavelength polarimetric radar observations during stratiform precipitation events, *Atmospheric Measurement Techniques*, *15*(13), 3969–3999, doi: 10.5194/amt-15-3969-2022.

Toledo, F., J. Delanoë, M. Haeffelin, J. C. Dupont, S. Jorquera, and C. Le Gac (2020), Absolute calibration method for frequency-modulated continuous wave (FMCW) cloud radars based on corner reflectors, *Atmospheric Measurement Techniques*, *13*(12), 6853–6875, doi: 10.5194/amt-13-6853-2020.

Toledo Bittner, F. (2021), Improvement of cloud radar products for fog surveillance networks: fog life cycle analyses and calibration methodologies, Ph.D. thesis, Institut Polytechnique de Paris, France.

Tørseth, K., W. Aas, K. Breivik, A. M. Fjeraa, M. Fiebig, A. G. Hjellbrekke, C. Lund Myhre, S. Solberg, and K. E. Yttri (2012), Introduction to the European Monitoring and Evaluation Programme (EMEP) and observed atmospheric composition change during 1972-2009, *Atmospheric Chemistry and Physics*, *12*(12), 5447–5481, doi: 10.5194/acp-12-5447-2012.

Tridon, F., and A. Battaglia (2015), Dual-frequency radar doppler spectral retrieval of rain drop size distributions and entangled dynamics variables, *Journal of Geophysical Research*, *120*(11), 5585–5601, doi: 10.1002/2014JD023023.

Tridon, F., A. Battaglia, E. Luke, and P. Kollias (2017), Rain retrieval from dual-frequency radar Doppler spectra: validation and potential for a midlatitude precipitating case-study, *Quarterly Journal of the Royal Meteorological Society*, *143*(704), 1364–1380, doi: 10.1002/qj.3010.

Tridon, F., A. Battaglia, and S. Kneifel (2020), Estimating total attenuation using Rayleigh targets at cloud top: Applications in multilayer and mixed-phase clouds observed by ground-based multifrequency radars, *Atmospheric Measurement Techniques*, *13*(9), 5065–5085, doi: 10.5194/amt-13-5065-2020.

Trömel, S., et al. (2021), Overview: Fusion of radar polarimetry and numerical atmospheric modelling towards an improved understanding of cloud and precipitation processes, *Atmospheric Chemistry and Physics*, *21*(23), 17,291–17,314, doi: 10.5194/acp-21-17291-2021.

Turner, D. D., S. A. Clough, J. C. Liljegren, E. E. Clothiaux, K. E. Cady-Pereira, and K. L. Gaustad (2007), Retrieving Liquid Water Path and Precipitable Water Vapor From the Atmospheric Radiation Measurement (ARM) Microwave Radiometers, *IEEE Transactions on Geoscience and Remote Sensing*, *45*(11), 3680–3690, doi: 10.1109/TGRS.2007.903703.

Turner, D. D., M. P. Cadeddu, U. Lohnert, S. Crewell, and A. M. Vogelmann (2009), Modifications to the Water Vapor Continuum in the Microwave Suggested by Ground-Based 150-GHz Observations, *IEEE Transactions on Geoscience and Remote Sensing*, *47*(10), 3326–3337, doi: 10.1109/TGRS.2009.2022262.

Bibliography

Turner, D. D., S. Kneifel, and M. P. Cadeddu (2016), An Improved Liquid Water Absorption Model at Microwave Frequencies for Supercooled Liquid Water Clouds, *Journal of Atmospheric and Oceanic Technology*, *33*(1), 33–44, doi: 10.1175/JTECH-D-15-0074.1.

Ulbrich, C. W., and D. Atlas (1998), Rainfall Microphysics and Radar Properties: Analysis Methods for Drop Size Spectra, *Journal of Applied Meteorology*, *37*(9), 912–923, doi: 10.1175/1520-0450(1998)037<0912:RMARPA>2.0.CO;2.

Vaillant De Guélis, T., A. Schwarzenböck, V. Shcherbakov, C. Gourbeyre, B. Laurent, R. Dupuy, P. Coutris, and C. Duroure (2019), Study of the diffraction pattern of cloud particles and the respective responses of optical array probes, *Atmospheric Measurement Techniques*, *12*(4), 2513–2529, doi: 10.5194/amt-12-2513-2019.

Vardiman, L. (1978), The Generation of Secondary Ice Particles in Clouds by Crystal–Crystal Collision, *Journal of the Atmospheric Sciences*, *35*(11), 2168–2180, doi: 10.1175/1520-0469(1978)035<2168:TGOSIP>2.0.CO;2.

Verlinde, J., M. P. Rambukkange, E. E. Clothiaux, G. M. McFarquhar, and E. W. Eloranta (2013), Arctic multilayered, mixed-phase cloud processes revealed in millimeter-wave cloud radar Doppler spectra, *Journal of Geophysical Research: Atmospheres*, *118*(23), 13,199–13,213, doi: 10.1002/2013JD020183.

Vignon, É., N. Besic, N. Jullien, J. Gehring, and A. Berne (2019), Microphysics of Snowfall Over Coastal East Antarctica Simulated by Polar WRF and Observed by Radar, *Journal of Geophysical Research: Atmospheres*, *124*(21), 11,452–11,476, doi: 10.1029/2019JD031028.

Vignon, É., S. P. Alexander, P. J. DeMott, G. Sotiropoulou, F. Gerber, T. C. J. Hill, R. Marchand, A. Nenes, and A. Berne (2021), Challenging and Improving the Simulation of Mid-Level Mixed-Phase Clouds Over the High-Latitude Southern Ocean, *Journal of Geophysical Research: Atmospheres*, *126*(7), 1–21, doi: 10.1029/2020JD033490.

Viltard, N., C. L. Gac, A. Martini, Y. Lemaître, N. Pauwels, J. Delanoë, and G. Lesage (2019), Développements radar au LATMOS pour l'études des propriétés microphysiques des nuages et des précipitations, in *ENVIREM 2019*, p. 6, Palaiseau, France.

Vogl, T., and M. Radenz (2022), pyPEAKO, https://pypeako.readthedocs.io/en/latest/ (last access: 20 February 2023).

Vogl, T., M. Maahn, S. Kneifel, W. Schimmel, D. Moisseev, and H. Kalesse-Los (2022), Using artificial neural networks to predict riming from Doppler cloud radar observations, *Atmospheric Measurement Techniques*, *15*(2), 365–381, doi: 10.5194/amt-15-365-2022.

von Terzi, L., J. Dias Neto, D. Ori, A. Myagkov, and S. Kneifel (2022), Ice microphysical processes in the dendritic growth layer: a statistical analysis combining multi-frequency and polarimetric Doppler cloud radar observations, *Atmospheric Chemistry and Physics*, *22*(17), 11,795–11,821, doi: 10.5194/acp-22-11795-2022.

Wang, Y., Y. You, and M. Kulie (2018), Global Virga Precipitation Distribution Derived From Three Spaceborne Radars and Its Contribution to the False Radiometer Precipitation Detection, *Geophysical Research Letters*, *45*(9), 4446–4455, doi: 10.1029/2018GL077891.

Wang, Z., et al. (2012), Single Aircraft Integration of Remote Sensing and In Situ Sampling for the Study of Cloud Microphysics and Dynamics, *Bulletin of the American Meteorological Society*, *93*(5), 653–668, doi: 10.1175/BAMS-D-11-00044.1.

Wegener, A. (1911), *Thermodynamik der Atmosphäre*, Barth, J.A., Leibzig.

Westwater, E. R., Y. Han, M. D. Shupe, and S. Y. Matrosov (2001), Analysis of integrated cloud liquid and precipitable water vapor retrievals from microwave radiometers during the Surface Heat Budget of the Arctic Ocean project, *Journal of Geophysical Research: Atmospheres*, *106*(D23), 32,019–32,030, doi: 10.1029/2000JD000055.

Wexler, A. R., R. J. Reed, and J. Honig (1954), Atmospheric Cooling by Melting Snow, *Bulletin of the American Meteorological Society*, *35*(2), 48–51.

White, C. H., A. K. Heidinger, and S. A. Ackerman (2022), Probing the Explainability of Neural Network Cloud-Top Pressure Models for LEO and GEO Imagers, *Artificial Intelligence for the Earth Systems*, *1*(4), 1–19, doi: 10.1175/AIES-D-21-0001.1.

Wieder, J., et al. (2022), Retrieving ice-nucleating particle concentration and ice multiplication factors using active remote sensing validated by in situ observations, *Atmospheric Chemistry and Physics*, *22*(15), 9767–9797, doi: 10.5194/acp-22-9767-2022.

Wildeman, S., S. Sterl, C. Sun, and D. Lohse (2017), Fast Dynamics of Water Droplets Freezing from the Outside In, *Physical Review Letters*, *118*(8), 084,101, doi: 10.1103/PhysRevLett.118.084101.

Williams, C. R., and K. S. Gage (2009), Raindrop size distribution variability estimated using ensemble statistics, *Annales Geophysicae*, *27*(2), 555–567, doi: 10.5194/angeo-27-555-2009.

Williams, C. R., R. M. Beauchamp, and V. Chandrasekar (2016), Vertical Air Motions and Raindrop Size Distributions Estimated Using Mean Doppler Velocity Difference From 3- and 35-GHz Vertically Pointing Radars, *IEEE Transactions on Geoscience and Remote Sensing*, *54*(10), 6048–6060, doi: 10.1109/TGRS.2016.2580526.

Wilson, J. W. (1977), Effect of Lake Ontario on Precipitation, *Monthly Weather Review*, *105*(2), 207–214, doi: 10.1175/1520-0493(1977)105<0207:EOLOOP>2.0.CO;2.

Wolfensberger, D., M. Gabella, M. Boscacci, U. Germann, and A. Berne (2021), RainForest: a random forest algorithm for quantitative precipitation estimation over Switzerland, *Atmospheric Measurement Techniques*, *14*(4), 3169–3193, doi: 10.5194/amt-14-3169-2021.

Yau, M. K., and R. R. Rogers (1989), *A Short Course in Cloud Physics*, Elsevier.

Bibliography

Young, G., T. Lachlan-Cope, S. J. O'Shea, C. Dearden, C. Listowski, K. N. Bower, T. W. Choularton, and M. W. Gallagher (2019), Radiative Effects of Secondary Ice Enhancement in Coastal Antarctic Clouds, *Geophysical Research Letters*, *46*(4), 2312–2321, doi: 10.1029/2018GL080551.

Zawadzki, I., F. Fabry, and W. Szyrmer (2001), Observations of supercooled water and secondary ice generation by a vertically pointing X-band Doppler radar, *Atmospheric Research*, *59-60*, 343–359, doi: 10.1016/S0169-8095(01)00124-7.

Zeiler, M. D., D. Krishnan, G. W. Taylor, and R. Fergus (2010), Deconvolutional networks, in *2010 IEEE Computer Society Conference on Computer Vision and Pattern Recognition*, pp. 2528–2535, IEEE, San Francisco, CA, USA, doi: 10.1109/CVPR.2010.5539957.

Zhang, G., J. Vivekanandan, and M. K. Politovich (1999), Scattering effects on microwave passive remote sensing of cloud parameters, in *8th Conference on Aviation, Range, and Aerospace Meteorology*, pp. 497–501, American Meteorological Society, Dallas, TX, USA.

ANNE-CLAIRE BILLAULT-ROUX

+41 79 537 36 95 ⋄ anne-claire.billault-roux@epfl.ch

Chemin des bosquets 3b, 1009 Pully (CH)

EDUCATION

Doctoral studies, Environmental remote sensing laboratory, EPFL (*Switzerland*) 2019 – 2023
  Thesis: "Snowfall microphysics: a dual-frequency and Doppler spectral perspective"
  Supervisor: Prof. Alexis Berne

Master of science, Environmental Engineering, University of California, Berkeley (*USA*) 2017 – 2018
  Major: Environmental fluid mechanics

Engineering studies, École polytechnique (*France*) 2014 – 2018

WORK EXPERIENCE

Teaching Assistant, EPFL (*Switzerland*) 2019 – 2022
  BSc courses: Remote Sensing, Electromagnetism
  MSC courses: Spatial Statistics and Analysis, Atmospheric Processes

Volunteer, L'Arche (*France*) 2018 – 2019

Teaching Assistant, University of California, Berkeley (*USA*) 2018
  BSc course: Introduction to Computer Programming

Research intern, Helmholtz Zentrum Berlin (*Germany*) 2017
  Research topic: Industry-compatible process for the fabrication of high-efficiency solar cells

Intern as an engineer in the industry, Moët & Chandon (*France*) 2016
  Launched the upgrading of a manufacturing line to improve the safety of equipment

Oral examiner in Physics, Lycée Sainte Geneviève (*France*) 2016

SKILLS

Programming languages	Python, Matlab, Bash (Advanced)
	R, C++, Fortran (Basics)
Various tools & software	Latex, Microsoft Office, QGIS, Inkscape
Languages	French (native language)
	English (fluent)
	German (intermediate)

PUBLICATIONS

- Billault-Roux, A.-C., P. Georgakaki, J. Gehring, L. Jaffeux, A. Schwarzenboeck, P. Coutris, A. Nenes, A. Berne (2023). Distinct secondary ice production processes observed in radar Doppler spectra: insights from a case study. Under review for *Atmospheric Chemistry and Physics*, doi:/10.5194/egusphere-2023-478

- Jorquera, S., F. Toledo Bittner, J. Delanoë, A. Berne, A.-C. Billault-Roux, A. Schwarzenboeck, F. Dezitter, N. Viltard, A. Martini (2023). Calibration transfer methodology for cloud radars based on ice cloud observations. *Journal of Atmospheric and Oceanic Technology*, in press, doi:10.1175/JTECH-D-22-0087.1

205

- Billault-Roux, A.-C., G. Ghiggi, L. Jaffeux, A. Martini, N. Viltard, A. Berne (2023). Dual-frequency spectral radar retrieval of snowfall microphysics: a physics-driven deep learning approach. *Atmospheric Measurement Techniques*, 16(4), 911–940, doi:10.5194/amt-16-911-2023

- Billault-Roux, A.-C. and J. Grazioli et al. (2023). ICE GENESIS: Synergetic aircraft, ground-based, remote sensing and in-situ measurements of snowfall microphysical properties. *Bulletin of the American Meteorological Society*, 104(2), E367—E388, doi:10.1175/BAMS-D-21-0184.1

- Ferrone, A., A.-C. Billault-Roux, A. Berne (2022). ERUO: a spectral processing routine for the Micro Rain Radar PRO (MRR-PRO). *Atmospheric Measurement Techniques*, 15(11), 3569-–3592, doi:10.5194/amt-15-3569-2022.

- Grazioli, J., G. Ghiggi, A.-C. Billault-Roux, A. Berne (2022). MASCDB, a database of images, descriptors and microphysical properties of individual snowflakes in free fall. *Scientific Data*, 9, 186, doi:10.1038/s41597-022-01269-7.

- Georgakaki, P., G. Sotiropoulou, É. Vignon, A.-C. Billault-Roux, A. Berne, A. Nenes (2022). Secondary ice production processes in wintertime alpine mixed-phase clouds. *Atmospheric Chemistry and Physics*, 22(3), 1965–1988, doi:10.5194/acp-22-1965-2022.

- Gehring, J., É. Vignon, A.-C. Billault-Roux, A. Ferrone, A. Protat, S. P. Alexander, A. Berne (2022). Orographic Flow Influence on Precipitation During an Atmospheric River Event at Davis, Antarctica. *Journal of Geophysical Research: Atmospheres*, 127(2), doi:10.1029/2021JD035210.

- Billault-Roux, A.-C. and A. Berne (2021). Integrated water vapor and liquid water path retrieval using a single-channel radiometer. *Atmospheric Measurement Techniques*, 14(4), 2749–2769, doi:10.5194/ amt-14-2749-2021

- Gehring, J., A. Ferrone, A.-C. Billault-Roux, N. Besic, K. D. Ahn, G. Lee, A. Berne (2021). Radar and ground-level measurements of precipitation collected by the École Polytechnique Fédérale de Lausanne during the International Collaborative Experiments for PyeongChang 2018 Olympic and Paralympic winter games. *Earth System Science Data*, 13(2), 417–433, doi:10.5194/essd-13-417-2021

CONFERENCES

- Billault-Roux, A.-C., G. Ghiggi, L. Jaffeux, A. Martini, N. Viltard, A. Berne (2022). Snowfall microphysics retrieved from X- and W-band Doppler spectrograms: a deep-learning based approach. 11th *European Conference on Radar in Meteorology and Hydrology*, Locarno, Switzerland.

- Billault-Roux, A.-C., G. Ghiggi, L. Jaffeux, A. Martini, N. Viltard, A. Berne (2022). Snowfall microphysics retrieved from X- and W-band Doppler spectrograms: a deep-learning based approach. 10th *Workshop of the International Precipitation Working Group*, Fort Collins, Colorado, United States.

- Billault-Roux, A.-C., G. Ghiggi, A. Berne (2022). Dual-frequency spectral radar retrieval of snowfall microphysics: a deep-learning based approach. *EGU General Assembly*, Vienna, Austria.

- Billault-Roux, A.-C., M. Monnet, J. Grazioli, J. Delanoë, S. Jorquera, N. Viltard, A. Martini, C. Le Gac, N. Pauwels, G. Lesage, A. Berne (2021). ICE GENESIS 2021 campaign: Ground-based observations of snowfall. 3rd *International Summer Snowfall Workshop*, Virtual event.

- Billault-Roux, A.-C. and A. Berne (2019). Dual-frequency spectral radar retrieval of snow microphysical properties. 2nd *International Summer Snowfall Workshop*, Hyytiälä Research Station, Finland.

« La neige ne se décrit pas, aussi je la laisse en blanc. »

— Henry Russell, *Souvenirs d'un montagnard*

Signs of secondary ice production occurring in an orographic cloud? Photograph of graupel and columnar crystals observed on 10 December 2022 in Chamonix, France.